Vertical External Cavity Surface Emitting Lasers Utilising Quantum Dot Active Regions

A thesis presented in fulfilment
of the requirements for the degree of
Doctor of Philosophy

By

Peter Jürgen Schlosser

Department of Physics, University of Strathclyde

2011

Signed: Date:

Für

Mutti & Vati

Ihr seid der Grundstein
für alles was ich bin und bisher erreicht habe.
Das Fundament
das mich in jeder Hinsicht stützt;
auf das ich stets und uneingeschränkt Vertrauen kann.

Danke

Live is like a lucid dream…
but sometimes rewarding!

Acknowledgement

This work wouldn't have been possible without the help and contribution of various people. My gratitude and thanks belongs to:

- My first supervisor Dr. Jennifer E. Hastie. Thank you for accepting me as a PhD student; for welcoming me to your young research group and for giving me the opportunity to become part of this team, even after the end of my three year project. Thanks also for your understanding, trust, encouragement and support even outside your duties as a supervisor, such as with the exchange programme with PKU and for listening to my worries.
- Dr. Stephane Calvez, my second internal supervisor. I am very grateful and indebted to you for the extended and very valuable discussions, your explanations and hints towards experimental setups and theoretical understanding. Thanks also for your support around MathCad related programming issues.
- Prof. Martin D. Dawson for the support over the whole period of my PhD project. I am aware that many important aspects with respect to my project passed your careful and final supervision.
- Dr. Thorsten Ackemann, for being my external supervisor and chairing my first and second year viva.

My gratitude also belongs to:

- Dr. Andrey, B. Krysa, from the EPSRC National Centre for III-V Technologies at the University of Sheffield. His expertise and devotion towards the growth, development and improvement of the InP QDs. For his valuable input towards this project with any growth and property related aspect.
- Dr. Martin T. Andersen, during that time PhD student at the Technical University of Denmark, who visited the Institute of Photonics over a period of three months and with whom I had the opportunity to conduct the sum frequency generation experiments, discussed in chapter 5.

- Dr. Julie Lutti from Cardiff University. Who although very close to her maternity leave showed much patience towards my questions and spent much time and energy with me in the lab for the time resolved PL measurements at the Department of Physics and Astronomy (Cardiff University, group of Prof. Peter M. Smowton).
- Wang Lei, a PhD student at the School of Physics (Peking University, group of Prof. X. Hu), who helped to do the cathodoluminescence/SEM and TEM images. I'm also very thankful for his help and support outside university matters during my stay at PKU and for being a good friend.
- Mrs. Lynda McLaughlin for her kindness and help with any administrative matter.
- The PhD students at the IoP. We've shared so much time, discussions, talks and worries together. They'll always remain in my memory.
- All the IoP staff not mentioned by name, but deserve my thanks nonetheless.

I am futher indebted to:

- Dieter M. Schlosser, my brother, who was always there for me, as long as I can remember. Danke Bruder! Schade, dass wir so weit voneinander entfernt Leben und nicht mehr viel Zeit miteinander verbringen können.
- Prof. Stephan Sotier, whom I see as a mentor during my undergraduate studies. I wouldn't have been able study abroad or start a PhD project in the UK without his support.
- Herr Bacher, my physics teacher in twelfth grade. He gave me guidance and convinced me to study Physics.
- Family Booth, who became more than landlords and friends to me during the past four years. I see them as an extension to my family.
- All my family and friends, who remain unnamed here thanks, thanks, thanks to all of you.

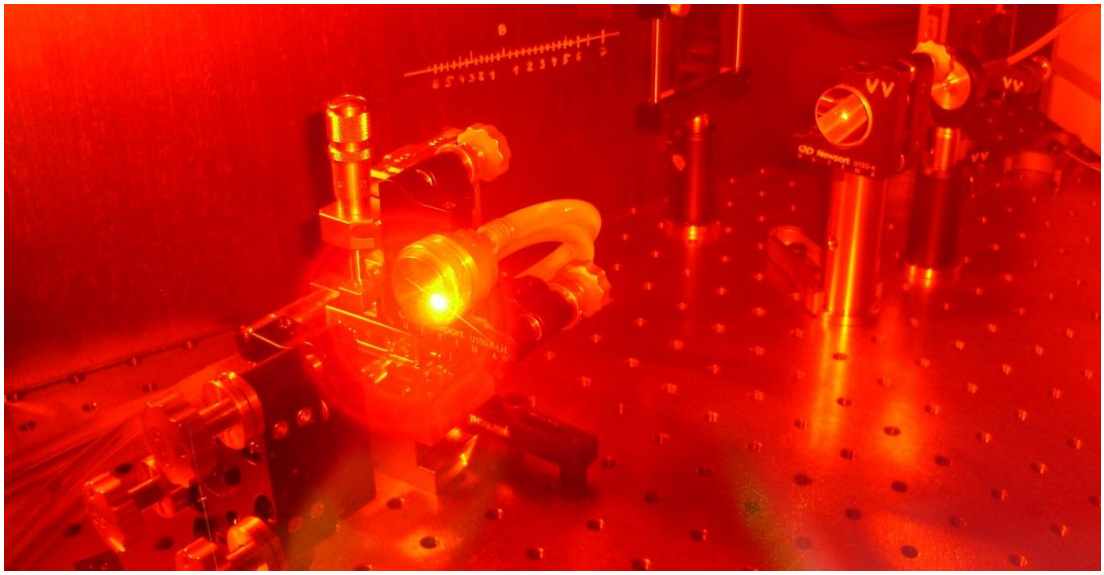

First demonstration of laser emission from a VECSEL incorporating multiple InP quantum-dot-layers inside the active region for the generation of visible light in the 700-760 nm range.

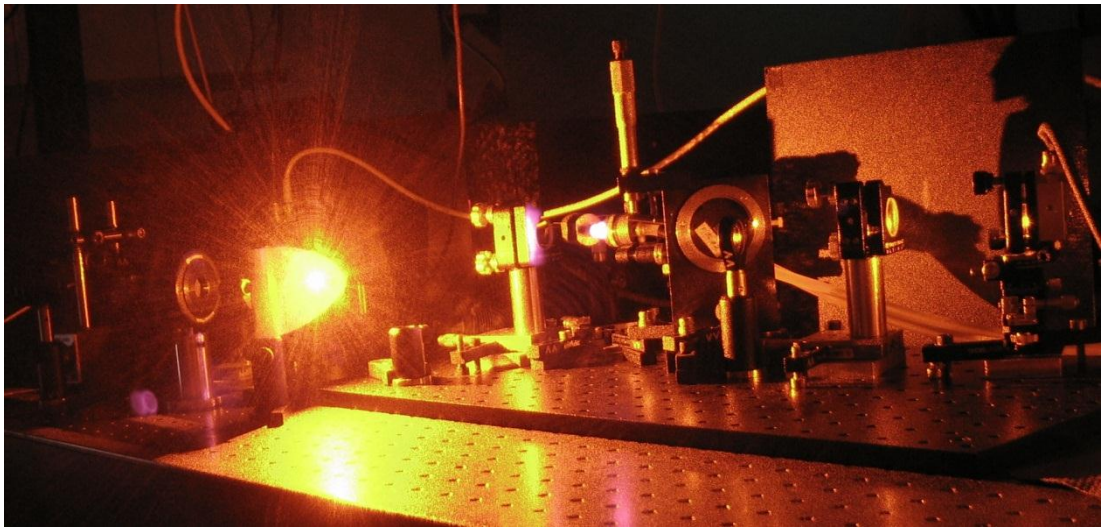

Generation of visible light at 593 nm via sum-frequency non-linear conversion inside a QW-based VECSEL cavity in combination with a single passing solid-state-laser beam.

Abstract

This work discusses the design and characterisation, together with the first demonstration of quantum dot based vertical external cavity surface emitting lasers (VECSELs). The author had the opportunity to research InAs/GaAs submonolayer quantum dot based devices of the first growth campaign, designed for emission at 1040 nm. These devices suffered from a very short lifetime. Conclusions drawn from the characterisation work helped to improve the fabrication process, which led to more stable devices. Following this initial work, InP quantum dots embedded in GaInP quantum wells were used as gain layers in $(Al_xGa_{1-x})_{0.51}In_{0.49}P$ VECSELs for the first time. These devices showed fundamental emission around 730 nm, a wavelength region which could not be addressed by surface emitting laser devices so far. InP quantum dots and their fabrication are not nearly as well researched as their InAs/GaAs counterparts. It is thus not surprising that the characterised structures suffered from a rough surface morphology, which could be related to non-coherently strained dots. Difficulties to match the designed resonances to the peak quantum dot gain also limited the laser performance of these devices. Nevertheless, the first demonstration of laser emission proves the feasibility and further development in growth might lead to major improvements in future.

In a parallel project, generation of visible yellow-orange light was achieved utilising the high intra-cavity powers of a 1060 nm quantum well VECSEL in combination with the single passing 1342 nm beam from a diode pumped solid state laser. A non-linear crystal, cut and periodically poled for quasi phase matched sum frequency mixing was placed inside the high finesse VECSEL cavity for efficient conversion of coherent light at 593 nm.

Table of Contents

Chapter 1:

Introduction

Vertical external cavity surface-emitting lasers (VECSELs) are a relatively new laser format. First demonstrated in 1991 by Jiang et al. [1], they are closely related to the vertical cavity surface emitting laser (VCSEL), which was first realised in 1979 by Soda et al. [2], depicted in Fig. 1-1 b). The surface-emitting format of VCSEL devices, where a very thin active region is sandwiched between two high reflecting mirrors (usually monolithically grown) leads to a low laser threshold current density and the generation of near diffraction limited output beams, advantageous for e.g. efficient coupling of light into optical fibres for telecommunications. They are fabricated on a wafer scale, and thus can be mass produced. Quality control is done without post growth processing, which makes the fabrication cheap. High "wall-plug" efficiencies, together with their superb output beam profile have contributed to their commercial success in recent years. Despite the advantages of this cavity design, it restricts the maximum output power to the mW range, due to the very short cavity length, high reflectivity values of the two fixed cavity mirrors and small apertures, required to achieve high beam qualities [3].

VECSELs are able to overcome these limitations by replacing one of the integrated high reflective mirrors with an external output coupler and using optical pumping schemes for carrier excitation. They combine the previously mentioned advantages characteristic to VCSELs with the high output powers and external cavity arrangement characteristic of solid-state lasers.

Since the first demonstration of VECSELs, a very steep curve in structure improvement and application versatility has been achieved, recently summarised in different publications by Calvez et al. and Schulz et al. in [4,5] and a book "Semiconductor Disk Lasers" [6]. Commercial products have also emerged for a

variety of different applications for science, communication, medicine, forensics and displays. They have also started to replace expensive and bulky solid-state and gas laser systems in some areas. Due to the very close relationship to VCSELs, together with the confusion caused by the similarly sounding acronym, different names have come into use. In the literature, VECSELs are also known as optically-pumped semiconductor lasers (OPSLs) or semiconductor disk lasers (SDLs). Herein the acronym VECSEL is used throughout.

This chapter provides an overview of semiconductor lasers, how they function and the development of the VECSEL format from edge emitting diode laser devices (see Fig. 1-1 a). Reported VECSEL structures are summarised using quantum well and quantum dot active regions, with respect to their maximum output power and emission wavelength, both for fundamental emission and non-linear frequency conversion. Further important recent developments using the versatility of the VECSEL format are also summarised. The chapter concludes with an outline of the following chapters.

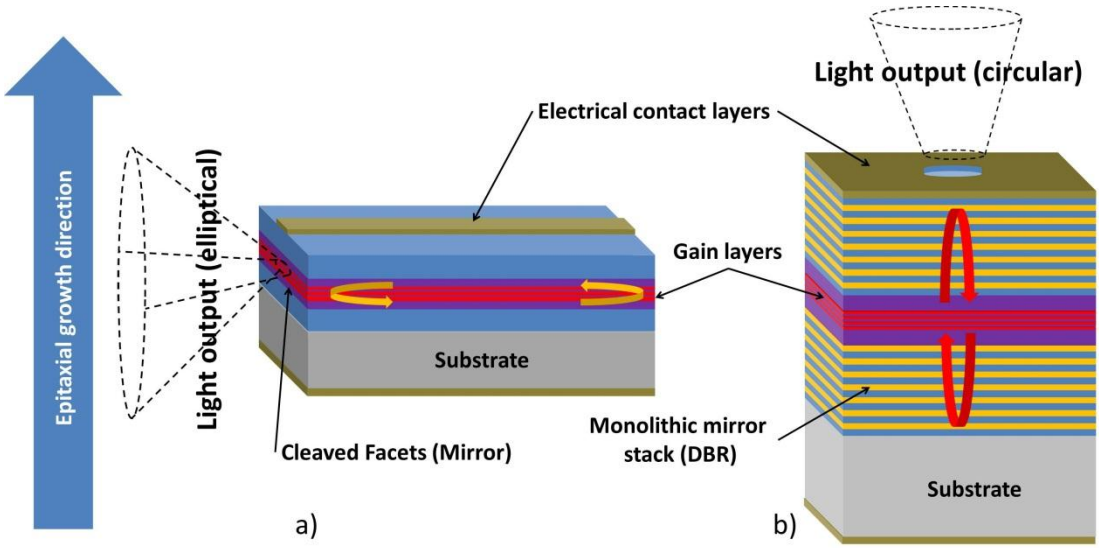

Fig. 1-1 Comparison between basic schematic of electrically injected a) edge emitting diode laser structure and b) VCSEL with indication of the epitaxial growth direction and output beam characteristics [7].

1.1 From the diode laser to the VECSEL

This work deals with group III-V semiconductor devices fabricated by Metal Organic Vapour Phase Epitaxy (MOVPE). The following introduction presents a short discussion on the development of semiconductor laser devices from the diode up to the invention of the VECSEL.

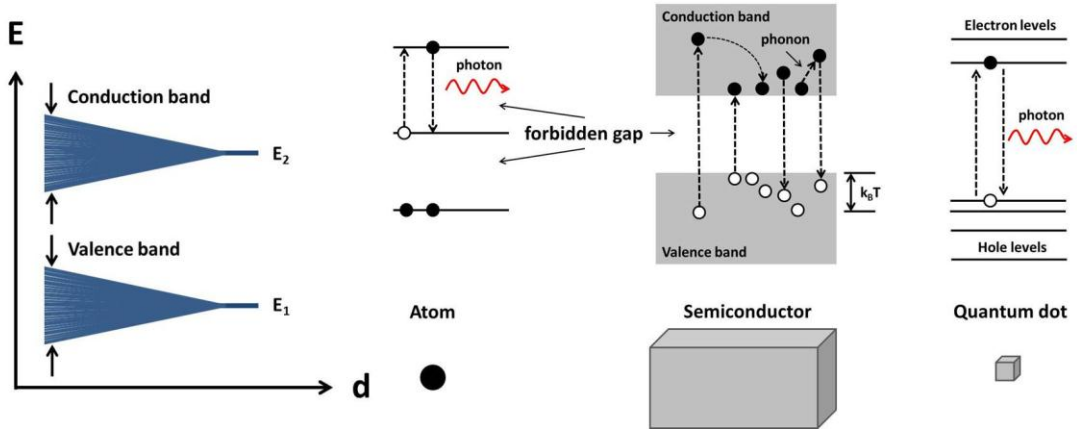

Fig. 1-2 Left: Atomic energy levels as a function of atomic separation in a bulk material with N atoms [8]. Right: Schematic of the energy level/band distribution, with radiative photon transitions present in an atom (left), bulk semiconductor (middle) and an epitaxial quantum dot (right) [9].

A solid-state crystal is a structure of N atoms, ordered within a periodic lattice. Each of these atoms consists of a positively charged atomic nucleus, surrounded by electron orbitals. Inner electrons are tightly bound to the nucleus and effectively form a positively charged ion. Electrons from the partially filled outer orbitals are called valence electrons and define important properties, such as the chemical binding and carrier transport behaviour. The formation of energy bands can be understood as illustrated in Fig. 1-2 left, where E_1 and E_2 denote the electron ground state and excited state respectively. If the distance, d, between neighbouring atoms within a periodic crystal consisting of N atoms is large, the atoms can be regarded as isolated and the energy levels are degenerate. A reduction of the distance between the atoms causes an increasing overlap of the electron wavefunctions. Pauli's exclusion principle forces the N-fold degenerate levels to split into an energy band of N closely spaced levels. The ground state levels E_1 corresponds thus to the valence band and

the excited state E_2 to the conduction band [8], also shown in the schematic of Fig. 1-2 right.

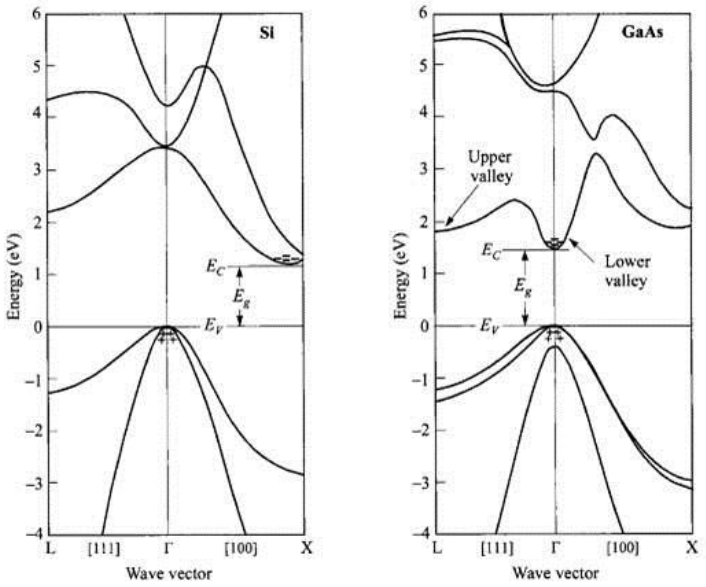

Fig. 1-3 Energy bandgap vs. wave vector for Silicon (Si), being an indirect and Gallium Arsenide (GaAs) a direct semiconductor. Electrons occupying the upper and holes the lower energy state are denoted by – and + signs. E_C and E_V mark the band edges of the upper (conduction) and lower (valence) band respectively. The Bandgap energy is denoted as E_g [10].

A way to analyse the band structure in the vicinity of a band maximum or minimum of a group III-V semiconductor is the application of the **k·p** method [11]. Valence electrons are delocalised in a semiconductor and can be described by Bloch wavefunctions, taking the periodic potential of the crystal lattice into account. Substitution of the wavefunction into Schrödinger's wave equation gives the eigenvalues of the electron energy, E, in dependence on the momentum, k. For group III-V semiconductors with the crystalline lattice structure in the zincblende configuration the conduction and valence bands can be described by atomic orbital models. The conduction band is s-like and the valence band p-type in nature, being split into three distinct subbands, the heavy-hole (hh), light-hole (lh), and the spin-orbit split off band (so). Fig. 1-3 shows the calculated energy-momentum (E-k) relationship for Silicon (Si) and Gallium Arsenide (GaAs), having an indirect and direct transition respectively [10]. The single conduction and three valence bands are depicted for GaAs, where the so-band is separated from the hh- and lh-bands. The hh-band is the ground state in an unstrained III-V semiconductor. As shown in this

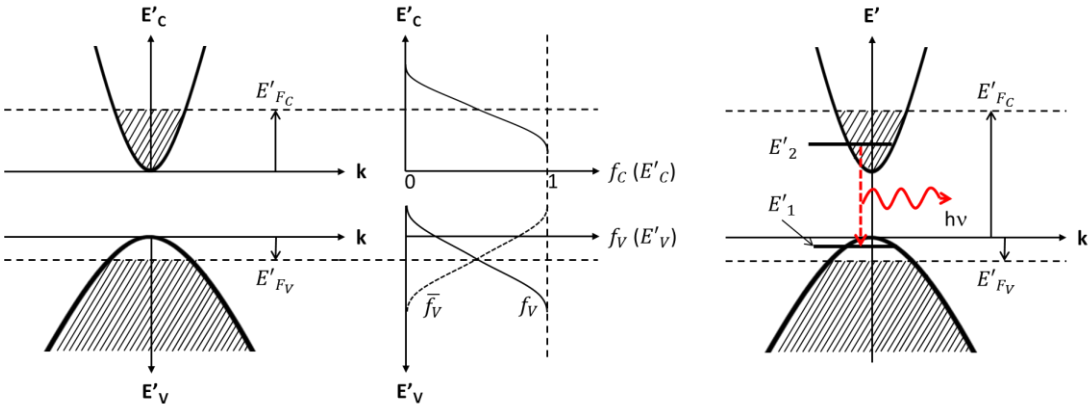

Fig. 1-4 Left: E-k relationship of the conduction and valence band. Hashed regions denote states occupied with electrons. Middle: Occupation probability $f_c(E_c)$ and $f_v(E_v)$ of the conduction band and valence band. $\bar{f}_v = (1 - f_v)$ and denotes the occupation probability of hole states in the valence band. Right: Condition for achieving net gain in a semiconductor. E'_{F_C}, E'_{F_V} are the quasi-Fermi levels and E'_2, E'_1 are two energy levels in the conduction and valence band respectively with the energy separation hν [12].

figure, the energy-band structure of a semiconductor has an energy bandgap, E_g, being the minimum separation between the conduction and valence band edge, denoted by E_C and E_V. In this region the presence of electrons is forbidden. In case of a direct bandgap semiconductor, the electrons and holes near the conduction and valence band edge respectively have the same momentum and recombination can occur directly by the emission of a photon. Non-radiative recombination is dominant in indirect bandgap semiconductors, as direct radiative transitions are much less likely. The recombination process requires an intermediate momentum transfer from the electron to the lattice atoms in form of vibrational energy (i.e. phonons), increasing the temperature. Thus laser devices are based on direct bandgap semiconductors. The population of the conduction and valence band with electrons and holes respectively is also depicted in Fig. 1-4, where free charge carriers can be generated by optical or electrical excitation. Energy bands make carrier excitation in semiconductors very flexible as the number of transitions corresponds to the available number of states in either the conduction or valence band. Fast intraband relaxation processes (~1 ps), such as electron-phonon interactions reduce the energy of these excited carriers until they reach the lowest available state, where they are stored for a time range of ~1 ns before they recombine radiatively. This much longer upper-state lifetime, compared to the intraband relaxation time, creates a quasi-equilibrium of the carriers within the bands, even though the overall system is

not in a state of thermal equilibrium. The boundary between occupied and vacant states within the band is called quasi-Fermi level, E_F'. E_F' increases with carrier density. The probability that a state within the conduction or valance band is occupied with an electron is $f_C(E_C')$ and $f_V(E_V')$ respectively:

$$f_c(E_C') = \frac{1}{1 + exp\left[\left(E_C' - E_{F_C}'\right)/\mathrm{k}_B\mathrm{T}\right]} \qquad \text{Equation [1-1]}$$

and

$$f_V(E_V') = \frac{1}{1 + exp\left[\left(E_{F_V}' - E_V'\right)/\mathrm{k}_B\mathrm{T}\right]}. \qquad \text{Equation [1-2]}$$

where $\mathrm{k}_B T$ is the thermal energy incorporating Boltzmann's constant and crystal temperature. The probability that the holes occupy the states within the valence band is $\overline{f_v} = (1 - f_v)$ as shown in Fig. 1-4 middle. The right hand side of this figure shows the case where net gain is achieved. E_2', E_1' are two energy states within the conduction and valence band with the energy separation hυ. These energy levels lie between the band edges and the quasi-Fermi levels E_{F_C}' and E_{F_V}'. The general condition for net gain is $f_c(E_2') > f_V(E_1')$ and it can be shown that this corresponds to:

$$E_2' - E_1' < E_{F_C}' - E_{F_V}' \qquad \text{Equation [1-3]}$$

This is the case, when the stimulated emission exceeds the absorption rate, which is fulfilled if the upper state E_2' lies within a zone, which is occupied by electrons and and E_1' within an empty one. The energy separation between these two states is larger than the bandgap energy, thus:

$$E_g \leq (E_2' - E_1' = h\upsilon) \leq E_{F_C}' - E_{F_V}' \qquad \text{Equation [1-4]}$$

$E_{F_C}' - E_{F_V}' = E_g$ is called transparency condition, where the absorption is equal to the stimulated emission rate.

It is important to state that the effective mass of the holes in the valence band is much larger than that of electrons in the conduction band for III-V semiconductors. According to this asymmetry, the density of states is larger in the valence band and

the quasi-Fermi level enters the conduction band before it can reach the valence band edge. In order to achieve transparency, higher carrier densities are required [12]. Improvement can be achieved either by:

- p-type doping, where the Fermi level is brought closer to the valence band edge
- misfit strain, changing the band structure and thus the effective mass of holes in the valence bands [13]

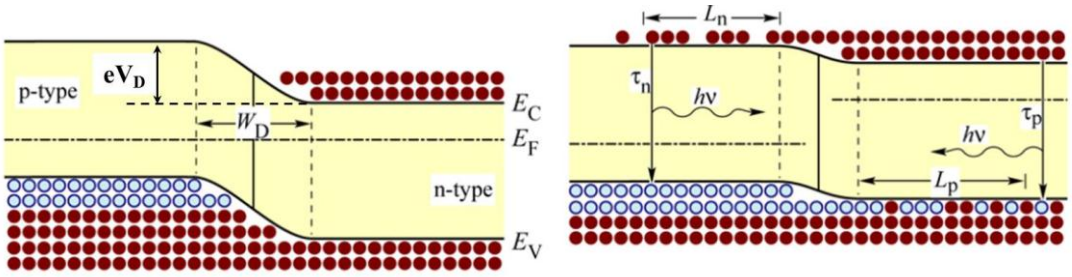

Fig. 1-5 Heterojunction between a p- and n-type semiconductor. No bias (left) and forward bias (right) applied. W_D represents the depletion layer width. E_C, E_V and E_F are the conduction band edge, valence band edge and Fermi level energy. L_n, L_p are the diffusion length τ_n, τ_p the upper state lifetimes of electrons and holes respectively. hν is the photon energy [14].

Doping is a way to alter the electrical properties of a semiconductor and is required primarily for electrically-pumped devices. Doping changes the majority carrier density, creating p- or n-type semiconductors. This shifts the Fermi energy, E_F, from the bandgap centre (undoped) towards the valence band (p-type) or conduction band (n-type) edge respectively. Bringing an n- and p-type semiconductor of the same composition into contact, creates a heterojunction as depicted in Fig. 1-5 [14]. The depletion layer, W_D, marks the transition region between p- and n-type nature, where the holes and electrons near the junction diffuse into the region of opposite conductivity type, creating a high resistivity area depleted of free carriers. When no bias voltage is applied to the junction, the depleted area experiences a potential, called diffusion voltage V_D, created by the dopants within the region. The Fermi energy, E_F, in this case is constant throughout the junction. This potential is a barrier for the free carriers, preventing them from diffusing into the region of opposite conductivity type. Application of a bias enables the control of the barrier height such that a forward-bias decreases the potential barrier. If the applied forward-bias is high

enough carriers can overcome the barrier and diffuse into the region of opposite conductivity type, where they are able to recombine radiatively, Fig. 1-5 (right). The mean diffusion length is depicted by L_n and $L_p$with upper state lifetimes of τ_n and τ_p for electrons and holes respectively. This figure also illustrates that the distribution of the carriers depends on the diffusion length with the carrier density decreasing with distance from the depletion region. In terms of semiconductor laser structures, this allowed pulsed laser action to be achieved only at low temperatures with high threshold current densities. The first semiconductor heterostructure laser used an electrically pumped heterojunction between p- and n-doped GaAs and was published by Hall et al. [15] in 1962 (only two years after the first demonstration of laser emission by Maiman et al. [16] using a ruby crystal). A way to improve this was the development of the double-heterojunction (DH) or double-heterostructure (DHS) depicted in Fig. 1-6 (left), where a lower bandgap semiconductor of thickness W_{DH} was sandwiched between higher bandgap compounds (barriers) to confine the generated carriers within a defined region, increasing the carrier density and thus decreasing the threshold current density. The appearance of the double-heterojunction allowed a more efficient carrier and optical (waveguiding) confinement and continuous wave (cw) room temperature emission was reported in the 1970 e.g. [17]. The thickness W_{DH} of these confinement layers was still large with respect to the de Broglie wavelength ($\lambda = h/p$) of free charge carriers, where h is Planck's constant and p the momentum [18]. Reduction of the W_{DH} to thicknesses in the range or smaller than the de Broglie wavelength (10 nm), confines particles to discrete energy levels within the conduction and valence band, illustrated in Fig. 1-7 for different degrees of quantum confinement. On this basis, van der Ziel and Dingle et al. introduced the quantum well (QW) based diode laser in 1975 [19,20] which allowed a further improvement of semiconductor laser devices. Control of the QW thickness and lattice mismatch (strain) allows for more flexibility to set the emission wavelength aside from the choice of material composition. Fig. 1-6 (right) shows carrier relaxation of excited charge carriers from the barrier states into the QW ground state via phonon emission, from where they recombine radiatively.

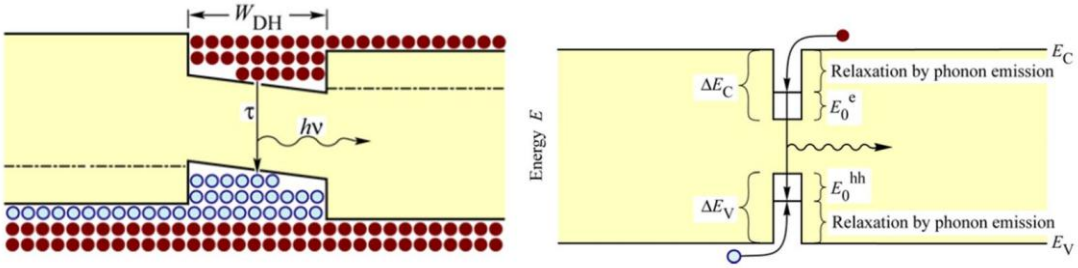

Fig. 1-6 Left: Forward-biased double-heterojunction with width W_{DH}. Right: Schematic of a relaxation process of free charge carriers from the barriers into the confined states, i.e. of a quantum well [14]. ΔE_C and ΔE_V are the conduction and valence band edge offsets between the barrier (larger bandgap material) and the QW. E_0^e and E_0^{hh} stand for the difference between band edge and ground state energy in the QW conduction and valence band respectively

Theoretical and experimental studies on gain sheets with confinement in zero (bulk), one (QW), two (quantum wire) and three (quantum dot) dimensions were undertaken in the 1980s. Asada et al. [21] studied the development of the threshold current density with increasing dimensionality of confinement; Arakawa and Sakaki [22] studied the temperature stability of the threshold current density with increasing confinement. These groups concluded that the increasing confinement leads to an increasing localisation of the density of states closer to the band edges (see Fig. 1-7), resulting in a:

- higher material gain,
- lower transparency and thus lower threshold carrier density,
- higher thermal stability.

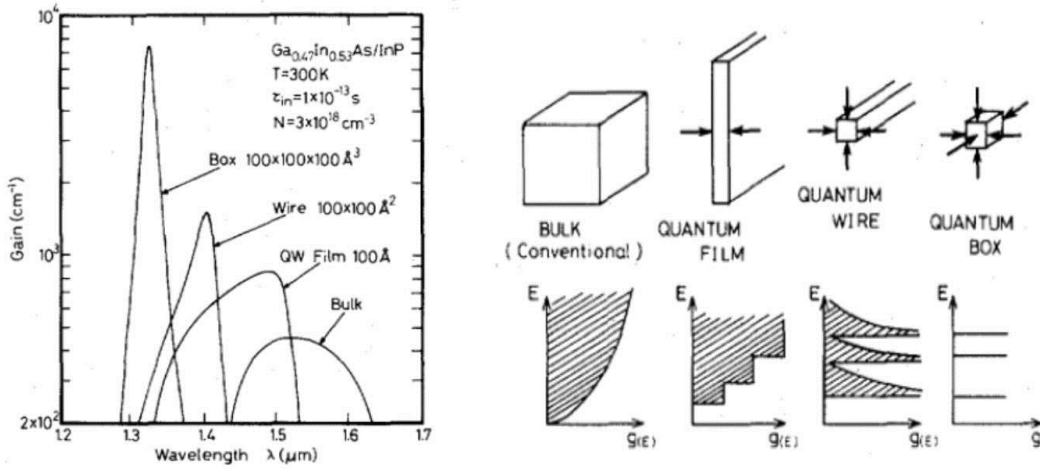

Fig. 1-7 Left: Calculated material gain for QDs (quantum box), quantum wire, QW (film) and bulk. Right: Density of states for increasing quantum confinement. Graphs taken from [21].

A breakthrough in the fabrication of quantum dot (QD) based lasers occurred in 1993 by Ledentsov et al. [9], where InGaAs islands were grown in GaAs, sandwiched by AlGaAs and optically excited. Fig. 1-8 gives an illustration of the evolution of the room temperature threshold current density of semiconductor lasers with time, where advances in fabrication techniques and carrier confinement have enabled on-going reduction of the threshold carrier density.

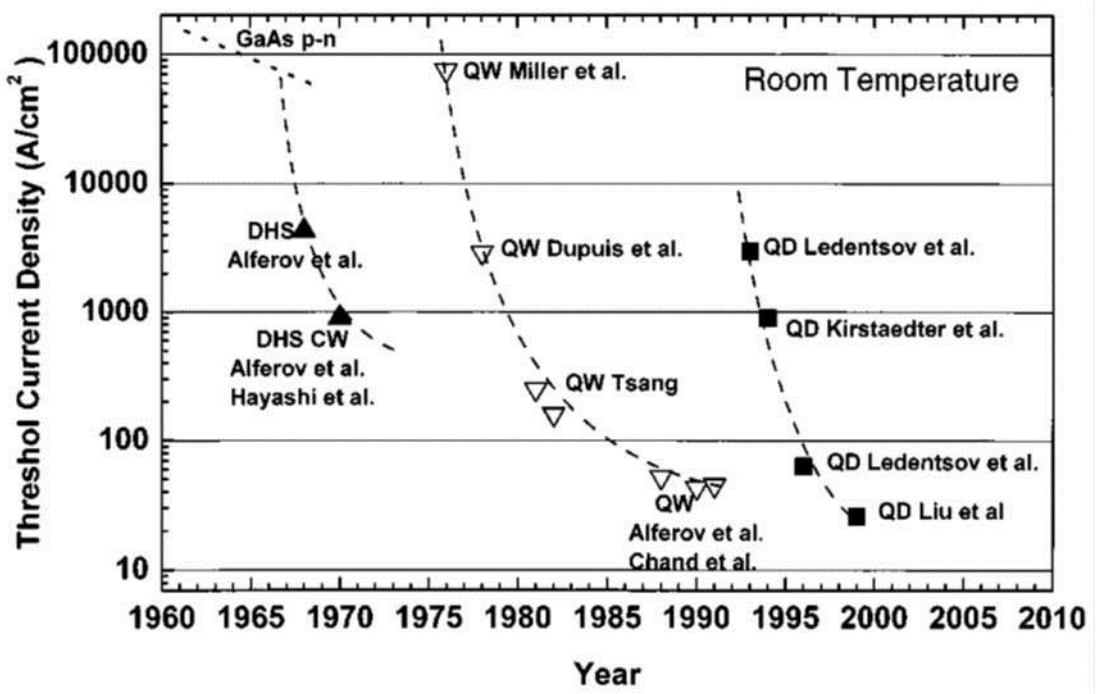

Fig. 1-8 Evolution of the threshold current density of semiconductor laser diodes with time and increasing quantum confinement. Graph taken from [9].

Fig. 1-1 compares the basic structural and output characteristics of electrically-injected vertical cavity surface emitting lasers (VCSELs) with respect to edge emitting diode lasers and puts this in relation to the direction of epitaxial growth. The direction of optical emission for an edge-emitting device is parallel to the gain layer. Electrical injection occurs via stripe contacts at the bottom and top layer. The reflectivity of the cleaved facets is around 30 % for GaAs or InP based devices and usually high enough to achieve laser emission; coatings to increase the reflectivity can be applied to reduce the threshold current density. It is also apparent from the figure that the output beam is elliptical in shape as it suffers from diffraction due to the very thin gain layer thickness in the growth direction, resulting in an

astigmatic and divergent mode profile. The length of the cavity (a few hundreds of micrometres) causes also multiple longitudinal modes.

Taking the simplified version of the threshold condition of a laser device into account the threshold gain can be calculated according to [12]:

$$g_{th}\Gamma = \alpha_{total} + \frac{\ln\left(\frac{1}{R_1 R_2}\right)}{2L}. \qquad \text{Equation [1-5]}$$

Where g_{th} is the gain required to reach threshold, α_{total} are the combined cavity losses due to scattering, estimated to be around 10 cm^{-1} for this example. L is the device length in the range of 300 µm and is equal to the length of the gain region in an edge emitter. R_1 and R_2 are the reflectivities of the cleaved edges. The low optical confinement factor, Γ of 0.016 is defined by the gain layer thickness and the waveguided optical mode size in the direction perpendicular to the QW plane (for a 10 nm thick QW and a mode diameter of 1 µm according to $\Gamma = d_{QW}/0.62w_{mode}$). The threshold gain for the given values is around 3000 cm^{-1}.

The development described so far was for edge-emitting devices as shown in Fig. 1-1 a). If a surface-emitting device is considered such as shown in Fig. 1-1 b), where the optical field resonates in a direction perpendicular to the layer plane providing the gain, reflectivity values > 99 % are required to reach the same threshold condition. Such high reflectivity values cannot be achieved by metal mirrors. The active region is thus sandwiched by distributed Bragg reflectors (multi-layer stacks of high and low refractive index layer pairs with layer thicknesses of $\lambda_{laser}/4n$, where λ_{laser} is the laser emission wavelength and n the refractive index of the layer). The total gain layer thickness, L, is only ~10 nm for a single QW (to use the same thickness as in previous example). Due to the very short interaction length between the optical field and the carrier distribution, resonance effects are applied in order to enhance the oscillating field and optimise the overlap. This scheme is called resonant periodic gain (RPG), described by Corzine et al. [23] and for enhanced modal gain ($g \cdot \Gamma$). The optical confinement factor, Γ, is considered to be close to 2 in this case, if the thin QW is placed at the field antinode.

Surface-emitting laser devices were demonstrated first in 1966 by Stillman et al. [24] where gain was provided by a very thin CdSe sheet, pumped by a GaAsP diode laser. This idea was further developed and lead amongst other things to the realisation of the electrically-injected vertical cavity surface emitting laser (VCSEL) shown in Fig. 1-1 b) by Soda et al. [2]. Advantages of the short interaction length in this surface emitting devices are a low laser threshold and the avoidance of spatial hole burning. Diffraction-limited, circular transverse mode profiles can be achieved by the adjustment of the output aperture in the top contact to the cavity mode size. This, on the other hand limits the maximum achievable output power to only few mW. The large longitudinal mode separation due to the very short cavity length can also be used for single longitudinal mode oscillation [3].

Optically-pumped semiconductor thin-disk lasers or VECSELs are very similar to VCSELs, but offer a range of advantages, which are discussed in the following section.

1.2 The VECSEL (basic configuration and properties)

The development of VECSELs really took off in the mid 1990's due to advances in epitaxial growth techniques. In 1997 Kuznetsov et al. [25] realised and established the structural concept of these devices as a distinct class of semiconductor based laser. A schematic of the bandgap structure of a VECSEL subcavity and a laser cavity arrangement is shown in Fig. 1-9. The principle of operation is depicted on the right hand side. Compared to electrically-injected VCSELs, VECSELs are usually Optically-pumped and one of the integrated top DBRs is replaced by an external output coupling mirror, leaving only one DBR topped by a gain region. This explains the frequently used term: "gain mirror". The pump is absorbed within the active region (pump absorption barriers), where the carriers relax into the active layer states, from where they recombine radiatively. The energy released during the relaxation processes heats the structure; the heat sink illustrates necessary thermal

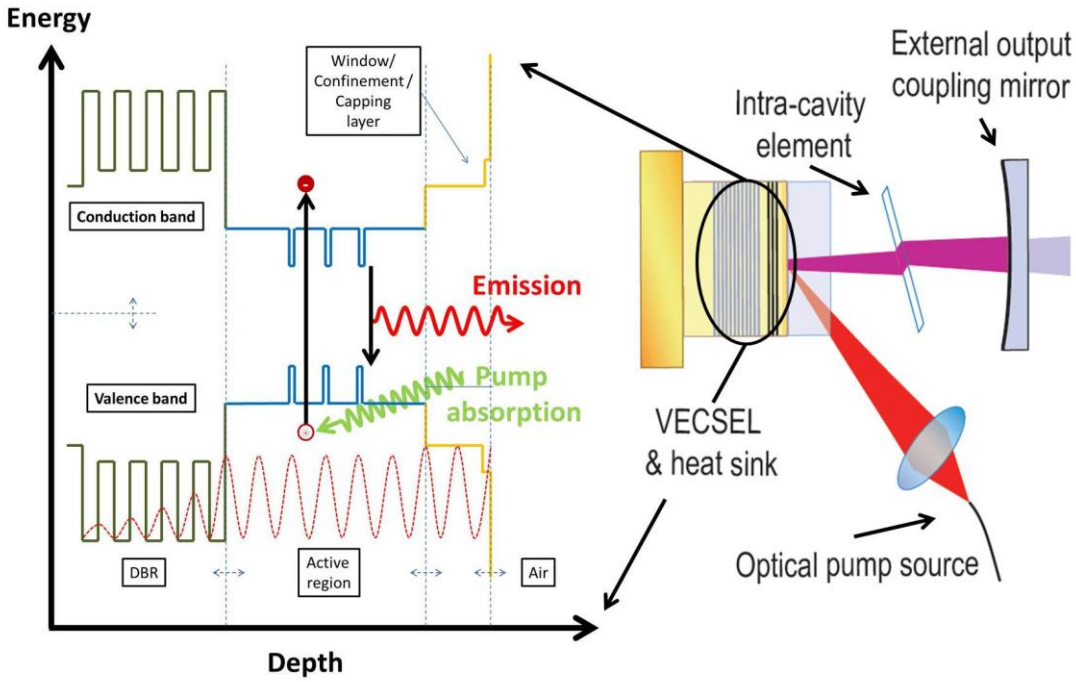

Fig. 1-9 Principle of operation of a VECSEL. Left: Bandgap structure for conduction and valence band, divided into the DBR, active and window/confinement region. Carrier excitation, by pump absorption within the barriers and radiative recombination within the gain layer states is also illustrated. Right: Laser cavity arrangement, showing thermal management via heat sink, optical pumping and intra-cavity elements.

management for heat extraction. The external end mirror concludes the laser cavity, allowing cavity adjustment for power scaling and access to the intra-cavity field for beam processing, such as transverse mode and wavelength conversion, tuning, low noise non-linear mixing, single frequency operation and stable mode-locking, etc. Furthermore the semiconductor nature makes emission wavelength engineering possible by the choice of material composition, layer thickness and strain of the gain layers; usually the gain is provided by quantum wells, but recently, as described in this thesis, multiple layers of quantum dots have been used. Unlike VCSEL structures, VECSELs are power scalable up to currently 20 W from a single gain chip in the fundamental TEM_{00} mode as stated by Rudin et al. [26]. The left hand side of Fig. 1-9 shows the conduction and valence band structure of the subcavity, divided into the DBR, active and window/confinement region. The DBR has a high reflectivity stopband, centred at the laser emission wavelength. The active region consists of the pump absorption barriers and gain layers with a lower bandgap. Gain layers are positioned at the electric field antinodes (illustrated by the red dashed line)

for resonant periodic gain. Generated charge carriers are confined within the active region by a transparent window layer. A capping layer may also be used to prevent oxidation of the underlying layers.

Optical pumping makes doping unnecessary, removing some of the constraints on the fabrication process with respect to electrical and thermal management, oxidation and passivation but also electrical contacting.

Reasons for the success of VECSELs lie in the intrinsic properties of these devices summarised in Table 1-1. In summary, these laser structures combine the flexibility to choose the emission and pumping wavelength, together with a broad spectral gain bandwidth and short carrier lifetime [27], intrinsic for semiconductor lasers, with the high power and outstanding beam qualities of conventional solid state lasers [6]. Furthermore, standardised fabrication processes allow wafer-based mass production of these so called gain mirrors, which reduces the cost of the end product with respect to solid state or gas lasers.

Recent developments have been driven by constant improvements in

- Growth quality: Increasing the device lifetime and laser performance.
- New compounds and gain structures in order to increase laser performance and establish access to new wavelength ranges. A large variety of material compositions is now available for these purposes. Replacement of the QWs with QDs as gain materials contributed as well to this development. Wafer fusion of dissimilar material compositions is another possibility.
- Improvements in thermal management such as the use of thermal heat spreaders and thinned devices [28].

Non-linear frequency conversion is a further way to extend the wavelength coverage of VECSELs into the near-UV, mid-IR or Teraherz range which will be discussed in the following part of this chapter.

Semiconductor based		
✓	Monolithic fabrication	Integration of mirror and active region
✓	Wavelength engineering	Emission wavelength set by material composition, strain and layer thicknesses
✓	Broad absorption bandwidth	Choice of optical pumping source easy
✓	Broad gain bandwidth	Wide wavelength tuning, short pulses
✓	Coupled gain	Single mode operation
✓	Short carrier lifetime	Stable laser emission, low noise levels, no energy stored in gain material
✓	Non-linear conversion	Stable, low noise emission due to single mode & short lifetime
External cavity		
✓	Arrangement versatility	Single transverse mode, optimised pump and cavity mode matching/power scaling, intra-cavity focus adjustment, optimised output coupling, single frequency etc.
✓	Intra-cavity elements	Beam processing, wavelength tuning, frequency conversion etc.
×	Extended cavities	Cavity dimensions can become large
Other attributes		
✓	Surface normal arrangement	Very short absorption length, pump and cavity mode easy to match due to small interaction length
✓	Usually optically-pumped	No doping, no metal contacting, no post growth processing necessary
×	Usually optically-pumped	Optical pumping scheme necessary
×	Thermal management	Large heat load introduction into small area, thermal rollover, power limitations
×	Low gain	Sensitive to losses, low optimum output coupling
✓	Generic design	

Table 1-1: Overview of important VECSEL properties

1.3 Spectral emission wavelength coverage of VECSELs

As already stated above, one of the most important properties of semiconductor lasers is the possibility to 'design' the emission wavelength. This gives a large flexibility to produce application targeted devices. This is illustrated in terms of VECSEL performance for fundamental emission using QWs in Fig. 1-10 and for QDs in Fig. 1-11. Examples for indirect light generation of light by non-linear conversion are shown in Fig. 1-12. Photon up-conversion, i.e. from the near-IR to the UV-visible range, is achieved by x^{th}-harmonic generation and sum-frequency mixing. Down conversion towards longer wavelengths, by optical parametric oscillation (OPO), stimulated Raman scattering and difference-frequency mixing.

1.3.1 Quantum well based VECSELs

Gain regions based on group III-V semiconductor quantum wells are the standard in current VECSEL devices and are integrated in most of the reported structures. Two exceptions are group IV-VI devices, where the growth methods aren't well established yet, and gain sheets based on group III-V quantum dot-based active regions. Fig. 1-10 represents a selection of reported QW-based devices. The variety of QW compositions for fundamental, continuous wave and near room temperature (RT) emission at the different wavelength ranges is represented in the graph. The near-UV and visible (VIS) spectral range, important in spectroscopic, medical and bio-photonic applications can be accessed by InGaN/GaN devices around 400 nm which showed so far output powers in μW range, Park et al. [29,30] and more than 1 W in the red (640-690 nm) by GaInP/GaAs [31,32]. GaAs/GaAs [33,34] and InAlGaAs/GaAs [35] QWs cover the 850 nm range with output powers around 1 W. InGaAs QWs emit between 920-1180 nm with output powers >10 W, around 1 μm [26,36-39]. The near-IR spectral range is of interest for fibre communication, pumping of fibre lasers and amplifiers, optical storage, laser printing etc. VECSELs operating in this range stand in direct competition with well-established solid state lasers, such as doped YVO_4 lasers, which they have started to replace (an example for this is the VERDI laser system from Coherent [40]). GaInNAs QWs target the important optical fibre communication spectral range between 1190-1320 nm with multi-Watt output power, having the disadvantage to be difficult to grow, due to the required Nitrogen content. The same range was recently covered as well by wafer-fused AlGaInAs QW VECSELs, where the gain region is grown separately lattice-matched to InP substrates and the AlGaAs based DBR on GaAs substrates [41]. Wafer-fused structures prove more promising compared to the dilute Nitride compounds due to the ability to fabricate high quality devices, with low non-radiative centre concentration and better laser performance. They might be the future method of choice to target this spectral range [42-44]. InGaAsP/InP devices show fundamental emission in the fibre communication range around 1550 nm and were reported to have output power of > 800 mW [45]. GaIn(As)Sb QWs emit

between 2-3 µm and are possibly applicable in molecular spectroscopy/gas sensing, due to the presence of strong molecular absorption lines in this spectral range [46], and in free space communication. GaInSb QW devices show multi-Watt emission [47-52]. Lead-salt structures based on bulk and QW active regions have reached pulsed room temperature and low temperature cw operation with output powers of several tens of mW. They can cover the spectral range between 3-10 µm, making them suitable for gas sensing and spectroscopy [46].

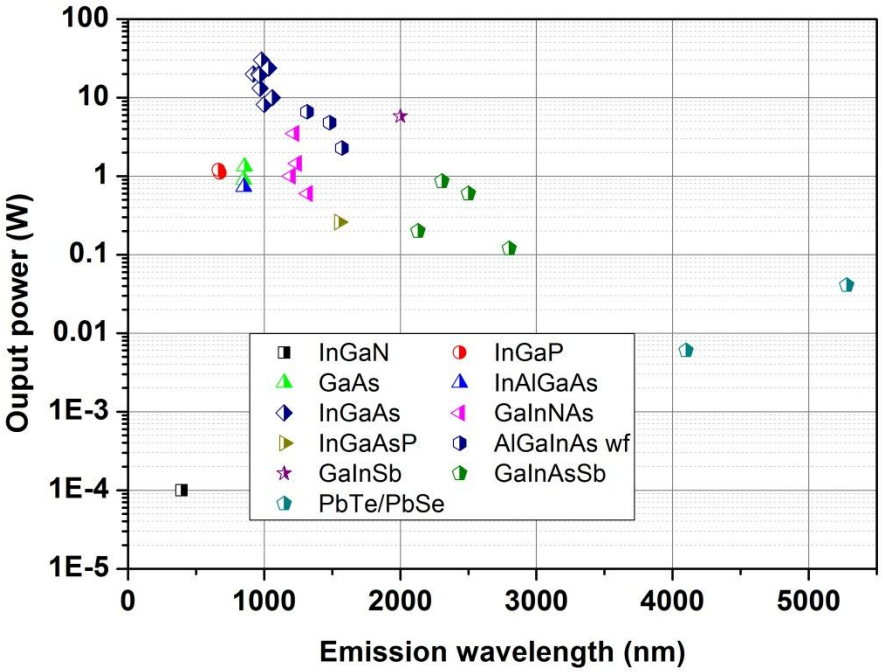

Fig. 1-10 Diagram of selected published QW based VECSEL devices, showing achievable output powers in dependence on the emission wavelength for InGaN [29,30], InGaP [31,32], GaAs [33,53], InAlGaAs [35], InGaAs [26,36-39,54,55], GaInNAs [56-58], InGaASP [45], AlGaInAs (wf = wafer fusion) [41,43,44], GaInSb [47], GaInAsSb [48-52] QWs and PbTe/PbSe [59,60] bulk/QWs.

It is apparent from the summary in Fig. 1-10, that the best reported devices in terms of differential efficiency (~ 50 %) and output power are based on InGaAs QWs. A maximum output power of 20 W from a single gain chip device was reported by Rudin et al. in the fundamental TEM_{00} mode [26]. Higher powers were achieved with higher transverse modes, Chilla et al. [36] or multiple gain chip devices in the 1 µm range. Multi-chip cavities were reported to achieve output powers close to 100 W in this wavelength range [61]. The emission efficiency decreases rapidly with wavelength in both directions towards shorter and longer wavelengths, due to

growth, compositional, strain and/or carrier confinement constraints; leaving several gaps in example in the green-yellow (450-600 nm), the long wavelength visible range (700-800 nm) or in the transition region between near and mid-IR (1600-2000 nm). Current and future research is concerned to close these gaps, especially in the application rich visible range. Possible candidates for the access of the whole visible range from the blue to the red are group II-VI semiconductors based on ZnCdSe QWs grown on top of GaAs and InP substrates [62,63]. The drawback of these compositions is the difficulty of p-doping for electrical pumping and Cd out-diffusion from QWs, limiting the lifetime of electrically-injected devices despite high quality growth [64]. Optical pumping as usually applied to VECSELs would make doping unnecessary and could help to improve the device lifetime. MgZnSSe/GaAs and MgZnCdSe/InP DBR structures also suffer from a low refractive index difference and increasingly difficult growth with increasing Mg composition for near lattice-matched structures [65,66]. This sets limitations to the maximum reflectivity and stopband width, important for VECSELs due to their sensitivity to any losses and for tunability. New, unknown lattice-matched compositions of group II-VI, IV-VI, III-V quaternaries and quinternaries, might offer larger refractive index differences for DBRs and better optical and carrier confinement.

1.3.2 Quantum dot VECSELs

QD based VECSELs are a very recent development, with breakthroughs in 2008 and 2009 involving our group and described in this work. There are several reasons for the utilisation of self-assembled QDs as gain material in contrast to the commonly used QWs:

- Quantum confinement in all three dimensions [21,22]:
    - Makes laser emission from discrete excited dot states possible.
    - Reduces the transparency carrier density, thus the threshold power density.

    - Increases the thermal stability of the threshold power density.
    - Enables efficient carrier localisation within the dot states [67].
- Inhomogeneous gain broadening due to the size distribution within the dot ensemble and the possible existence of excited dot states can create a very broad and flat gain spectrum which could be used for broadly tunable continuous wave light sources [68].
- The broad gain spectrum increases the thermal stability of the laser emission wavelength [69].
- The formation of self-assembled QDs requires higher strains than QWs are able to tolerate. Thus QDs allow the use of compositions with a:
    - higher lattice-mismatch,
    - lower energy bandgap, for extension of the emission wavelength towards longer wavelength.

InAs QDs were used in VCSEL devices such as demonstrated by Lott et al. [70] in 1999 prior to the incorporation into a VECSEL structure. The transition towards the development of QD-based VECSELs followed, via the partial removal of the VCSELs top mirror reported by Lott et al. [71] in 2005. Fig. 1-11 gives an overview of reported QD-based VECSEL devices. Results and citations to this graph are found in Table 3-2 in the InAs/GaAs submonolayer QD VECSEL chapter, where a more thorough discussion is presented. All reported QD-based VECSEL devices incorporate dots in the Stranski-Krastanow (S-K) growth mode. Two different types of dots exist in this growth mode, denoted as S-K and submonolayer (SML) QDs. SML dots are a special subtype and described in more detail in Section 2.4.3. As can be seen in the graph, InAs/GaAs QDs cover the whole spectral range from 950-1300 nm, achieving multi-Watt power from single devices with differential efficiencies up to 30 % in the 1.04 μm range. Intra-cavity second harmonic generation (SHG) by QD-based VECSEL devices was demonstrations for the generation of green, yellow/orange and red light by Rautiainen et al. [72] and Butkus et al. [73], see also (Chapter 3, Table 3-2).

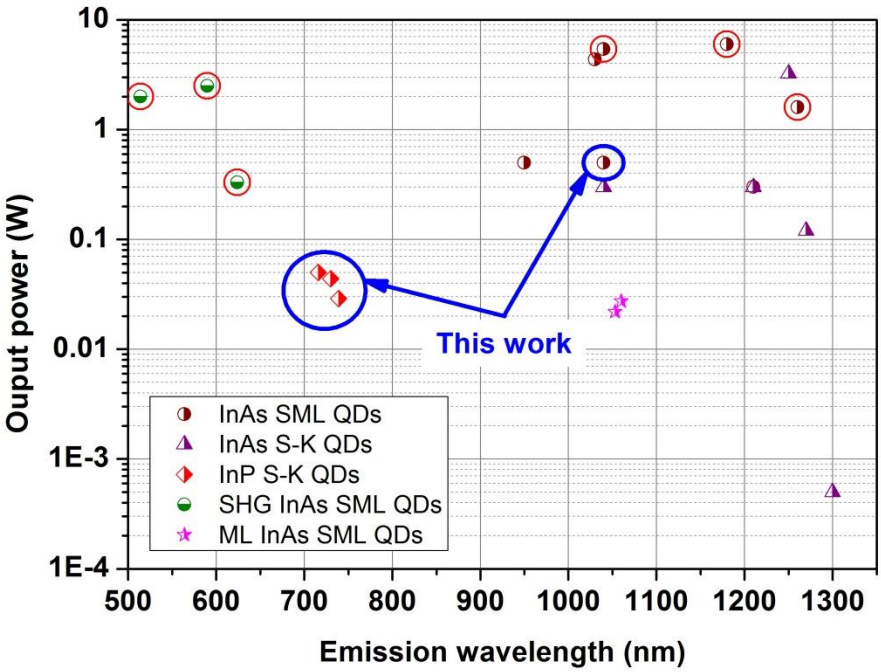

Fig. 1-11 Diagram displays all known current results for QD based VECSEL structures. Larger circles surrounding some results are for clarification and mark second harmonic generation results together with their fundamental emission. ML stands for mode-locking [74,75], SHG for second harmonic generation results[72,73,76], S-K and SML for Stranski-Krastanow and submonolayer QDs respectively. (InAs S-K [71,77,78], InP S-K [79], InAs SML [73-77,80-82].

A major part of this thesis is concerned with the development of InP QD VECSELs based on the AlGaInP material system, for the emission between 700-780 nm (see Chapter 4) [79]. The spectral range above 700 nm is of interest as it is difficult to reach by conventional lasers and semiconductor compositions, with the exception of edge emitting devices utilising compressively strained InAlGaAs or tensile strained GaAsP QWs. Structures based on InAlGaAs suffer from a low device lifetime due to problems involved with the aluminium (Al) content. Al rich QWs emit below 750 nm, but have an increased affinity towards impurity (oxygen) incorporation and suffer from a close proximity of the indirect/direct bandgap minima [83]. Aluminium free GaAsP QWs have an increased reliability, lower threshold and higher internal efficiency, however they are tensile strained and cannot be used for surface emitting devices [13]. InP QDs discussed in this thesis were so far the only VECSEL structures reported to emit in this wavelength range.

A further strand of work with VECSELs is passive mode-locking. Passive mode-locking is the most common way to generate short laser pulses. The usual scheme in mode-locked VECESL devices is the use of semiconductor saturable absorber mirrors (SESAM). SESAMs are very similar in their generic design setup, with a distributed Bragg reflector, an absorption region, incorporating multiple QWs or QD-layers and a top capping layer. Important optical properties of SESAMs are their nonlinear optical reflectivity and the required recovery time from the absorption process. These absorption mirrors usually replace one of the external mirrors. The principle of these devices is based on intensity dependent absorption of the circulating field. With increasing field the absorption medium becomes more and more saturated, which increases the reflectivity of the DBR structure. Thus pulses of high intensity experience lower losses and low intensity pulses are suppressed, forcing the laser to operate in a pulsed mode, where the phases of the individual frequency lines are locked to each other. The repetition rate between two subsequent pulses is indirectly proportional to the cavity round trip time, thus thigh repetition rates are achieved with the shortest cavities. Due to the locking of the modes, the power of one of these short pulses is much higher than the average output power. Südmeyer et al. have summarised high average output power mode-locked VECSEL results in [6]. Mode-locked devices were demonstrated with InGaAs based QW VECSELs in the 950-1040 nm range, InGaNAs QW VESCELs for the 1200-1300 nm range, InGaAsP QW VECSELs for the 1550 nm and GaInSb QWs for the 2 μm range. All devices have pulse durations in the pico-femtosecond range with average output powers up to the W range and GHz repetition rates. Mode-locking of QD based VECSEL and or SESAM devices have also been reported, which was already stated in Fig. 1-11. From InAs/GaAs QD-based VECSELs 18 ps pulses were generated with a repetition rate of 2.57 GHz and an average power of 27 mW, as reported by Hoffmann et al. [84] and [75]. Although these first results lie behind the performance of QW-based VECSEL devices, the potential for the use of QDs as gain material are:

- Generation of shorter pulses due to the broader inhomogeneous gain bandwidth.

- Improved gain dynamics.
- More temperature stable operation, advantageous for the fabrication of highly integrated, possibly electrically pumped devices (MIXSEL [85]), incorporating the saturable absorber and gain mirror within one device.

One of the grown InP QD VECSELs described in Section 4.5 (where more information is presented) was used as a SESAM inside a Ti:sapphire laser to generate self-started passive mode-locking in the 750 nm range. 518 fs pulses at a repetition rate of 128 MHz and 190 mW average power were achieved.

1.3.3 Non-linear frequency conversion

The last section introduced most recent QD-based VECSEL devices used for frequency-doubling in order to access the visible range. The external cavity format with the high circulating field and the short upper-state carrier lifetime of semiconductors are well suited for intra-cavity beam processing such as non-linear frequency conversion. Here latest developments in this field of application for QW-based VECSELs are presented.

Harmonic generation was demonstrated fairly quickly after the first appearance of the VECSEL concept by Raymond et al. [86] in 1999. Further advances in non-linear conversion took a bit longer to be achieved, but to-date include intra-cavity optical parametric oscillation (OPO) by Stothard et al. in 2009 [87], where OPO was achieved in a coupled cavity configuration, utilising the intra-cavity field of a 1060 nm VECSEL for the generating a 1.60 μm and 3.05 μm signal and idler wave respectively. Sum-frequency generation (SFG) by Hartke et al. [27] in 2008 from a single device with dual mode operation. In Chapter 5, we access the yellow-orange range in this way, by mixing a single passing solid-state laser beam with the intra-cavity field of a 1060 nm QW VECSEL. Teraherz generation of

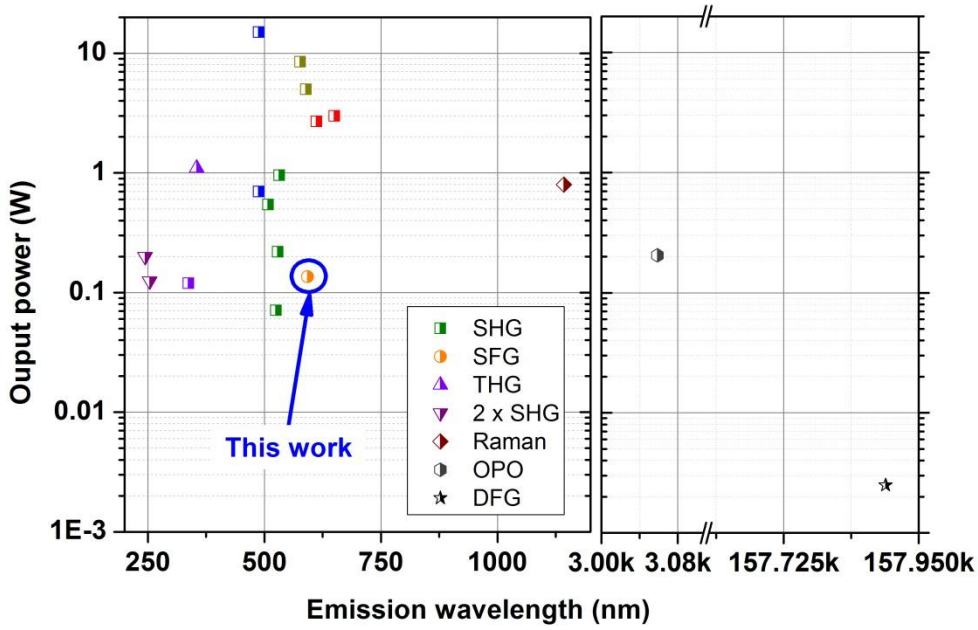

Fig. 1-12 Summary of some recent nonlinear frequency conversion experiments using QW based VECSEL structures. Most results are second harmonic (SHG) to the visible blue and green [27,36,90,92-96] and red [99,100]. The deep and near-UV is addressed by SHG [31], by two fold frequency doubling (2xSHG) from IR to visible blue (intra-cavity) to deep UV (external cavity) [92,93] and by third harmonic generation (THG) [98]. Orange generation by sum frequency generation (SFG) [101] as well as difference frequency generation (DFG) to the THz range [88] has been achieved. Results on so-called Raman conversion [89] and optical parametric oscillation (OPO) [87] for frequency down conversion were also published.

> 2 mW and 0.5 mW at 1.9 and 1 THz respectively by difference-frequency mixing was reported by Scheller et al. [88] in 2010, using two closely spaced longitudinal modes of a near-IR device. A VECSEL utilising stimulated Raman scattering was demonstrated by Parrotta et al. [89] in 2011. All these processes are very efficient inside VECSEL cavities. Table 1-1 summaries the most important properties of this type of laser.

- The short-upper state carrier lifetime in the ns range prohibits energy storage within the gain medium. The energy is thus stored in form of a high oscillating field within a high finesse external cavity.
- Single mode operation is supported in semiconductor lasers due to gain coupling [90].

- No special hole burning due to the very short interaction length between the resonating field and the gain medium.

These properties are advantageous in terms of stable non-linear frequency conversion, as no longitudinal mode competition and thus no so-called "green problem", reported for solid-state lasers with long upper-state lifetimes by Baer et al. [91] is present. The large flexibility of the cavity arrangement allows the placement of non-linear crystals at beam waists inside the cavity. Tight focussing and thus high pump densities are necessary for efficient conversion in non-linear processes. Due to this configuration, large nonlinear coefficient materials are not necessary, especially as the oscillating intra-cavity field passes the crystal multiple times. Fig. 1-12 summarises results published on frequency conversion by the use of QW based VECSELs. The highest, multi-Watt output powers were reported in the blue/green range (460-590 nm) [27,36,90,92-96]. This is not surprising, as the best VECSEL structures for fundamental emission are based on InGaAs QWs and emit around 1 μm (see Fig. 1-10). The deep (<300 nm) and near-ultra violet (UV) (300-380 nm) range can be reached by multiple, i.e. two times second harmonic generation from the near infra-red (IR) to the green by intra-cavity conversion in the first step and in a second step to the deep UV using an external cavity [92,93,97]. Other methods are by third harmonic generation (THG) from the near-IR [98] or by second harmonic generation (SHG) from the visible red [31]. The red spectral range was also targeted via SHG by the use of GaInNAs or AlGaInAs wafer-fused structures [99,100], having higher output powers than reported by direct generation from GaInP QW based structures [31,32].

1.4 VECSEL applications

The rest of this chapter is concerned with the introduction of some VECSEL application fields. Commercially available devices are for example the frequency doubled VECSELs from Coherent [40]. These devices emit at specific wavelength in the UV-yellow range with output powers from the tens of mW to the 10 W level.

They are manufactured to target application specific wavelengths or for high power in order to replace conventional, expensive, bulky and/or complicated solid-state and gas laser systems and are advertised as "all solid-state optically pumped semiconductor lasers (OPSL)", suitable for medical, life sciences & research, forensics and entertainment, some of which are portable and battery driven. Directly electrically-pumped VECSELs, so called 'NECSELs' frequency-doubled to blue - 465, green - 532 and red - 620 nm were also reported by NOVALUX in 2006/07 for laser television and projection. OSRAM used another approach for the generation of green light by monolithic integration of pump diode lasers between the active region and DBR structure [102], only to name a few. Also interesting is the generation of short and ultrashort light pulses in the picosecond to femtosecond time range, which will have an impact on a variety of scientific and commercial applications [6] such as:

- Time-resolved spectroscopy for the examination of dynamic processes in physical, biological, chemical, etc. specimen.
- Multi-photon imaging and two photon excitation microscopy due to nonlinear interactions with matter caused by the high pulse powers.
- Long distance optical fibre communication for improved data transmission and higher bandwidth.
- Short distance (1-100 m) optical communication interconnectors for faster transmission rates between processor and other computer systems
- Optical clocking for better data synchronisation and better performance of microprocessors.
- Laser projection

Self-started passive mode-locking (Hoogland et al. [103]) and cavity field dumping Savitski et al. [104] are two different ways to achieve high energetic, short pulses. Frequency stabilised (e.g. [105-107]) operation can be achieved by the use of an output coupling mirror, e.g. mounted to a piezoelectric actuator in order to stabilise the frequency with respect to a reference locking signal. Narrow linewidth, tunable, high power sources with circular near diffraction limited output beams and long coherence length are required for high resolution spectroscopy, communications,

interference lithography etc. The high beam quality together with their wavelength versatility makes VECSELs also very attractive as intra- and extra-cavity pumps, i.e. for exotic laser crystals with absorption ranges difficult to reach by other lasers. With respect to this, Hempler et al. reported a VECSEL pumped Cr^{2+}:ZnSe [108] laser for emission in the mid-IR.

1.5 Thesis outline

This thesis is mostly concerned with the design and characterisation of VECSEL structures utilising quantum dot active regions. Chapter 2 gives an in depth discussion on the VECSEL design and fabrication criteria, from the choice of material compositions, to the setup of the distributed Bragg reflector (DBR) and the semiconductor subcavity, including the active region and carrier confinement layers. Resonance effects for field enhancement and thermal management for heat extraction are also addressed. Laser performance modelling using the method introduced by Kuznetsov et al. [109] is also discussed. The chapter concludes with a discussion on epitaxial growth methods, the influence of strain on the bandgap structure of group III-V semiconductors and the formation of self-assembled QDs. Indicated in Fig. 1-11 (blue circles) are the two different structures discussed respectively in Chapter 3 and 4 incorporating InAs/GaAs submonolayer QDs for laser emission in the 1030 nm and InP S-K QDs for emission in the 710-760 nm spectral region. In both cases this was the first demonstration of laser emission for InAs/GaAs (in 2008 [110]) and for InP (in 2009 [79]) QD-based VECSELs respectively. The InAs/GaAs SML QD devices achieved maximum output powers of 0.5 W with a slope efficiency of 17 %, but suffered from a short lifetime. Conclusions drawn from the analysis helped to improve the performance and today a large variety of different structures have been reported by different groups in the range between 950-1300 nm. InP QD VECSELs are still in the early experimental stage. Work discussed in Chapter 4 demonstrates the feasibility of these devices for light generation in the 700-780 nm range. Light in this spectral window is suitable for example in medical applications such as

photodynamic therapy, sensing, imaging and biophotonics, due to the so called medical absorption window, as shown in Fig. 1-13, for superior transmission through tissue and minimised auto-fluorescence [111]. Output powers up to 50 mW with a slope efficiency of 5.7 % were achieved around 740 nm with a broad tuning range of more than 25 nm. Characterisation of the growth revealed a high defect density, originating from non-coherently strained QDs, which penetrated to the surface, causing a rough surface morphology. This makes bonding of intracavity heatspreader for thermal management difficult. These findings show that the fabrication of defect-free InP QDs, important for good laser performance is not as far matured as their InAs counterparts. Future improvements in the growth are expected to lead to better laser performance.

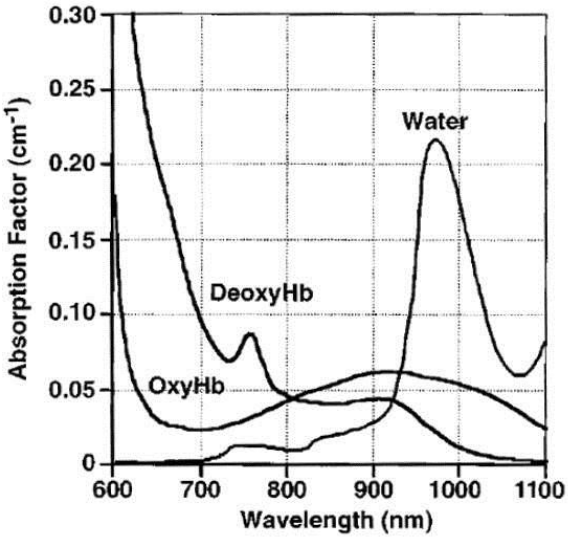

Fig. 1-13 Absorption spectra of the blood cells oxy- and deoxyhemoglobin together with water, creating the medical absorption window in the range of 700-900 nm, suitable for medical applications [111].

In Chapter 5, sum-frequency generation of yellow-orange light at 593 nm was demonstrated inside a VECSEL cavity and is indicated by the blue circle in Fig. 1-12. A periodically-poled nonlinear crystal was placed at a beam waist inside a 1060 nm InGaAs QW-based VECSEL cavity. Non-linear conversion was achieved by the combination with a single passing 1342 nm beam from a diode pumped Nd:YVO_4 laser. 136 mW with a conversion efficiency of 17 % (with respect to the single passing beam) could be achieved.

Chapter 6 gives an overall conclusion of the discussions in the three experimental chapters.

References

1. W. B. Jiang, S. R. Friberg, H. Iwamura, and Y. Yamamoto, "High powers and subpicosecond pulses from an external-cavity surface-emitting InGaAs/InP multiple quantum well laser," Applied Physics Letters **58**, 807-809 (1991).

2. H. Soda, K. Iga, C. Kitahara, and Y. Suematsu, "GaInAsP/InP Surface Emitting Injection Lasers," Jpn. J. Appl. Phys. **18**, 2329-2330 (1979).

3. C. Wilmsen, H. Temkin, and L. A. Coldren, *Vertical-Cavity Surfrace-Emitting Lasers: Design, Fabrication, Characterization, and Applications*, (Cambridge University Press, Cambridge, UK, 1999).

4. S. Calvez, J. E. Hastie, M. Guina, O. G. Okhotnikov, and M. D. Dawson, "Semiconductor disk lasers for the generation of visible and ultraviolet radiation," Laser & Photonics Review **3**, 407-434 (2009).

5. N. Schulz, J.-M. Hopkins, M. Rattunde, D. Burns, and J. Wagner, "High-brightness long-wavelength semiconductor disk lasers," Laser & Photonics Review **2**, 160-181 (2008).

6. O. G. Okhotnikov, D. Bimberg, M. Guina, D. Burns, S. Calvez, M. D. Dawson, J. E. Hastie, J.-M. Hopkins, A. J. Kemp, U. Keller, M. Kuznetsov, N. Laurand, D. J. H. C. Maas, A. Mooradian, U. W. Pohl, M. Rattunde, B. Rösener, A. Shchergrov, T. Südmeyer, A. Tandon, J. Wagner, and G. Yoffe, *Semiconductor Disk Lasers. Physics and Technology*, O. G. Okhotnikov, ed., (WILEY-VCH Verlag GmbH & Co. KGaA, Weinheim, Weinheim, 2010).

7. http://spie.org/x35258.xml?pf=true&ArticleID=x35258, Seurin, J.-F., "Harnessing light for high-power applications," 10-6-2009, SPIE

8. O. Svelto, *Principles of Lasers*, David C.Hanna, ed., (Springer, New York, 1998).

9. N. N. Ledentsov, M. Grundmann, F. Heinrichsdorff, D. Bimberg, V. M. Ustinov, A. E. Zhukov, M. V. Maximov, Z. Alferov, and J. A. Lott, "Quantum-dot heterostructure lasers," Selected Topics in Quantum Electronics, IEEE Journal of **6**, 439-451 (2000).

10. S. M. Sze, *Physics of Semiconductor Devices*, (John Wiley & Sons, New York, Chichester, Brisbane, Toronto, Singapore, 1981).

11. S.-L. Chuang, "Theory of Electronic Band Structures in Semiconductors," in *Physics of Photonic Devices,* G. Boreman, ed., (Wiley, New Jersey, 2009), pp. 113-178.

12. O. Svelto, "Solid-State, Dye, and Semiconductor Lasers," in *Principles of Lasers,* D. C. Hanna, ed., (Springer, New York, 1998), pp. 365-418.

13. D. P. Bour, R. S. Geels, D. W. Treat, T. L. Paoli, F. Ponce, R. L. Thornton, B. S. Krusor, R. D. Bringans, and D. F. Welch, "Strained $Ga_xIn_{1-x}P/(AlGa)_{0.5}In_{0.5}P$ heterostructures and quantum-well laser diodes," Quantum Electronics, IEEE Journal of **30**, 593-607 (1994).

14. E. F. Schubert, "LED basics: Electrical properties," in *Light-Emitting Diodes,* (Cambridge University Press, Cambridge, New York, Melbourne, Madrid, Cape Town, Singapore, Sao Paulo, 2006), pp. 59-85.

15. R. N. Hall, G. E. Fenner, J. D. Kingsley, T. J. Soltys, and R. O. Carlson, "Coherent Light Emission From GaAs Junctions," Phys. Rev. Lett. **9**, 366 (1962).

16. T. Maiman, "Stimulated Optical Radiation in Ruby," Nature **187**, 493-494 (1960).

17. I. Hayashi, M. Panish, P. Foy, and S. Sumski, "Junction Lasers which Operate Continuously at Room Temperature," Appl. Phys. Lett. **17**, 109 (1970).

18. E. Hering, R. Martin, and M. Stohrer, "Festkörperphysik," in *Physik für Ingenieure,* (Springer-Verlag Berlin Heidelberg, Berlin; Heidelberg; New York; Barcelona; Hongkong; London; Mailand; Paris; Tokio, 2002), pp. 633-698.

19. J. van der Ziel, R. Dingle, R. Miller, W. Wiegmann, and W. Nordland, "Laser oscillation from quantum states in very thin $GaAs/Al_{0.2}Ga_{0.8}As$ multilayer structures," Appl. Phys. Lett. **26**, 463 (1975).

20. Dingle, R. and Henry, C. H., Quantum effects in heterostructure lasers, 3,982,207, 21-9-1976, Patent.

21. M. Asada, Y. Miyamoto, and Y. Suematsu, "Gain and the threshold of three-dimensional quantum-box lasers," Quantum Electronics, IEEE Journal of **22**, 1915-1921 (1986).

22. Y. Arakawa and H. Sakaki, "Multidimensional quantum well laser and temperature dependence of its threshold current," Applied Physics Letters **40**, 939-941 (1982).

23. S. W. Corzine, R. S. Geels, J. W. Scott, R. H. Yan, and L. A. Coldren, "Design of Fabry-Perot surface-emitting lasers with a periodic gain structure," Quantum Electronics, IEEE Journal of **25**, 1513-1524 (1989).

24. G. E. Stillman, M. D. Sirkis, J. A. Rossi, M. R. Johnson, and J. Holonyak, "Volume Excitation of an Ultrathin Single-Mode CdSe Laser," Applied Physics Letters **9**, 268-269 (1966).

25. M. Kuznetsov, F. Hakimi, R. Sprague, and A. Mooradian, "High-power (>0.5-W CW) diode-pumped vertical-external-cavity surface-emitting semiconductor lasers with circular TEM_{00} beams," Photonics Technology Letters, IEEE **9**, 1063-1065 (1997).

26. B. Rudin, A. Rutz, M. Hoffmann, D. J. H. C. Maas, A. R. Bellancourt, E. Gini, T. S³dmeyer, and U. Keller, "Highly efficient optically pumped vertical-emitting semiconductor laser with more than 20 W average output power in a fundamental transverse mode," Opt. Lett. **33**, 2719-2721 (2008).

27. R. Hartke, V. Baev, K. Seger, O. Back, E. Heumann, G. Huber, M. Kuhnelt, and U. Steegmüller, "Experimental study of the output dynamics of intracavity frequency doubled optically pumped semiconductor disk lasers," Applied Physics Letters **92**, 101107-3 (2008).

28. A. J. Kemp, G. J. Valentine, J. M. Hopkins, J. E. Hastie, S. A. Smith, S. Calvez, M. D. Dawson, and D. Burns, "Thermal management in vertical-external-cavity surface-emitting lasers: finite-element analysis of a heatspreader approach," Quantum Electronics, IEEE Journal of **41**, 148-155 (2005).

29. S. H. Park and H. Jeon, "Microchip-Type InGaN Vertical External-Cavity Surface-Emitting Laser," Optical Review **13**, 20-23 (2006).

30. S. H. Park, J. Kim, H. Jeon, T. Sakong, S. N. Lee, S. Chae, Y. Park, C. H. Jeong, G. Y. Yeom, and Y. H. Cho, "Room-temperature GaN vertical-cavity surface-emitting laser operation in an extended cavity scheme," Applied Physics Letters **83**, 2121-2123 (2003).

31. J. E. Hastie, L. G. Morton, A. J. Kemp, M. D. Dawson, A. B. Krysa, and J. S. Roberts, "Tunable ultraviolet output from an intracavity frequency-doubled red vertical-external-cavity surface-emitting laser," Applied Physics Letters **89**, 061114-3 (2006).

32. T. Schwarzbäck, M. Eichfelder, W. M. Schulz, R. Roßbach, M. Jetter, and P. Michler, "Short wavelength red-emitting AlGaInP-VECSEL exceeds 1.2 W continuous-wave output power," Applied Physics B: Lasers and Optics 1-6 (2010).

33. J. E. Hastie, M. Hopkins, S. Calvez, W. J. Chan, D. Burns, R. Abram, E. Riis, A. I. Ferguson, and M. D. Dawson, "0.5-W single transverse-mode operation

of an 850-nm diode-pumped surface-emitting semiconductor laser," Photonics Technology Letters, IEEE **15**, 894-896 (2003).

34. S. S. Beyertt, M. Zorn, T. Kubler, H. Wenzel, M. Weyers, A. Giesen, G. Trankle, and U. Brauch, "Optical in-well pumping of a semiconductor disk laser with high optical efficiency," Quantum Electronics, IEEE Journal of **41**, 1439-1449 (2005).

35. S. J. McGinily, R. H. Abram, K. S. Gardner, R. Erling, A. I. Ferguson, and J. S. Roberts, "Novel Gain Medium Design for Short-Wavelength Vertical-External-Cavity Surface-Emitting Laser," Quantum Electronics, IEEE Journal of **43**, 445-450 (2007).

36. J. L. A. Chilla, S. D. Butterworth, A. Zeitschel, J. P. Charles, A. L. Caprara, M. K. Reed, and L. Spinelli, "High-power optically pumped semiconductor lasers," R. Scheps and H. J. Hoffman, eds., (SPIE, San Jose, Ca, USA, 2004), pp. 143-150.

37. F. Demaria, S. Lorch, S. Menzel, M. Riedl, F. Rinaldi, R. Rosch, and P. Unger, "Design of highly-efficient high-power optically-pumped semiconductor disk lasers," in *Semiconductor Laser Conference, 2008. ISLC 2008. IEEE 21st International*, (2008), pp. 139-140.

38. S. Lutgen, T. Albrecht, P. Brick, W. Reill, J. Luft, and W. Späth, "8-W high-efficiency continuous-wave semiconductor disk laser at 1000 nm," Appl. Phys. Lett. **82**, 3620 (2003).

39. W. Tsuei-Lian, Y. Kaneda, J. M. Yarborough, J. Hader, J. V. Moloney, A. Chernikov, S. Chatterjee, S. W. Koch, B. Kunert, and W. Stolz, "High-Power Optically Pumped Semiconductor Laser at 1040 nm," Photonics Technology Letters, IEEE **22**, 661-663 (2010).

40. http://www.coherent.com/products/?771/Optically-Pumped-Semiconductor-Laser-OPSL-Technology, Coherent, "Optically Pumped Semiconductor Laser (OPSL) Technology," 2011, Coherent

41. J. Rautiainen, J. Lyytikäinen, A. Sirbu, A. Mereuta, A. Caliman, E. Kapon, and O. G. Okhotnikov, "2.6 W optically-pumped semiconductor disk laser operating at 1.57-μm using wafer fusion," Opt. Express **16**, 21881-21886 (2008).

42. J. Rautiainen, J. Lyytikäinen, L. Toikkanen, J. Nikkinen, A. Sirbu, A. Mereuta, A. Caliman, E. Kapon, and O. G. Okhotnikov, "1.3-μm Mode-Locked Disk Laser With Wafer Fused Gain and SESAM Structures," Photonics Technology Letters, IEEE **22**, 748-750 (2010).

43. J. Lyytikäinen, J. Rautiainen, L. Toikkanen, A. Sirbu, A. Mereuta, A. Caliman, E. Kapon, and O. G. Okhotnikov, "1.3-μm optically-pumped

semiconductor disk laser by wafer fusion," Opt. Express **17**, 9047-9052 (2009).

44. J. Lyytikainen, J. Rautiainen, A. Sirbu, V. Iakovlev, A. Laakso, S. Ranta, M. Tavast, E. Kapon, and O. G. Okhotnikov, "High-Power 1.48-μm Wafer-Fused Optically Pumped Semiconductor Disk Laser," Photonics Technology Letters, IEEE **23**, 917-919 (2011).

45. H. Lindberg, M. Strassner, E. Gerster, and A. Larsson, "0.8 W optically pumped vertical external cavity surface emitting laser operating CW at 1550 nm," Electronics Letters **40**, 601-602 (2004).

46. L. S. Rothman, I. E. Gordon, A. Barbe, P. F. Bernath, D. C. Benner, M. Birk, V. Boudon, L. R. Brown, A. Campargue, J.-P. Champion, K. Chance, L. H. Coudert, V. Dana, V. M. Devi, J.-M. Flaud, R. R. Gamache, A. Goldman, D. Jacquemart, I. Kleiner, N. Lacome, W. J. Lafferty, J.-Y. Mandin, S. T. Massie, S. N. Mikhailenko, C. E. Miller, N. Moazzen-Ahmadi, O. V. Naumenko, A. V. Nikitin, J. Orphal, V. I. Perevalov, A. Perrin, A. Predoi-Cross, C. P. Rinsland, M. Rotger, M. Šimecková, M. A. H. Smith, K. Sung, S. A. Tashkun, J. Tennyson, R. A. Toth, and J. Vander Auwera, "The 2008 HITRAN molecular spectroscopic database," Journal of Quantitative Spectroscopy & Radiative Transfer **110**, 533-572 (2009).

47. D.Burns, J.-M.Hopkins, A.J.Kemp, B.Rösener, N.Schulz, C.Manz, K.Köhler, M.Rattunde, and J.Wagner, "Recent developments in high-power short-wave mid-infrared semiconductor disk lasers," in *Proc. SPIE*, (2009), pp. 719311.

48. J. M. Hopkins, A. J. Maclean, D. Burns, E. Riis, N. Schulz, M. Rattunde, C. Manz, K. Köhler, and J. Wagner, "Tunable, Single-frequency, Diode-pumped 2.3μm VECSEL," Opt. Express **15**, 8212-8217 (2007).

49. J. M. Hopkins, R. D. Preston, A. J. Maclean, S. Calvez, H. Sun, J. NG, M. Steer, M. Hopkinson, and D. Burns, "High performance 2.2 μm optically-pumped vertical external-cavity surface-emitting laser," Journal of Modern Optics **54**, 1677-1683 (2007).

50. J. M. Hopkins, N. Hempler, B. Rösener, N. Schulz, M. Rattunde, C. Manz, K. Köhler, J. Wagner, and D. Burns, "High-power, (AlGaIn)(AsSb) semiconductor disk laser at 2.0 μm," Opt. Lett. **33**, 201-203 (2008).

51. J. Nikkinen, J. Paajaste, R. Koskinen, S. Suomalainen, and O. G. Okhotnikov, "GaSb-Based Semiconductor Disk Laser With 130-nm Tuning Range at 2.5 μm," Photonics Technology Letters, IEEE **23**, 777-779 (2011).

52. B. Rösener, M. Rattunde, R. Moser, S. Kaspar, T. Töpper, C. Manz, K. Köhler, and J. Wagner, "Continuous-wave room-temperature operation of a 2.8 μm GaSb-based semiconductor disk laser," Opt. Lett. **36**, 319-321 (2011).

53. S. S. Beyertt, U. Brauch, F. Demaria, N. Dhidah, A. Giesen, T. Kubler, S. Lorch, F. Rinaldi, and P. Unger, "Efficient Gallium-Arsenide Disk Laser," Quantum Electronics, IEEE Journal of **43**, 869-875 (2007).

54. K. S. Kim, J. R. Yoo, S. M. Lee, S. J. Lim, J. Y. Kim, J. H. Lee, S. H. Cho, T. Kim, and Y. J. Park, "Highly efficient InGaAs QW vertical external cavity surface emitting lasers emitting at 1060nm," Journal of Crystal Growth **287**, 629-632 (2006).

55. L. Fan, C. Hessenius, M. Fallahi, J. Hader, H. Li, J. V. Moloney, W. Stolz, W. Stolz, J. T. Murray, and R. Bedford, "Highly strained InGaAs/GaAs multiwatt vertical-external-cavity surface-emitting laser emitting around 1170 nm," Appl. Phys. Lett. **91**, 131114 (2007).

56. S. L. Vetter, J. E. Hastie, V. M. Korpijarvi, J. Puustinen, M. Guina, O. Okhotnikov, S. Calvez, and M. D. Dawson, "Short-wavelength GaInNAs/GaAs semiconductor disk lasers," Electronics Letters **44**, 1069-1070 (2008).

57. et al, J. Konttinen. High-power (>1 W) dilute nitride semiconductor disk laser emitting at 1240 nm. New Journal of Physics 9[5], 140. 2007.

58. J. M. Hopkins, S. A. Smith, C. W. Jeon, H. D. Sun, D. Burns, S. Calvez, M. D. Dawson, T. Jouhti, and M. Pessa, "0.6 W CW GaInNAs vertical external-cavity surface emitting laser operating at 1.32μm," Electronics Letters **40**, 30-31 (2004).

59. M. Rahim, M. Arnold, F. Felder, I. Zasavitskiy, and H. Zogg, "Mid-Infrared Lead-Salt VECSEL (Vertical External Cavity Surface Emitting Laser) for Spectroscopy," (2008), pp. 183-186.

60. M. Rahim, A. Khiar, F. Felder, M. Fill, D. Chappuis, and H. Zogg, "Above Room Temperature Lead Salt VECSELs," Physics Procedia **3**, 1145-1148 (2010).

61. O. G. Okhotnikov and M. Guina, "Red Semiconductor Disk Lasers by Intracavity Frequency Conversion," in *Semiconductor Disk Lasers. Physics and Technology*, O. G. Okhotnikov, ed., (WILEY-VCH Verlag GmbH & Co. KGaA, Weinheim, 2010), pp. 119-143.

62. M. C. Tamargo, S. Guo, O. Maksimov, Y. C. Chen, F. C. Peiris, and J. K. Furdyna, "Red-green-blue light emitting diodes and distributed Bragg reflectors based on ZnCdMgSe lattice-matched to InP," Journal of Crystal Growth **227-228**, 710-716 (2001).

63. A. Smith, "Diode pumped visible Vertical External Cavity Surface Emitting Lasers," (University of Strathclyde, (2010).

64. K. Kishino and I. Nomura, "Yellow-green emitters based on beryllium-chalcogenides on InP substrates," phys. stat. sol. (c) **1**, 1477-1486 (2004).

65. T. Morita, H. Shinbo, T. Nagano, I. Nomura, A. Kikuchi, and K. Kishino, "Refractive index measurements of MgZnCdSe II-VI compound semiconductors grown on InP substrates and fabrications of 500-600 nm range MgZnCdSe distributed Bragg reflectors," Journal of Applied Physics **81**, 7575-7579 (1997).

66. S. Guo, O. Maksimov, M. Tamargo, F. Peiris, and J. Furdyna, "Distributed Bragg reflectors for visible range applications based on (Zn,Cd,Mg)Se lattice matched to InP," Appl. Phys. Lett. **77**, 4107 (2000).

67. J. M. Gerard, O. Cabrol, and B. Sermage, "InAs quantum boxes: Highly efficient radiative traps for light emitting devices on Si," Applied Physics Letters **68**, 3123-3125 (1996).

68. M. Butkus, C. J. Hamilton, G. P. Malcolm, I. Krestnikov, D. Livshits, and E. U. Rafailov, "Wavelength tuning in quantum dot semiconductor disc lasers," in *Semiconductor Laser Conference (ISLC), 2010 22nd IEEE International*, (2010), pp. 79-80.

69. F. Klopf, S. Deubert, J. P. Reithmaier, and A. Forchel, "Correlation between the gain profile and the temperature-induced shift in wavelength of quantum-dot lasers," Applied Physics Letters **81**, 217-219 (2002).

70. J. A. Lott, N. N. Ledentsov, V. M. Ustinov, A. Y. Egorov, A. E. Zhukov, P. S. Kop'ev, Z. Alferov, and D. Bimberg, "Vertical cavity lasers based on vertically coupled quantum dots," Electronics Letters **33**, 1150-1151 (1997).

71. J. A. Lott, A. R. Kovsh, N. N. Ledentsov, and D. Bimberg, "GaAs-Based InAs/InGaAs Quantum Dot Vertical Cavity and Vertical External Cavity Surface Emitting Lasers Emitting Near 1300 nm," in *Lasers and Electro-Optics, 2005. CLEO/Pacific Rim 2005. Pacific Rim Conference on*, (2005), pp. 160-161.

72. J. Rautiainen, I. Krestnikov, J. Nikkinen, and O. G. Okhotnikov, "2.5 W orange power by frequency conversion from a dual-gain quantum-dot disk laser," Opt. Lett. **35**, 1935-1937 (2010).

73. M. Butkus, J. Rautiainen, O. G. Okhotnikov, C. J. Hamilton, G. P. A. Malcolm, S. S. Mikhrin, I. L. Krestnikov, D. A. Livshits, and E. U. Rafailov, "Quantum Dot Based Semiconductor Disk Lasers for 1-1.3 μm," Selected Topics in Quantum Electronics, IEEE Journal of **PP**, 1-9 (2011).

74. M. Hoffmann, Y. Barbarin, D. J. Maas, M. Golling, T. Südmeyer, U. Keller, I. L. Krestnikov, S. S. Mikhrin, and A. R. Kovsh, "First Modelocked Quantum Dot Vertical External Cavity Surface Emitting Laser," (Optical Society of America, 2009), pp. ME5.

75. M. Hoffmann, Y. Barbarin, J. D. Maas, A.-R. Bellancourt, M. Shafiei, M. Golling, T. Südmeyer, U. Keller, I. L. Krestnikov, S. S. Mikhrin, and A. R. Kovsh, "All Quantum Dot Modelocked Vertical External Cavity Surface Emitting Laser," (Optical Society of America, 2009), pp. JThE13.

76. M. Butkus, C. J. Hamilton, D. Jackson, G. P. A. Malcolm, I. Krestnikov, D. Livshits, and E. U. Rafailov, "Green second harmonic generation in quantum dot semiconductor disc lasers," in *Laser Optics, St. Petersburgh, Russia 2010,* (2010).

77. T. D. Germann, A. Strittmatter, U. W. Pohl, D. Bimberg, J. Rautiainen, M. Guina, and O. G. Okhotnikov, "Quantum-dot semiconductor disk lasers," Journal of Crystal Growth **310**, 5182-5186 (2008).

78. A. R. Albrecht, T. J. Rotter, C. P. Hains, A. Stintz, J. V. Moloney, K. J. Malloy, and G. Balakrishnan, "Multi-watt 1.25 μm quantum dot VECSEL," Electronics Letters **46**, 856-857 (2010).

79. P. J. Schlosser, J. E. Hastie, S. Calvez, A. B. Krysa, and M. D. Dawson, "InP/AlGaInP quantum dot semiconductor disk lasers for CW TEM_{00} emission at 716 - 755 nm," Opt. Express **17**, 21782-21787 (2009).

80. T. D. Germann, A. Strittmatter, J. Pohl, U. W. Pohl, D. Bimberg, J. Rautiainen, M. Guina, and O. G. Okhotnikov, "High-power semiconductor disk laser based on InAs/GaAs submonolayer quantum dots," Applied Physics Letters **92**, 101123 (2008).

81. M. Butkus, K. G. Wilcox, J. Rautiainen, O. G. Okhotnikov, S. S. Mikhrin, I. L. Krestnikov, A. R. Kovsh, M. Hoffmann, T. Südmeyer, U. Keller, and E. U. Rafailov, "High-power quantum-dot-based semiconductor disk laser," Opt. Lett. **34**, 1672-1674 (2009).

82. J. Rautiainen, I. Krestnikov, M. Butkus, E. U. Rafailov, and O. G. Okhotnikov, "Optically pumped semiconductor quantum dot disk laser operating at 1180 nm," Opt. Lett. **35**, 694-696 (2010).

83. M. A. Emanuel, J. A. Skidmore, M. Jansen, and R. Nabiev, "High-power InAlGaAs-GaAs laser diode emitting near 731 nm," Photonics Technology Letters, IEEE **9**, 1451-1453 (1997).

84. M. Hoffmann, Y. Barbarin, D. Maas, M. Golling, I. Krestnikov, S. Mikhrin, A. Kovsh, T. Südmeyer, and U. Keller, "Modelocked quantum dot vertical external cavity surface emitting laser," Applied Physics B: Lasers and Optics **93**, 733-736 (2008).

85. D. J. H. C. Maas, A. R. Bellancourt, B. Rudin, M. Golling, H. J. Unold, T. Südmeyer, and U. Keller, "Vertical integration of ultrafast semiconductor lasers," Applied Physics B: Lasers and Optics **88**, 493-497 (2007).

86. T. D. Raymond, W. J. Alford, M. H. Crawford, and A. A. Allerman, "Intracavity frequency doubling of a diode-pumped external-cavity surface-emitting semiconductor laser," Opt. Lett. **24**, 1127-1129 (1999).

87. D. J. Stothard, J. M. Hopkins, D. Burns, and M. H. Dunn, "Stable, continuous-wave, intracavity, optical parametric oscillator pumped by a semiconductor disk laser (VECSEL)," Opt. Express **17**, 10648-10658 (2009).

88. M. Scheller, J. M. Yarborough, J. V. Moloney, M. Fallahi, M. Koch, and S. W. Koch, "Room temperature continuous wave milliwatt terahertz source," Opt. Express **18**, 27112-27117 (2010).

89. D. C. Parrotta, W. Lubeigt, A. J. Kemp, D. Burns, M. D. Dawson, and J. E. Hastie, "Continuous-wave Raman laser pumped within a semiconductor disk laser cavity," Opt. Lett. **36**, 1083-1085 (2011).

90. R. Hartke, E. Heumann, G. Huber, M. Kühnelt, and U. Steegmüller, "Efficient green generation by intracavity frequency doubling of an optically pumped semiconductor disk laser," Applied Physics B: Lasers and Optics **87**, 95-99 (2007).

91. T. Baer, "Large-amplitude fluctuations due to longitudinal mode coupling in diode-pumped intracavity-doubled Nd:YAG lasers," J. Opt. Soc. Am. B **3**, 1175-1180 (1986).

92. Y. Kaneda, J. M. Yarborough, L. Li, N. Peyghambarian, L. Fan, C. Hessenius, M. Fallahi, J. r. Hader, J. V. Moloney, Y. Honda, M. Nishioka, Y. Shimizu, K. Miyazono, H. Shimatani, M. Yoshimura, Y. Mori, Y. Kitaoka, and T. Sasaki, "Continuous-wave all-solid-state 244 nm deep-ultraviolet laser source by fourth-harmonic generation of an optically pumped semiconductor laser using CsLiB6O10 in an external resonator," Opt. Lett. **33**, 1705-1707 (2008).

93. J. Paul, Y. Kaneda, T. L. Wang, C. Lytle, J. V. Moloney, and R. J. Jones, "Doppler-free spectroscopy of mercury at 253.7 nm using a high-power, frequency-quadrupled, optically pumped external-cavity semiconductor laser," Opt. Lett. **36**, 61-63 (2011).

94. A. J. Maclean, A. J. Kemp, S. Calvez, K. Jun-Youn, K. Taek, M. D. Dawson, and D. Burns, "Continuous Tuning and Efficient Intracavity Second-Harmonic Generation in a Semiconductor Disk Laser With an Intracavity Diamond Heatspreader," Quantum Electronics, IEEE Journal of **44**, 216-225 (2008).

95. S. Hilbich, W. Seelert, V. Ostroumov, Ch. Kannengiesser, R. v.Elm, J. Mueller, E. Weiss, H. Zhou, and J. Chilla, "New wavelengths in the yellow-orange range between 545 nm and 580 nm generated by an intracavity frequency-doubled optically pumped semiconductor laser," (Proc. SPIE, 2007), pp. 64510C.

96. M. Fallahi, C. Hessenius, F. Li, J. Hader, L. Hongbo, J. V. Moloney, W. Stolz, and S. W. Koch, "High power tunable yellow laser using InGaAs/GaAs vertical external-cavity surface-emitting lasers," in *Semiconductor Laser Conference, 2008. ISLC 2008. IEEE 21st International*, (2008), pp. 169-170.

97. J. Paul, K. Yushi, W. Tsuei-Lian, L. Christian, V. M. Jerome, and J. Jason, "Precision Spectroscopy of Atomic Mercury in the Deep Ultraviolet Based on Fourth-Harmonic Generation from an Optically Pumped External-Cavity Semiconductor Laser," (Optical Society of America, 2010), pp. CTuS6.

98. Chilla, Juan L. A., Coherent Inc., Personal Communication, 2008.

99. J. Rautiainen, A. Härkönen, V. M. Korpijärvi, P. Tuomisto, M. Guina, and O. G. Okhotnikov, "2.7 W tunable orange-red GaInNAs semiconductor disk laser," Opt. Express **15**, 18345-18350 (2007).

100. A. Rantamäki, A. Sirbu, A. Mereuta, E. Kapon, and O. G. Okhotnikov, "3 W of 650 nm red emission by frequency doubling of wafer-fused semiconductor disk laser," Opt. Express **18**, 21645-21650 (2010).

101. M. T. Andersen, P. J. Schlosser, J. E. Hastie, P. Tidemand-Lichtenberg, M. D. Dawson, and C. Pedersen, "Singly-resonant sum frequency generation of visible light in a semiconductor disk laser," Opt. Express **17**, 6010-6017 (2009).

102. S. Illek, T. Albrecht, P. Brick, S. Lutgen, I. Pietzonka, M. Furitsch, W. Diehl, J. Luft, and K. Streubel, "Vertical-External-Cavity Surface-Emitting Laser With Monolithically Integrated Pump Lasers," Photonics Technology Letters, IEEE **19**, 1952-1954 (2007).

103. S. Hoogland, S. Dhanjal, A. C. Tropper, J. S. Roberts, R. Haring, R. Paschotta, F. Morier-Genoud, and U. Keller, "Passively mode-locked diode-pumped surface-emitting semiconductor laser," Photonics Technology Letters, IEEE **12**, 1135-1137 (2000).

104. V. G. Savitski, J. E. Hastie, S. Calvez, and M. D. Dawson, "Cavity-dumping of a semiconductor disk laser for the generation of wavelength-tunable micro-Joule nanosecond pulses," Opt. Express **18**, 11933-11941 (2010).

105. L. G. Morton, H. D. Foreman, J. E. Hastie, M. D. Dawson, and E. Riis, "Actively Stabilised Single-Frequency Red VECSEL," (Optical Society of America, 2007), pp. WB7.

106. M. A. Holm, D. Burns, A. I. Ferguson, and M. D. Dawson, "Actively stabilized single-frequency vertical-external-cavity AlGaAs laser," Photonics Technology Letters, IEEE **11**, 1551-1553 (1999).

107. A. Garnache, M. Myara, A. Bouchier, J. P. Perez, P. Signoret, I. Sagnes, and D. Romanini, "Single frequency free-runing low noise compact external-cavity VCSELs at high power level (50mW)," in *Optical Communication, 2008. ECOC 2008. 34th European Conference on,* (2008), pp. 1-2.

108. N. Hempler, J. M. Hopkins, B. Rösener, M. Rattunde, J. Wagner, V. V. Fedorov, I. S. Moskalev, S. B. Mirov, and D. Burns, "Semiconductor disk laser pumped Cr^{2+}:ZnSe lasers," Opt. Express **17**, 18136-18141 (2009).

109. M. Kuznetsov, F. Hakimi, R. Sprague, and A. Mooradian, "Design and characteristics of high-power (>0.5-W CW) diode-pumped vertical-external-cavity surface-emitting semiconductor lasers with circular TEM_{00} beams," Selected Topics in Quantum Electronics, IEEE Journal of **5**, 561-573 (1999).

110. P. J. Schlosser, S. Calvez, J. E. Hastie, S. Jin, T. D. Germann, A. Strittmatter, U. W. Pohl, D. Bimberg, and M. D. Dawson, "Characterisation of an InAs Quantum Dot Semiconductor Disk Laser," (Optical Society of America, 2008), pp. CWD5.

111. B. Chance, M. Cope, E. Gratton, N. Ramanujam, and B. Tromberg, "Phase measurement of light absorption and scatter in human tissue," Review of Scientific Instruments **69**, 3457-3481 (1998).

Chapter 2:

VECSEL theory and design criteria

This chapter is concerned with the theoretical understanding of VECSEL devices, which are multilayer structures, incorporating different material compositions, usually monolithically grown. This puts constraints on the choice of these compositions with respect to the lattice constant, necessary for a high growth quality. Other important material properties, such as the refractive index and energy bandgap are also presented, which are important to develop an understanding for the generic VECSEL design. A further important matter in terms of VECSEL devices is the efficient thermal management for extraction of the pump induced heat load from the active region. This section is followed by a short introduction to quantum confinement and gain modelling based on QW devices and described by Kuznetsov et al. in [1]. At the end of this chapter will be a discussion on material, structural and growth related issues with a focus on the fabrication of quantum dot (QD) layers.

2.1 Semiconductor alloys

The spectral coverage of QW and QD based VECSEL devices presented in Fig 1.10, Fig. 1.11 and Fig. 1.12 give a good overview of the emission wavelength flexibility of semiconductor lasers both for the fundamental emission and for colour conversion. A few gaps in spectral coverage still remain. Fig. 2-1 shows the lattice constant together with the corresponding energy bandgap of the most common group III-V semiconductor binary compounds, used in optoelectronic devices [2]. Some group IV elemental crystals and group II-VI binary compounds are also included. The empirical Vegard's [3] law is used to calculate the lattice constant of a ternary

compound a_{ABC}, based on the values for the contributing binaries, a_{AB} and a_{AC}, in dependence on the mole fraction.

$$a_{A_xB_{1-x}C}(x) = x \cdot a_{AC} + (1-x)a_{BC}, \qquad \text{Equation [2-1]}$$

This expression can be taken to calculate the corresponding energy bandgap by the introduction of a bowing parameter, b [3]. The bowing parameter is a measure for the lattice distortion in a periodic crystal due to the random distribution of the substituted (alloy) atoms [4].

$$E_{A_xB_{1-x}C}(x) = x \cdot E_{AC} + (1-x)E_{BC} - x(1-x)b, \qquad \text{Equation [2-2]}$$

The interconnecting lines for ternary compound semiconductors are shown in Fig. 2-1 as solid lines for direct transitions. Indirect transitions are illustrated by dashed lines. The fabrication of high quality structures for optoelectronic purposes requires substrates with a low defect density. GaAs, InP and GaSb are some of the used

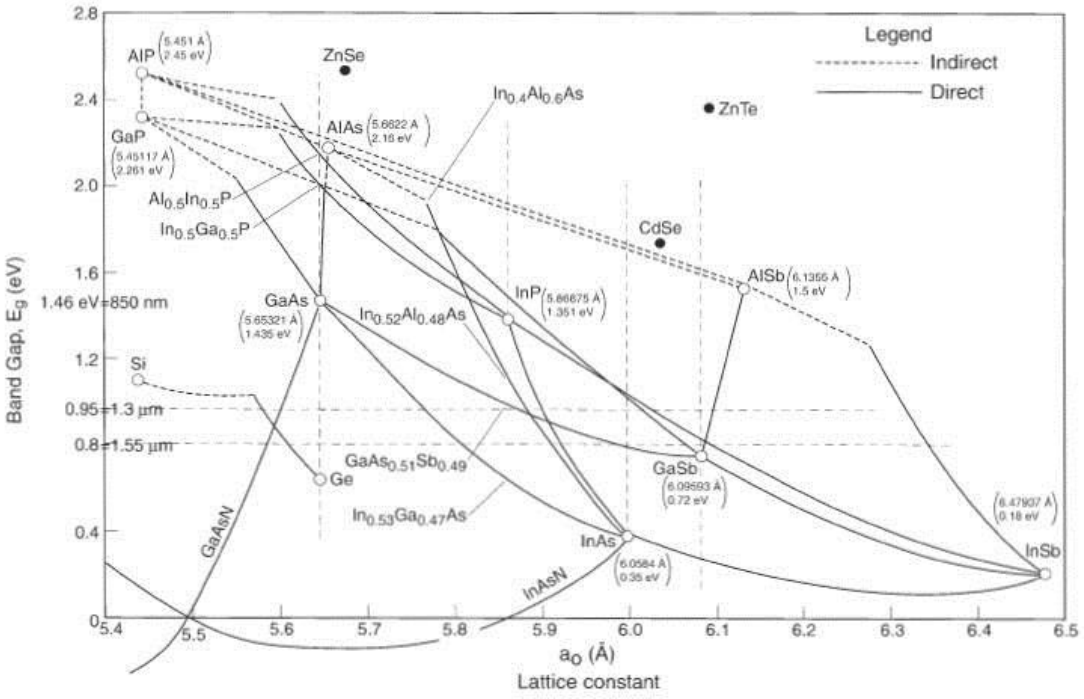

Fig. 2-1 Bandgap energy vs. lattice constant diagram of the most important group IV, III-V and some group II-VI elements, binary and ternary compounds. The energy scale spans from the mid-infrared to the visible blue region. The vertical dashed lines mark the lattice matching condition of the most common substrates of group III-V semiconductors, such as GaAs, InP, InAs and GaSb. [2]

substrate materials. The vertical dashed lines in Fig. 2-1 represent the lattice-matched condition for the corresponding substrate. Every alloy composition, intersecting these lines fulfils the (near) lattice-matched condition and can theoretically be used. The vast range of possible bandgap energy coverage by semiconductor alloys is thus reduced to materials where a suitable substrate is available.

Chapter	Material system	Used as	Mole fractions x	References	
				Dielectric constants	Energy bandgap
3 & 4	**GaAs**	Substrate	0	[5,6]	[3]
	$Al_xGa_{1-x}As$	DBR	0.98 / 0.2	[5,6]	[3]
3	**$Al_xGa_{1-x}As$**	Confinement/Barrier	0.3 / 0	[5,6]	[3]
	InAs/GaAs	SML QDs	-	N/A	N/A
	$Al_xGa_{1-x}As$	DBR	0.35 / 1	[5,6]	[3]
4	**$(Al_xGa_{1-x})_{0.51}In_{0.49}P$**	Barriers	0.3 / 0.6 / 0	[7,8]	[9,10]
	$InP/Ga_{0.51}In_{0.49}P$	DWELL	-	N/A	N/A

Table 2-1: Summary of the material compositions used for the VECSEL structures discussed in Chapters 3 and 4 together with the references where parameters can be found.

All devices of concern for this thesis were grown on the binary substrate Gallium Arsenide (GaAs). The used high reflective DBRs are based on the ternary compound $Al_xGa_{1-x}As$, where the similarity in the lattice constant between AlAs ($a_{AlAs} = 5.6622$ Å) and GaAs ($a_{GaAs} = 5.65321$ Å) [2], allows the growth of nearly lattice matched structures in the whole range of $0 \leq x_{Al} \leq 1$. Broad stopband ($\geq 100\,nm$) AlGaAs DBRs may be fabricated for high reflection from the red to the mid-IR region.

The active regions of the structures discussed in Chapter 3 incorporate InAs/GaAs submonolayer (SML) QDs imbedded within a GaAs matrix and in Chapter 4 $InP/Ga_{0.51}In_{0.49}P$ quantum-dots-in-a-well (Dwell) imbedded in an ($(Al_xGa_{1-x})_{0.51}In_{0.49}P$) matrix and are listed in Table 2-1. The matrix materials are lattice-matched to the substrate to avoid strained growth and serve as pump absorption barriers. Further information on the specific designs can be found within the respective chapters. A very general design of a VECSEL is depicted in Fig. 1.9. As the main topic of this thesis is the development of an InP/AlGaInP based QD VECSEL, the following discussion refers to this material system in particular. In summary, the VECSEL gain structure consists of:

- a monolithically grown, lattice-matched DBR on top of a suitable substrate.
- the active region grown directly on the DBR, consisting of the pump absorbing barriers, integrating the QWs or QD gain layers.
- strain compensation layers adjacent to the gain layers or placed within the barriers can be used in order to counteract the build-up of strain.
- for purposes of carrier confinement within the active region a transparent window layer is used together with a capping layer to avoid oxidation.

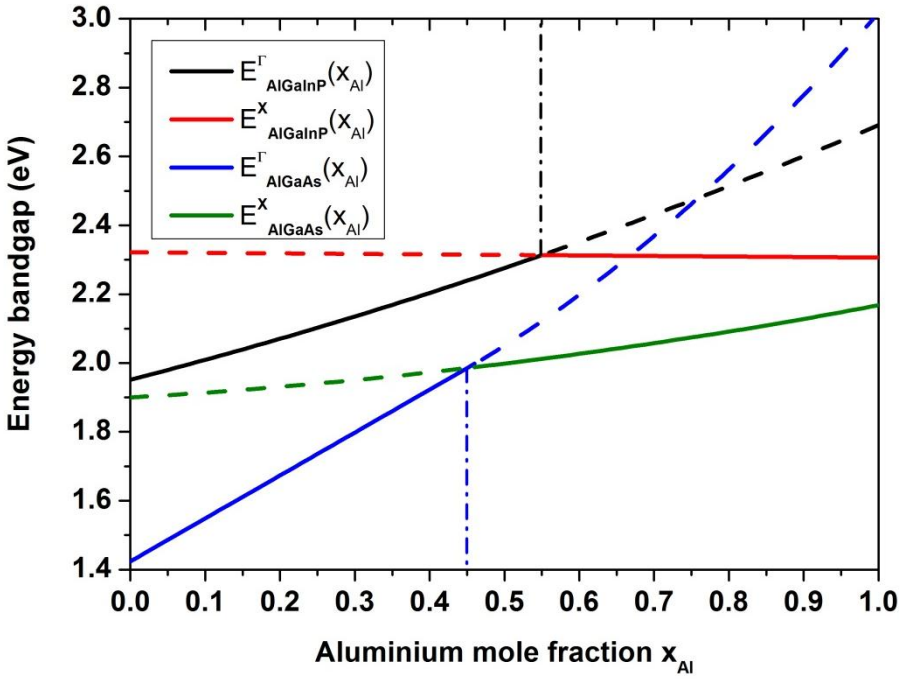

Fig. 2-2 Room temperature energy bandgap of lattice matched $(Al_xGa_{1-x})_{0.51}In_{0.49}P$ and $Al_xGa_{1-x}As$ for direct (black/blue) and indirect (red/green) transition, suggesting crossing points around $x_{Al} = 0.55$ and $x_{Al} = 0.45$ respectively. Solid lines stand for the lowest available energy transition at a specific mole fraction of a composition.

Fig. 2-2 represents the room temperature (RT) dependence of the direct (E_Γ) and indirect (E_X) transition energy on the aluminium mole fraction x_{Al} of $(Al_xGa_{1-x})_{0.51}In_{0.49}P$ and $Al_xGa_{1-x}As$. The model uses equation [2-2] together with binary compound band and bowing parameters (for ternary and quaternaries) given in Vurgaftman et al. [3] and Adachi et al. [5] respectively. The solid lines mark the lowest available bandgap transition. Crossing points, where the transition characteristic changes from direct to indirect nature around $x_{Al} = 0.55$ and $x_{Al} = 0.45$ respectively. The publication of Najda et al. [10] suggests, a crossing point at $x_{Al} = 0.6$ for $(Al_xGa_{1-x})_{0.51}In_{0.49}P$, where also the largest transition energy is located.

Knowledge of the dielectric coefficients is required for the calculation of the refractive index pattern, the reflection and the electric field within the subcavity. Fig. 2-3 represents the modelled refractive indices in dependence on the wavelength of $Al_xGa_{1-x}As$, used for the DBR [5], and of $(Al_xGa_{1-x})_{0.51}In_{0.49}P$, used for the active region [7]. [5] and [7] apply model dielectric functions (MDF), which uses critical-point energies in order to describe the dielectric function in dependence on the photon energy of a material compound. These critical points are closely related to the optical properties of solids, such as bandgap energies, absorption coefficients and refractive indices. The distinct kinks in the figure indicate the absorption edge. The vertical red and green dashed lines illustrate the designed emission wavelength (740 nm) and the pump wavelength (532 nm) respectively.

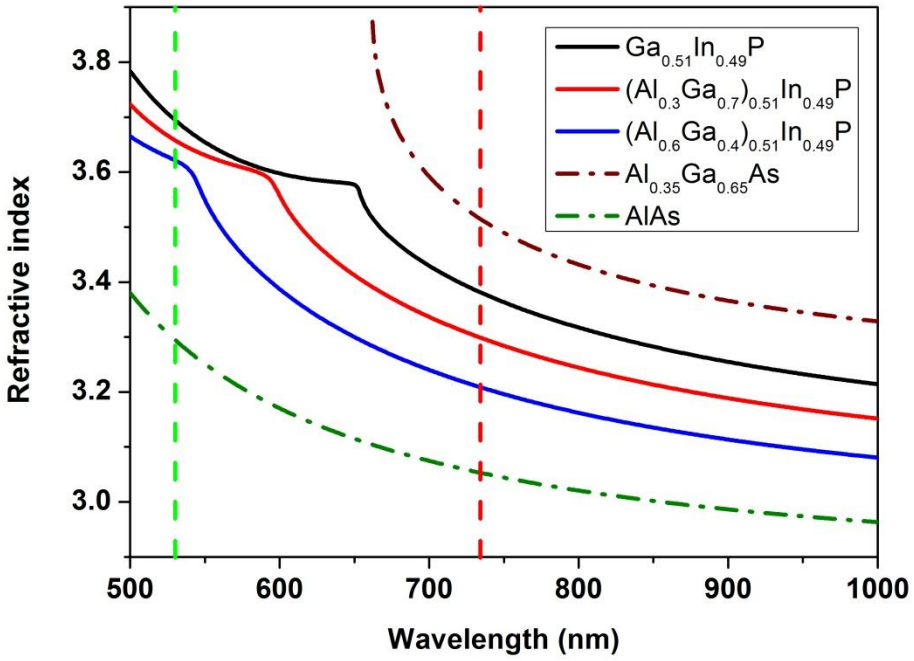

Fig. 2-3 Refractive index plotted with wavelength for different aluminium mole fractions of lattice-matched (to GaAs) quaternary $(Al_xGa_{1-x})_{0.51}In_{0.49}P$ (solid black: x_{Al}=0, red: x_{Al}=0.3, blue: x_{Al}=0.6) and ternary $Al_xGa_{1-x}As$ (dash-dotted brown: x_{Al}=0.35, green: x_{Al}=1) compositions. The green and red vertical dashed lines depict the pump wavelength and the possible design wavelength.

2.2 Multi-layer VECSEL structures

2.2.1 Characteristic matrix

In order to be able to express the wave propagation in a stratified medium (multi-layer structure), the assumption of thin dielectric films is used, where the dielectric constants are considered as constant. The characteristic matrix, $\begin{bmatrix} E \\ F \end{bmatrix}$, of a single film is dependent on the layer thickness, t, the propagating waves' wavelength, λ, the refractive index, n, and the angle, θ, of the incident wave onto the first boundary surface and is described by [11]:

$$\begin{bmatrix} E \\ F \end{bmatrix} = \begin{bmatrix} A & B \\ C & D \end{bmatrix} = \begin{bmatrix} \cos(\delta) & -\frac{i}{\eta}\sin(\delta) \\ -i\,\eta\sin(\delta) & \cos(\delta) \end{bmatrix}, \qquad \text{Equation [2-3]}$$
$$\delta = \frac{2\pi}{\lambda} nt\,cos\theta,$$

with $\eta = n \cdot \sqrt{\frac{\varepsilon_0}{\mu_0}}$ the optical admittance for oblique incidence. μ_0 and ε_0 being the permeability and permittivity of free space respectively. The interest of this work is focussed on the wave propagation normal to the surface and $\theta = 0$. In this case, the refractive index of s- and p-polarised light is the same. For a stratified medium with a finite layer number the characteristic matrix now becomes

$$\begin{bmatrix} E \\ F \end{bmatrix} = \left(\prod_{k=1}^{m} \begin{bmatrix} \cos(\delta_k) & -\frac{i}{\eta_k}\sin(\delta_k) \\ -i\,\eta_k\sin(\delta_k) & \cos(\delta_k) \end{bmatrix} \right) \begin{bmatrix} 1 \\ \eta_{subs} \end{bmatrix}. \qquad \text{Equation [2-4]}$$

Here η_{subs} stands for the optical admittance of the substrate. The ratio $Y = \frac{F}{E}$ can now be understood as the total optical admittance of the assembly. The total reflectivity of the multi-layer stack

$$R = \left| \frac{(A + Bn_{subs})n_i - (C + Dn_{subs})}{(A + Bn_{subs})n_i + (C + Dn_{subs})} \right|^2 = \left| \frac{\eta_i - Y}{\eta_i + Y} \right|^2 \qquad \text{Equation [2-5]}$$

is also dependent on the medium of the incident wave, denoted by the index, i, and exiting wave (here usually the substrate), denoted by the index, $subs$.

2.2.2 Distributed Bragg reflector

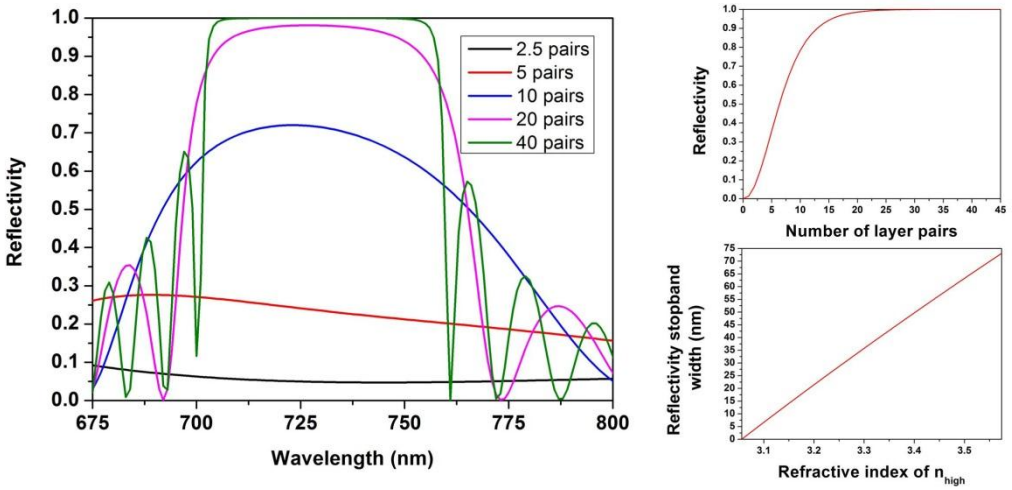

Fig. 2-4 Left: Reflectivity spectrum of an $Al_xGa_{1-x}As$ DBR as used for the design in Chapter 4 for 2.5, 5, 10, 20 and 40 layer pairs. The refractive indices are n_{low}=3.056 (AlAs) and n_{high}=3.522 ($Al_{0.35}Ga_{0.65}As$). Top right: Reflectivity stopband centre reflectivity in dependence on layer pairs. Bottom right: Reflectivity stopband width in dependence on the high refractive index (difference between high and low refractive index by variation of the high refractive indices between n_{high}=3.056-3.574 and constant n_{low}=3.056).

The largest part of the roughly 4-7 µm thick VECSEL structure is the distributed Bragg reflector (DBR). A DBR is a periodic succession of layer-pairs with high and low refractive index, having a thickness of $\lambda_{design}/4n$ each, where λ_{design} is the design wavelength. Partial reflections occur at every interface but reflected beams experience a phase shift of π only where the beam propagates in direction from a low towards a high refractive index layer. Both layer thickness and phase shift cause a constructive interference of all internally reflected beams at the structure surface, increasing the reflectivity at around λ_{design}. The total reflectivity and reflectivity stopband width scales with the difference in refractive index between the high and low index layer ($\Delta n = n_{high} - n_{low}$). The larger this difference, the fewer repeats are necessary to achieve the required high reflectivity values of R > 99.9 %. Fig. 2-4

left: shows the reflectivity stopband for different number of repeats of the low (AlAs: $n_{low} = 3.056$) and high ($Al_{0.35}Ga_{0.65}As$: $n_{high} = 3.522$) refractive index layers, as used for the structure design in Chapter 4. The graphs on the right side of Fig. 2-4 illustrate the dependence of the stopband centre reflectivity with number of layer pairs (top) and the estimated width of the reflectivity stopband in dependence on the refractive index difference (bottom). These calculations are based on the following equations [2-6] and [2-7] for the reflectivity stopband width and total centre reflectivity respectively [12].

$$\Delta\lambda_{stopband} = \frac{\lambda_{design}}{\pi} \frac{\Delta n}{\left(\frac{1}{n_{high}} + \frac{1}{n_{low}}\right)^{-1}} \qquad \text{Equation [2-6]}$$

$$R(N) = \left[\frac{1 - \left(\frac{n_{low}}{n_{high}}\right)^{2N}}{1 + \left(\frac{n_{low}}{n_{high}}\right)^{2N}}\right]^2 \qquad \text{Equation [2-7]}$$

VECSELs are low gain lasers and tolerate only very few percents of total losses. Therefore the minimization of the mirror transmission/absorption by the high reflection of the monolithically integrated DBR is necessary. The wide reflectivity stopband enables broad tuning of the laser emission, making use of the broad semiconductor gain spectrum. A DBR must thus be non-absorptive for the laser emission wavelength in order to enable laser action. In the optimal case, it should also be highly reflective for the pump wavelength, reducing the heat introduction within deeper lying layers. This is not always practical, e.g. for the present situation (using material compositions for the design of the InP QD VECSELs as stated in Chapter 4), the $\lambda_{design}/4n$-thick $Al_xGa_{1-x}As$ layers of the DBR with a suitably large refractive index difference, are absorptive for the pump wavelength (532 nm). Reabsorption of the generated laser light (denoted by the red dashed line in Fig. 2-3) within the DBR was avoided by the choice of an aluminium mole fraction of $x_{Al} = 0.35$ for the high refractive index layer of the DBR. This limits the refractive index difference and dictates the number of DBR pairs necessary to reach the required reflectivity.

A way to circumvent excessive pump light absorption within the DBR is by preventing it from reaching the DBR.

2.2.3 Subcavity configuration

For the design of the gain region grown on top of the DBR, the laser subcavity, different factors have to be taken into account, which are discussed in the following:

- Total subcavity length
- Total number and distribution of gain layers
- Available materials for pump absorbing barriers, gain layers, strain compensation layers, transparent window layer, capping layer
- Resonance effects

2.2.3.1 Subcavity length and configuration criteria

In order to avoid pump light absorption within the DBR only layers transparent to the pump wavelength should be used. Where this is not possible, the pump light can be prevented from reaching the DBR by adjustment of the subcavity length. Illustrated in Fig. 2-5 is the pump absorption together with the refractive index pattern of the subcavity for a VECSEL structure, similar to one used in Chapter 4. The absorption coefficient calculation of the $(Al_xGa_{1-x})_{0.51}In_{0.49}P$ compositions is taken from Schubert et al. [7] and leads to an estimated pump absorption in the active region of about 98 % of the pump wavelength (532 nm). A further extension of the subcavity beyond this length has to be taken with caution to avoid unpumped QWs.

A further aspect, important for the total subcavity length and configuration is the room temperature carrier diffusion length. It is only a few micro-meters in bulk GaAs samples [13]. Under the consideration of the multiple interfaces and gain layers inside the active region, which act as carrier traps and potential barriers the

free carrier mobilities and thus the diffusion lengths within the active region of a VECSEL are likely to be lower. Regarding as well that the system $(Al_xGa_{1-x})_{0.51}In_{0.49}P$, used in this example is a quaternary compound, the carrier mobilities are expected to be lower compared to a binary system due to the presence of more, differently sized atoms, which are randomly distribution within the crystal lattice, affecting the lattice periodicity, thus increasing scattering events. It has also been stated in Bour et al. [14] and Yokotsuka et al. [15] that the hole mobility of $(Al_xGa_{1-x})_{0.51}In_{0.49}P$ is very low in comparison to AlGaAs compounds. With this in mind, too long subcavities might introduce absorption losses, if the deeper lying gain layers are not pumped sufficiently.

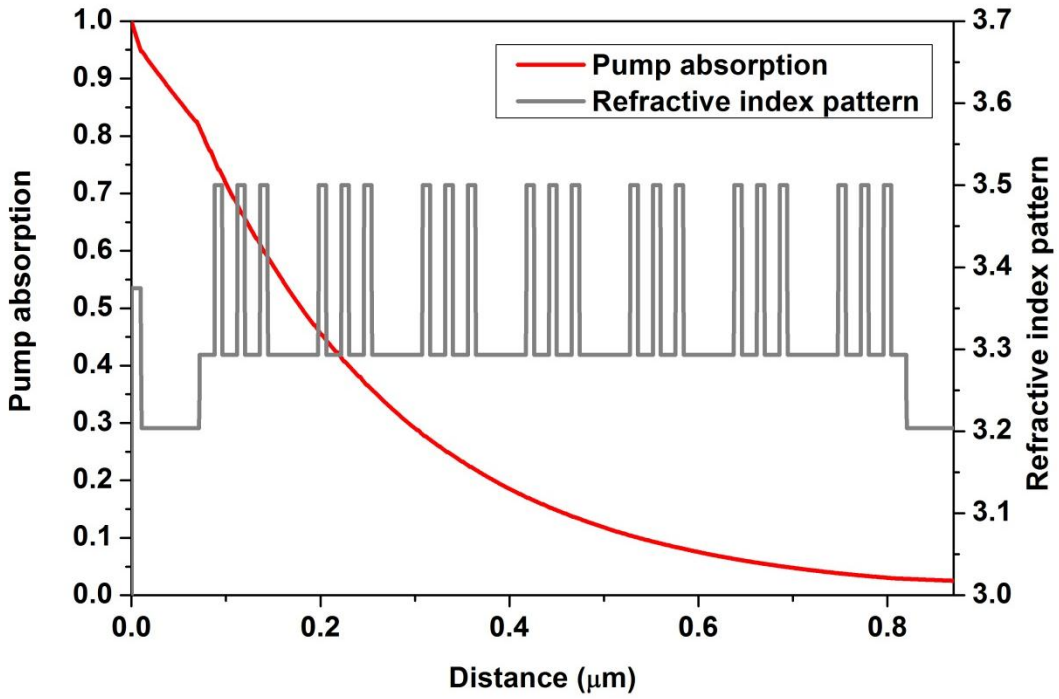

Fig. 2-5 Absorption of the incident 532 nm pump beam displayed together with the refractive index pattern of the designed structure. An estimated absorption value of 98 % is designed.

The total subcavity length also defines the number of available field anti-nodes, at which gain layers can be positioned (see following discussion on RPG). A decision about the total number of gain layers and their distribution across the available anti-nodes is also necessary. With respect to the gain layer distribution two approaches were reported: uniform and non-uniform distribution. In the first case, which seems to be the standard approach with respect to number of reported devices,

the carrier distribution within the active region is considered to be homogeneous and gain layers are distributed equally at the antinodes. In the second case, the carrier mobility is thought to be low and their distribution is supposed to follow the decaying pump intensity due to absorption, as can be seen in Fig. 2-5. More gain layers are placed at the anti-nodes near the surface, with decreasing number for deeper lying anti-nodes [16]. A different way to ensure a homogeneous distribution of the generated carriers across the available gain layers is the use of larger bandgap barrier layers to subdivide the active region as was reported by Geske et al. in case of optically pumped VCSELs [17] and also realised in a dual-wavelength VECSEL structure by Leinonen et al. [18].

Important restrictions can be made as well by the available material compositions. 'Standard' VECSEL structures for the emission in the near-IR range utilise a window layer. This layer has a larger bandgap compared to the barrier composition, is transparent for both, pump and laser light and has the two purposes:

- to confine the generated carriers to the active region
- prevent them from escaping to the surface, where they recombine non-radiatively.

In the case of $(Al_xGa_{1-x})_{0.51}In_{0.49}P$ based structures the offset in bandgap energy with respect $Ga_yIn_{1-y}P$ QWs is maximised for $x_{Al} = 0.6$ as was illustrated in Fig. 2-2, offering the highest confinement potential. $Ga_yIn_{1-y}P$ QWs are thus usually imbedded within this material compound. At present, there is no suitable material composition known to the author with a higher energy bandgap that could be used as a lattice- matched, transparent carrier confinement window on top of the active region; thus free charge carriers, generated in the active region can diffuse to the surface and recombine non-radiatively, reducing the efficiency of these structures. Furthermore, the necessary $Ga_{0.51}In_{0.49}P$ capping layer used to prevent the oxidation of aluminium in the underlying structure has an even lower bandgap compared to the barrier layer, supporting diffusion towards the surface.

The influence of resonance effects on the effective gain is stated in the following subsections.

2.2.3.2 Resonance effects

Due to the very small gain medium thickness of only a few nanometres per QW and even less for QD-layers, VECSEL structures contain several gain layers in order to maximise the modal gain. Furthermore, the position of these layers with respect to the resonating field becomes important.

Resonant periodic gain (RPG) refers to the placement of the gain layers at the position of the field antinodes at the designed laser emission wavelength in order to optimise the overlap between the optical field and the gain layers (see Fig. 2-6 right for clarification). This overlap is denoted by the three dimensional optical confinement factor $\Gamma = \Gamma_x \Gamma_y \Gamma_z$. It can be reduced to the longitudinal confinement factor $\Gamma \approx \Gamma_z$ in case of QWs; under the consideration that z is the direction of field propagation, which is the growth direction in a vertically-emitting laser. In contrast, there is no optical confinement in the two lateral directions x, y, thus the confinement factors can be regarded to be unity $\Gamma_x = \Gamma_y = 1$. Γ_z is a critical parameter in surface emitting devices [19], represented by equation [2-8]:

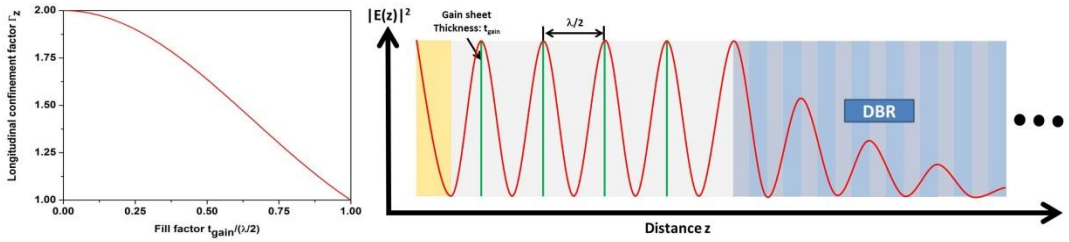

Fig. 2-6 left: Calculated longitudinal confinement factor Γ_z in dependence on the fill factor $t_{gain}/(\lambda/2)$. Right: Principle of a VECSEL structure with resonant periodic gain (RPG), showing the overlap between the standing subcavity field and the gain layers to enhance the interaction between the field and the carrier distribution.

$$\Gamma_z = \frac{\int_{L_{QWgain}} |E(z)|^2 dz}{\int_{L_{cavity}} |E(z)|^2 dz}. \qquad \text{Equation [2-8]}$$

L_{QWgain} and L_{cavity} stand for the total thickness of the gain layers (QWs) and the total cavity length respectively. This equation can be transformed by integration into equation [2-9]

$$\Gamma_z \equiv \Gamma_{RPG} = \frac{N \cdot t_{gain}}{L_{cavity}} \left(1 + sinc \left[\pi \left(\frac{t_{gain}}{\lambda/2} \right) \right] \right). \qquad \text{Equation [2-9]}$$

N stands for the number of gain layers. The effective gain layer thickness is t_{gain} and L_{cavity} is the cavity length, which is a multiple of $\lambda/2$. The function in the brackets describes enhancement with fill factor, $[t_{gain}/(\lambda/2)]$, which has the form of a $sinc$-function with the maximum value of 2 for very thin gain sheets and 1 in case of a bulk gain region as illustrated in Fig. 2-6 left side. The periodic placement of the gain layers acts also as a wavelength selective filter function, because only modes with a wavelength equal to the gain layer spacing experience enhancement. Thus a correct placement of the gain layers at the field antinodes for RPG is required [20].

A discussion on QD devices is more complicated, as optical confinement occurs in all three directions. The three dimensional confinement factor $\Gamma = \Gamma_x \Gamma_y \Gamma_z = \Gamma_{xy} \Gamma_z$ can be separated into the longitudinal confinement Γ_z and the lateral confinement factor Γ_{xy}. The lateral confinement factor is defined as the ratio between the area covered by QDs (number of QDs times the average QD base area) and the total area, equation [2-10]. The longitudinal confinement factor on the other hand is the overlap of the electric field in vertical z-direction with the quantum dots, equation [2-11].

$$\Gamma_{xy} = \frac{N_{QD} A_{QD}}{A}. \qquad \text{Equation [2-10]}$$

$$\Gamma_z = \frac{\int \int_A \int_{QD} |E(z)|^2 dz}{A \cdot \int_{L_{cavity}} |E(z)|^2 dz}. \qquad \text{Equation [2-11]}$$

The upper equations indicate that the confinement factor is here dependent on the areal coverage of the QDs and thus on the dot density. For dot layers with a low dot density, the overlap between the subcavity field and the gain can be low, leading to a low net gain, despite the high material gain of dots as previously shown in (Chapter 1 Fig 1.7).

Resonant and anti-resonant subcavity: The position of the field anti-nodes of the generated laser radiation in these structures is set by the alternating $\lambda_{design}/4n$-thick

layers of the integrated DBR. The length of the subcavity can be adjusted in such a way that an electric field antinode is positioned at the semiconductor/air interface, enabling resonant behaviour. A structure with a resonant subcavity experiences an increased field within the subcavity. This results in a decreased pump threshold power, as laser modes close to the resonating field modes experience enhancement. An anti-resonant structure has a node at the semiconductor/air interface and thus no electric field enhancement occurs. The advantage of an anti-resonant design lies in decreased scattering losses at the structure surface and a broader tuning behaviour. The shape of the effective gain spectrum is also less influenced by the subcavity field and follows that of the intrinsic gain spectrum [21]. Furthermore, the anti-resonant nature has the effect that subcavity field modes are present at the shorter and longer wavelength side of the gain spectrum, which experiences further broadening of the effective gain bandwidth and thus allows for wider tuning ranges compared to resonant structures (under the expense of increased pump threshold powers). A more thorough illustration about this behaviour in dependence on the longitudinal confinement factor is discussed by Tropper et al. in [16], from which Fig. 2-7 is taken.

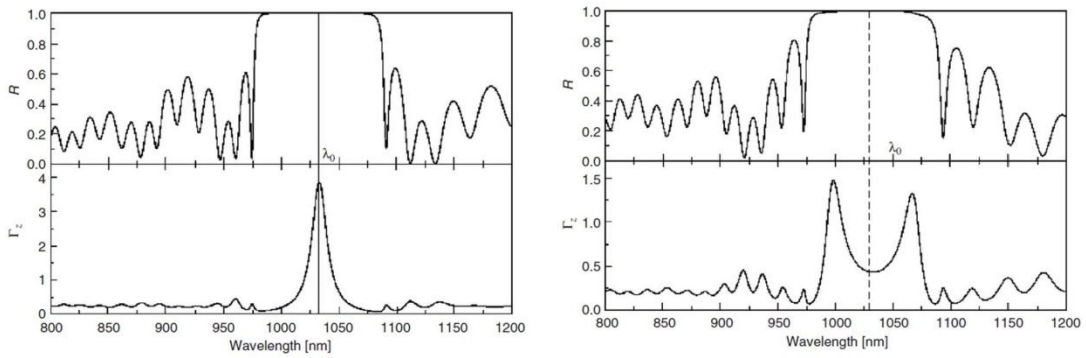

Fig. 2-7 Illustration of the reflectivity stopband (R) and the longitudinal confinement factor Γ_z for a resonant (left) and anti-resonant (right) subcavity structure [16].

2.2.3.3 Gain/resonance overlap

The previous discussion on RPG and subcavity resonance suggests that a well-established overlap between the maximum effective gain and the resonance effects is

required for good laser performance. Therefore the influence of thermal effects has to be regarded as well. Bulk semiconductors have temperature dependent bandgap energy. Two mechanisms have been identified by Varshni [22], to be responsible for a shift of the relative position between the conduction and the valence band, causing the energy bandgap to decrease with temperature for commonly used semiconductor compounds:

- an increase of the lattice deformation with temperature,
- an increase in electron lattice interaction

The temperature variation of the bandgap energy $E_{gap}(T)$ is defined by the "Varshni"-formula:

$$\mathrm{E}_{gap}(T) = \mathrm{E}_0 - \frac{\alpha T^2}{T+\beta}. \qquad \text{Equation [2-12]}$$

E_0 is the energy gap at absolute zero ($T = 0K$) and α and β are Varshni parameters, which are available for the most commonly used semiconductor compounds. The thermal shift of the bandgap energy has a linear behaviour at elevated temperatures, especially around the usual working temperature of semiconductor devices. Table 2-2 gives the Varshni parameters for the binary compounds included in the lattice-matched quaternary $(Al_xGa_{1-x})_{0.51}In_{0.49}P$ compounds, which are used to estimate the thermal bandgap according to a simulation reported in [9]. Vegard's law, (see equation [2-2]) is used here for the calculation for the ternary and quaternary compositions. The thermal dependence of the QW or QD energy bandgap obeys the Varshni relationship as well, which expresses itself in a redshift of the emission with increasing temperature. The optical thicknesses of the multiple layers in a VECSEL structure are also temperature dependent, causing a red-shift of the designed resonances. The rate of this resonance shift is however lower than that caused by the thermal dependence of the QW or QD emission wavelength [16] for InGaAs and AlGaInP compositions by about a factor of 3.

Material	Bandgap E_{0K} (eV)	Bandgap E_{300K} (eV)	Parameter $\alpha \cdot 10^{-3}$ (eV/K)	Parameter β (eV/K)	Bowing parameter b (eV)
GaP	2.857	2.78	2.857	2.78	-
AlP	3.637	3.56	3.637	3.56	-
InP	1.411	1.34	1.411	1.34	-
$Al_{0.52}In_{0.48}P$		2.614*			-0.48
$Ga_{0.52}In_{0.48}P$		1.927*			0.65
$(Al_xGa_{1-x})_{0.52}In_{0.48}P$					0.18

Table 2-2: Varshni parameters and bandgap energy of binary GaP, AlP and InP compounds at 0 and 300 K. Bowing parameter, b, for the calculation of the lattice matched ternaries $Al_{0.52}In_{0.48}P$ and $Ga_{0.52}In_{0.48}P$ and quaternary compounds. Values taken from Liu, C. Y (2003). Values marked by * are calculated intermediate results for the ternaries.

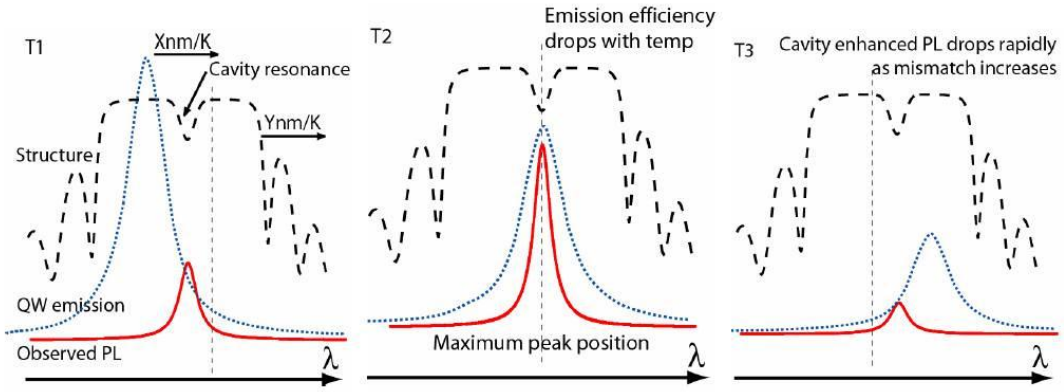

Fig. 2-8 A schematic illustration of the temperature dependent overlap between the QW emission (blue dotted line) and detected surface photoluminescence (red solid line) as the QW emission moves through the resonance (labelled with an arrow for T1). The broad reflectivity stopband is indicated by the black dashed line. Three conditions are represented T1, T2 and T3. Only at T2 is the QW emission peak matched to the resonance, which leads to optimum laser conditions with maximum output power. Graph taken from Hopkins [23].

Therefore, devices based on QWs are often designed with an offset, allowing the QW emission to move into the resonance position at working temperature, as discussed in Hopkins et al. [23], from which the graphs in Fig. 2-8 were taken. The three sketches depict the different conditions present at three distinct temperatures in a VECSEL structure. At T1, the emission efficiency of the QWs is highest, because temperature dependent carrier escape mechanisms are low in this case. The QW emission doesn't match the designed resonances (Fabry-Perot resonance and/or RPG) of the subcavity due to the designed offset. With increasing temperature they move into overlap due to the larger thermal shift of the QW emission. At the matching point, T2, the

overlap is optimal and the laser performance optimised (lowest pump threshold power, highest achievable output power). T2 is the targeted temperature for device operation. With further temperature increase, the overlap decreases together with the emission efficiency and the laser performance reduces until laser action ceases. This is also known as thermal rollover, limiting the performance of VECSELs drastically at elevated temperatures. From this argument it becomes clear that thermal management to counter-act the effect of increasing temperatures introduced by higher pump power densities is essential and introduced in the following section.

2.2.4 Thermal management

Research on this topic has been published by several groups and references [23-25] give a summary of work done on thermal modelling of VECSEL structures. Kemp et al. [24] and [25] gave a consistent numerical method, by the use of a finite element analysis, for the estimation of the temperature increase inside a VECSEL structure under realistic pumping conditions. The model assigns the nanometre thick layers into groups of similar purpose/material composition, such as the substrate, DBR, active region, confinement/capping layer with an average thermal resistivity of these regions. This is done in order to reduce the model complexity and required computing power. The conclusion of the study is that the thermal resistivity of the DBR has the most significant impact on the temperature rise for cooling through the bottom of the structure. Fig. 2-8 illustrates the significance of the temperature in the gain region. With increasing temperature the radiative efficiency of the QW or QDs decreases due to an increase of the thermal escape/non-radiative recombination rate of the charge carriers. The influence of the temperature on the resonance position and the emission wavelength was discussed in the previous section. It illustrates the importance of thermal management for good laser performance. With respect to this, QD structures are thought to offer improved thermal stability due to the three dimensional carrier confinement. So-called thermally stable operation of a VECSEL was reported by Germann et al. [26] for InGaAs S-K type QDs, where the heat sink

temperature was varied between 5-35 °C and where both the differential efficiency and the threshold pump power remained constant, although the differential efficiency was with around 2 % very low.

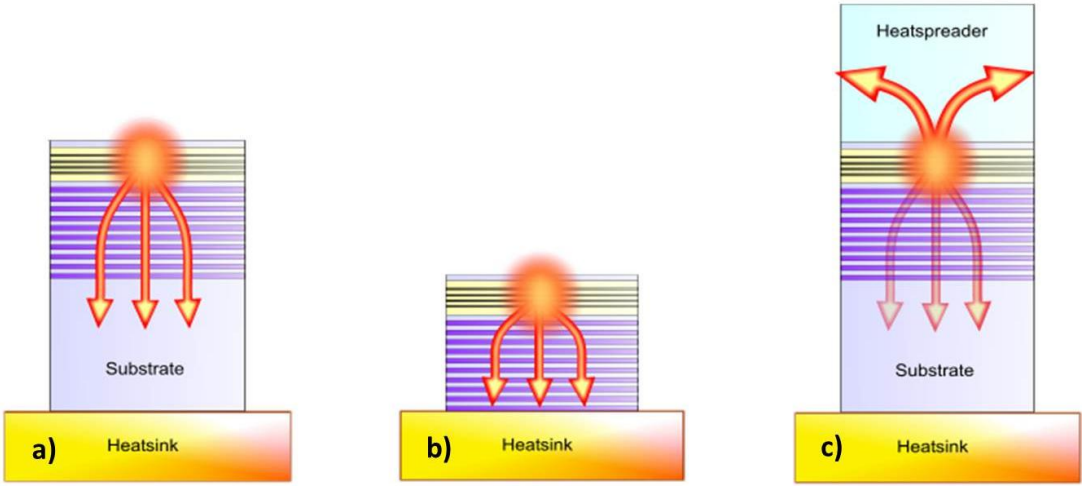

Fig. 2-9 A schematic illustration of the heat flow within a pumped VECSEL structure for a) an unprocessed device, b) a thinned device and c) the intra-cavity heatspreader approach. Graphs taken from Hopkins [23].

Characteristic for optically-pumped VECSEL structures is the very short absorption length, which is usually in the range between 1-2 μm (usually the subcavity length, see Section 2.2.3). The total pump intensity is absorbed in a region very close to the surface. The best way for thermal management is to prevent heat introduction into the active region in the first place by the choice of the pump wavelength, trying to keep the quantum defect as small as possible. The quantum defect, η_{quant}, is the energy ratio of the pump and the emitted laser radiation (equation [2-25]). The higher the quantum defect, the larger the heat load introduction into the lattice, which can not be used for radiative recombination [27], increasing the temperature of the active region. Despite of this, three different schemes have been used so far for thermal management issues and can be seen in Fig. 2-9:

- The unprocessed structure, bonded to a heat sink of high thermal conductivity. Here, the sample is mounted as it is onto a temperature controlled heat sink. The heat has to be removed through the active region, the DBR and the substrate.

- The thinned device. In this case, the substrate is completely or partially removed and the DBR attached to a heat sink of high thermal conductivity, removing/minimising the influence of the substrate. The path of the heat extraction goes through the DBR, which can be a considerable thermal barrier, depending on the thermal conductivity of the compositions.
- Attachment of a transparent and thermally conductive material to the intracavity surface of the VECSEL structure. This arrangement brings a material of high thermal conductivity close to the region where the maximum heat load is introduced by the pump. The heat flow is now mainly towards the sample surface. This minimises the main path length of the heat inside the structure and by-passes the DBR.

As can be seen by the first two thermal management schemes, a very important issue for a VECSEL structure is the thermal conductivity of the used material compositions, especially the thermal barrier introduced by the DBR structure. The DBR makes the heat extraction more difficult with increasing number of layer pairs and thermal resistivity. It is shown by Kemp et al. in [25] that heat extraction is most efficient via a transparent intra-cavity heatspreader approach for materials with a poor thermal conductivity and/or where the pump spot size is small (Ø < 200 μm). Structures with a higher thermal conductivity (which is the case for structures emitting around 1 μm and based on InGaAs and AlGaAs compositions) the thinned device outperforms the intracavity heatspreader scheme for larger pump spot diameters (Ø > 200 μm). This is interesting in terms of power scaling of VECSEL devices, where high power lasers emitting around 1 μm work best in the thinned device scheme.

Power scaling was described as a property of thin disk lasers based on doped dielectrics, i.e. Nd:YAG, Yb:YAG crystals by Giesen et al. [28], and was used for thermal management in order to increase the laser output power under simultaneous restriction of the heat rise inside the crystals. Surface emitting devices allow the output power to be scaled with the pump spot size (laser cavity mode size) under the consideration, that the pump intensity remains the same. Ideally, the laser output power in this case would increase linearly with pumped area, if the direction of the

heat flow would be unidirectional along the optical axis. This is not the case in real semiconductor thin disk lasers (VECSEL) as the heat flow occurs also in the in-plane direction, restraining the linearity and putting an upper limit to the power scalability. The method of choice for thermal management in the current devices was the heatspreader approach for the following reasons:

- The high thermal resistivity of the 40.5 pair DBR is by-passed, reducing the total temperature rise within the gain region.
- Technological advances allowed the use of low loss, low birefringent synthetic CVD grown diamond heatspreaders. Diamond has the highest thermal conductivity of up to 2000 $Wm^{-1}K^{-1}$ of all materials [29]. The suitability for efficient heat extraction by the utilisation of the heatspreader method were first demonstrated for silicon carbide (SiC), sapphire (Al_2O_3) and diamond (D) by [30-33].
- No post growth processing procedure is required.
- The optical contacting of the heatspreader by the use of liquid capillary bonding, described by Liau et al. in [34] is fairly easy to achieve and suits research purposes very well, as the bonding process is non-destructive and reversible.

Other considerations on the negative side are:

- The higher refractive index of the heatspreader material with respect to the semiconductor air interface reduces the Etalon effect and thus the subcavity field of a resonant structure.
- Many suitable crystals for the use as heatspreaders are birefringent. This will introduce depolarisation losses, especially where folded cavity arrangements and intracavity elements are used [35,36].
- The introduction of an etalon, due to the two plane parallel facets of an uncoated heatspreader modulates the continuous laser output signal in dependence on the etalon thickness. Reflectivity losses at the surface can be minimised by the help of antireflection (AR) coatings. Wedged heatspreaders introduce reflection losses.

Further technological advances for example in the use of wafer-fusion for the production of DBRs with higher thermal conductivity, could also improve the thermal management [37].

2.3 Laser performance modelling

2.3.1 One dimensional confinement in a well with finite potential height

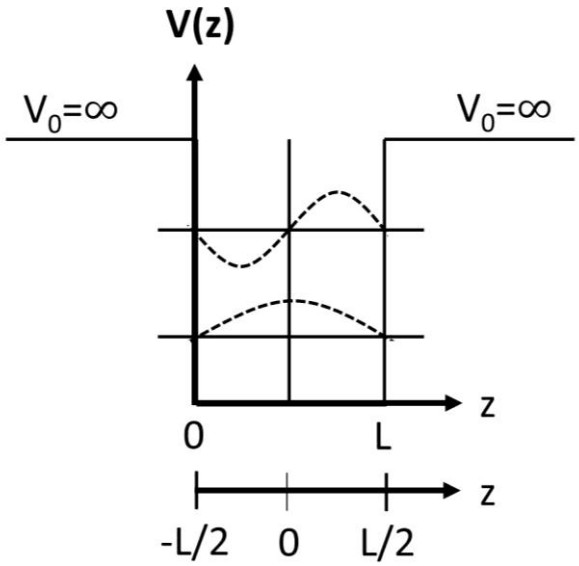

Fig. 2-10 Schematic of a potential well of width L with infinite barrier height V_0. Shown are the wavefunctions for the ground (n=1) and first excited (n=2) state [38].

The previously mentioned advantageous behaviour in terms of thermal stability and gain are a cause of quantum confinement effects and arise where the de Broglie wavelength of a trapped particle is similar to the dimensions of the potential well in which it is localised. The evolution of the wavefunction of the particle can be described by the Schrödinger equation. The time independent Schrödinger equation for finite barrier is

$$\left[-\frac{\hbar^2}{2}\frac{\partial}{\partial z}\frac{1}{m^*}\frac{\partial}{\partial z}+V(z)\right]\phi(z)=E\phi(z), \qquad \text{Equation [2-13]}$$

where the symbols have their usual meaning with ħ being the reduced Planck constant, m^* stands for the effective mass (m_w and m_b for the well and barrier region). V and E are the potential and particle energy. ϕ stands for solutions for the Schrödinger equation for the given boundary conditions and correspond to eigenenergy values. z is the direction of wave propagation. The potential energy inside a given quantum well of thickness L is set to zero and outside to V_0.

$$V(z) = \begin{cases} V_0, & |z| = {}^{L}/_{2} \\ 0, & |z| < {}^{L}/_{2} \end{cases}, \qquad \text{Equation [2-14]}$$

The solution of an even wavefunction can be described by

$$\phi(z) = \begin{cases} C_1 e^{-\alpha(|z| - {}^{L}/_{2})}, & |z| = {}^{L}/_{2} \\ C_2 \cos(kz), & |z| < {}^{L}/_{2} \end{cases}, \qquad \text{Equation [2-15]}$$

with

$$k = \sqrt{2m_w E/\hbar}, \quad \alpha = \sqrt{2m_b (V_0 - E)/\hbar}, \qquad \text{Equation [2-16]}$$

The eigenequation for boundary conditions, where the wavefunction ϕ and its derivative $\left(\frac{1}{m^*}\right)\left(\frac{\partial\phi}{\partial z}\right)$ are continuous at the well/barrier interface is.

$$\alpha = k\frac{m_b}{m_w}\tan\left(k\frac{L}{2}\right). \qquad \text{Equation [2-17]}$$

Substitution of equations [2-16] into [2-17] yields the expression for the eigenenergy which depends on the QW thickness, L.

$$E\left(1 + \frac{m_b}{m_w}\tan^2\left(\sqrt{2m_w E/\hbar}\frac{L}{2}\right)\right) - V_0 = 0, \qquad \text{Equation [2-18]}$$

Equation [2-18] enables the calculation of the transition energy of a quantum well is dependence on the quantum well thickness. Fig. 2-11 shows the calculated transition energy with well thickness of $Ga_yIn_{1-y}P$ QWs surrounded by $(Al_xGa_{1-x})_{0.5}In_{0.5}P$ barriers, where $x_{Al} = 0.6$ and under further consideration of the valence band behaviour with strain. The MathCad programme for the calculation was written by

Dr. Jennifer E. Hastie at the Institute of Photonics and is based on a model stated in [38] (Physics of Photonic Devices by Chuang). It can be seen that the transition energy increases with decreasing width and increasing Gallium content, y, (decreasing strain) until the lattice-matched condition is reached y = 0.51, after which the strain will increase with opposite sign (This is not shown here as tensile strained QWs are not favourable in surface emitting devices). The influence of strain on the bandgap will be discussed in the Section 2.4.2 in more detail.

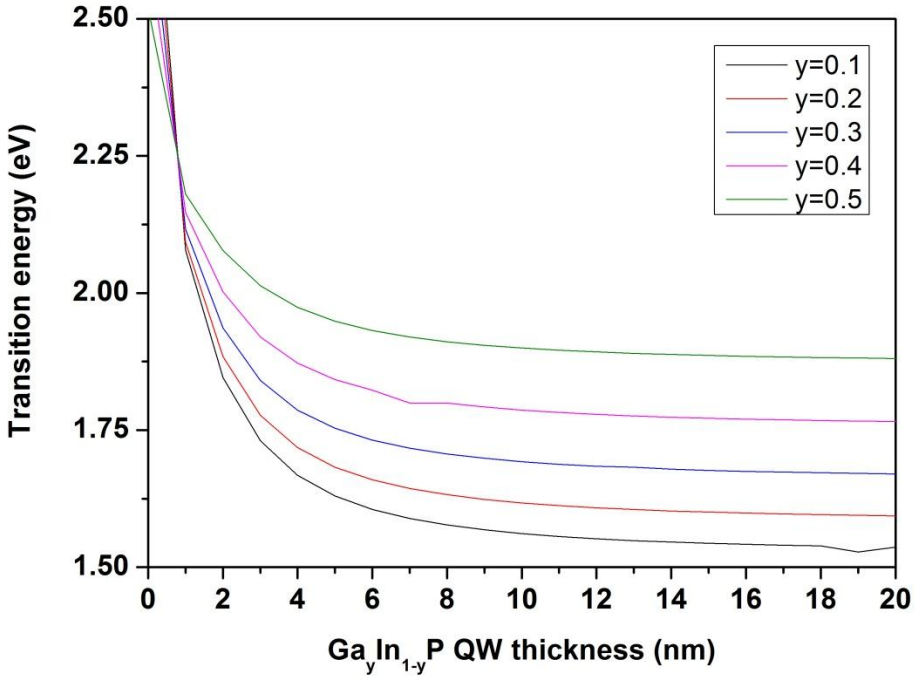

Fig. 2-11 Transition energy with well thickness calculated for $Ga_yIn_{1-y}P$ QWs with $(Al_{0.6}Ga_{0.4})_{0.5}In_{0.5}P$ barriers.

In the case of QDs, not only the volume and strain effects but also the shape influences the transition energy. The calculation of energy states for three dimensional confinement of dots was shown by Bimberg et al. in [39] "Quantum dot heterostructures". Fig. 2-12 is taken from this book as an illustration of the calculated wavefunctions for the first three electron and hole states of a pyramidal InAs/GaAs quantum dot with base length 13.6 nm by application of the **k·p** theory. The **k·p** theory is based on the Bloch theorem, which uses the periodic crystal potential to describe the electronic band structure.

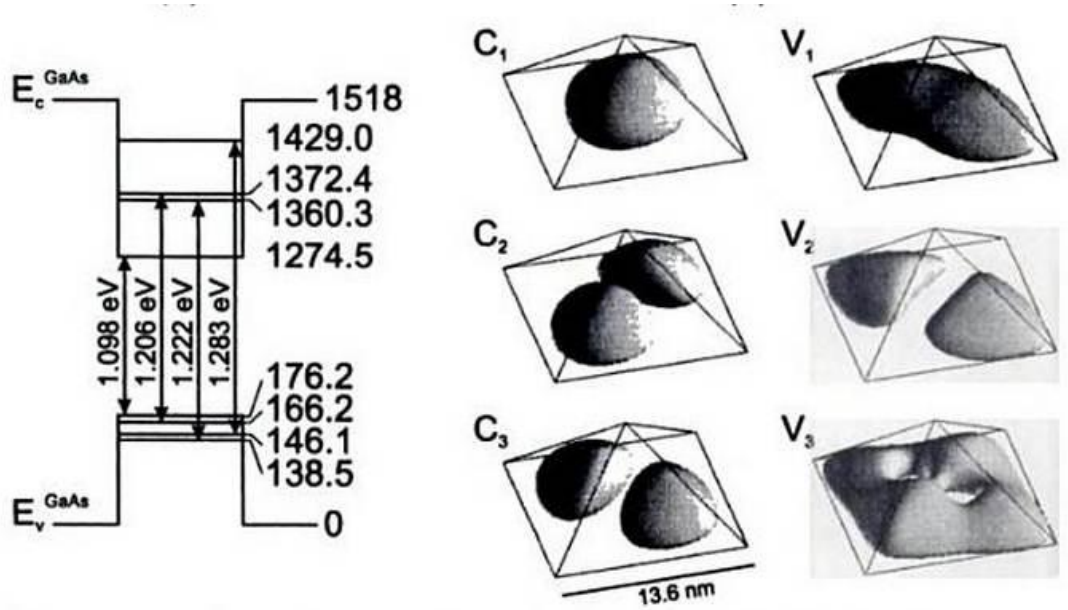

Fig. 2-12 Left: Schematic of the energy level distribution of the first three electron and hole states together with the transition energies within a pyramidal InAs/GaAs QD of base length 13.6 nm. Right the corresponding wavefunctions [39].

2.3.2 QW based VECSEL performance modelling as a function of the gain

The modelling of optically-pumped VECSEL structures was described by Kuznetsov et al. [40]. For the estimation of the QW gain, a logarithmic dependence on the carrier density is used.

$$g = g_0 \ln\left(\frac{N}{N_0}\right), \qquad \text{Equation [2-19]}$$

where N stands for the carrier density and N_0 for the transparency carrier density. g_0 is the material gain. The dependence of N on the pump power can be expressed by

$$N = \frac{\eta_{abs} \cdot P_{pump}}{\frac{h \cdot c}{\lambda_{pump}} \cdot L_{QWgain} \cdot A_{Pump}} \tau(N). \qquad \text{Equation [2-20]}$$

Where h and c are the Planck constant and the velocity of light, P_{pump} and A_{Pump} are the incident pump power and the pump spot area respectively. The total gain thickness is L_{QWgain}, which is the sum over the total number of QWs, N_{QW}, in the

cavity, having the thickness, t_{QW}. η_{abs} is the pump absorption efficiency and τ the carrier lifetime, which is dependent on the monomolecular, A, bimolecular, B, and the Auger, C, recombination coefficients. The coefficients A and C stand for non-radiative recombination processes such as carrier capture by intra-band energy levels and Auger escape respectively. The coefficient B describes the radiative recombination process, where two particles, hole and electron, interact with each other under light emission.

$$\tau(N) = (A \cdot N + B \cdot N^2 + C \cdot N^3)^{-1}. \qquad \text{Equation [2-21]}$$

At laser threshold, the gain and total losses of the system are equal, thus

$$R_{IM}R_{OC}T_{loss}exp\left(2\Gamma_z g_{th}L_{QWgain}\right) = 1. \qquad \text{Equation [2-22]}$$

The reflectivity coefficients of a two mirror resonator and the total cavity losses are given by R_{IM}, the integrated epitaxially grown mirror, R_{OC}, the external output coupler and T_{loss}. Γ_z is the longitudinal confinement factor, which is defined in equation [2-7]. The laser threshold conditions are given by equations [2-23] and [2-24] and the estimated output power by [2-25]

$$N_{th} = N_0(R_{IM}R_{OC}T_{loss})^{-\left(2\cdot\Gamma_z\cdot g_{th}\cdot L_{QWgain}\right)^{-1}}, \qquad \text{Equation [2-23]}$$

$$P_{th} = N_{th}\frac{h\cdot c}{\lambda_{pump}}\frac{L_{QWgain}\cdot A_{Pump}}{\eta_{abs}\cdot\tau(N_{th})}, \qquad \text{Equation [2-24]}$$

$$P_{laser} = \left(P_{pump} - P_{th}\right)\cdot\eta_{diff}, \qquad \text{Equation [2-25]}$$

Here, P_{pump} is the incident pump power and η_{diff} the differential efficiency, which can be defined as $\eta_{diff} = \eta_{abs}\cdot\eta_{quant}\cdot\eta_{out}$ with $\eta_{quant} = \frac{\lambda_{pump}}{\lambda_{laser}}$ being the quantum defect. The standard way of pumping VECSELs efficiently is by the excitation of the charge carriers into the pump light absorbing barriers form where they relax into the ground level states of the gain medium. This requires sometimes much higher pump photon energy compared to the emitted laser light. The more η_{quant} differs from unity, the more heat is introduced into the structures' lattice and thermal management becomes necessary in order to reduce any detrimental heat effects as discussed before. The cavities output efficiency η_{out} is

$$\eta_{out} = \frac{\ln(R_{OC})}{\ln(R_{IM}R_{OC}T_{loss})}. \qquad \text{Equation [2-26]}$$

This model describes a very good method for the estimation of important design parameters, such as the optimum number of QWs to be inserted inside the cavity or the optimum output coupling value as can be seen in Fig. 2-13.

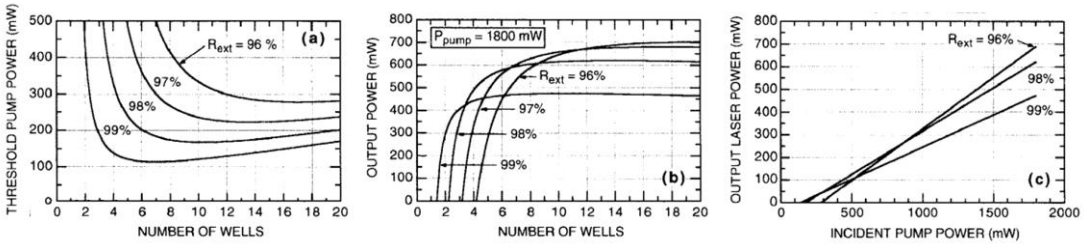

Fig. 2-13 Example of the calculated laser performance by Kuznetsov et al. [40] for an InGaAs QW VECSEL device, showing: a) the threshold power with number of QWs for different output coupling coefficients. b) the laser output power with number of QWs for different output coupling coefficients. c) power transfer characteristic for different output coupler coefficients.

2.3.3 Gain in QD VECSELs

In gain calculations for QD structures the logarithmic dependence of the gain on the carrier density is no longer valid. Several possible population states of the ground state inside a single QD, i.e. completely empty, partially filled with one electron or hole, single exciton, charged exciton or completely filled, together with the spin degeneracy which has to be taken into account (so that the QD ground state can occupy two excitons), have the consequence that a single QD ground state can be filled in many different ways with the same amount of available carriers, making it difficult to calculate the gain dependence on the injected carrier density. The theory quickly becomes more difficult if excited states are also taken into account.

The ground state threshold carrier density N_{th} can be described by

$$N_{th} = N_{QD}\left(1 + \frac{1}{\Gamma_{xy}}\frac{1}{\Gamma_z}\frac{\alpha_{tot}}{g_{mat}^{sat}}\right). \qquad \text{Equation [2-27]}$$

where N_{QD} is the number of QDs, α_{tot} the total cavity losses and g_{mat}^{sat} the saturated material gain. The ground state gain is considered to increase linearly with increasing carrier density and reaches a saturation level, where all ground state levels are occupied with two excitons ($N = 2N_{QD}$). Transparency is reached when all dots are filled with one exciton as can be seen in Fig. 2-14 [39].

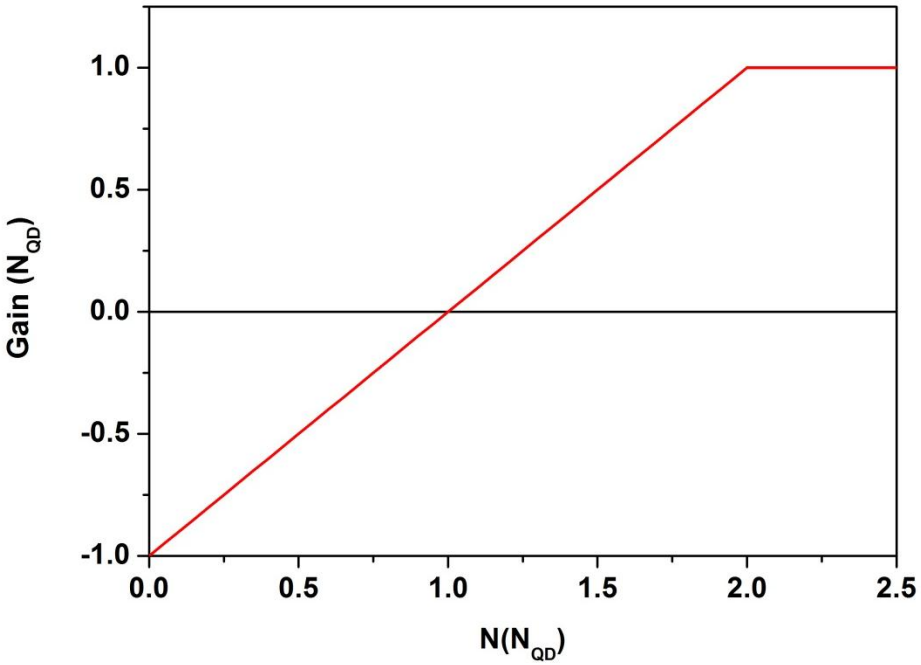

Fig. 2-14 Ground state gain normalised to the quantum dot density in dependence on the carrier density. Transparency condition is reached if all QDs are filled with one exciton.

In the initial development of QD VECSELs, it has been shown empirically that large numbers of QD layers are required, compared with an optimum number 10-15 for QWs. Future work is planned to adapt the VECSEL model for QD-layers, however in most cases the sub-cavity length and growth set the upper limit. The absorption length sets the boundaries of the subcavity length as discussed above. Growth related restrictions are for example the minimum allowed separation between two adjacent QD-layers for defect free QDs, limiting the maximum allowed number of QD-layers placed at a single field anti-node. Further information on growth of heterostructures and QDs is given below.

2.4 Growth methods

The requirements for monolithic growth of semiconductor laser structures with their multitude of different layer thicknesses, material compositions, doping levels etc. are stringent for repeatability and accuracy. Different methods for the fabrication of semiconductor devices are available today based on liquid phase (LPE), vapour phase (VPE) and molecular beam epitaxy (MBE). The development of these different processes was determined by the need to grow different material compositions on top of each other, under constraints on material source availability, material growth quality etc. One example for a chemical vapour epitaxy process is "Metal Organic Chemical Vapour Deposition" (MOCVD), also known as Metal Organic Vapour Phase Epitaxy (MOVPE) or Organo Metalic Vapour Phase Epitaxy (OMVPE). All the structures described in this work are fabricated exclusively by the MOCVD method which is briefly introduced here, based on the discussion in Chapter 4 of reference [41]. The operational principles of a horizontal flow reactor are depicted in Fig. 2-15, where the working principle can be divided into four stages. Stage one is the gas handling section where the majority of the metal organic precursors are in the liquid phase and need to be brought into the vapour phase via the help of elemental hydrogen (H_2), acting as carrier gas, which streams thorough the precursor bath (bubbler) and carries the metal organic compound with it; some of the group V sources are already in the gas phase such as hydrides, i.e. Arsine (AsH_3) and Phosphine (PH_3). An elaborate system of three-way valves and mass flow controllers is required in order to establish a constant overall pressure at the source for reproducible growth rates. Variations in the total gas flow or switching transients due to necessary changes (switching on/off) of partial gas pressures of the different components in the growth reactor must be prevented. This is realised by the integrated "continuously purged 5/2-way valves" in the run/vent manifolds. Stage two is the growth chamber/reactor itself. In general these reactors can be separated into horizontal and vertical gas flow with respect to the wafer surface. As the organo-metallic gas or hydride molecules, such as trimethylgallium (TMG), trimethylindium (TMIn), phosphine (PH3), etc. stream across the heated susceptor,

they break down into their different components, which react with the wafer surface to form the epitaxial layers. The third stage of this type of growth reactor is the pressure control part, mainly consisting of a throttle valve and the vacuum pump for maintaining process pressures in the range between about 1/100 – 1 atmosphere. The last stage is the exhaust gas treatment facility, consisting of the scrubber. The exhaust gas treatment is important, as highly toxic waste products such as arsenic hydride (AsH_3) are part of the gas mixture. These hazards can be reduced by the use of alternative precursors such as tertiarybutylarsine (TBA) [42] although they come with the expense of increased background doping [43].

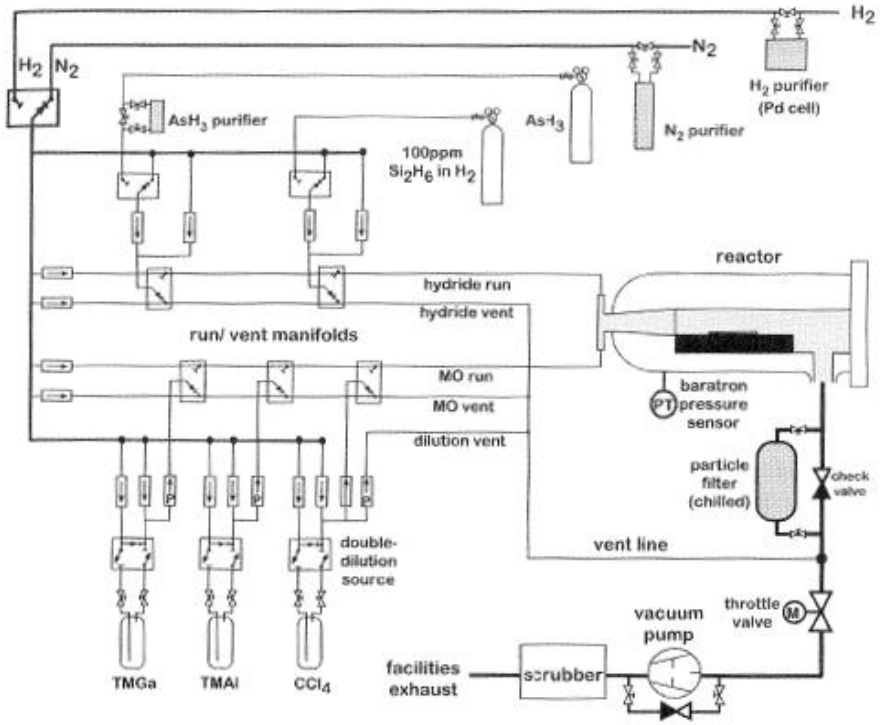

Fig. 2-15 A schematic of a MOCVD reactor showing the gas handling section, the reactor chamber, the pressure and exhaust gas control systems [41].

The reactor used for the growth of the InP/AlGaInP QD VECSELs described in Chapter 4 is a Semicon MR350 low pressure (100 Torr) horizontal flow channel reactor with a nonrotating susceptor [44]. As can be seen on the left hand side of Fig. 2-16, the reactor consists of two tubes; a round outer and a rectangular inner tube. The pressure in the outer chamber is slightly higher compared to the inner one. The rectangular shape of the inner chamber enables a more homogeneous gas flow. The wafer rests on a heated graphite susceptor which is placed inside the rectangular

inner tube and the temperature is set by a heater coil outside the round chamber. A homogeneous and uniform deposition is difficult to achieve with this type of reactor for several reasons:

- The temperature control together with a uniform temperature distribution across the unrotated susceptor are challenging.
- The gas flow is directional, meaning that the reactants in the gas become depleted in the time it takes to pass the wafer. The side of the wafer closest to the gas inlet experiences a faster growth rate compared to the part, furthest away if the susceptor is not rotated. The form, friction and temperature gradients of the chamber walls can mitigate a homogeneous laminar gas flow and enable recirculation and turbulences creating thickness and compositional non-uniformities across the wafer.

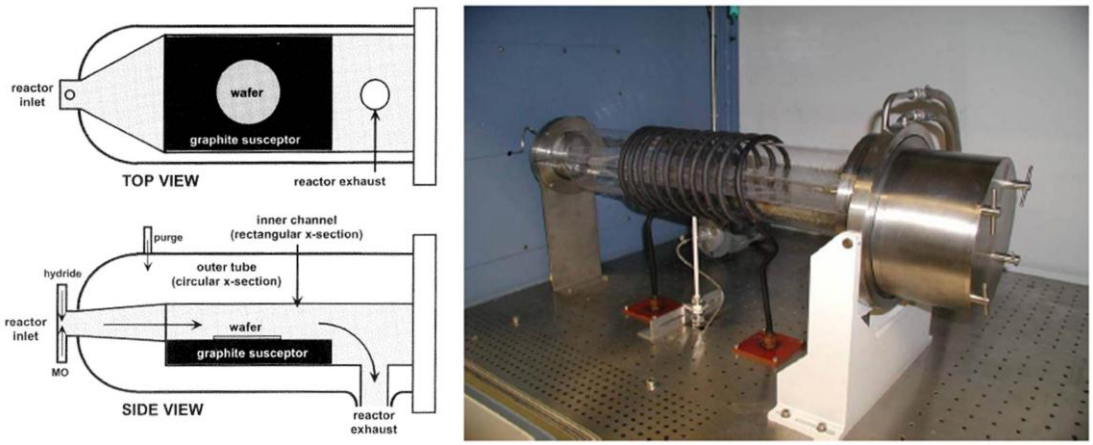

Fig. 2-16 Left: Schematic of a horizontal flow channel reactor illustrated in the top and side view [41]. Right: MR350 reactor, used for the fabrication of the InP/$Ga_{0.51}In_{0.49}P$ Dwell VECSEL structures by the National Centre of III-V Technologies at the University of Sheffield [44].

The non-uniformity across a two inch wafer, caused by the formerly mentioned reasons is usually 5 % [45] which can also be seen in the post growth wafer characterisation of an InP/$Ga_{0.51}In_{0.49}P$ QD calibration growth wafer sample in Appendix A.3 (MR2959). These are negative effects for the fabrication of commercial products, where non-homogeneities are undesirable and other, more complicated MOCVD reactor designs either with horizontal and vertical gas flow are much more suitable for large growth capacities and more homogeneous epitaxial layer deposition. For research purposes, these layer thickness variations offer a

further degree of freedom and prove advantageous, i.e. for surface emitting structures, where resonances or the emission wavelength of QWs are affected and slight variations like these can be very helpful, as they allow the examination of the structure performance for a set of different, small changes.

2.4.1 Heteroepitaxy and strain effects

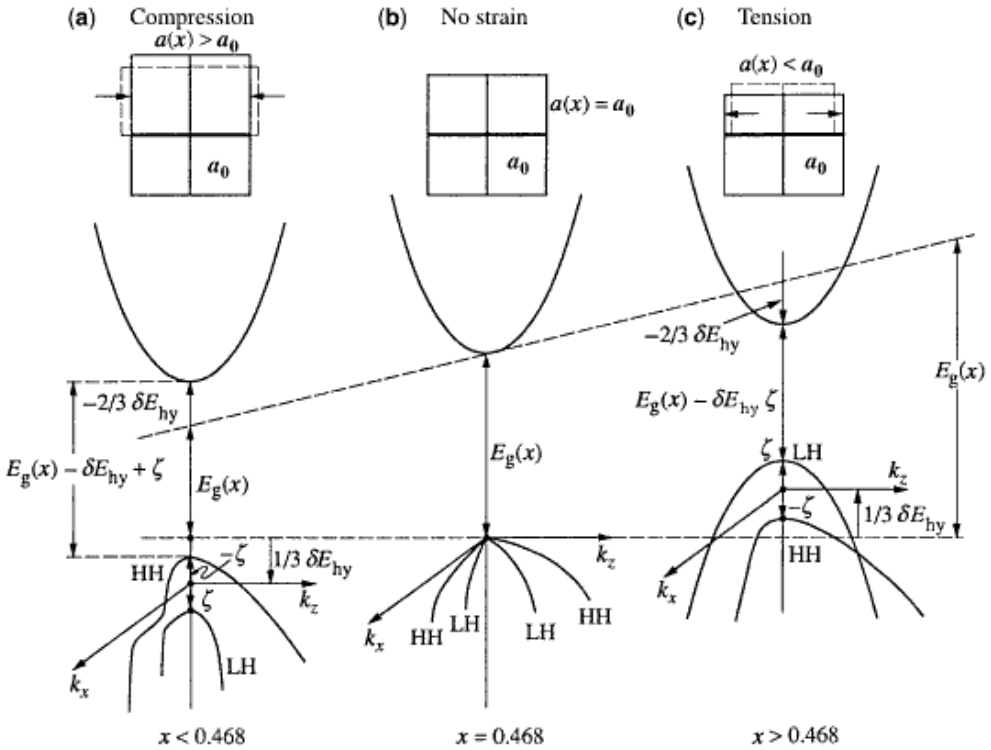

Fig. 2-17 Schematic of the bandgap structure behaviour of bulk $Ga_xIn_{1-x}As$ under biaxial strain in dependence on the Ga mole fraction x. a) compressive strain (no strain), b) lattice matched condition and c) tensile strain [38]. The upper diagrams illustrate the deformation of the crystal lattice for the three different cases.

Heteroepitaxy describes the growth of dissimilar material layers on top of each other. Standard methods to establish this are given in the previous section on the growth. With these methods it is possible to produce high quality, monolithic single crystal structures of a vast range of different materials, consisting only of one single element, such as carbon, silicon and germanium, or binaries like GaAs, InP and GaN or ternaries, quaternaries and so on. Intentional doping for the control of electrical

conductivity is also possible with these methods. There are still constraints with respect to strain build-up in the multilayer structures. The upper sketches in Fig. 2-17 illustrate schematically the growth of strained epilayers on top of a substrate with the in-plane lattice constant a_0. If the averaged lattice constant $a(x)$ of the epilayer composition differs from the underlying substrate, it generates a misfit strain. This can be understood in the following way. The newly deposited atoms can ideally occupy only lattice positions defined by the substrate. This means, that the epilayer atoms have to adopt the substrates' lattice constant. Due to the difference $\Delta a = a_0 - a(x)$, the newly deposited atoms grow with distorted lattice structure in order to match the lattice of the underlying substrate at its interface. This circumstance causes also a deformation of the crystallographic structure along the growth direction [46]. The in-plane misfit strain ε_{mf} is defined in ref. [47] and can be expressed as the sum over the strain which can be accommodated elastically ε_{el} and plastically δ_{pl} [46].

$$\varepsilon_{mf} = \frac{\Delta a}{a_0} = \varepsilon_{el} + \delta_{pl}, \qquad \text{Equation [2-28]}$$

The misfit strain is negative if the original lattice constant of the epilayer is larger than that of the substrate which causes it to be compressively strained [48]. Positive misfit strain causes tensile strain. For epilayer thicknesses below the critical thickness, t_{crit}, defined by Matthews & Blakeslee [49,50], $\delta_{pl} \approx 0$ in equation [2-28] and can be neglected. Here the misfit energy can be accommodated purely elastically and the growth of the epilayer is coherent. Plastic strain relaxation is the energetically most favourable process when the epilayer thickness exceeds t_{crit} [50]. This is illustrated by the hashed area in Fig. 2-18 (right) for strained $Ga_yIn_{1-y}P$ QWs grown on lattice matched $(Al_{0.6}Ga_{0.4})_{0.5}In_{0.5}P$ [14,51]. In VECSEL devices strain is usually introduced mainly in gain layers, be it QD-layers or strained QWs, for reasons discussed in Section 2.4.2. The inclusion of multiple gain layers in order to increase the modal gain of these structures requires strain balancing, if the accumulated strain becomes too high. The method of zero-stress of QW structures by Ekins-Daukes et al. [47] describes the strain balancing of two consecutive layers, where the first is strained either compressively or tensile and the second one in

opposition under consideration of the layer thicknesses, elastic stiffness constants and lattice parameters. The condition for zero average in plane stress is given by the following expression:

$$t_1 A_1 \varepsilon_1 a_1 + t_2 A_2 \varepsilon_2 a_2 = 0, \qquad \text{Equation [2-29]}$$

with the indices 1 and 2 indicating the parameters for the first and second layer and where the layer thickness, elastic misfit strain, and lattice constant are depicted by t, ε and a respectively. The parameter A is given by the elastic stiffness coefficients C_{11} and C_{12} of the material of the corresponding layer:

$$A = C_{11} + C_{12} - \frac{2C_{12}^2}{C_{11}}. \qquad \text{Equation [2-30]}$$

Balancing the strain with respect to the underlying substrate yields:

$$a_{sub} = \frac{t_1 A_1 a_1 {a_2}^2 + t_2 A_2 a_2 {a_1}^2}{t_1 A_1 {a_2}^2 + t_2 A_2 {a_1}^2}. \qquad \text{Equation [2-31]}$$

The Matthews & Blakeslee relation describes the dependence of the critical thickness on the misfit strain. This sets limitations on the use of strain in QWs, which tolerate only small values of misfit strain. Self-assembled QDs on the other hand require much higher strain levels for their formation and offer an alternative to the use of QWs. Nonetheless, too high strain levels have an effect on QDs as well. Indications that slightly tensile-strained $Ga_yIn_{1-y}P$ QWs on top of InP QD-layers, forming a dot-in-a-well, which is grown on top of an $(Al_{0.3}Ga_{0.7})_{0.51}In_{0.49}P$ matrix show improved PL performance with respect to the use of a lattice-matched $Ga_{0.51}In_{0.49}P$ QWs and is discussed in Chapter 4 later in more detail. The introduction of threading dislocations, originating in non-coherently strained QDs is also a cause of high strain levels inside larger islands, which can't be accommodated elastically [52] see Section 4.4.5. Dislocations stop only at interfaces, boundaries or other defects and can penetrate the whole structure, growing into the newly deposited layers. They are usually the cause for non-radiative carrier recombination effects and hamper the efficiency or lifetime of the fabricated devices.

2.4.2 Strain and its effects on the bandgap structure

As mentioned above, strain is caused when the lattice constants of a grown layer and the substrate differ from each other. On the one hand, where the growth quality of heterostructures is concerned, misfit strain is not desirable. On the other hand, it is often not avoidable and in many cases even required. Strain affects both the electro-optical properties and the formation (self-assembling) mechanisms in semiconductor devices [39]. The emission wavelength of quantum wells i.e. can also be adjusted by misfit strain. Other important laser properties, such as the polarisation of the gain or the threshold carrier density are also affected by biaxial strain. For group III-V semiconductors with a zincblende crystal lattice configuration the conduction and valence bands can be described by an atomic orbital model, where the conduction band has a spherical s-type atomic orbital. The valence band is split into three distinct subbands, the heavy-hole (hh), light-hole (lh), and the spin-orbit split off band (so), making it p-type in nature. A representative example based on the bulk $Ga_xIn_{1-x}As$ is illustrated in Fig. 2-17, taken from Chuang et al. in [38]. A similar discussion on $Ga_xIn_{1-x}P$ QWs with lattice-matched $(Al_xGa_{1-x})_{0.5}In_{0.5}P$ barriers was given by Bour et al. in [14]. The authors state that compressive strain has two different effects.

- intermixing of the different valence bands in favour of the hh-band.
- a change in the effective hole mass characteristics of the hh-band, resulting in a reduction of the density of hole states around the wave vector $k = 0$. This causes an improved symmetry between the density of states in the conduction and hh-band.

The result is a lower pump power threshold as population inversion can be achieved more easily. The altered intermixing of the subbands due to misfit strain becomes also remarkable in the energy bandgap shift, depicted in Fig. 2-17 and in case of $Ga_xIn_{1-x}P$ QWs in Fig. 2-18 left hand side taken from Olson et al. [48] and the right hand sight figure from Bour et al. [14]. Fig. 2-18 left describes an almost linear shift

of the bandgap with misfit strain ranging between $-0.3\ \% \leq \varepsilon_{mf} \leq 0.3\ \%$. Higher strain levels in both directions cause degradation of the crystal quality under generation of cracks (tension) and dislocations (compression). These can act as non-radiative carrier recombination centres, limiting the device's lifetime and performance. Fig. 2-18 right shows that the polarisation of the emitted field is also dependent on the strain. This is particularly important for surface-emitting devices. Nomenclature defines light with the electric field vector oscillating in the direction parallel to the epilayer plane as transverse electric (TE) and in the direction parallel to the growth direction (normal to the surface) as transverse magnetic (TM) polarised. The gain of the hh transition is TE polarised, thus this polarisation is dominant for lattice-matched or compressively-strained QWs. Tensile strain causes the lh-subband to become the ground state and is responsible for TM polarised oscillation [14]. Tensile strained QWs are therefore not desirable for surface emitting laser structures.

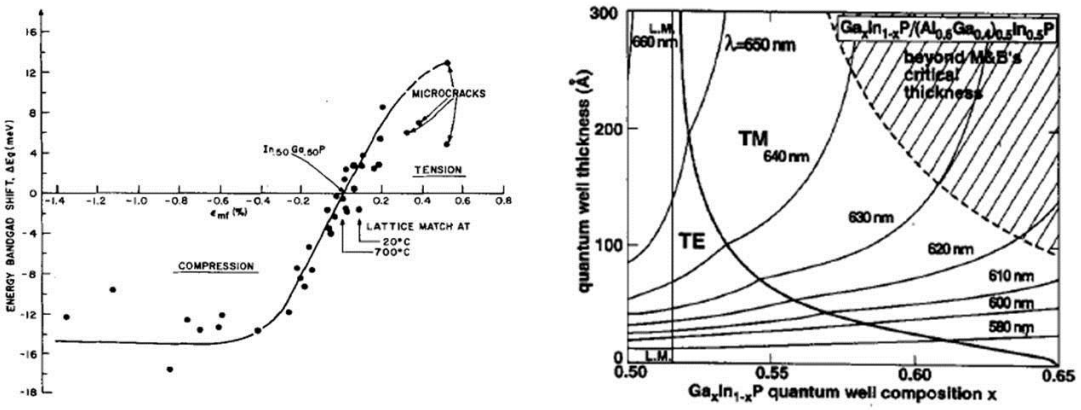

Fig. 2-18 Strain related effects on group III-V semiconductor materials. Left: Energy bandgap shift with misfit strain in case of $Ga_xIn_{1-x}P$ epilayers on GaAs [48]. Right: Strain effects on the QW emission wavelength and polarisation behaviour of, in this case $Ga_xIn_{1-x}P$ QWs embedded in $(Al_{0.6}Ga_{0.4})_{0.5}In_{0.5}P$ in dependence on the Ga mole fraction x. The hatched region indicates the material state where strain is beyond the Mathews-Blakeslee critical thickness above which structural degradation occurs [14].

The importance of strain and its management inside a multi-layer structure such as VECSELs becomes clear from the previous discussion. The first published VECSEL study by Kuznetsov et al. [40] already contained strain balancing layers in order to compensate for the accumulated compressive-strain from the QWs.

2.4.3 Self-assembled quantum dots

As mentioned above, misfit strain is important for the formation of self-assembled QDs. In terms of QWs the allowed misfit strain is restricted to low and moderate strain levels of usually < ±1 % in the in-plane direction (depending on the critical layer thickness) before serious degradation of the structural quality sets in. In contrast to this, QDs are not only capable to accommodate higher misfit strains their three dimensional formation process requires in fact higher amounts of compressive strain. In case of the InAs or InP QDs grown on materials lattice matched to GaAs substrates, the misfit strain is around 7.2 and 3.7 % respectively. There are also limitations on misfit strain in QDs, which has an effect on the total amount of material deposition for the formation of coherently strained (defect free) QDs and ultimately on their size and size distribution. Growth parameters, such as III-V ratio, growth temperature, deposition rate, growth interruption time, pressure and nominal layer thicknesses, substrate orientation, all affect the properties of the QDs [39]. The higher tolerance of self-assembled QDs towards lattice mismatch opens up new possibilities to combine these structures with other barrier compositions, which lie outside the range of the material constraints for QWs. This enables laser emission at wavelengths outside the scope of QW structures by improving the carrier confinement or shifting the emission wavelength towards longer wavelengths as will be discussed in Chapter 4 in more detail. Furthermore, the self-assembled growth of QDs usually results in a larger size distribution and causes a broad gain bandwidth [53]. The three dimensional carrier confinement in QDs causes atom like energy level configuration with discrete energy levels, which could allow not only ground but also excited state radiative emission, if available and other advantageous properties already mentioned above. The VECSEL structures developed in this work utilise two different types of QDs: Stranski-Krastanow (SK) and submonolayer (SML) QDs, shown in Fig. 2-19 b). Both types are grown by molecular beam epitaxy (MBE) and metal organic chemical vapour deposition (MOCVD). QDs in the Stranski-Krastanow growth mode pass a series of different transitions during their

formation illustrated in Fig. 2-19 a) [54]: two-dimensional (2-D) growth of the so-called "wetting layer", where the deposited atoms cover the surface. Diffusion and strain related drift forces these atoms to accumulate and form one-atomic-layer-thick islands. These islands expand with increasing amount of deposited atoms until they cover the entire surface. For on-going deposition, the 2-D layer-by-layer growth continues until a critical effective layer thickness, t_{cw}, is reached. This growth is depicted in section (A) where the time scale refers to the growth time under constant deposition rate.

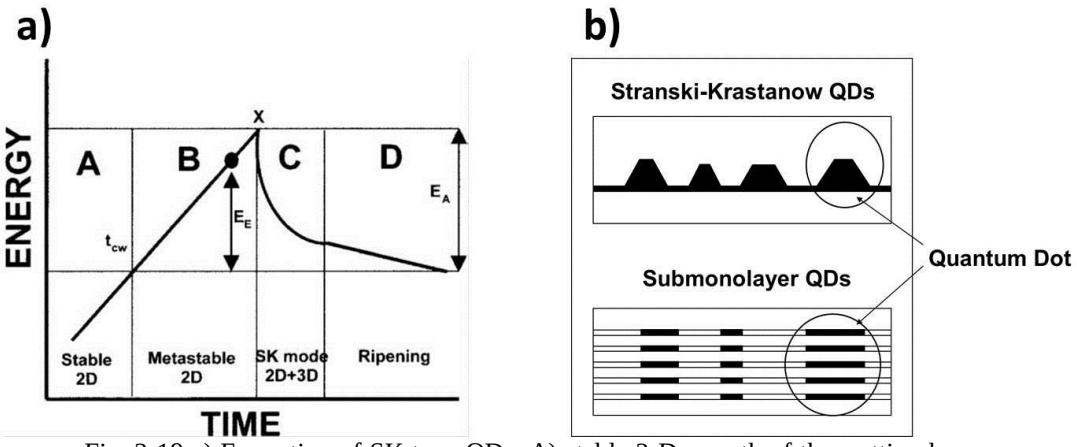

Fig. 2-19 a) Formation of SK type QDs. A) stable 2-D growth of the wetting layer. B) supercritical 2-D growth with excess energy stored in the layer. C) strain driven 2-D to 3-D transition after activation energy has been reached. 3-D formation minimises the excess energy in the layer. D) QD ripening with further strain energy decrease until stable condition is reached [54]. b) sketch of a SK QD-layer and a SML QD-layer.

- at the point where the wetting layer is equal to t_{cw} the stable 2-D growth goes over into a metastable 2-D growth. The metastable stage (B) describes the range between t_{cw} and the point, x, at which the 2-D to 3-D transition sets in. The energy difference between the two end points of stage (B) is defined as the activation energy, E_A.
- stage (C) illustrates this transition, which is driven purely by strain relaxation in order to minimise the excess energy, E_E, stored in the metastable wetting layer.
- the last stage (D), is island ripening, where the already formed 3-D islands relax further in order to release the excess strain energy completely to form stable QDs. In the case of InAs on GaAs, and InP on GaInP (lattice-matched

to GaAs substrates), the critical wetting layer thickness corresponds to ~1.5 [55] and 1.8 [56] monolayers (ML) respectively.

S-K QDs possess a very broad and even gain bandwidth, suitable for temperature insensitive laser performance and excited state radiative transitions [26,43]. Submonolayer (SML) QDs are formed when layers with a nominal thickness of less than one monolayer (ML) of two different material compositions (i.e. InAs/GaAs) are grown successively on top of each other in the following way:

- Nucleation of 1ML thick 2-D islands in the same way as in stage (A) of SK growth. The difference here is that there is not enough material to cover the entire surface area.
- The material composition is changed abruptly and the remaining gaps are filled and the 2-D islands are covered.

The two steps are repeated several times in order to create the SML QDs as illustrated in Fig. 2-19 b). Due to a strain gradient, caused by the dissimilar lattice constants, the new two dimensional islands arrange themselves on top of the buried islands, leading to an ordered stacking. The advantage of this type of QD is that they are more homogeneous in size distribution. They can be grown with an ultra-high dot density per QD-layer (in the range of 10^{11}-10^{12} cm^{-2}), which enables higher modal gain levels and stronger PL emission intensity compared to S-K type QDs [57]. Additionally, their volume and thus their quantum confinement can be adjusted simply by setting the number of repeats of the two growth steps (see Chapter 3) and keeping the deposition time for the two repeats unchanged or variation of the deposition time for a constant number of repeats, thus nominal submonolayer thickness [25].

So far, an introduction to VECSELs, together with an overview of latest achievements in the development of these devices was given in Chapter 1. This chapter was concerned with the theoretical background and growth, important for the design of VECSEL structures. The rest of this thesis will be concerned with the structure design, experimental work and analysis applied for the development of VECSEL structures utilising QD-based active regions, both for InAs/GaAs QDs

(Chapter 3) and InP QDs (Chapter 4) respectively. Chapter 5 is concerned with the generation of visible light from the infra-red via sum-frequency generation. A general conclusion is presented in Chapter 6.

References

1. M. Kuznetsov, F. Hakimi, R. Sprague, and A. Mooradian, "High-power (>0.5-W CW) diode-pumped vertical-external-cavity surface-emitting semiconductor lasers with circular TEM_{00} beams," Photonics Technology Letters, IEEE **9**, 1063-1065 (1997).

2. P. Gail, "Advanced Semiconductors Buyers' Guide 2003/2004," Advanced Semiconductors Buyers' Guide 2003/2004 93-95 (2004).

3. I. Vurgaftman, J. R. Meyer, and L. R. Ram-Mohan, "Band parameters for III-V compound semiconductors and their alloys," Journal of Applied Physics **89**, 5815-5875 (2001).

4. J. A. Van Vechten and T. K. Bergstresser, "Electronic Structures of Semiconductor Alloys," Phys. Rev. B **1**, 3351 (1970).

5. S. Adachi, "GaAs, AlAs, and $Al_xGa_{1-x}As$: Material parameters for use in research and device applications," Journal of Applied Physics **58**, R1-R29 (1985).

6. M. A. Afromowitz, "Refractive index of $Ga_{1-x}Al_xAs$," Solid State Communications **15**, 59-63 (1974).

7. M. Schubert, J. A. Woollam, G. Leibiger, B. Rheinlander, I. Pietzonka, T. Sass, and V. Gottschalch, "Isotropic dielectric functions of highly disordered $Al_xGa_{1-x}InP$ (0<=x<= 1) lattice matched to GaAs," Journal of Applied Physics **86**, 2025-2033 (1999).

8. H. Tanaka, Y. Kawamura, and H. Asahi, "Refractive indices of $In_{0.49}Ga_{0.51-x}Al_xP$ lattice matched to GaAs," Journal of Applied Physics **59**, 985-986 (1986).

9. C. Y. Liu, S. Yuan, J. R. Dong, S. J. Chua, M. C. Y. Chan, and S. Z. Wang, "Temperature-dependent photoluminescence of GaInP/AlGaInP multiple quantum well laser structure grown by metalorganic chemical vapor deposition with tertiarybutylarsine and tertiarybutylphosphine," Journal of Applied Physics **94**, 2962-2967 (2003).

10. S. P. Najda, A. H. Kean, M. D. Dawson, and G. Duggan, "Optical measurements of electronic bandstructure in AlGaInP alloys grown by gas source molecular beam epitaxy," Journal of Applied Physics **77**, 3412-3415 (1995).

11. H. A. Macleod, "Basic theory," in *Thin-film optical filters,* (Adam Hilger Ltd., Bristol, 1986), pp. 11-70.

12. C. Wilmsen, H. Temkin, and L. A. Coldren, *Vertical-Cavity Surfrace-Emitting Lasers: Design, Fabrication, Characterization, and Applications*, (Cambridge University Press, Cambridge, UK, 1999).

13. www.ioffe.ru/SVA/NSM/Semicond/GaAs, Ioffe Physical Technical Institute, "GaAs Electrical properties," 2005, Ioffe Physical Technical Institute

14. D. P. Bour, R. S. Geels, D. W. Treat, T. L. Paoli, F. Ponce, R. L. Thornton, B. S. Krusor, R. D. Bringans, and D. F. Welch, "Strained $Ga_xIn_{1-x}P/(AlGa)_{0.5}In_{0.5}P$ heterostructures and quantum-well laser diodes," Quantum Electronics, IEEE Journal of **30**, 593-607 (1994).

15. T. Yokotsuka, "Growth of heavily Be-doped AlInP by gas source molecular beam epitaxy," Appl. Phys. Lett. **58**, 1521 (1991).

16. A. C. Tropper and S. Hoogland, "Extended cavity surface-emitting semiconductor lasers," Progress in Quantum Electronics **30**, 1-43 (2006).

17. J. Geske, K. G. Gan, Y. L. Okuno, J. Piprek, and J. E. Bowers, "Vertical-cavity surface-emitting laser active regions for enhanced performance with optical pumping," Quantum Electronics, IEEE Journal of **40**, 1155-1162 (2004).

18. T. Leinonen, S. Ranta, A. Laakso, Y. Morozov, M. Saarinen, and M. Pessa, "Dual-wavelength generation by vertical external cavity surface-emitting laser," Opt. Express **15**, 13451-13456 (2007).

19. S. W. Corzine, R. S. Geels, J. W. Scott, R. H. Yan, and L. A. Coldren, "Design of Fabry-Perot surface-emitting lasers with a periodic gain structure," Quantum Electronics, IEEE Journal of **25**, 1513-1524 (1989).

20. M. Y. A. Raja, S. R. J. Brueck, M. Osinski, C. F. Schaus, J. G. McInerney, T. M. Brennan, and B. E. Hammons, "Resonant periodic gain surface-emitting semiconductor lasers," Quantum Electronics, IEEE Journal of **25**, 1500-1512 (1989).

21. M. A. Holm, D. Burns, P. Cusumano, A. I. Ferguson, and M. D. Dawson, "High-Power Diode-Pumped AlGaAs Surface-Emitting Laser," Appl. Opt. **38**, 5781-5784 (1999).

22. Y. P. Varshni, "Temperature dependence of the energy gap in semiconductors," Physica **34**, 149-154 (1967).

23. J. M. Hopkins, S. Calvez, A. J. Kemp, J. E. Hastie, S. A. Smith, A. J. Maclean, D. Burns, and M. D. Dawson, "High-power vertical external-cavity surface-emitting lasers," phys. stat. sol. (c) **3**, 380-385 (2006).

24. A. J. Kemp, G. J. Valentine, J. M. Hopkins, J. E. Hastie, S. A. Smith, S. Calvez, M. D. Dawson, and D. Burns, "Thermal management in vertical-external-cavity surface-emitting lasers: finite-element analysis of a heatspreader approach," Quantum Electronics, IEEE Journal of **41**, 148-155 (2005).

25. O. G. Okhotnikov, D. Bimberg, M. Guina, D. Burns, S. Calvez, M. D. Dawson, J. E. Hastie, J.-M. Hopkins, A. J. Kemp, U. Keller, M. Kuznetsov, N. Laurand, D. J. H. C. Maas, A. Mooradian, U. W. Pohl, M. Rattunde, B. Rösener, A. Shchergrov, T. Südmeyer, A. Tandon, J. Wagner, and G. Yoffe, *Semiconductor Disk Lasers. Physics and Technology*, O. G. Okhotnikov, ed., (WILEY-VCH Verlag GmbH & Co. KGaA, Weinheim, Weinheim, 2010).

26. T. D. Germann, A. Strittmatter, J. Pohl, U. W. Pohl, D. Bimberg, J. Rautiainen, M. Guina, and O. G. Okhotnikov, "Temperature-stable operation of a quantum dot semiconductor disk laser," Applied Physics Letters **93**, 051104-3 (2008).

27. M. Schmid, S. Benchabane, F. Torabi-Goudarzi, R. Abram, A. I. Ferguson, and E. Riis, "Optical in-well pumping of a vertical-external-cavity surface-emitting laser," Applied Physics Letters **84**, 4860-4862 (2004).

28. A. Giesen, H. Hügel, A. Voss, K. Wittig, U. Brauch, and H. Opower, "Scalable concept for diode-pumped high-power solid-state lasers," Applied Physics B: Lasers and Optics **58**, 365-372 (1994).

29. www.diamond-materials.com, Diamond Materials, "The CVD diamond booklet," 2008, Diamond Materials GmbH

30. W. J. Alford, T. D. Raymond, and A. A. Allerman, "High power and good beam quality at 980 nm from a vertical external-cavity surface-emitting laser," J. Opt. Soc. Am. B **19**, 663-666 (2002).

31. J. E. Hastie, M. Hopkins, S. Calvez, W. J. Chan, D. Burns, R. Abram, E. Riis, A. I. Ferguson, and M. D. Dawson, "0.5-W single transverse-mode operation of an 850-nm diode-pumped surface-emitting semiconductor laser," Photonics Technology Letters, IEEE **15**, 894-896 (2003).

32. J. M. Hopkins, S. A. Smith, C. W. Jeon, H. D. Sun, D. Burns, S. Calvez, M. D. Dawson, T. Jouhti, and M. Pessa, "0.6 W CW GaInNAs vertical external-cavity surface emitting laser operating at 1.32μm," Electronics Letters **40**, 30-31 (2004).

33. S. H. Park, J. Kim, H. Jeon, T. Sakong, S. N. Lee, S. Chae, Y. Park, C. H. Jeong, G. Y. Yeom, and Y. H. Cho, "Room-temperature GaN vertical-cavity surface-emitting laser operation in an extended cavity scheme," Applied Physics Letters **83**, 2121-2123 (2003).

34. Z. L. Liau, "Semiconductor wafer bonding via liquid capillarity," Applied Physics Letters **77**, 651-653 (2000).

35. A. J. Maclean, A. J. Kemp, S. Calvez, K. Jun-Youn, K. Taek, M. D. Dawson, and D. Burns, "Continuous Tuning and Efficient Intracavity Second-Harmonic Generation in a Semiconductor Disk Laser With an Intracavity Diamond Heatspreader," Quantum Electronics, IEEE Journal of **44**, 216-225 (2008).

36. F. van Loon, A. J. Kemp, A. J. Maclean, S. Calvez, J. M. Hopkins, J. E. Hastie, M. D. Dawson, and D. Burns, "Intracavity diamond heatspreaders in lasers: the effects of birefringence," Opt. Express **14**, 9250-9260 (2006).

37. J. Rautiainen, J. Lyytikäinen, A. Sirbu, A. Mereuta, A. Caliman, E. Kapon, and O. G. Okhotnikov, "2.6 W optically-pumped semiconductor disk laser operating at 1.57-μm using wafer fusion," Opt. Express **16**, 21881-21886 (2008).

38. S. L. Chuang, *Physics of Photonic Devices*, (John Wiley & Sons, Inc., Hoboken, New Jersey, 2009).

39. D. Bimberg, M. Grundmann, and N. N. Ledentsov, *Quantum Dot Heterostructures*, D. Bimberg, ed., (John Wiley & Sons Ltd, Baffins Lane, Chichester, West Sussex PO 19 1UD, England, D-69469 Weinheim, Germany, 1999).

40. M. Kuznetsov, F. Hakimi, R. Sprague, and A. Mooradian, "Design and characteristics of high-power (>0.5-W CW) diode-pumped vertical-external-cavity surface-emitting semiconductor lasers with circular TEM_{00} beams," Selected Topics in Quantum Electronics, IEEE Journal of **5**, 561-573 (1999).

41. C. Wilmsen, H. Temkin, and L. A. Coldren, *Vertical-Cavity Surface-Emitting Lasers: Design, Fabrication, Characterization, and Applications*, (Cambridge University Press, Cambridge, UK, 1999).

42. R. L. Sellin, I. Kaiander, D. Ouyang, T. Kettler, U. W. Pohl, D. Bimberg, N. D. Zakharov, and P. Werner, "Alternative-precursor metalorganic chemical vapor deposition of self-organized InGaAs/GaAs quantum dots and quantum-dot lasers," Applied Physics Letters **82**, 841-843 (2003).

43. T. D. Germann, A. Strittmatter, U. W. Pohl, D. Bimberg, J. Rautiainen, M. Guina, and O. G. Okhotnikov, "Quantum-dot semiconductor disk lasers," Journal of Crystal Growth **310**, 5182-5186 (2008).

44. http://www.epsrciii-vcentre.com/epitaxyservices.aspx?tab=2, Krysa, A. B., Stevens, B., and Morris, D., "Metalorganic Chemical Vapour Phase Deposition or Arsenide and Phosphide Materials," 2010, University of Sheffield

45. V. Y. Bondarev, V. I. Kozlovsky, A. B. Krysa, J. S. Roberts, and Y. Skasyrsky, "Scanning e-beam pumped resonant periodic gain VCSEL based on an MOVPE-grown GaInP/AlGaInP MQW structure," Journal of Crystal Growth **272**, 559-563 (2004).

46. L. M. McGill, "MOCVD Growht of InGaP-based Heterostructures for Light Emitting Devices," (Departement of Materials Science and Engineering, PhD thesis: Massachusetts Institute of Technology, (2004).

47. N. J. Ekins-Daukes, K. Kawaguchi, and J. Zhang, "Strain-Balanced Criteria for Multiple Quantum Well Structures and Its Signature in X-ray Rocking Curves," Crystal Growth & Design **2**, 287-292 (2002).

48. G. H. Olsen, C. J. Nuese, and R. T. Smith, "The effect of elastic strain on energy band gap and lattice parameter in III-V compounds," Journal of Applied Physics **49**, 5523-5529 (1978).

49. P. J. Orders and B. F. Usher, "Determination of critical layer thickness in $In_xGa_{1-x}As/GaAs$ heterostructures by x-ray diffraction," Applied Physics Letters **50**, 980-982 (1987).

50. R. People and J. C. Bean, "Calculation of critical layer thickness versus lattice mismatch for $Ge_xSix1-x/Si$ strained-layer heterostructures," Applied Physics Letters **47**, 322-324 (1985).

51. D. P. Bour, T. L. Paoli, R. L. Thornton, D. W. Treat, Y. S. Park, and P. S. Zory, "Polarized electroluminescence spectra of $Ga_xIn_{1-x}P/(Al_{0.6}Ga_{0.4})_{0.5}In_{0.5}P$ quantum wells," Applied Physics Letters **62**, 3458-3460 (1993).

52. F. Bugge, U. Zeimer, M. Sato, M. Weyers, and G. Tränkle, "MOVPE growth of highly strained InGaAs/GaAs quantum wells," Journal of Crystal Growth **183**, 511-518 (1998).

53. A. Strittmatter, T. D. Germann, J. Pohl, U. W. Pohl, D. Bimberg, J. Rautiainen, M. Guina, and O. G. Okhotnikov, "1040 nm vertical external cavity surface emitting laser based on inGaAs quantum dots grown in Stranski-Krastanow regime," Electronics Letters **44**, 290-291 (2008).

54. M. D. Kim, H. S. Lee, J. Y. Lee, T. W. Kim, K. H. Yoo, and G. H. Kim, "Formation process and lattice parameter of InAs/GaAs quantum dots," Journal of Materials Science Letters **22**, 1767-1770 (2003).

55. D. Leonard, K. Pond, and P. M. Petroff, "Critical layer thickness for self-assembled InAs islands on GaAs," Phys. Rev. B **50**, 11687 (1994).

56. N. Carlsson, W. Seifert, A. Petersson, P. Castrillo, M. E. Pistol, and L. Samuelson, "Study of the two-dimensional-three-dimensional growth mode transition in metalorganic vapor phase epitaxy of GaInP/InP quantum-sized structures," Applied Physics Letters **65**, 3093-3095 (1994).

57. T. D. Germann, A. Strittmatter, J. Pohl, U. W. Pohl, D. Bimberg, J. Rautiainen, M. Guina, and O. G. Okhotnikov, "High-power semiconductor disk laser based on InAs/GaAs submonolayer quantum dots," Applied Physics Letters **92**, 101123 (2008).

Chapter 3

InAs/GaAs submonolayer quantum dot based VECSELs

This chapter discusses the characterisation of a submonolayer quantum dot (SML QD) based VECSEL. It is divided into four sections, the first of which gives a short and very general overview of work done on In(Ga)As/GaAs based VECSELs prior to the present project up to the introduction of In(Ga)As QDs as gain material. The specific structure design and growth parameters are presented in the second part followed by spectroscopic and laser characterisation, discussed in section three. Early involvement of this group, under the supervision of Dr. Stephane Calvez at the Institute of Photonics (University of Strathclyde, Glasgow, UK), in the development of these QD based VECSELs was performed in terms of structure design and characterization of the first grown SML QD devices, which successfully demonstrated laser emission [1,2]. Other collaborating partner institutions in the course of the EU funded NATAL project (EU FP6 NATAL contact no. 016769) were the groups of Prof. Dieter Bimberg at the Technische Universität Berlin, Institut für Festkörperphysik, Germany, who carried out structure fabrication and of Prof. Oleg G. Okhotnikov of the Optoelectronics Research Centre, Tampere University of Technology, Finland, involved in structure characterisation. Advances of these and other research groups on the new QD based VECSEL devices subsequent to this work, are summarised in section four, both for S-K and SML QD growth modes.

3.1 Towards In(Ga)As QD based VECSELs

The InGaAs/GaAs material system is so far the most studied and developed semiconductor composition used for VECSEL device production. It has superior

properties in terms of carrier confinement, gain, thermal conductivity, and most importantly, it can be easily lattice matched to the GaAs substrate, allowing epitaxial growth on top of Al(Ga)As/Ga(Al)As DBRs. The spectral coverage of VECSELs with different material compositions of the active region was introduced in Chapter 1, where it has also been stated that the laser performance of InGaAs QW based devices decreases rapidly for wavelengths outside the 920-1180 nm region due to:

- Poor carrier confinement at short wavelengths,
- Strain related constraints at long wavelengths,

reducing the efficiency. Regarding the former, decreasing Indium (In) in the QWs decreases the lattice mismatch and increases the energy bandgap, but reduces the confinement potential between $In_xGa_{1-x}As$ QW and the GaAs barrier. Thermal escape mechanisms become more significant and cause reduced radiative emission efficiency. In the second case an increase in x_{In} mole fraction would decrease the energy bandgap, but increases the lattice mismatch and thus increase misfit strain, setting the upper wavelength limit. In order to circumvent this poorer performance, other material compositions/alloys for substrate, DBR and QW based active region have been used as was already presented in Chapter 1. Vertical-cavity surface emitting laser devices (VCSEL) incorporating QDs were successfully demonstrated prior to this work, e.g. in Lott et al. [3] and the first report on a VECSEL-like structure based on InAs/InGaAs QDs in a well was published by the same group in 2005 [4]. In this case a VCSEL structure with a 3-λ long micro-cavity, utilizing the RPG concept for gain enhancement was processed after growth and testing into a VECSEL structure by partial removal of the top mirror. Over 120 mW of output power around 1270 nm were demonstrated with an optical efficiency of more than 5 %. The demonstrated emission wavelength was also higher than the upper limit of 1180 nm for QW VECSELs. It is thus not surprising that the first QD based VECSEL, which was designed as such was demonstrated in the InGaAs/GaAs material system by Strittmatter et al. [5] exploiting the first excited state of InGaAs QDs grown in the Stranski-Krastanow (S-K) regime. These quantum dots had a ground state and first excited state emission at 1100 nm and 1040 nm respectively, due to the higher gain available from the first excited state the laser was designed for

emission at the latter. This was done by placing the centre of the DBR mirror and resonances at 1040 nm. At the same time structures incorporating SML QDs, emitting at the same wavelength were also grown and tested, which are discussed in the following sections.

3.2 Design and growth

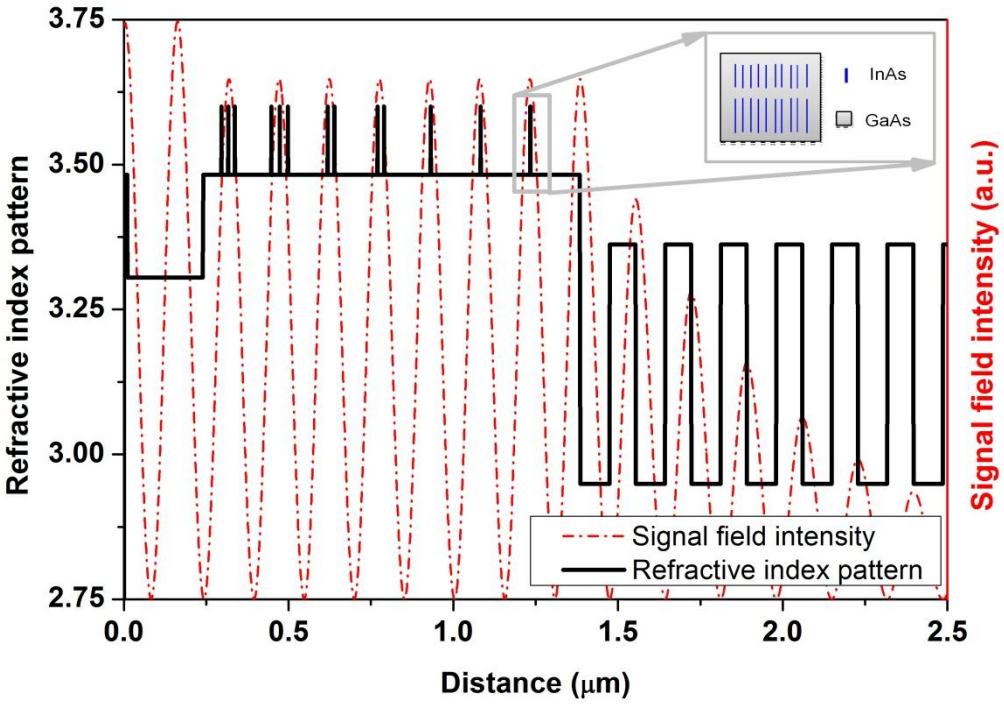

Fig. 3-1 VECSEL gain structure design for 1040 nm emission using InAs/GaAs sub-monolayer quantum dots. The refractive index pattern is represented by the black solid line and the signal field intensity by the red dash-dotted line. An illustration of the 10 cycles of InAs/GaAs sub-monolayer QDs surrounded by a GaAs matrix/capping is given in the inset.

Fig. 3-1 shows the refractive index profile and the field intensity in the designed structure. (Characterisation on this structure was also published by Germann et al. [1] independently, where further details of the growth procedure can be found). The MathCad design is presented in Appendix A.7 and was created by Dr. Stephane Calvez. The VECSEL was grown on top of an undoped (100) GaAs substrate by metal organic chemical vapour deposition (MOCVD). A sequence of 35.5 pairs of

λ/4 thick, nearly lattice-matched $Al_{0.98}Ga_{0.02}As/Al_{0.2}Ga_{0.8}As$ layers were deposited on top of the substrate to form a high reflective distributed Bragg reflector (DBR) with a calculated reflectivity of R_{DBR} = 99.96 % and a total stopband width exceeding 90 nm, centred at 1040 nm. The active region was set to be resonant at the same wavelength and incorporated 13 SML InAs/GaAs QD-layers non-uniformly distributed at the seven field antinodes and was grown directly on top of the DBR. An offset of 20 nm between the room temperature peak gain and the subcavity resonance was introduced, as commonly used for QW structures to accommodate for the thermal dependence of the dot emission. The active region consisted mainly of GaAs serving the multiple purposes as the growth matrix for the QD deposition, as separators between adjacent SML QD-layers within a group and as pump absorption barriers. The non-uniform distribution of 2x3, 2x2 and 3x1 SML QD-layers was chosen with respect to the exponentially decaying pump field intensity with penetration depth , accommodating as many gain layers as possible in the first few field antinodes (see Section 2.2.3.1 for further clarification). Estimated pump absorption of about 80 % within the active region was supposed to ensure sufficiently high carrier densities in all dot layers. With this in mind, the first design used the non-uniform QD-layer distribution in order to avoid any reabsorption of the emitted laser light from the deeper lying, unpumped dots. The SML QD-layers consisted of 10 cycles of 0.5 ML (0.15 nm) InAs and 2.3 ML (0.65 nm) GaAs and were separated by 20 nm thick GaAs spacer layers within a group to avoid structural coupling. A 230 nm thick $Al_{0.3}Ga_{0.7}As$ window layer was grown on top of the active medium in order to prevent the photo-generated charge carriers from escaping to the surface. A 10 nm thick GaAs cap-layer concluded the 7.4 μm thick structure to protect the aluminium containing layers from oxidation.

3.3 Characterization

For initial characterization purposes, temperature dependent spectroscopy and tests inside a laser cavity were done. The spectroscopic measurements taken were

reflectivity, surface as well as edge photoluminescence (PL). By the use of different growth calibration structures, which consisted only of one single SML QD-layer with different cycle numbers and where the structure is described in more detail below, edge-PL measurements were carried out in order to examine the un-modulated PL emission in dependence on the SML QD height. Laser and output power decay experiments are also discussed in a further subsection of this chapter.

3.3.1 Spectroscopic characterization

3.3.1.1 Photoluminescence test sample characterisation

For a closer examination of the SML QD emission behaviour with temperature and QD height, edge photoluminescence measurements were taken for the growth calibration structures. These samples were grown on top of a (100) GaAs substrate. The substrate was first covered by a 500 nm thick GaAs buffer layer, followed by 50 nm of $Al_{0.6}Ga_{0.4}As$ and 146 nm GaAs, all deposited at 700 °C. A single submonolayer QD-layer with 5, 10 or 20 cycles of 0.5 ML InAs / 2.7 ML GaAs was grown at 500 °C and capped by 6 nm GaAs. These QDs had a higher GaAs fraction compared to the dots used in the VECSEL structure, which resulted in a shorter emission wavelength. The structures were concluded by a sequence of 140, 20 and 50 nm thick layers of GaAs, $Al_{0.6}Ga_{0.4}As$ and GaAs respectively at a growth temperature of 600 °C. A sample containing one single 9-nm-thick $In_{0.18}Ga_{0.82}As$ QW-layer, tuned to emit around the QD emission wavelength, was also used for comparison. All following reflectivity and PL measurements were undertaken using an ISA JOBIN YVON – SPEX spectrum analyser model HR460 with a 1200 lines/mm grating. The optically excited signal was first collimated by the collection lens, the beam than chopped by a beam chopper and finally focussed onto the entrance slit of the spectrum analyser using a 300 mm focal lens. The chopper was connected to a Lock-In-Amplifier (Stanford-Research-System, Model: SR530) for measurement/signal synchronisation and amplification. Detection of the spectrally

resolved signal occurred via an InGaAs photodiode, which was positioned at the exit slit of the spectrum analyser monochromator unit (See experimental set-up descriptions in the Appendix A.8). The used spectral resolution was 1 nm.

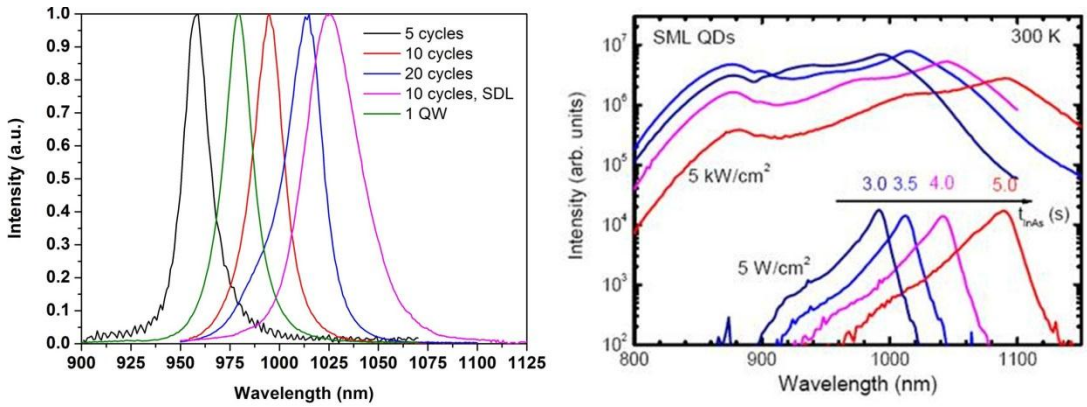

Fig. 3-2 Left: Normalized edge-PL spectra at room temperature for growth calibration structures containing one SML QD-layer with 5 (black), 10 (red) and 20 (blue) cycles of InAs/GaAs and a single QW (green). Edge PL emission of the completed VECSEL structure containing 13 SML QD layers with a different InAs/GaAs mole fraction ratio is given by the pink line. Right: Emission spectra of 5 cycle SML QDs for high and low excitation in dependence on the deposition time, t_{InAs}. Courtesy: Udo W. Pohl, Technische Universität Berlin, Institut für Festkörperphysik.

Edge PL is the unmodulated emission of the quantum dot ensemble collected from the sample facet. The 532 nm laser beam from a commercial frequency doubled diode pumped Nd:YVO_4 laser was focussed with a focal lens (f = 50 mm) onto the surface under normal incidence close to the edge. The PL was collected at an angle with respect to the layer plane in order to avoid the superposition of the signal with wave-guided photoluminescence (PL). PL spectra were taken with a pump spot size of about Ø = 60 µm and a maximum excitated power of 20 mW corresponding to a pump density of ~700 W/cm^2. The edge PL was collected and collimated in this case by a microscope lens, having a focal length of f = 6.3 mm and a numerical aperture (NA) of 0.4. (The schematic experimental setup can be seen in the Appendix A.8). Measurements were done in a temperature range between 10-90 °C, where the temperature was controlled by the help of a Peltier thermo-electric element onto which the sample was attached with conductive silver paste. The experimental results were finally compared to the completed VECSEL sample under investigation, having 13 layers of 10 cycle SML QDs. Several things can be taken from Fig. 3-2 left, which shows normalised, edge PL emission of all growth calibration structures and

compares them with the completed VECSEL device. The emission wavelength of the SML QDs increases with increasing cycle number from 958 nm, 995 nm and 1014 nm as expected due to the increased QD volume (stacking in growth direction). The comparison of the room temperature full width at half maximum (FWHM) values for the growth calibration samples are 16 nm, 18 nm and 22 nm for the 5, 10 and 20 cycled SML QD-layers slightly increasing with emission wavelength and very similar to the value of the single QW (16 nm). This might be due to the very uniform size distribution of this type of QDs as reported in [6] and due to the relatively low pump density. The edge-PL peak of the completed VECSEL structure is with 32 nm broader and also considerably red-shifted with respect to the 10 cycled SML QD-layer calibration growth sample. The broader peak width could be explained by the increased number of QD-layers (13 in total) within the active region of the VECSEL. Stacking several of these structures on top of each other leads to a vertical ordering due to the induced strain fields of the underlying QDs but also to an increase in size [6]. The higher emission wavelength is perhaps caused by the lower GaAs ratio in the SML QD-layers implemented in the VECSEL structure compared to the growth calibration samples. The right hand side of Fig. 3-2 illustrates the variation of the emission wavelength of a single 5 cycle SML QD layer sample in dependence on the InAs deposition time, t_{InAs}, i.e. the nominal layer thickness. The peak emission wavelength can be varied in the range of just below 1000 to 1100 nm by increasing the growth time from 3 to 5 s. A flat wide broadening of the emission spectrum is recognisable at a high excitation density towards lower wavelength. This behaviour can be understood such, that smaller QDs become populated at high excitation levels. The very flat spectra make broad wavelength tuning and temperature stable operation possible. Fig. 3-3 depicts the thermal dependence of the SML QD emission. The measured increase in emission wavelength with temperature, $\frac{\Delta\lambda}{\Delta T} = 0.35\,{}^{nm}/_{\mathrm{K}}$, is the same for all growth calibration samples, including the QW, and correspond well with the literature value of 0.3 nm/K for InGaAs QW structures near 1 µm emission [7]. In both cases, SML QD and single QW the PL emission wavelength depends on the energy bandgap shift with temperature and follows the Varshni relation as was reported to happen for InAs/GaAs S-K QDs by Dai, et al. [8]. A possible reason for the lower temperature dependence of the VECSEL

structure could be that the detected edge-PL emission is modulated by the resonance effect of the subcavity in the vertical direction, due to the presence of the DBR and is discussed in further detail below.

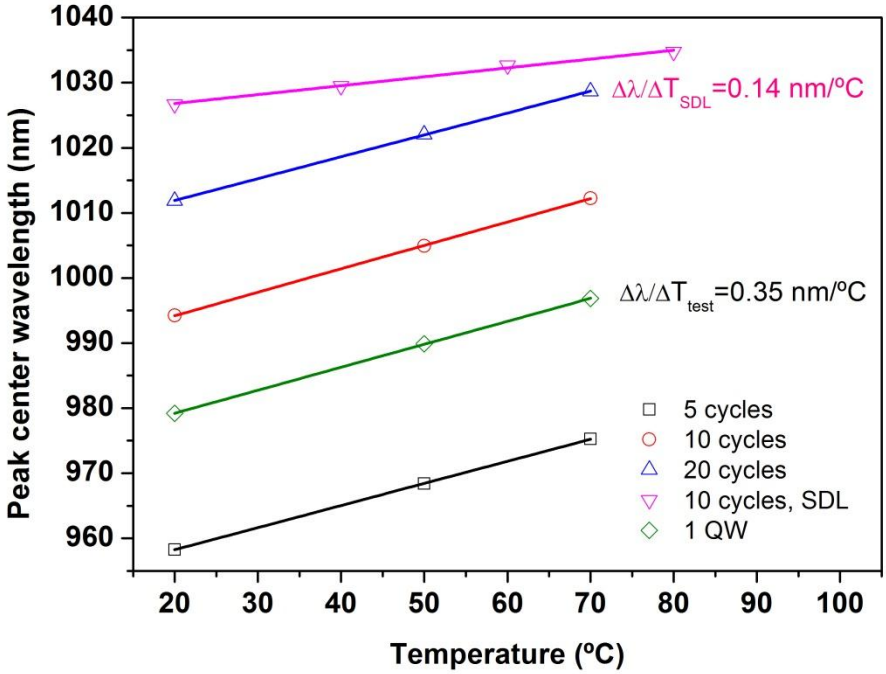

Fig. 3-3 Edge PL thermal behaviour of the SML QD with 5 (black squares), 10 (red circles), 20 (blue upwards triangles) cycled and the single QW (green diamond) growth calibration structures. The thermal shift of the VECSEL gain region (10 cycles of InAs/GaAs SML QDs) is represented by the pink downwards triangles.

3.3.1.2 VECSEL characterisation

Further spectroscopic characterisation of the completed VECSEL structure was carried out to determine the positions of the subcavity resonance, the photoluminescence peak position, and their behaviour with respect to temperature and/or pump density.

The reflectivity stopband position and width, together with enhanced absorption/resonance feature(s), are probed by the use of a broad emitting white light tungstate lamp. The light is focussed onto the sample surface with a spot size of about Ø = 2 mm in diameter. The reflected light is collimated and chopped by a

beam chopper and finally focussed onto the entrance slit of the spectrum analyser. The detected spectrum was then divided by the signal of a reference silver mirror. The experimental arrangement for the surface PL measurement was very similar to the already described edge PL set-up, only that the pump beam was incident under an angle of 30 ° and the PL collected in the direction perpendicular to the surface by a focal lens (f = 80 mm). In this configuration, the PL emitted by the quantum dots is modulated by the subcavity between DBR and semiconductor/air interface. (See experimental set-up descriptions in the Appendix A.8).

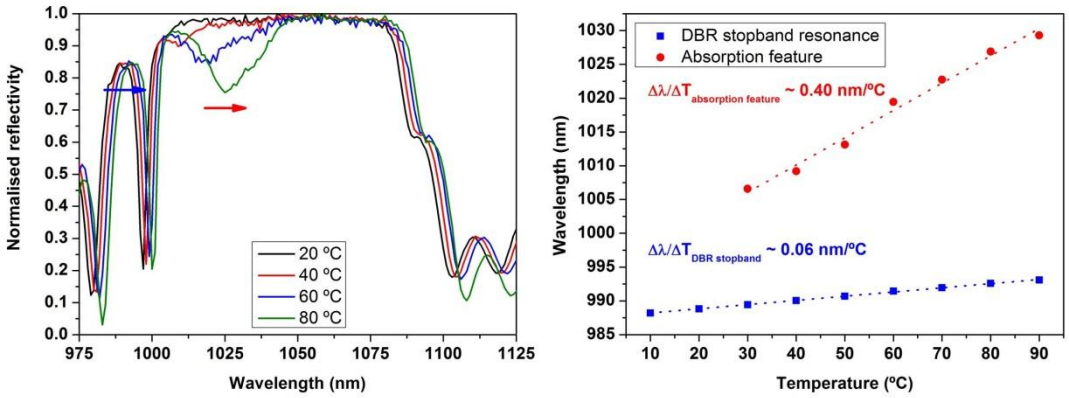

Fig. 3-4 Left: Temperature dependent reflectivity spectra at 20 (black), 40 (red), 60 (blue) and 80 °C (green). Right: Thermal shift of the absorption feature (red circles) and reflectivity stopband (blue squares) indicated by the arrows in the reflectivity spectra.

One set of measurements including reflectivity, surface or edge PL, was taken under controlled conditions, where the temperature, pump spot position and the pump density were kept constant, thus the intensities can be related to each other. The measured reflectivity spectra in a temperature range of 10-90 °C are shown in Fig. 3-4 (left). The thermal shifts of the DBRs stopband and the distinct absorption feature are shown in Fig. 3-4 (right). The measured thermal shift of the absorption feature is $\frac{\Delta\lambda}{\Delta T_{abs.}} = 0.40\ nm/^0\mathrm{C}$ and corresponds to the thermal dependence of the growth calibration structures. The increase of the enhanced absorption feature with elevated temperatures is a sign of increased matching between the subcavity resonance and the SML QD gain. The estimated red-shift of the DBR reflectivity stopband $\frac{\Delta\lambda}{\Delta T_{DBR}} = 0.06\ nm/^0\mathrm{C}$ is in contrast much weaker and caused by the temperature dependent refractive index. Surface PL spectra at various temperatures

are presented in Fig. 3-5 (left) together with the room temperature reflectivity spectrum for clarification. Three different features can be recognised and are indicated by the arrows, which represent the positions at which the data points in Fig. 3-5 (right) are taken for the determination of the shift rates. The sharp peak in the surface PL at the left is a resonance feature caused by the DBR reflectivity stopband edge. Noticeable in this graph is the increasing surface PL intensity of the merging two centre peaks. This is characteristic for an improving match between the gain and the subcavity resonance/RPG, discussed in previous Section 2.2.3.3. The fast shifting peak has a rate of $\frac{\Delta\lambda}{\Delta T_{SML\ QD}} = 0.43\,{}^{nm}/_{^0\mathrm{C}}$, similar to the absorption feature in the reflectivity stopband and is caused by the thermal dependence of the bandgap energy of the SML QDs. The peak with the slow shift rate has the same thermal dependence as the DBR reflectivity stopband of $\frac{\Delta\lambda}{\Delta T_{subcav\ res}} = 0.06\,{}^{nm}/_{^0\mathrm{C}}$ and is caused by subcavity resonance. The graph in Fig. 3-5 (right) suggests that the matching point is reached at around 80 °C and corresponds well with the expected working temperature of the device under realistic pumping conditions.

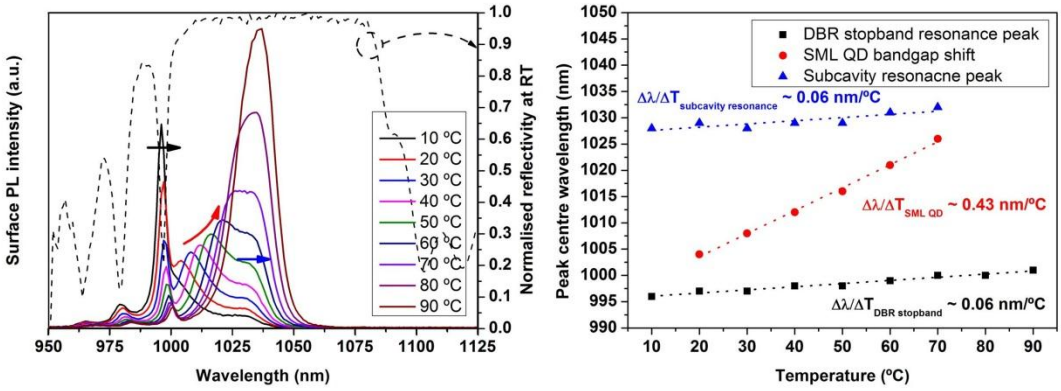

Fig. 3-5 Left: Surface photoluminescence spectra in a temperature range of 10-90 °C. The room temperature reflectivity spectrum (dashed line) is shown for clarification of the peak positions. Right: Thermal shift ratios of the subcavity resonance (blue triangles), SML QD PL (red circles) and the reflectivity stopband (black squares).

Ideally the edge-PL spectra, shown in Fig. 3-6, should be related to the un-modulated (by the subcavity effect) SML QD photoluminescence. The estimated thermal shift ratio in this case is $\frac{\Delta\lambda}{\Delta T_{Edge\ PL}} = 0.14\,{}^{nm}/_{^0\mathrm{C}}$ and is illustrated in Fig. 3-2 together with the edge PL of the growth calibration structures. This shift is considerably lower

than the previously determined value in terms of the reflectivity and surface PL measurements. An explanation could be that the detected edge photoluminescence is still modulated by the subcavity resonance, which is possibly caused by waveguided PL and scattered light at the rough interfaces due to the three dimensional island growth. An indication for this argument can be found in Fig. 3-5, where the 20 °C curve has a local peak maximum around 1005 nm (thought to be the SML QD ensemble emission) which corresponds very well with the room temperature peak PL emission of the 10 cycle growth calibration structure in Fig. 3-2 (left). Fig. 3-6 also illustrates the decrease in emission efficiency with increasing temperature. The thermally induced carrier escape from the dots into the higher lying barrier states and the subsequent non-radiative recombination are a cause of this decay. The small, sharp spikes in the edge-PL spectrum at 1064 nm are caused by the second order diffraction of the 532 nm pump light at the spectrometer grating and are not a feature of the QD emission.

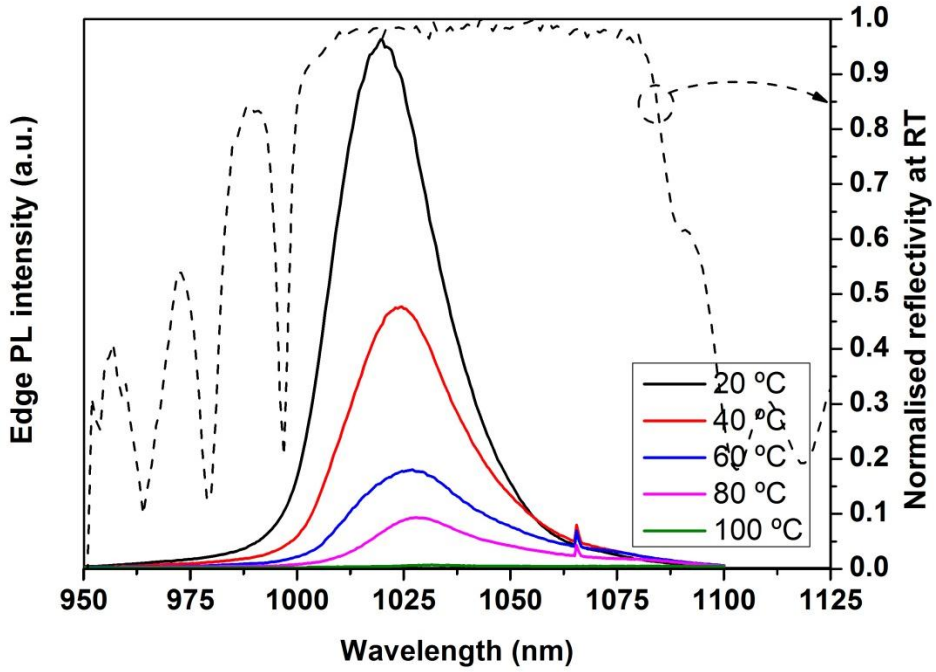

Fig. 3-6 Edge photoluminescence spectra in a temperature range from 20-100 °C. Also presented is the normalised room temperature reflectivity for clarification.

A final discussion on the increased red-shift of the surface PL peak compared to the determined peak shift of the growth calibration structures is given below. One would expect the surface PL shift rate to be either equal to the shift rate of the subcavity

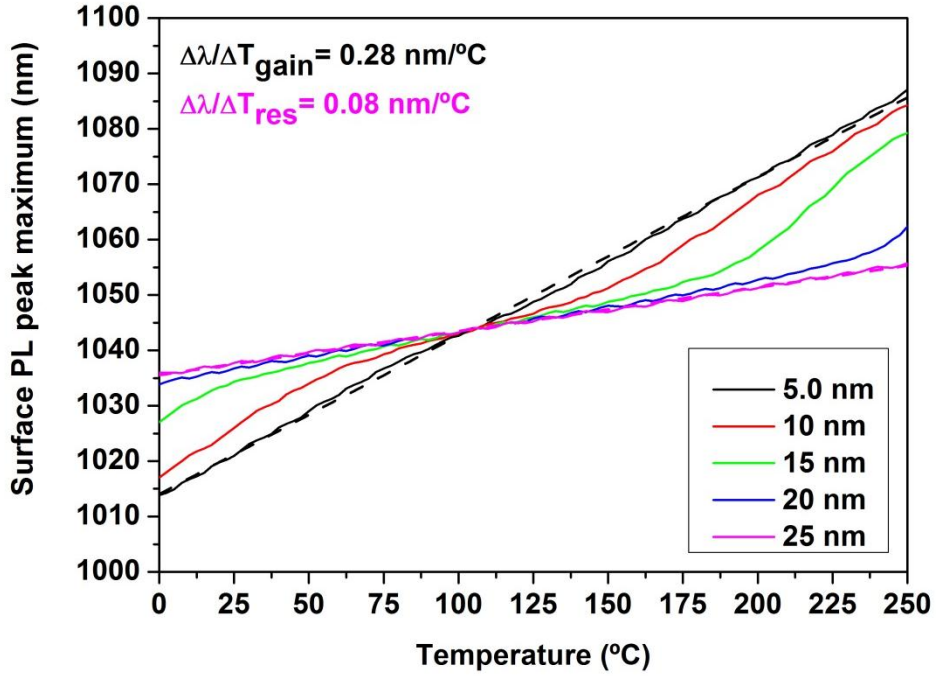

Fig. 3-7 Graph from [9] illustrates the simulated surface-PL behaviour of a QW based IR VECSEL in a range of 250 °C for different gain bandwidths. The thermal behaviour of the QW gain dominates the surface-PL if the gain bandwidth is narrow. For a very broad gain bandwidth the surface-PL shift is controlled by the subcavity resonance.

resonance or the PL peak emission of the QD bandgap energy. In fact, the rate is higher and might be explained by the effect of mode pulling. Theoretical investigations on the thermal behaviour of the surface-PL in dependence on the gain bandwidth and the subcavity resonance enhancement were undertaken and compared with experimental results in the case of near-IR InGaAs QW based VECSELs by Giet et al. [9]. The calculations in Fig. 3-7 are taken from [9] and illustrate the thermal dependence of the surface-PL, which is dominated by the subcavity resonance, when the QW gain bandwidth is large (FWHM > 20 nm). In that case the thermal shift rate of the surface PL peak centre becomes $\frac{\Delta\lambda}{\Delta T_{res}} = 0.08\,{}^{nm}/_{^0\mathrm{C}}$ (literature value for resonance shift of InGaAs caused by the refractive index change with temperature $\frac{\Delta\lambda}{\Delta T_{resonance}} = 0.1\,{}^{nm}/_{^0\mathrm{C}}$ [7]). On the other hand, in the case of a narrow gain bandwidth (FWHM < 10 nm), the red-shift rate of $\frac{\Delta\lambda}{\Delta T_{gain}} = 0.28\,{}^{nm}/_{^0\mathrm{C}}$ is governed by the thermal dependence of the InGaAs QW bandgap energy (literature value $\frac{\Delta\lambda}{\Delta T_{bandgap}} = 0.3\,{}^{nm}/_{^0\mathrm{C}}$ [7]). For intermediate

cases, both effects compete with each other, resulting in transition regions. The dashed lines represent the dependence of the bandgap energy and the resonance position with temperature and are approached asymptotically by the simulated curves. It can be seen that for temperature regions away from the crossing point (point where peak gain and resonance position are matched) the thermal shift rate can be higher than the bandgap energy redshift. SML QDs are considered to be very uniform in size compared to the QDs of the S-K growth mode. The gain bandwidth and shape is expected to be narrower due to this fact. It is also dependent on the excitation level, as can be seen in [1] and Fig. 3-2 right, thus causing the surface PL to behave similarly to an intermediate case in the graph.

3.3.2 Laser characterization

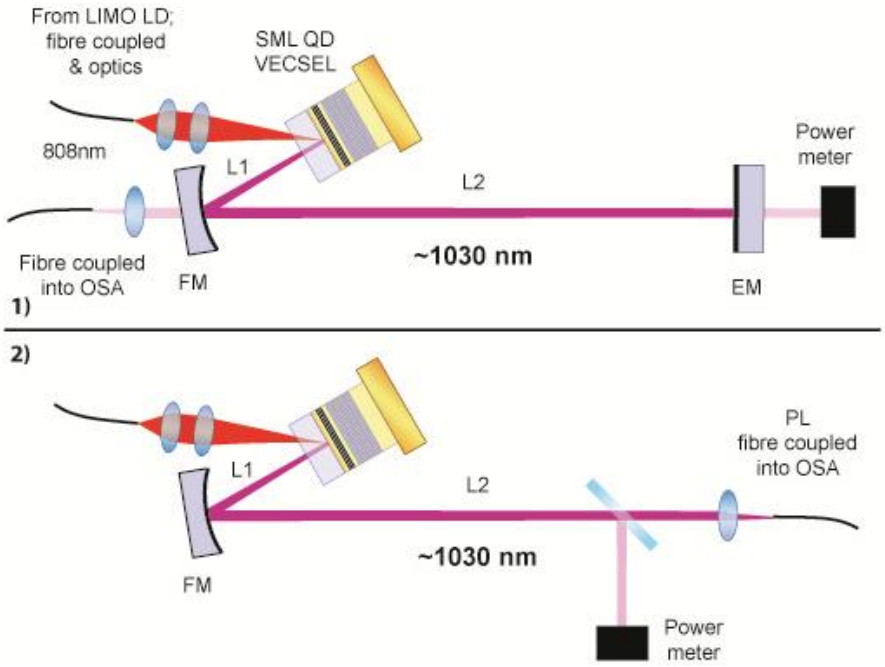

Fig. 3-8 Experimental arrangements: 1) Completed three mirror V-shaped laser resonator for power transfer and laser output power decay measurements. 2) Setup for photoluminescence decay measurements.

Laser performance tests were undertaken with the experimental arrangement shown in Fig. 3-8. The three mirror V-shaped cavity consists of the gain structure as a plane end mirror, a high reflective (HR) folding mirror (FM) with a 100 mm radius of

curvature at a distance $L1 = 56\,mm$ from the VECSEL and a plane HR or 1 % output coupling end mirror (EM) at a distance of $L2 = 168\,mm$ from the curved mirror. The cavity arm dimensions were chosen to match the cavity mode to a pump spot diameter size of $\emptyset = 60\mu m$. A fibre coupled diode laser with an emission wavelength of 808 nm served as pump. A 250-µm-thick natural diamond heatspreader was liquid capillary bonded (see Liau et al. [10]) to the intra-cavity surface for thermal management [11]. The bonded sample was mounted into a water/glycol cooled brass mount, set to 10 °C.

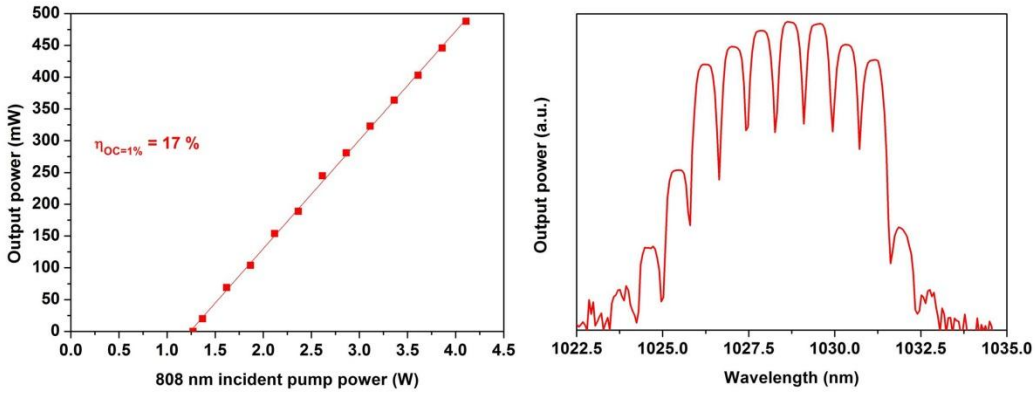

Fig. 3-9 Left: Power transfer: Laser output power with incident pump power below the onset of thermal rollover for 1 % output coupling. Right: Free running laser emission spectrum, modulated by the etalon effect of the diamond heatspreader, plotted on a semi-logarithmic scale.

Fig. 3-9 left shows the power transfer measurement of the SML QD VECSEL structure. The right hand side of the figure shows a representative free running laser emission spectrum with a centre wavelength around 1029 nm and a total width of roughly 10 nm. The fringes in the spectrum are caused by the intracavity diamond heat spreader and are separated by about 0.8 nm according to the expression:

$$\Delta\lambda_{modul} = \frac{\lambda_{laser}^2}{2n_D L_D}. \qquad \text{Equation [3-1]}$$

$\Delta\lambda_{modul}$ is the fringe separation of the modulated laser output spectrum, λ_{laser} the laser emission wavelength and $n_D = 2.392$ [12] and $L_D = 250$ µm are the diamond refractive index and thickness respectively. The measured value corresponds very well to the thickness of the diamond heat spreader. The achieved maximum output power was around 500 mW with a differential efficiency of 17 %

for a 1 % output coupler. Table 3-1 compares laser performance values from this work to that reported in Germann et al. in [1]. The tested samples were from the same wafer.

Sample	P_{thr} (W)	η (%)	P_{max} (W)	λ_{pump} (nm)	λ_{laser} (nm)	$Ø_{pump\ spot}$ (mm)
This work	1.25	17	0.5	808	1029	60
[1]	6.5	12.4	1.4	808	1034	180

Table 3-1 Comparison of the experimental results from this work with published values form [1]. The indices: thr and max stand for threshold and maximum output power. η is the differential efficiency.

Discrepancies result from a different cavity setup and pump condition. The laser cavity was optimised near the onset of thermal rollover (4.1 W incident pump power see Fig. 3-10 left) and the pump power was lowered towards the pump threshold power, which occurred at 1.3 W. The output power decayed within only a few minutes, affecting the power transfer and differential efficiency measurement. This decay of the output power accelerated with increasing pump power, hence pump-induced temperature. A more thorough discussion of this problem is given later in this section.

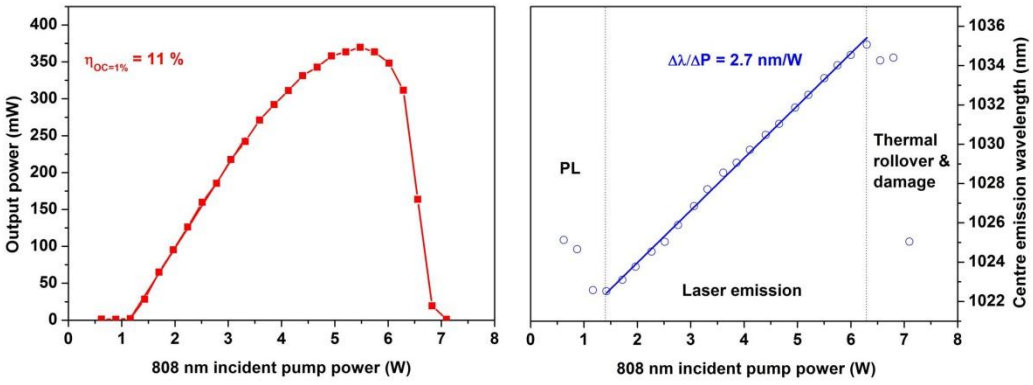

Fig. 3-10 Left: Power transfer curve over the total incident pump power range (red squares). Dependence of the laser emission centre wavelength on the incident pump power (blue circles). Right: Central emission wavelength of the tree running laser spectrum with incident pump power.

The power transfer curve of the same sample is given in Fig. 3-10 (left) for the whole available incident pump power range. The pump threshold is here 1.2 W and a differential efficiency of 11 % for an output coupling of 1 % was measured. The onset of thermal rollover occurs around 4 W pump power. A maximum output power

of 370 mW is achieved at a pump power of 5.5 W before the output power decreases rapidly and laser emission ceases at around 7 W. It was not possible to regain laser emission at the same pump spot, indicating permanent damage. It is thought that the measured behaviour of the power transfer curve is a superposition of conventional thermally-induced rollover (discussed in previous Sections 2.2.3.3 and 2.2.4) and the rapid output power decay. The transmitted signal through the high reflective folding mirror was focused into a fibre, which was coupled to an IR optical spectrum analyser (Hewlett Packard - Optical Spectrum Analyser 86142A with a maximum spectral resolution of 0.05 nm). The blue data points in Fig. 3-10 (right) are the weighted centre emission wavelength. A linear increase in laser emission wavelength with pump power is recognisable with a rate of change $\Delta\lambda/\Delta P = 2.7\ nm/W$ for pump powers above threshold up to just beyond rollover. In this region, the wavelength scales linearly with temperature of the gain sheets as was stated by Kemp et al. in [13] in case of InGaAs QW VECSELs. The same group reports non-linear behaviour of the wavelength tuning with temperature in the ranges below threshold and above thermal rollover. For pump powers below threshold, the detected PL centre wavelength decreases with increasing pump power. This effect might be explained by state filling, meaning the population of shallower dot energy states (smaller dots) with increasing pump intensity. It causes a broadening and overall blue shift of the PL signal and is illustrated in Fig. 3-2 on the right hand side. The blue shift for the highest pump powers, above rollover behaves opposite to that stated in [13]. Kemp et al. report a super-linear red-shift of the emission wavelength with pump power and attribute this to an increased heat load introduction with decreasing device efficiency. The detected blue-shift for the present QD structure is not fully understood yet but might be explained by the onset of thermally-induced permanent damage. This damage was attributed to a high carbon density within the aluminium containing DBR structure and is believed to have caused excessive heating due to a higher absorption coefficient. This might have supported the generation of defects in larger dots, causing increased non-radiative recombination, which would lead to a blue-shift of the emission wavelength. Dai et al. [8] show in a photoluminescence study of InAs/GaAs QD layers with temperature and nominal layer thickness, that PL

quenching is dominated by non-radiative recombination processes at interface defects of large QDs.

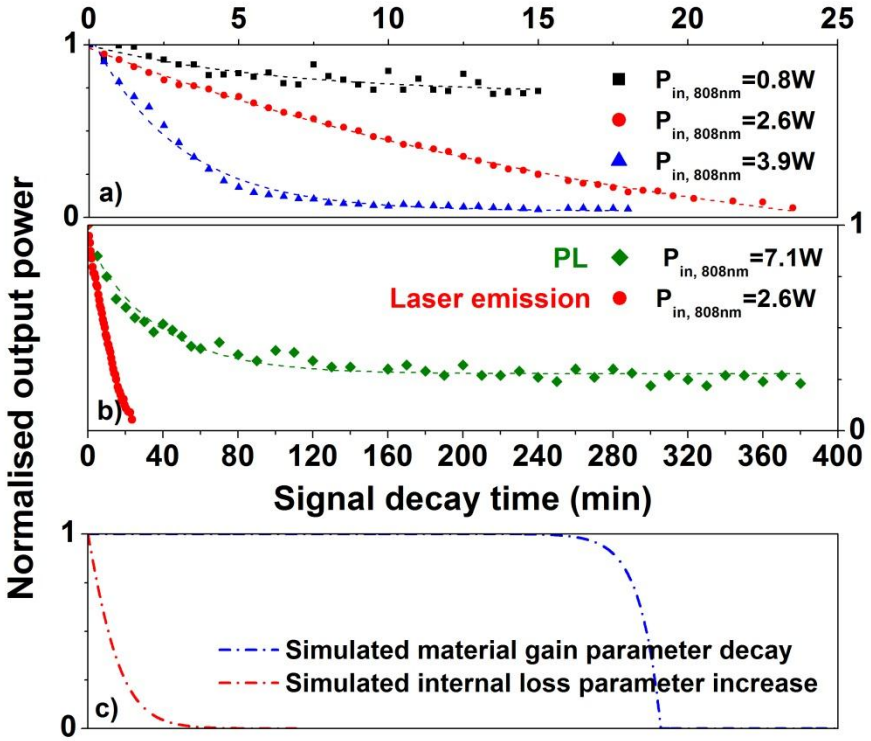

Fig. 3-11 a) Measured laser output power decay for different incident pump intensities. Dashed lines are mono exponential fits to the data points. b) Measured laser output power (red circles) and photoluminescence (green diamonds) decay for comparison on the same time scale. c) Simulated decay behaviour for the gain decay (blue) and increased cavity losses (red). The calculated parameters for QW gain and cavity transmission losses were multiplied by the mono exponential decay function indicated by the green line.

For a further study of these effects, decay measurements were first carried out on the working laser, setup 1 depicted in Fig. 3-8, where the laser output power against time was recorded (Fig. 3-11 a)) for different pump powers. Laser emission ceased within a few minutes dependent on the incident pump intensity. The setup was then changed according to Fig. 3-8 setup 2, where the sample was pumped with a maximum available pump power of 7.1 W and surface PL decay was detected by an optical spectrum analyser (OSA) and a power meter. The decaying PL signal was measured over the time range of 6 hours. The normalised decay is illustrated in Fig. 3-11 b) for photoluminescence decay (green) and laser decay (red) for comparison, set to the same time scale. The decay behaviour can be described by a mono exponential dependence.

The already mentioned model by Kuznetsov et al. [14] (see also Section 2.3.4), was altered to model qualitatively the output power with time for a mono-exponentially increasing cavity loss or decreasing material gain coefficient. The results of this calculation can be seen in Fig. 3-11 c), where the blue and red line represent output power time dependence for decaying gain or increasing loss coefficient respectively. The shape of the simulation functions is compared with the detected decay behaviour. The similarity between the measured exponential power decay and the simulated exponential increase of the cavity losses is a good indication that the issue with the declining output power was rather linked to the losses than to the QD gain.

The lifetime of AlGaAs DBRs has previously been shown to depend significantly on growth conditions and it is suggested here that this might be a factor. This assumption could be confirmed by the growers: where the alternative precursor tertiarybutylarsine (TBA, or $C_4H_9AsH_2$) was used as a substitute for the commonly used highly hazardous arsine (AsH_3) for both the AlGaAs/GaAlAs DBR and the gain region including the SML QDs (see Sellin et al. [15] for further information on the QD growth with alternative precursors). The new precursor caused a high carbon background p-type doping of all AlGaAs layers, affecting especially the DBR region [16]. Carbon increases the absorption coefficient and causes excessive heat introduction into the DBR layers, leading to fast structural deterioration. It was suggested to replace the alternative As-precursor with arsine for the DBR only, as was done in the case of S-K QD structures (design B in Germann et al. [16]). Background doping was reduced by more than an order of magnitude from $p = 5 \cdot 10^{17}$ cm^{-3} to $2 \cdot 10^{16}$ cm^{-3} here and deterioration was not detected in subsequent work.

3.4 Conclusion and overview of recent progress in InAs/GaAs QD VECSELs

Opto-electronic devices based on In(Ga)As QDs are widely studied and were chosen for the initial demonstrations of a QD-based VECSELs, both in the S-K and the SML

growth mode. Especially the successful implementation of QDs in a vertical-cavity surface emitting laser (VCSEL) was a driving motivation behind this project. In this chapter a 1030 nm SML QD structure was discussed in terms of initial photoluminescence characterization and laser properties. Output powers as high as 500 mW were demonstrated with a slope efficiency of 17 % and a pump threshold of 1.3 W. Higher output powers of samples from the same wafer have been achieved by Germann et al. [1] for a larger pump spot size, thus higher pump powers. A rapid decay of the laser emission and photoluminescence was found, leading to permanent destruction of the samples during the pumping process. The experimental results were quantitatively compared to a simulation based on the gain calculation of Kuznetsov et al. [14]; extended by a mono-exponential time dependent term for the gain or the internal loss coefficient. The finding suggested a thermally-induced increase in internal loss and was allocated to the DBR rather than the active region. This was supported by the high carbon background doping ($p=5\cdot10^{17}$ cm^{-3}) of the $Al_xGa_{1-x}As$ DBR layers caused by the used alternative TBA precursor for the mirror fabrication. The increased carbon doping level caused a higher absorption coefficient and higher heat introduction, reducing the lifetime [16]. More recent samples grown and studied only after this project showed improvement due to a thinner spacer layer thickness, which allowed the implementation of a higher number of QDs into the subcavity, increasing the modal gain drastically and leading to multi-watt output powers in a range between 1000-1300 nm. Studies on waveguides incorporating quantum dot gain layers with different optical confinement and modal gain by Klopf et al. [17] have revealed that the highest thermal stability is achieved by devices with lowest modal gain. The redshift of the bandgap with increasing temperature is most effectively compensated a by the blue-shift of the emission wavelength with higher pump intensities in this case as a consequence of the broad gain profile. The discussion by Giet et al. [9] concerning the thermal dependence of the surface PL on the gain bandwidth of QW VECSELs leads to a similar conclusion. According to this it is believed that the use of anti-resonant subcavity designs could further lead to a higher thermal stability and even broader wavelength tunability.

Following the early work dicussed in this chapter, VECSELs based on both SML QDS and S-K QDs have been developed and reported. In both cases multi-Watt output powers around 1040 nm [5,18] for SML and for S-K QDs at 1180 nm [19] and 1250 nm [20] have been achieved so far. A mode-locked device with 27 mW pulse power, a pulse width of 18 ps and with a repetition rate of 2.57 GHz utilizing a SML QDs for gain and a QW semiconductor saturable absorber mirror (SESAM) structure for passive mode-locking was demonstrated by Hoffmann et al. for an emission around 1060 nm [21]. Several gain chips incorporating 35 to 39 SML QDs (9 cycled InAs/GaAs (0.2ML/0.2ML)) were used to demonstrate second harmonic generation of 514, 590 and 624 nm visible light in the green, red and yellow. In the case of yellow SHG, a multi-gain cavity arrangement with two VECSEL gain chips, having a fundamental emission around 6 W at 1180 nm, was used for the generation of 2.5 W continuous wave output at 590 nm. The multi-gain setup was required due to the very low gain and high sensitivity of the QDs towards losses introduced by the nonlinear conversion [22]. Improvements have been made especially on the minimization of the spacer thicknesses between two adjacent QD-layers. In all reported cases the gain layers were placed at the electric field antinodes for resonant periodic gain. For a maximal modal gain, multiple QD-layers were placed at these antinodes, where the total number of implemented QD-layers is dependent on the spacer thickness between neighbouring dot layers, as the subcavity dimensions are restricted by the absorption length of the pump light. The first journal publications in 2008 used 45 nm thick spacers (S-K) in order to avoid strain induced coupling between the QD-layers, which would lead to a gradual increase in QD-sizes of the successively grown QD-layers within a group and the device was restricted to 21 gain layers. In recent work, however, the separator thickness could be reduced to 6-10 nm allowing the implementation of up to 39 QD-layers and output power up to 4 W from a single device at 1180 nm was reported. Similar achievements have been made for SML QD devices [16,18].

Year & Citation	# of QD-sheets	QD type	QD compound	Heat removal	Laser λ / nm	Power P / W	Slope eff. η / %
2005 [5]	17	S-K	InAs QD in $In_{0.25}Ga_{0.75}As$ QW	Thin.	1270 / ~1300(f)	0.120 / 0.005(f)	5/ N/A
2008 This work	**13**	**SML**	**InAs / GaAs (0.5ML/2.3 ML)**	**D**	**1040**	**0.5**	**17**
2008 [16]	13	SML	InAs/GaAs (0.5ML/2.3 ML)	D	1040	1.4	12.4
2008 [16](a)	13	S-K	$In_{0.65}Ga_{0.35}As$ (2.7 ML)	D	1040(a)	0.3(a)	6
2008 [16]	10	SML	InAs/GaAs (0.25ML/2.3 ML)	D	950	0.5	4
2008 [16]	21	S-K	$In_{0.65}Ga_{0.35}As$ (2.7 ML)	D	1210	0.3	2
2009 [18]	35	SML	9 x InAs/GaAs (0.2ML/0.2ML)	D	1030	4.35	22
2009 [25] (b)	35	SML	9 x InAs/GaAs (0.2 ML/0.2ML)	Non	1060	0.0274*	N/A
2009 [26] (b)	35	SML	9 x InAs/GaAs (0.25 ML/0.33ML)	Non	1053	0.022*	N/A
2010 [20]	12	S-K	InAs QD in $In_{0.15}Ga_{0.85}As$ QW	Inv.	1250	3.25	11
2010 [19,22] (c)/(d)	39	SML	9 x InAs/GaAs (0.2 ML/0.2ML)	D	1180(c)/ 590(d)	6(c)(e)/ 2.5(d)	14(e)
2011 [27,28]	35	SML	9 x InAs/GaAs (0.2 ML/0.2ML)	D	1040/ 514(d)	6/ 2(d)	29
2011 [27,29]	39	SML	9 x InAs/GaAs (0.2 ML/0.2ML)	D	1260/ 624(d)	1.6/ 0.33	7

Table 3-2 Summary of reported InGaAs quantum dot based semiconductor disk laser devices for emission in the range between 900 nm and 1.3 µm. S-K and SML stand for QDs grown in the Stranski-Krastanow and Sub-monolayer regime. D, Non, Thin. and Inv. depict thermal management via liquid capillary bonded intra-cavity diamond heatspreader (D), no measures taken (Non), thinned substrate (Thin.) and inverted growth with removed substrate (Inv.) respectively. (a) excited state emission, (b) mode-locked; *pulse power, (c) ground state emission, (d) used for SHG, (e) dual gain chip and (f) VCSEL pumped.

The publication by Albrecht et al. [20] seems to contradict the trend for more QD layers as this group used only 12 layers of InAs QDs and placed only one single QD-layer at each antinode. They were able to demonstrate 3.25 W of fundamental emission at 1.25 µm, which is comparable to InGaNAs/GaAs QW VECSELs [23] and offers a good alternative to the incorporation of dilute Nitride. These quantum dots were imbedded in 7 nm $In_{0.15}Ga_{0.85}As$ quantum wells and utilized the

dot-in-a-well scheme for improved carrier trapping. This, together with the improved enhancement due to the excellent alignment of each QD-layer with the RPG and a stronger subcavity field due to the missing intra-cavity heatspreader might explain the good performance. It also shows that QDs can be used to overcome the strain induced limitations of QWs for emission above 1180 nm up to 1370 nm. A summary of these achievements in chronological order can be found in Table 3-2. Except for the publication of InP QDs emitting in the visible red around 730 nm (Chapter 4), all results are made for In(Ga)As QDs. Rapid progress has been made in the development of QD based VECSEL devices. The first structures as reported here were all designed to be resonant at the emission wavelength [16]. This had the advantage of a low pump threshold, important for a first laser demonstration. However, with the very large and flat spectral bandwidth of QDs (see Fig. 3-2), an anti-resonant design could allow very broad wavelength tuning, exceeding that of QWs [24]. This result suggests that VECSEL devices with an anti-resonant subcavity would experience an optimised thermal stability.

VECSEL devices based on In(Ga)As QDs have a few disadvantages in comparison to their QW counterparts. Their current wavelength coverage (0.95-1.3 μm) corresponds in a wide range with that of InGaAs QWs (0.92-1.18 μm). QW structures outperform QDs in spectral regions covered by both. Despite these facts the very fast improvement curve of the laser performance during the first three years of their existence are very promising. Commercial companies, providing the growth for several of the mentioned research groups in Table 3-2 demonstrate as well the economic potentials for QD based VECSELs.

References

1. T. D. Germann, A. Strittmatter, J. Pohl, U. W. Pohl, D. Bimberg, J. Rautiainen, M. Guina, and O. G. Okhotnikov, "High-power semiconductor disk laser based on InAs/GaAs submonolayer quantum dots," Applied Physics Letters **92**, 101123 (2008).

2. T. D. Germann, A. Strittmatter, J. Pohl, U. W. Pohl, D. Bimberg, J. Rautiainen, M. Guina, and O. G. Okhotnikov, "Temperature-stable operation of a quantum dot semiconductor disk laser," Applied Physics Letters **93**, 051104-3 (2008).

3. N. Ledentsov, D. Bimberg, F. Hopfer, A. Mutig, V. Shchukin, A. Savel'ev, G. Fiol, E. Stock, H. Eisele, M. Dähne, D. Gerthsen, U. Fischer, D. Litvinov, A. Rosenauer, S. Mikhrin, A. Kovsh, N. Zakharov, and P. Werner, "Submonolayer Quantum Dots for High Speed Surface Emitting Lasers," Nanoscale Research Letters **2**, 417-429 (2007).

4. J. A. Lott, A. R. Kovsh, N. N. Ledentsov, and D. Bimberg, "GaAs-Based InAs/InGaAs Quantum Dot Vertical Cavity and Vertical External Cavity Surface Emitting Lasers Emitting Near 1300 nm," in *Lasers and Electro-Optics, 2005. CLEO/Pacific Rim 2005. Pacific Rim Conference on*, (2005), pp. 160-161.

5. A. Strittmatter, T. D. Germann, J. Pohl, U. W. Pohl, D. Bimberg, J. Rautiainen, M. Guina, and O. G. Okhotnikov, "1040 nm vertical external cavity surface emitting laser based on inGaAs quantum dots grown in Stranski-Krastanow regime," Electronics Letters **44**, 290-291 (2008).

6. D. Bimberg, M. Grundmann, and N. N. Ledentsov, *Quantum Dot Heterostructures*, D. Bimberg, ed., (John Wiley & Sons Ltd, Baffins Lane, Chichester, West Sussex PO 19 1UD, England, D-69469 Weinheim, Germany, 1999).

7. A. C. Tropper, H. D. Foreman, A. Garnache, K. G. Wilcox, and S. H. Hoogland, "Vertical-external-cavity semiconductor lasers," Journal of Physics D: Applied Physics **37**, R75-R85 (2004).

8. Y. Dai, J. Fan, Y. Chen, R. Lin, S. Lee, and H. Lin, "Temperature dependence of photoluminescence spectra in InAs/GaAs quantum dot superlattices with large thicknesses," J. Appl. Phys. **82**, 4489 (1997).

9. S. Giet, "Grating-Controlled Infra-Red Vertical External Cavity Surface Emitting Lasers," (2008).

10. Z. L. Liau, "Semiconductor wafer bonding via liquid capillarity," Applied Physics Letters **77**, 651-653 (2000).

11. A. J. Kemp, G. J. Valentine, J. M. Hopkins, J. E. Hastie, S. A. Smith, S. Calvez, M. D. Dawson, and D. Burns, "Thermal management in vertical-external-cavity surface-emitting lasers: finite-element analysis of a heatspreader approach," Quantum Electronics, IEEE Journal of **41**, 148-155 (2005).

12. www.diamond-materials.com, Diamond Materials, "The CVD diamond booklet," 2008, Diamond Materials GmbH

13. A. J. Kemp, A. J. Maclean, J. E. Hastie, S. A. Smith, J. M. Hopkins, S. Calvez, G. J. Valentine, M. D. Dawson, and D. Burns, "Thermal lensing, thermal management and transverse mode control in microchip VECSELs," Applied Physics B: Lasers and Optics **83**, 189-194 (2006).

14. M. Kuznetsov, F. Hakimi, R. Sprague, and A. Mooradian, "Design and characteristics of high-power (>0.5-W CW) diode-pumped vertical-external-cavity surface-emitting semiconductor lasers with circular TEM_{00} beams," Selected Topics in Quantum Electronics, IEEE Journal of **5**, 561-573 (1999).

15. R. L. Sellin, I. Kaiander, D. Ouyang, T. Kettler, U. W. Pohl, D. Bimberg, N. D. Zakharov, and P. Werner, "Alternative-precursor metalorganic chemical vapor deposition of self-organized InGaAs/GaAs quantum dots and quantum-dot lasers," Applied Physics Letters **82**, 841-843 (2003).

16. T. D. Germann, A. Strittmatter, U. W. Pohl, D. Bimberg, J. Rautiainen, M. Guina, and O. G. Okhotnikov, "Quantum-dot semiconductor disk lasers," Journal of Crystal Growth **310**, 5182-5186 (2008).

17. F. Klopf, S. Deubert, J. P. Reithmaier, and A. Forchel, "Correlation between the gain profile and the temperature-induced shift in wavelength of quantum-dot lasers," Applied Physics Letters **81**, 217-219 (2002).

18. M. Butkus, K. G. Wilcox, J. Rautiainen, O. G. Okhotnikov, S. S. Mikhrin, I. L. Krestnikov, A. R. Kovsh, M. Hoffmann, T. Südmeyer, U. Keller, and E. U. Rafailov, "High-power quantum-dot-based semiconductor disk laser," Opt. Lett. **34**, 1672-1674 (2009).

19. J. Rautiainen, I. Krestnikov, M. Butkus, E. U. Rafailov, and O. G. Okhotnikov, "Optically pumped semiconductor quantum dot disk laser operating at 1180 nm," Opt. Lett. **35**, 694-696 (2010).

20. A. R. Albrecht, T. J. Rotter, C. P. Hains, A. Stintz, J. V. Moloney, K. J. Malloy, and G. Balakrishnan, "Multi-watt 1.25 μm quantum dot VECSEL," Electronics Letters **46**, 856-857 (2010).

21. M. Hoffmann, Y. Barbarin, D. Maas, M. Golling, I. Krestnikov, S. Mikhrin, A. Kovsh, T. Südmeyer, and U. Keller, "Modelocked quantum dot vertical external cavity surface emitting laser," Applied Physics B: Lasers and Optics **93**, 733-736 (2008).

22. J. Rautiainen, I. Krestnikov, J. Nikkinen, and O. G. Okhotnikov, "2.5 W orange power by frequency conversion from a dual-gain quantum-dot disk laser," Opt. Lett. **35**, 1935-1937 (2010).

23. O. G. Okhotnikov, D. Bimberg, M. Guina, D. Burns, S. Calvez, M. D. Dawson, J. E. Hastie, J.-M. Hopkins, A. J. Kemp, U. Keller, M. Kuznetsov, N. Laurand, D. J. H. C. Maas, A. Mooradian, U. W. Pohl, M. Rattunde, B. Rösener, A. Shchergrov, T. Südmeyer, A. Tandon, J. Wagner, and G. Yoffe, *Semiconductor*

Disk Lasers. Physics and Technology, O. G. Okhotnikov, ed., (WILEY-VCH Verlag GmbH & Co. KGaA, Weinheim, Weinheim, 2010).

24. M. Butkus, C. J. Hamilton, G. P. Malcolm, I. Krestnikov, D. Livshits, and E. U. Rafailov, "Wavelength tuning in quantum dot semiconductor disc lasers," in *Semiconductor Laser Conference (ISLC), 2010 22nd IEEE International*, (2010), pp. 79-80.

Chapter 4:

InP/GaInP/AlGaInP quantum dot based VECSELs

This chapter describes the design and characterisation of the first InP QD VECSEL structures. Section 1 gives an introduction to this chapter and compares InP QDs with their more mature In(Ga)As counterparts, which were used for the demonstration of the first QD VECSELs discussed in Chapter 3. A summary of wafers grown for this project is given in Section 4.2. The structure design and growth parameters are discussed in Section 4.3. Laser performance, reflectivity, surface PL, edge PL, time resolved PL decay, but also surface morphology and structural examination in form of secondary electron microscopy, cathodoluminescence and transmission electron microscopy imaging are given in Section 4.4. A VECSEL structure, which was not able to achieve laser emission was also used as a semiconductor saturable absorper (SESAM) mirror inside a Ti:sapphire laser for passive mode locking [1], is briefly described in Section 4.5.

This project is a collaboration with Cardiff University, and the EPSRC National Centre for III-V Technologies at the University of Sheffield. Research on edge emitting laser devices based on InP QDs was undertaken by the collaborating groups prior to the current project. These two groups reported a record low room temperature threshold density of 190 A/cm^2 [2] for electrically-injected laser diodes emitting around 740 nm, utilising InP/$Ga_{0.51}In_{0.49}P$ dots-in-a-well, further referred to as QDs. The dot-in-a-well scheme combines the good carrier trapping efficiency of QWs with the high emission efficiency of QDs and is commonly used to increase the gain of QD structures at elevated temperatures [3,4]. Their expertise on the InP QD fabrication and research was combined in this project with our experience on QW based VECSEL structures in general and on $Ga_yIn_{1-y}P/(Al_xGa_{1-x})_{0.51}In_{0.49}P$ QW VECSELs in particular [5-7]. The motivation was to extend the emission wavelength

of the VECSELs based on AlGaInP towards 800 nm in order to fill the existing gap in wavelength coverage, present for this laser type between GaInP and GaAs QWs. Human tissue has a low absorption and low autofluorescence in this spectral range, called the medical absorption window. Light in this spectral window is suitable for example in medical applications such as photodynamic therapy, sensing and biophotonics [8].

4.1 AlGaInP material composition

4.1.1 Spectral coverage of $Ga_yIn_{1-y}P$ QWs

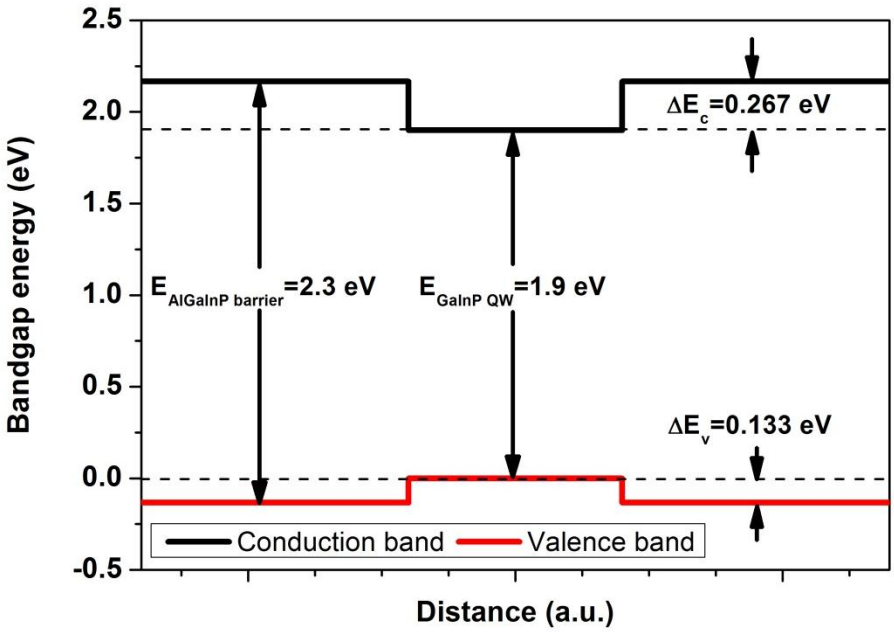

Fig. 4-1 Bandgap energy diagram of a $Ga_yIn_{1-y}P$ QW imbedded into $(Al_xGa_{1-x})_{0.51}In_{0.49}P$ barriers with $y_{Ga} = 0.51$ and $x_{Al} = 0.6$, lattice matched to GaAs substrate. The offset between QW and barrier conduction and valence band energy is 2/3 and 1/3 respectively. Zero energy position is chosen to be the valence band edge of the QW.

Some of the important optical and mechanical properties of the $(Al_xGa_{1-x})_{0.51}In_{0.49}P$ material, lattice-matched to a GaAs substrate, such as refractive index and energy bandgap were already presented in Chapter 2. The bandgap energy range covered by

this compound spans from 1.90 eV (653 nm) to 2.3 eV (540 nm) for $x_{Al} = 0 - 0.6$, above which the transition becomes indirect [9] (see Fig. 2-2). The dependence of the transition energy on QW thickness and Gallium mole fraction, y_{Ga}, (which also introduces strain for $y_{Ga} \neq 0.51$) was presented in (Fig 2-11). The energy bandgap offset of the conduction and valence band ground state of a nearly lattice-matched $Ga_yIn_{1-y}P$ QW with respect to an $(Al_xGa_{1-x})_{0.51}In_{0.49}P$ matrix is 2/3 to 1/3 respectively [10]. Fig. 4-1 represents this bandgap dependence for clarification, where a $Ga_{0.51}In_{0.49}P$ QW is buried within $(Al_{0.6}Ga_{0.4})_{0.51}In_{0.49}P$ barriers. Introduction of slightly compressively strained $Ga_yIn_{1-y}P$ QW together with thickness variation enables wavelength coverage from 640-690 nm in VECSEL structures. While tensile strain would extend the emission towards shorter wavelengths, it is not used for vertically-emitting devices due to the predominantly TM polarised nature of the emitted light. The upper wavelength limit is set by the maximum allowed lattice mismatch between QWs and the matrix, above which cracks result in deterioration of the structure (see Section 2.4.2). A possible way to overcome the strain related limitations and extend the emission wavelength of $(Al_xGa_{1-x})_{0.51}In_{0.49}P$ based VECSELS is the use of InP QDs as gain medium.

4.1.2 InP quantum dots

The implementation of Stranski-Krastanow type InP QDs grown on an $(Al_xGa_{1-x})_{0.51}In_{0.49}P$ matrix, with a nominal QD-layer thickness in a range of 2 - 15 ML allows the fabrication of devices emitting from 640-680 nm (covered by the matrix material)[11,12] to 760 nm (covered by a $Ga_yIn_{1-y}P$ QW)[2,13], see Fig. 4-6 top right, for an illustration of a dot in a well layer. The emission wavelength and other properties, such as size and emission efficiency depend on the growth matrix composition x_{Al}, the capping layer composition y_{Ga}, the nominal layer thickness/growth time, III-V ratio, growth temperature, substrate surface orientation and other parameters, some of which are shown in Table 4-1 by trend. The emission

QD growth variable	Variation	Effect	Ref
Growth time on growth matrix $(Al_xGa_{1-x})_{0.51}In_{0.49}P$	Increase from 7.5-22.5 ML @ 650 °C for x_{Al} = 0 & 0.6	Dot density decrease, Dot height increase, Emission wavelength blue-shift,	[11]
Growth temperature T_{growth}	Increase from 650-710 °C	Decrease in dot density, Increase in dot height. Emission wavelength blue-shift, PL peak narrowing	[14]
Growth matrix and capping layer composition $(Al_xGa_{1-x})_{0.51}In_{0.49}P$	Increasing x_{Al} mole fraction from 0 to 1	Highest dot density at x_{Al} = 0.15, Dot density decreasing until x_{Al} = 0.5, Dot density increasing until x_{Al} = 1.0, Strongest PL signal intensity x_{Al} = 0.2, Emission wavelength blue-shift, PL peak emission wavelength follows the trend of the growth matrix energy bandgap with x_{Al} composition	[14]
Capping $Ga_yIn_{1-y}P$ QW composition for a fixed growth matrix $(Al_{0.3}Ga_{0.7})_{0.51}In_{0.49}P$	Increasing y_{Ga} mole fraction	Emission wavelength blue-shift, Increased emission intensity due to strain balancing by tensile strained QWs.	[15]

Table 4-1 Overview of different growth parameters and the impact on InP QD properties.

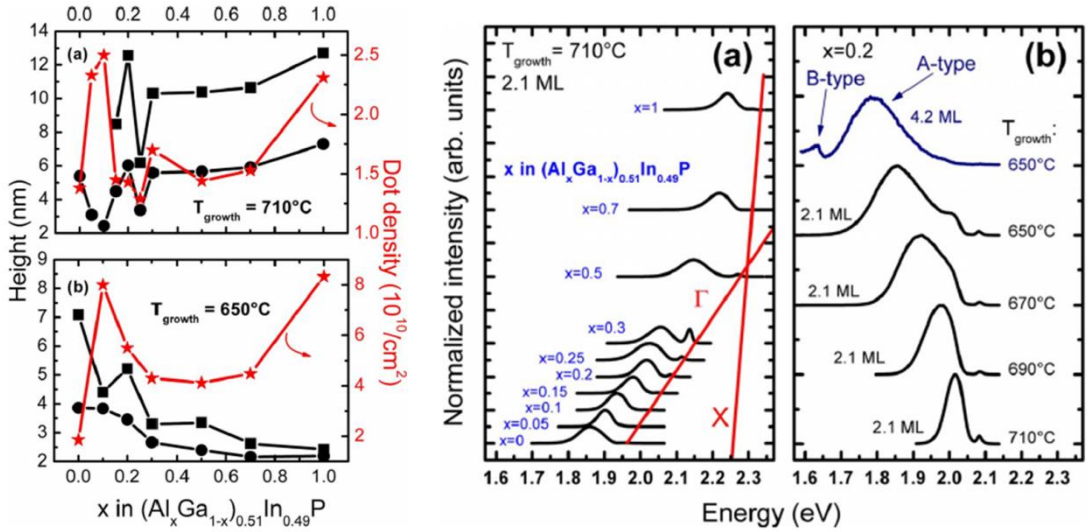

Fig. 4-2 Dot density, height and peak PL emission wavelength in dependence on the Aluminium mole fraction x_{Al} of the growth matrix/barrier composition $(Al_xGa_{1-x})_{0.51}In_{0.49}P$. The rightmost picture illustrates the shape and emission wavelength behaviour of 2.1 ML thick InP QDs with growth temperature [14].

wavelength tends to increase with decreasing x_{Al} mole fraction and decreasing deposition time, as described in [11]. An increase of the growth temperature causes a blue shift and peak narrowing as can be seen in the rightmost graph of Fig. 4-2, taken from Schulz et al. [14]. This group also showed that the dot ensemble emission wavelength follows closely the trend of the matrix bandgap with Aluminium composition x_{Al} (Fig. 4-2 middle). This was caused by Al and Ga incorporation from

the matrix into InP QDs at the elevated temperatures around 710 ^{0}C. The highest dot density with a maximum PL emission intensity was found to occur around a matrix composition of $x_{Al} = 0.2$ (see Fig. 4-2 left). The same publication also shows a decrease in dot density for an increase in growth temperature from 650 ^{0}C to 710 ^{0}C for InP QDs with a nominal layer thickness of 2.1 ML (the standard size of InP QDs), grown on the same optimum matrix composition of $x_{Al} = 0.2$. In case of the 2.1 ML thick InP QDs in the present work, which were grown on top of an $(Al_{0.3}Ga_{0.7})_{0.51}In_{0.49}P$ matrix and capped by an 8 nm thick $Ga_yIn_{1-y}P$ QW a change in emission wavelength with Ga mole fraction y_{Ga} was detected from PL measurements of different calibration growth structures, as can be seen in Fig. 4-3. With increasing y_{Ga} increases the misfit strain, resulting in a tensile strained QW, which partly compensates for the compressive strain of the QDs. This causes a decrease in peak PL emission wavelength from 740 nm for a lattice-matched QW composition of $y_{Ga} = 0.51$ towards 700 nm for a tensile strained case $y_{Ga} = 0.56$. The PL intensity

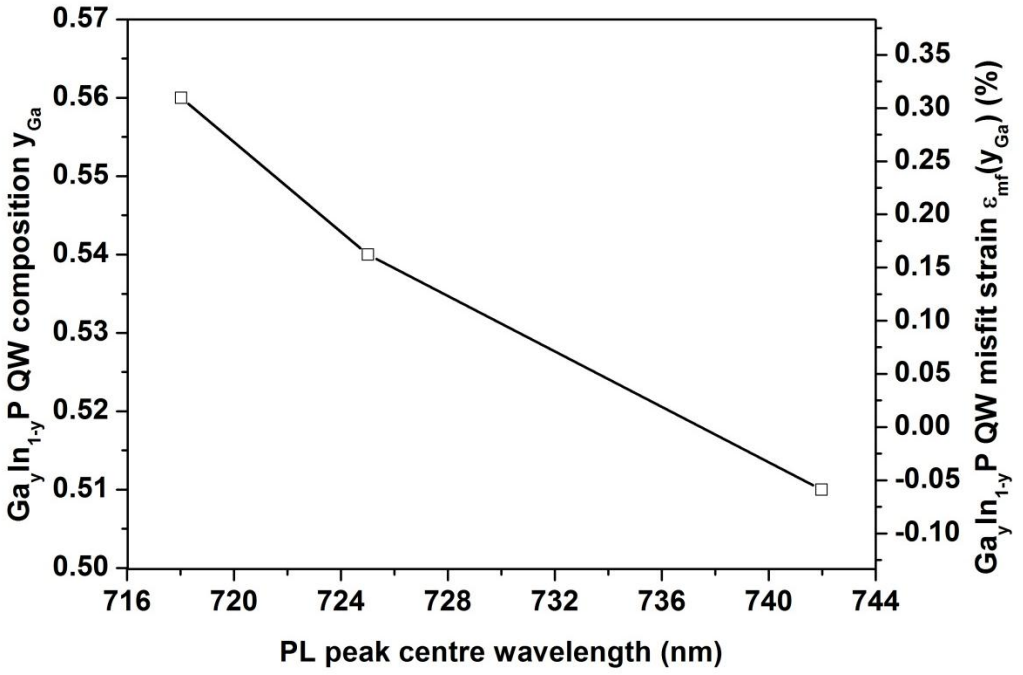

Fig. 4-3 Photoluminescence peak centre emission of the InP/$Ga_xIn_{1-x}P$ QD ensemble in dependence on the Ga mole fraction, which corresponds to the QWs misfit strain.

is thought to increase in this case, indicating an improved QD quality (oral communication by Dr. Andrey Krysa, grower at the EPSRC National Centre for III-V Technologies at the University of Sheffield). More details on the growth conditions of these calibration growth samples can be found in the following Section 4.2.

From this discussion it is possible to conclude, that both the matrix and QW composition have an effect on the emission wavelength and efficiency of the InP QDs. The increasing y_{Ga} tends to improve the emission efficiency of the QDs on the one hand. The caused emission wavelength blue-shift towards 700 nm, a wavelength very close to the strain related limit of $Ga_yIn_{1-y}P$ QWs, poses a problem on the other hand with regard to the target of the current project: The extension of the wavelength coverage range of $(Al_xGa_{1-x})_{0.51}In_{0.49}P$ based VECSEL structures towards 800 nm, thus one might have to compromise. With respect to the maximum carrier confinement in the QD, thus highest thermal stability, a matrix composition of $x_{Al} = 0.6$, close to the cross-over point of the direct to indirect transition (see Section 2.2) would be desirable, but with regard to the decreased dot density, this is not an option at the current stage. The lower x_{Al} (increased Ga) content of the matrix composition, which also serves as the pump absorbing barrier, is important from a structure design perspective as it results in an increased absorption coefficient at the pump wavelength. This restricts the subcavity dimensions, reducing the number of field antinodes and thus the number of gain layers, affecting the maximum achievable modal gain. The number of dot layers that can be incorporated in the gain region is also dependent on the required minimum distance between QD-layers within a group (see Section 4.3). Strain-induced structural coupling originating from already buried dots affects the formation of subsequent QD-layers [16] and can cause formation of non-coherently strained QDs (see Qiu et al. [17], Fig 3c). The separation layer allows the successive growth of non-correlated QDs. Its thickness defines the maximum number of QD-layers that can be accommodated at on single field antinode. The InP dot density is also influenced by the dot size and growth parameters.

4.1.3 Comparison with InAs QD based VECSELs

The estimated dot density of InP QDs is in the range of 10^9-10^{10} cm^{-2} [14,18,19], which is more than an order magnitude lower than for S-K type InAs dots, having densities in the range 10^{11} cm^{-2} [20]. It defines the areal coverage within the growth plane and thus the achievable modal gain. Advances in the fabrication of InAs QD layers allowed the growth of successive dot layers with very thin spacers (< 10 nm, [21]), leading to improved laser performance due to the ability to incorporate an increasing number of InAs QD-layers and was discussed in Section 3.4. This hasn't been achieved for InP QD structures so far. A further advantage of InAs QDs imbedded in GaAs with respect to the current material composition is the lower absorption coefficient at the standard pump wavelength (808 nm for InAs/GaAs vs. 532 nm for InP/AlGaInP QD structures), allowing a longer subcavity with the accessibility of more field antinodes. This enables the implementation of more QD-layers. Furthermore, $Al_xGa_{1-x}As/Al_yGa_{1-y}As$ DBRs can be fabricated to be non-absorptive for both the pump and the emission wavelength in the wavelength regions covered by InAs QD devices, improving thermal management. AlGaAs can also be applied as a transparent window/confinement layer, keeping photo generated carriers from recombination at the surface. All these arguments illustrate the better material properties of InAs/GaAs structures and indicate more flexibility in design parameters.

One advantage of InP QDs is a bimodal size distribution of two distinct dot sizes, as reported in [18,22,23], having the potential of a very broad gain bandwidth and thus temperature stable wavelength emission. In contrast to InAs based QD VECSELs, there is currently no competing QW-based VECSEL in the spectral range above 700 nm. In the case of InAs QDs the wavelength range beyond 1180 nm (upper limit of InGaAs QWs) can be accessed by other QW based material systems (e.g. GaInNAs QWs or wafer-fused devices based on InAlGaAs QWs) with comparable or better performance. Laser devices reported here perform in a wavelength range from 716-755nm with a circularly-symmetric TEM_{00} output beam. They are widely tunable in a range of 26 nm and output powers in the tens of mW so far.

4.2 Summary of grown structures

Wafer	No. of Dwells	λ_{QD} (nm)	Laser action	T_{QD} (°C)	t_{QD} (s)	QW y_{Ga}	th_{QW} (nm)	B1/B2/C x_{AL}	Remarks
MR2482	8 x 3	755	No	700	0.9	0.51	8	0.3/0.6/0.6	Used as SESAM in Ti:sapphire laser
MR2483	8 x 3	755	No	700	1.1	0.51	8	0.3/0.6/0.6	+ QD-layer thickness
MR2484	7 x 3	755	No	700	0.9	0.51	8	0.3/no/no	
MR2598	7 x 3	740	N/A	710	0.9	0.51	8	0.3/no/0.6	Calibration growth
MR2603	7 x 3	740	No	710	0.7	0.51	8	0.3/no/no	
MR2604	7 x 3	740	No	730	0.9	0.51	8	0.3/no/no	
MR2609	7 x 3	740	Yes	730	0.9	0.51	8	0.3/no/0.6	No stable emission
MR2615	**7 x 3**	**740**	**Yes**	**710**	**0.9**	**0.51**	**8**	**0.3/no/0.6**	**Stable emission**
MR2617	7 x 3	740	Yes	710	0.9	0.51	8	0.3/no/no	No stable emission
MR2959	7 x 3	735	N/A	710	1.1	0.54	8	0.3/no/0.6	Calibration growth
MR2961	7 x 3	730	No	710	1.1	0.54	8	0.3/no/0.6	
MR2962	7 x 3	730	No	710	1.1	0.54	8	0.3/no/0.6	Corrected DBR position
MR2963	7 x 3	730	No	710	1.1	0.54	8	0.3/no/0.6	- B1 and C layer thickness
MR2964	7 x 3	730	No	710	1.1	0.54	8	0.3/no/0.6	+ B1 and C layer thickness
MR2965	7 x 4	730	No	710	1.1	0.54	8	0.3/no/0.6	

Table 4-2 Summary of grown VECSEL structures, with full structure detail given Appendix A.1. No. of Dwells and λ_{QD} stand for the incorporated QD-layer (dot-in-a-well) number and designed QD ensemble peak emission. T_{QD}, t_{QD} and th_{QW} are the growth temperature of the QD layers, the QD growth time and the QW thickness. y_{Ga} the Gallium mole fraction of the QW ($Ga_yIn_{1-y}P$), x_{Al} the Aluminium mole fraction in barrier 1 (B1), barrier 2 (B2) and the confinement (C) layer. The symbols + and – indicated increased or decreased layer thickness of the barrier & confinement layers.

Table 4-2 gives a summary of all wafers grown during the course of this project. Three growth sessions were undertaken, marked by MR248X, MR26XX and MR29XX. The structure designs to all the listed wafers in the table are included in the Appendix A.1. Wafers MR2598 and MR2959 are growth calibration structures. They consist of the complete active region but without the DBR. This enables the characterisation of the dot ensemble PL emission without modification by the subcavity. Wafer maps of the dot ensemble surface-PL for both wafers are presented in the Appendix A.2 and A.3. They show no considerable change of the PL peak position across large parts of the wafer. Differences in PL intensity are thought to be caused by a changing dot density across the wafer. Wafer mapping is a standard

procedure at the end of the fabrication process and used for a pre-examination, including surface PL (and reflectivity for complete VECSEL structures) measurement of the whole wafer. They are delivered together with the structures. Fig. 4-4 is the structure design of the most complicated structure MR2482 and is used here to illustrate the different barrier and carrier confinement layers B1, B2 and C, with their composition and position within the subcavity.

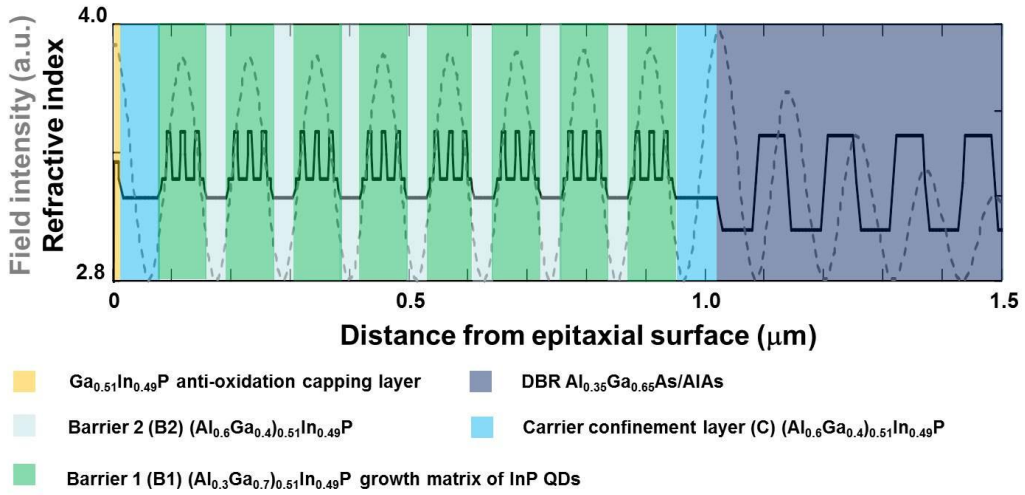

Fig. 4-4 Illustration of the most complicated structure design (MR2482) with the different barrier types (B1 & B2), the position of the carrier confinement layers confinement (C). The anti-oxidation capping layer at the top and parts of the DBR are also shown.

4.2.1 First growth campaign

The attempt during the first growth run was to implement as many QD layers into the active region as possible to maximise the modal gain. This was achieved by the use of two different barriers compositions B1 and B2 in wafers MR2482 and MR2483:

- B1 was $(Al_{0.3}Ga_{0.7})_{0.51}In_{0.49}P$ and used as spacer layers between QDs within a group and as growth matrix for the QDs.
- These layers were sandwiched by $(Al_{0.6}Ga_{0.4})_{0.51}In_{0.49}P$ being the composition of B2, which had lower absorption coefficient and helped to extend the active region thickness in order to incorporate a further antinode and thus 3 more QD-layers.

Growth conditions, such as growth time, growth temperature, composition and effective layer thicknesses for the QD-layer, capping QW, barrier (B1 & B2) and confinement (C) layers, were initially chosen based on previous experience with edge emitting devices by the collaborating groups [2,19,23-26]. Structures with two different barriers (B1 and B2), didn't permit liquid capillary bonding of a diamond heatspreader onto the sample surface, thus preventing laser tests. The best bonding behaviour of the first growth campaign was achieved with samples from wafer MR2484, the wafer with the simplest structure design, having only one single barrier type (B1) and no confinement layers. Although no laser action was achieved with any of these three wafers, the better bonding behaviour of wafer MR2484 led to the decision to use single barrier designs for the next growth campaign.

4.2.2 Second growth campaign

The second growth campaign included five wafers, three of which had the same basic design as MR2484 (MR2603, MR2604, MR2617) only the design wavelength was changed to 740 nm to match the QD ensemble PL peak position of the calibration growth MR2598. Wafers MR2609 and MR2615 included a confinement layer at either end of the active region. A thorough design description for wafer MR2615 is given in the following Section 4.3 (see also Fig. 4-6). A map of this wafer, including surface PL and reflectivity spectra at different positions across the wafer can also be found in Appendix A.4. The growth related layer thickness variations, visible in these spectra are caused by changes in the centre wavelength of the DBR reflectivity stopband and also of the designed resonances (subcavity and RPG). The position of the surface PL peak is an indication for the location of the subcavity resonance and can also be seen in the reflectivity spectrum, in form of the dip around the centre of the stopband. For this grown VECSEL structure the resonance is well matched with the mirror centre wavelength. The bonding ability of samples from all five wafers was comparable or better with respect to MR2484, but still considerably poorer than similar QW structures. Detaching of the diamond

heatspreader from the surface started usually immediately after bonding, limiting the bond time to maximum few hours. Despite the very limited time for laser tests, determined by the bonding duration, laser action was achieved. Samples from wafer MR2615 showed stable laser action. Unstable and short laser flashes where laser operation was achieved only for seconds, was demonstrated using samples from wafers MR2609 and MR2617. The laser results discussed in the following are all from cleaved (4 x 4 mm^2) samples of wafer MR2615. After these positive laser results a third growth campaign was undertaken in an attempt to improve the structure according to the findings discussed in the course of this chapter.

4.2.3 Third growth campaign

Wafers from the third growth campaign used the same basic laser design of wafer MR2615 with a variation in QD number per anti-node and a design wavelength around 730 nm. The intention behind the inclusion of three or four QDs per field antinode was to determine the effect of increased modal gain on the laser properties. The composition of the $Ga_yIn_{1-y}P$ QW (capping the InP QDs) was changed to a mole fraction of $y_{Ga} = 0.54$ as improved emission efficiency of the dots was expected (see also discussion above in Section 4.1.2). None of the tested structures from the third growth campaign allowed bonding of the diamond heatspreader and therefore no laser action was achieved with any of these samples. Microscopic imaging revealed a very rough surface morphology, covered with pyramidal features as can be seen in Fig. 4-5. A more thorough discussion on this matter is presented in Section 4.4.5. These features were present for all samples in every growth campaign. Despite all attempts to improve the QD growth and to match the QD ensemble peak emission better to the subcavity resonances during the last growth session, the surface roughness could not be improved. On the contrary it proved to be worse and it is believed that the nominal QD layer thickness was underestimated, which lead to the increased roughness. All this will be discussed in more detail below in the course of the characterisation of samples from wafer MR2615.

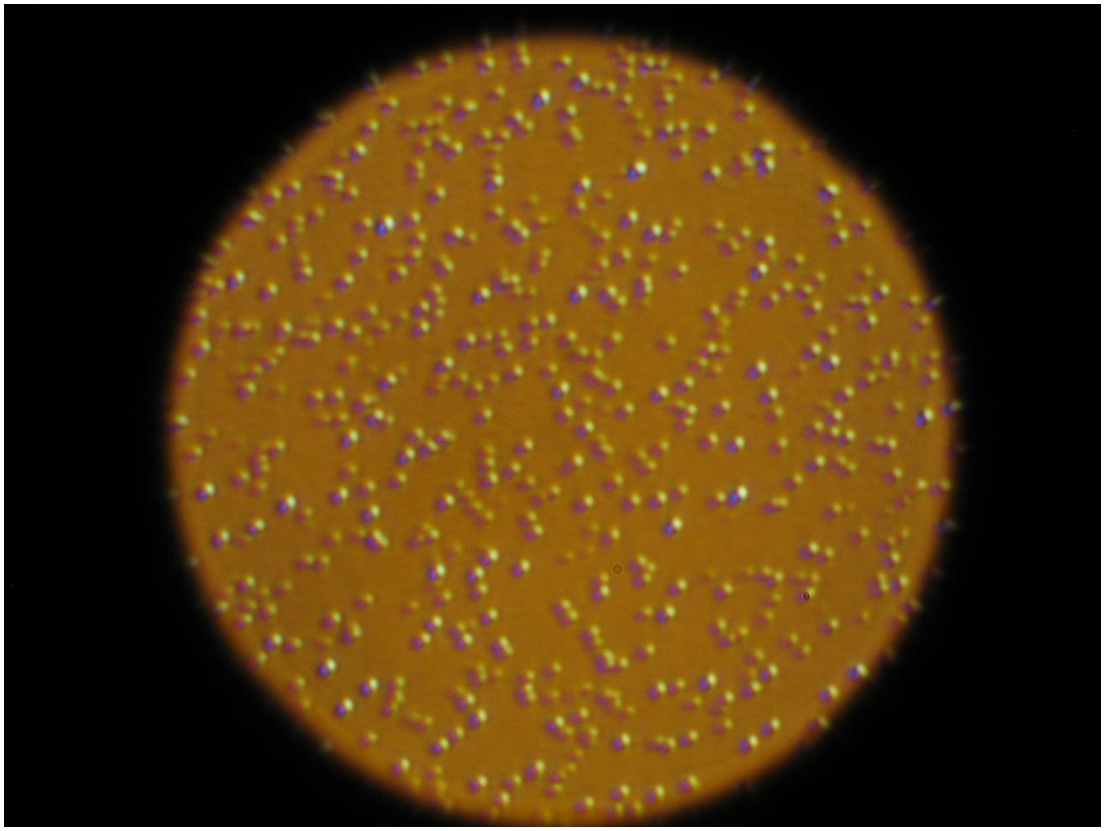

Fig. 4-5 Microscopic image showing the surface with a rough morphology for one sample from growth campaign three, preventing bonding of a diamond heatspreader to the surface for laser tests. The field of view diameter size is about Ø = 140 μm. Courtesy: Dr. Andrey Krysa, EPSRC National Centre for III-V Technologies at the University of Sheffield.

4.3 Design and growth

The InP QD based VECSEL structure (MR2615) was designed for emission around 740 nm; see Fig. 4-6 and Table 4-3 for a detailed description of the structure's design. Therefore the reflectivity stopband of the DBR, consisting of 40.5 repeats of $\lambda/4$-wavelength thick AlAs/$Al_{0.35}Ga_{0.65}As$ layer pairs with refractive indices of $n_{AlAs} = 3.05$ and $n_{AlGaAs} = 3.51$, was designed to be centred at 740 nm. The Al content of $x_{Al} = 0.35$ in the ternary DBR composition (as opposed to GaAs for maximum refractive index contrast) was used to prevent absorption of the signal field at the design wavelength. The description of the basic parameters of a DBR

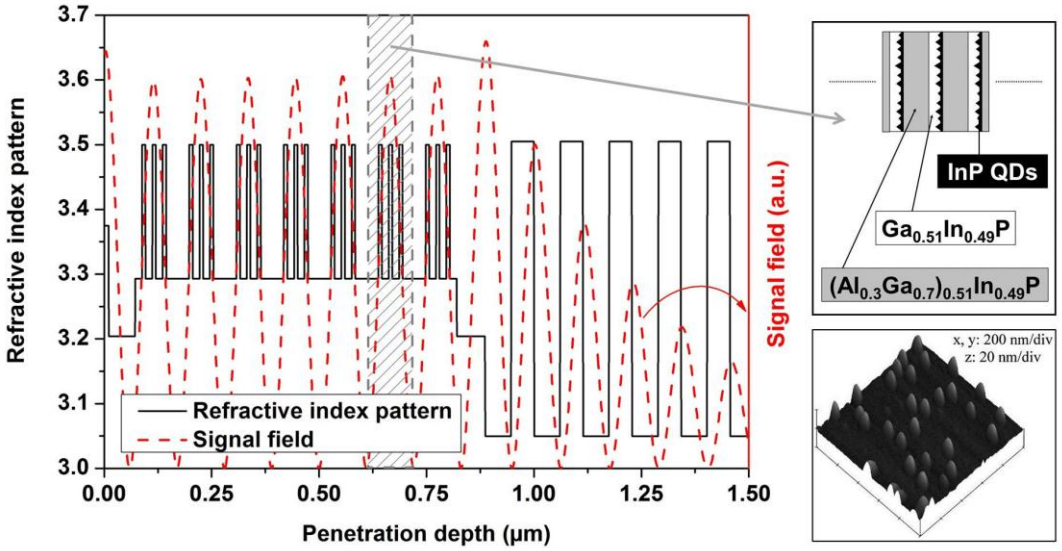

Fig. 4-6 Design of the InP QD VECSEL structure showing the refractive index pattern (black) and the signal field intensity of the generated signal at 740 nm (red dashed line). Each of the 7 field antinodes incorporate 3 InP/$Ga_{0.51}In_{0.49}P$ dot-in-a-well layers positioned for resonant periodic gain. A schematic of a QD group including the material compositions (grey hatched region) is depicted on the top right hand side. The inset at the bottom right hand side of the figure shows an AFM picture of the uncovered InP QDs [19].

structure was introduced in Section 2.2.2. The calculated total reflectivity stopband width was about 60 nm with a reflectivity of close to 99.99 % at the centre. With consideration to an expected lower modal gain of a QD-layer compared to a QW, the design focused on the optimisation of the available gain, including a low threshold power. Therefore, a resonant design, using the concept of RPG and a maximum amount of QD-layers (restricted by the total absorption length of the barriers at the pump wavelength) was chosen. No offset between room temperature photoluminescence and subcavity resonances, as described in Section 2.2.3.3, was used as a broad gain bandwidth of the QD ensemble was assumed. This was thought to cause a 'temperature stable' performance, similar to the reported results in ref. [27]; for InAs QD VECSELs at 1210 nm. The total length of the active region was slightly less than 900 nm, which corresponded to an estimated absorption of 98 % of the incident pump field at the pump wavelength of 532 nm (see Fig 2-5 in Section 2.2.3.1). This high percentage of absorption was required for efficient pumping and in order to avoid excessive heat introduction into the DBR region. The 3.5-λ thick active region was sandwiched by $(Al_{0.6}Ga_{0.4})_{0.51}In_{0.49}P$ layers for charge carrier confinement. A 10 nm thick $Ga_{0.51}In_{0.49}P$ capping layer concluded the structure,

preventing the underlying Al containing layers from oxidation. The active region consisted mainly of $(Al_{0.3}Ga_{0.7})_{0.51}In_{0.49}P$, which served three purposes:

- as pump absorbing barriers between the QD groups at the field antinodes,
- as matrix for the InP/$Ga_{0.51}In_{0.49}P$ QD growth,
- as separator between the QD-layers within in a group.

The $Ga_{0.51}In_{0.49}P$ QW, covering a QD-layer had a thickness of 8 nm, which was sufficient to cap the InP QD-layers (nominal thickness of 2.1 ML (6.2 Å)) and smoothen the interface after the three dimensional island growth. The optimum separator layer thickness was determined by Krysa et al. [19] to be 16 nm for the present QDs, restricting the number of gain layers at a field antinode to 3, maximum 4.

Description	Layer no.	Material composition	Mole fraction x_{Al}	Mole fraction y_{Ga}	Layer Thickness (nm)
Cap	20	$(Al_xGa_{1-x})_{0.51}In_{0.49}P$	0		10
Confinement	19	$(Al_xGa_{1-x})_{0.51}In_{0.49}P$	0.6		58
Barrier	18	$(Al_xGa_{1-x})_{0.51}In_{0.49}P$	0.3		16
Dot in a Well	17 x 6	6.2Å InP + $Ga_yIn_{1-y}P$ QW		0.51	8
Barrier	16 x 6	$(Al_xGa_{1-x})_{0.51}In_{0.49}P$	0.3		16
Dot in a Well	15 x 6	6.2Å InP + $Ga_yIn_{1-y}P$ QW		0.51	8
Barrier	14 x 6	$(Al_xGa_{1-x})_{0.51}In_{0.49}P$	0.3		16
Dot in a Well	13 x 6	6.2Å InP + $Ga_yIn_{1-y}P$ QW		0.51	8
Barrier	12 x 6	$(Al_xGa_{1-x})_{0.51}In_{0.49}P$	0.3		53
Dot in a Well	11	6.2Å InP + $Ga_yIn_{1-y}P$ QW		0.51	8
Barrier	10	$(Al_xGa_{1-x})_{0.51}In_{0.49}P$	0.3		16
Dot in a Well	9	6.2Å InP + $Ga_yIn_{1-y}P$ QW		0.51	8
Barrier	8	$(Al_xGa_{1-x})_{0.51}In_{0.49}P$	0.3		16
Dot in a Well	7	6.2Å InP + $Ga_yIn_{1-y}P$ QW		0.51	8
Barrier	6	$(Al_xGa_{1-x})_{0.51}In_{0.49}P$	0.3		16
Confinement	5	$(Al_xGa_{1-x})_{0.51}In_{0.49}P$	0.6		64
DBR	4	$Al_xGa_{1-x}As$	0		60
DBR	3 x 40	$Al_xGa_{1-x}As$	0.35		51.5
DBR	2 x 40	$Al_xGa_{1-x}As$	0		60
Buffer	1	GaAs	-		500
Substrate	0	n-GaAs	-		~350000

Table 4-3 Design of the VECSEL structure. The DBR consisted of 40.5 pairs AlAs/$Al_{0.35}Ga_{0.65}As$ and 7 repeats of the 3 InP/$Ga_{0.51}In_{0.49}P$ QDs within the active region. The $(Al_xGa_{1-x})_{0.51}In_{0.49}P$ layers are lattice matched to the GaAs substrate for a minimum strain build up in the structure. No attempt was undertaken for strain compensation.

In total 21 QD-layers grouped in 3 per field antinode for resonant periodic gain were integrated within these VECSELs. The structure was grown on top of a GaAs wafer with a diameter size of 2 inch by Metal Organic Chemical Vapour Deposition

(MOCVD) in a MR350 low-pressure (150 Torr) horizontal flow reactor, having a non-rotating susceptor. The (100) GaAs substrate was miss-oriented by 10 ° towards the <111> crystallographic direction in order to avoid superlattice ordering (i.e. Gallium- and Indium-rich monolayers in some of the (111) planes [28]) as best laser performance is achieved by disordered structures. A variation in the resonances and centre wavelength of the reflectivity stopband across the wafer was caused by the non-rotating susceptor (see Section 2.4). The size of the QDs indicated by the ensemble peak PL position was thought to remain constant across the wafer, where only the dot density changed in dependence on the effective layer thickness (see Appendix A.2). The whole VECSEL structure was grown at $T = 710\,°C$. This is in contrast to the optimum growth temperature of InP QDs, which is usually $T = 600\,^{0}C$ [18,29]. The elevated temperature was chosen in order to meet optimum growth conditions for the capping $Ga_{0.51}In_{0.49}P$ QWs [19], enabling the formation of smooth interfaces and a higher structure quality. The growth rates of the different material compositions applied for the wafer fabrication are given in Table 4-4.

Layer description	Growth rate	Material composition
Active region	~7.0 Å/s	$(Al_xGa_{1-x})_{0.51}In_{0.49}P$ for x_{Al} = 0, 0.3, 0.6
Gain material	~7.0 Å/s	InP/$Ga_{0.51}In_{0.49}P$ QD
DBR	~7.2 Å/s	AlAs
DBR	~10.2 Å/s	$Al_{0.35}Ga_{0.65}As$

Table 4-4 Growth rates for the different material compositions of the VECSEL structure.

4.4 Sample characterisation

In this section a discussion is given on laser performance and spectroscopic measurements of specific laser samples cleaved (4 x 4 mm^2 pieces) from wafer MR2615. Laser performance measurements are done for four samples denoted as sample A, B, C and D. Spectroscopic characterisation is shown representative for one particular sample from this wafer, denoted as sample C. Analysis of the other three samples A, B and D (showing slightly different resonance behaviour caused by the

growth related layer thickness variation) are also presented for comparison of the laser performance with respect to sample C. Samples A and C together with a piece from the growth calibration wafer MR2598 were probed during time-resolved PL measurements, analysing the effect of the subcavity resonance on the photon lifetime. Further growth quality characterisation by means of simultaneous cathodoluminescence/secondary electron microscopy (CL/SEM) imaging was carried out by the use of samples from wafers MR2484, MR2598, MR2615 together with a similar $Ga_yIn_{1-y}P/(Al_{0.6}Ga_{0.4})_{0.51}In_{0.49}P$ VECSEL containing 20 QWs (described in Hastie et al. [6]) for comparison. A piece of wafer MR2598 was also prepared for transmission electron microscopy (TEM), showing the active region.

4.4.1 Laser performance

All laser tests were carried out in a three mirror V-shaped cavity with the VECSEL gain structure acting as a high reflective (HR) plane end-mirror, as shown in Fig. 4-7. A curved HR folding mirror (FM) with a radius of curvature of 100 mm and a plane HR or output coupling end mirror (EM) with transmission 0.2 % concluded the external cavity. The cavity dimensions, i.e. the distances between VECSEL-FM (L1) and FM-EM (L2), were around 55 mm and 270 mm respectively in order to match the intra-cavity mode size to the incident pump beam with a diameter of $\emptyset_{pump} \sim 75 \mu m$. The samples were optically-pumped with powers up to 2.7 W at a wavelength of 532 nm, provided by a commercial frequency-doubled Nd:YVO_4 laser under an angle of incidence of less than $\theta_i < 30\,°$. For thermal management of the sample under pumped conditions, a 500-µm-thick, low birefringent, single crystal CVD grown diamond heatspreader [30] was liquid capillary bonded [31] to the intra-cavity surface of the VECSEL gain structure and clamped into a brass mount, kept at 7 °C by a chiller unit with a circulating water/glycol solution. The initial laser characterisation was carried out in a high finesse cavity using HR mirrors only. Power transfer measurements of the free-running laser were taken for the four

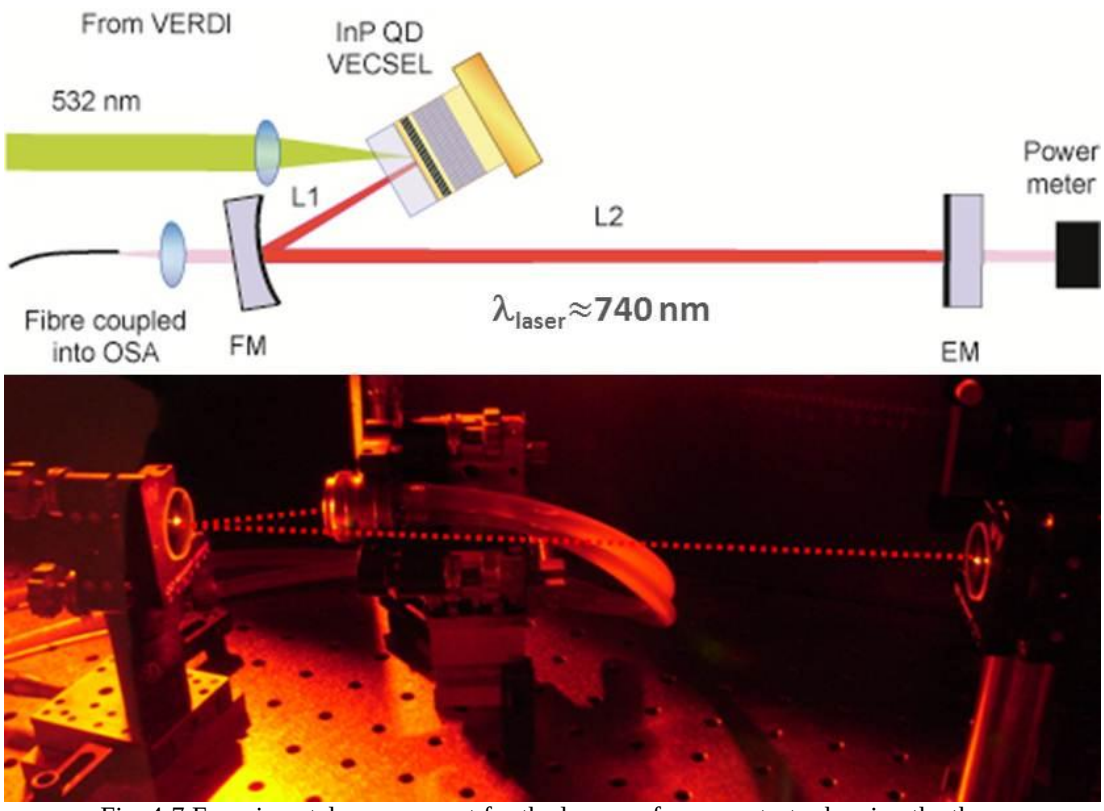

Fig. 4-7 Experimental arrangement for the laser performance tests showing the three mirror V-shaped cavity with the brass mount in the middle, holding the InP QD VECSEL structure the folding mirror (FM) and plane output coupling end mirror (EM). The intra-cavity beam is represented by the dashed red line. The 532 nm pump beam, coming from the left is not visible, because of the used filter.

samples A, B, C and D from wafer MR2615 and are shown in Fig. 4-8 left. The step in the curve of sample C, at ~0.5W incident pump power might be caused by mode hopping, due to the laser working in a higher transverse mode. These samples had laser emission wavelengths of 716, 729, 739 and 738 nm respectively, Fig. 4-8 right. The continuous laser emission spectra are about 4 nm in width and modulated by the etalon effect of the diamond heatspreader, producing characteristic multiple fringe spectra with a peak to peak separation of ~ 0.2 nm. The power transfer curves of samples A, C and D have similar values for maximum output power, differential efficiency and onset of thermal rollover. Sample B shows a poorer performance than the rest, believed to be related to the very short-lived bond of the diamond heatspreader, which posed a general handicap for the laser characterization of these structures. The reasons for this were already mentioned in Section 4.2 and will be discussed in more detail in Section 4.4.5. Samples C and D behaved very similarly in terms of pump power threshold, point of rollover and laser emission wavelength.

Sample A showed the highest laser threshold power and lowest emission wavelength. The maximum output power was also lower compared to the samples C and D, but thermal rollover occurred at nearly the same pump power as for the other three samples around ~1.5 W. Taking the free-running laser emission spectra of all four samples into account it seems that the pump threshold power may be related to the emission wavelength, and will be explained in Section 4.4.2.

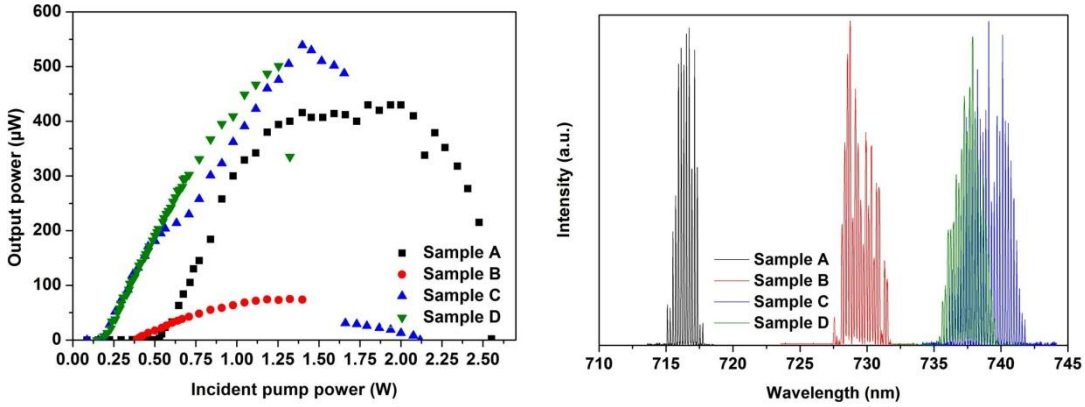

Fig. 4-8 Left: Power transfer curves for samples A (black squares), B (red dots), C (blue upwards triangles) and E (green downwards triangles). Right: Free running laser emission spectra (same colour coding for the samples).

A near diffraction limited beam propagation ratio $M^2 < 1.1$ was measured as can be seen in Fig. 4-9, left; the inset shows the beam profile close to its waist. The high finesse cavity arrangement minimised the cavity round trip losses and enabled broad wavelength tuning via the insertion of a 1 mm thick, rotatable Quartz birefringent filter (BRF). It was placed in the long cavity arm at Brewster's angle ($\theta_{Br} \cong 57°$ with respect to the cavity axis). The tuning ranges of samples B, C and D are represented in Fig. 4-9, right side and also shown in the spectra of Fig. 4-15. Sample A didn't permit the introduction of a BRF. Sample B had the narrowest tuning range of about 2.5 nm, followed by D and C with more than 17 and 25 nm respectively. A representative laser emission spectrum during the tuning experiments is shown in the inset of Fig. 4-9 on the right hand side. The emission peak has a resolution limited full width at half maximum $FWHM \approx 0.05\,nm$ and was measured by a fibre coupled near-IR optical spectrum analyser (Hewlett Packard - Optical Spectrum Analyser 86142A with a maximum spectral resolution of 0.05 nm).

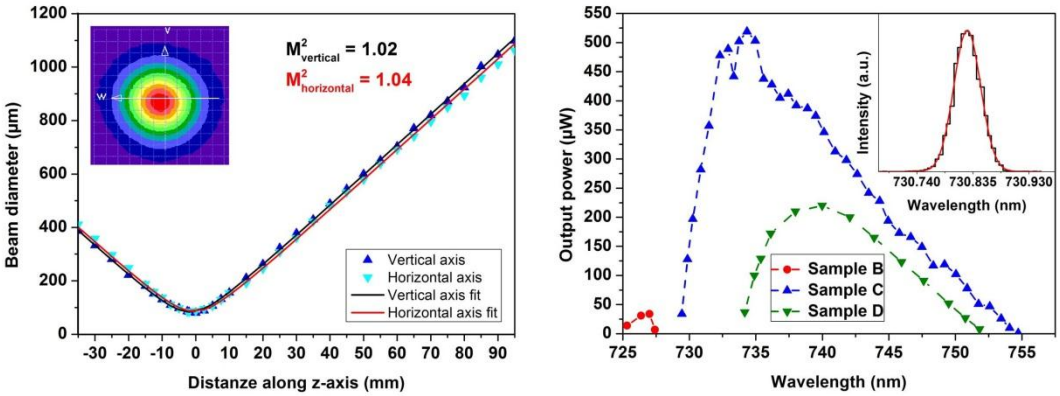

Fig. 4-9 Left: Measurement for the determination of the beam propagation factor. Inset: Beam profile close to the beam waist. Right: Tuning ranges of samples B (red dots), C (blue upward triangles) and D (green downward triangles). Inset: Laser emission spectrum during tuning for a 1 mm thick Quartz BRF inside the cavity.

Replacing the HR end mirror by a plane output coupler with 0.22 ± 0.2 % transmission, output powers of over 50 mW could be achieved as shown in Fig. 4-10. The power transfer behaviour of sample D for pump powers above 350 mW could not be explained so far. Table 4-5 presents a summary of the measured laser parameters, pump threshold, maximum output power and differential efficiency. The differential efficiency and the thermal rollover point were very similar in all cases with ~ 5 % and ~ 1.4 W respectively. The achievable output power therefore increased with decreasing pump threshold power or increasing laser emission wavelength.

MR2615 Samples	λ_{laser} **(nm)**	**High finesse cavity**				**0.2 % output coupling**		
		$\Delta\lambda_{tuning}$ (nm)	P_{thr} (mW)	P_{max} (µW)	η_{slope} (%)	P_{max} (mW)	P_{max} (mW)	η_{slope} (%)
A	716	-	500	430	0.06	632	29.0	4.65
B	730	2.1	390	75	0.01	397	44.0	5.05
C	739	25.3	185	539	0.05	232	50.3	5.70
D	738	17.6	190	501	0.06	225	15.7	6.76

Table 4-5 Summary of some measured laser performance parameters for the samples depicted in Fig. 4-8, Fig. 4-9 and Fig. 4-10. λ_{laser} - peak centre of the free running emission, P_{thr} - pump threshold power, P_{max} - maximum output power, η_{slope} - differential efficiency and $\Delta\lambda_{tuning}$ - total tuning range.

It was not possible to insert the BRF for wavelength tuning when the output coupling mirror was installed. Furthermore higher output coupling values (> 0.2 %) were also not permitted, most likely due to the low modal gain of the QD layers.

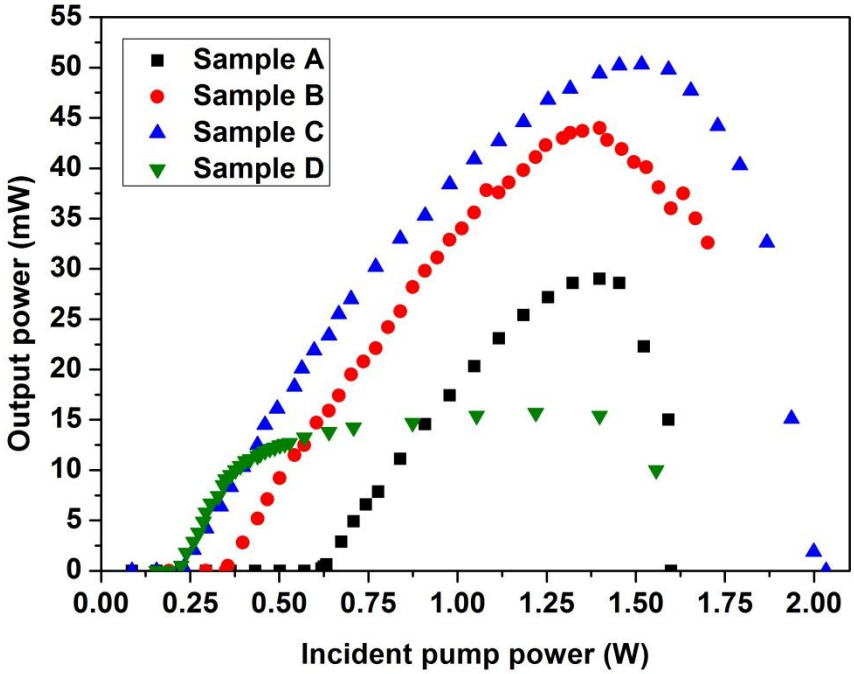

Fig. 4-10 Power transfer measurement for 0.2 % output coupling. Sample A (black squares), B (led dots), C (blue upward triangles), D (green downward triangles)

The implications of the overlap between the peak gain of the QD ensemble with the subcavity resonances are subject to the following Section, analysing the spectroscopic measurements.

4.4.2 Spectroscopic measurements

Reflectivity, surface and edge PL measurements for sample C were carried out over a temperature range of 20-80 °C. The description of the experimental arrangement was already given in Section 3.3 and is demonstrated in Appendix A.8. The only difference in this case was the use of a Silicon (Si) photodiode for signal detection in the visible wavelength range.

4.4.2.1 Reflectivity spectrum

The corresponding reflectivity spectra together with the calculated room temperature reflectivity, using the structure design model described in Chapter 2 and given in Appendix A.5 in full detail can be seen on the left side of Fig. 4-11. The thermal dependence of the absorption dip and the DBR stopband are presented on the right side of the same figure. The reflectivity stopband is centred at 747 nm, slightly red-shifted to the designed centre wavelength of 740 nm, and has a measured width of more than 50 nm. The thermal shift of $\sim 0.05\ nm/°C$ measured at the left edge of the reflectivity stopband (marked by a blue arrow) is caused by the optical thickness dependence (refractive indices and lattice constants) of the DBR's $Al_xGa_{1-x}As$ layers with temperature. The dependence of the subcavity resonance feature on temperature (dip in the reflectivity stopband near the centre wavelength, indicated by the red arrow) is $\sim 0.08\ nm/°C$. This shift is also caused by the refractive index change of the $(Al_xGa_{1-x})_{0.51}In_{0.49}P$ multilayer stack with temperature. The measured dip near the reflectivity stopband centre is not very pronounced, which is a possible indication that the peak position of the underlying QD ensemble might not be matched correctly to the RPG wavelength.

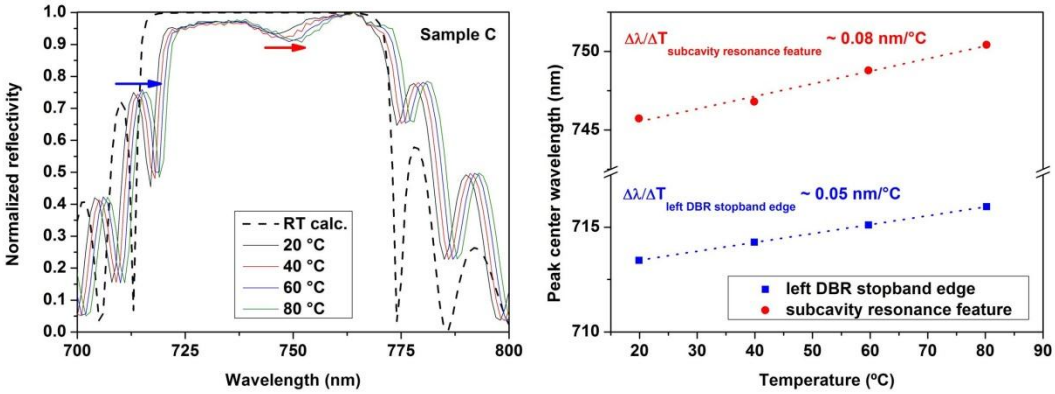

Fig. 4-11 Left: solid coloured lines depict measured reflectivity of sample C at 20, 40, 60 and 80 °C. The dashed black line shows the calculated room temperature reflectivity of the design, centred at 745 nm. Right: Shift of the subcavity resonance feature (red) and left DBR reflectivity stopband edge (blue) with temperature. The positions are also indicated by the red and blue arrows on reflectivity spectrum.

4.4.2.2 Edge photoluminescence

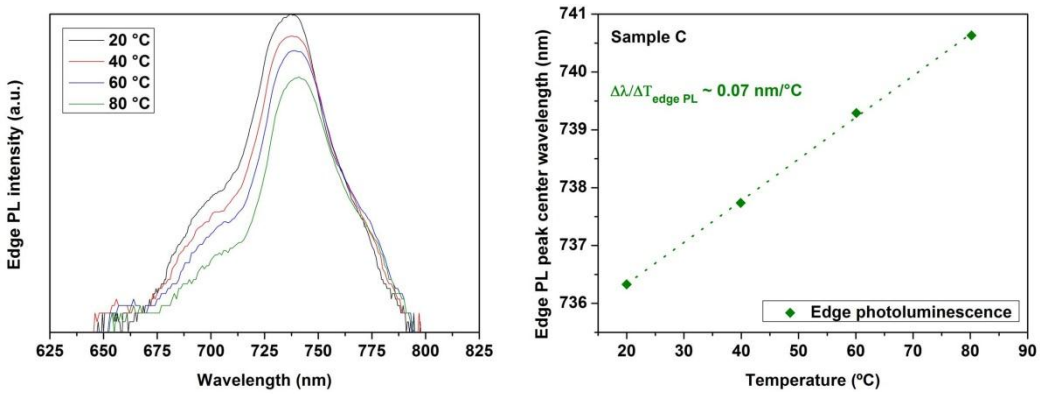

Fig. 4-12 MR2615 sample C. Left: Edge photoluminescence spectra on a logarithmic scale taken at 20, 40, 60 and 80 °C respectively are represented by the coloured solid lines. Right: Thermal shift ratio of the edge PL peak centre wavelength.

The measured edge PL of sample C from wafer MR2615 had a thermal dependence of $0.07 nm/°C$ (Fig. 4-12 left). This value corresponds very well with the shift of the subcavity resonance feature (dip at the centre of the DBR reflectivity stopband as shown in Fig. 4-11). This, together with the distorted shape of the PL peak could be an indication that the detected signal was modulated by the subcavity. Fig. 4-13 shows the measured edge PL signal of a sample from growth calibration wafer MR2598. This sample had no DBR as mentioned before due to which it was insured that modulation by the subcavity was avoided and the thermal shift of the underlying QD ensemble could be measured accurately. The measured peak centre wavelength shift with temperature is $0.13 nm/°C$. This is in good agreement with the thermal shift of the energy bandgap of $Ga_{0.52}In_{0.48}P$ QWs ($0.13\ nm/°C$) lattice-matched to GaAs, as was reported by Liu et al. [32]. It is also in good agreement with an experimentally determined value ($0.12\text{-}0.15\ nm/^0C$) of a similar QW based VECSEL structure with compressively strained (ε_{mf} = -0.5 %) $Ga_{0.45}In_{0.55}P$ QWs reported by Hastie et al [33]. Table 4-6 summarises the calculated (according to Liu et al. [32]) and measured temperature dependence of the energy bandgap for the different material compositions, present in the VECSEL subcavity.

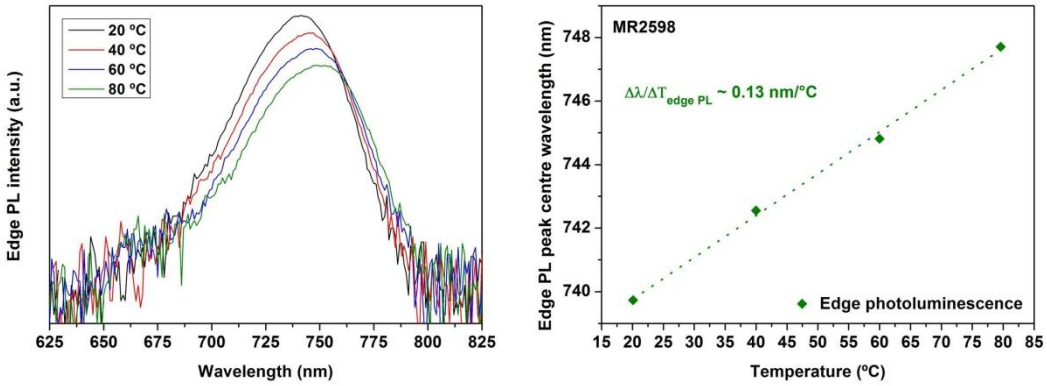

Fig. 4-13 Sample from MR2958. Left: Edge photoluminescence spectra on a logarithmic scale taken at 20, 40, 60 and 80 °C respectively are represented by the coloured solid lines. Right: Thermal shift ratio of the edge PL peak centre wavelength.

Material composition	Thermal dependence of $E_{gap}(T)$ / nm/K	
	Theory	Measurement
InP (bulk)	0.25	
InP/ $Ga_{0.51}In_{0.49}P$ (QD)		0.13
$Ga_{0.52}In_{0.48}P$	0.13	0.12-0.15*
$(Al_{0.3}Ga_{0.7})_{0.52}In_{0.48}P$	0.11	
$(Al_{0.6}Ga_{0.4})_{0.52}In_{0.48}P$	0.09	

Table 4-6 Calculated energy bandgap shift with temperature for material compositions present in the VECSEL subcavity. * measured thermal shift for a similar compressively strained $Ga_yIn_{1-y}P$ QW VECSEL structure with $y \approx 0.45$.

4.4.2.3 Surface photoluminescence

The room temperature surface PL peak position is at 747 nm and the thermal shift was measured to be of $\sim 0.09\ nm/°C$ as can be seen in Fig. 4-14. The RT reflectivity spectrum is also included in the graph in order to illustrate that the resonance feature corresponds well with the peaks in the surface PL spectra. The intensity of the surface PL signal decreases with increasing temperature, which can be attributed to the decreased quantum efficiency of the QDs at elevated temperatures due to increased carrier escape from the dots. The peak maximum of the edge PL at room temperature in Fig. 4-13 is close to 740 nm, which is about 6 nm short of the subcavity resonance (Fig. 4-11 and Fig. 4-15). The QD ensemble peak emission has a faster shift with temperature than the subcavity resonance/RPG as explained in Section 2.2.3.3 and thus moves closer to the resonance wavelength with

increasing temperature. The effect of the temperature induced charge carrier escape from the dot states into the wetting layer/barrier seems to be dominant at these elevated temperatures, reducing the emission efficiency despite the better overlap, resulting in a decreasing surface PL intensity. This would suggest that an optimised overlap at room temperature could be advantageous.

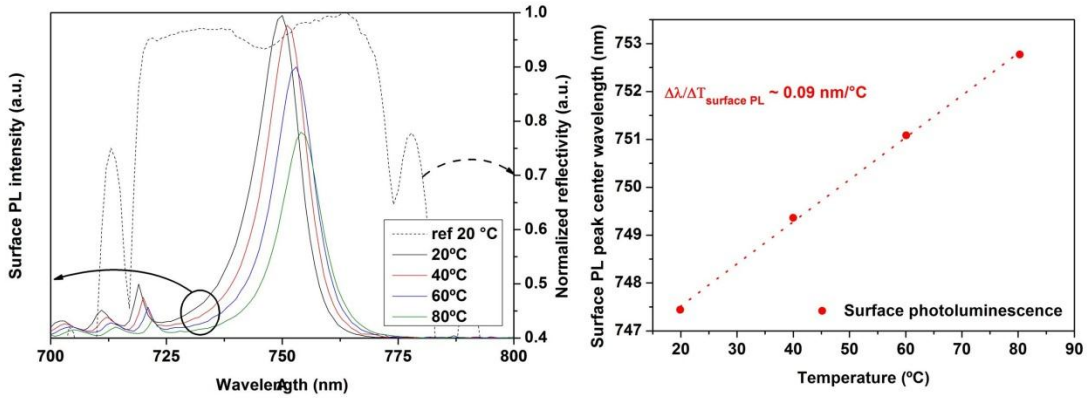

Fig. 4-14 Left: Surface photoluminescence (PL) spectra at 20, 40, 60 and 80 °C respectively are represented by the coloured solid lines. A room temperature reflectivity spectrum (black dashed line) is also represented for clarification. Right: Thermal shift ratio of the surface PL peak centre wavelength.

The room temperature reflectivity, surface PL, edge PL and free running laser emission spectrum were plotted together with the tuning ranges for samples A, B, C and D and are shown in Fig. 4-15. The plotted graphs reveal that the QD ensemble PL peak emission, corresponding to the dot size distribution, was shorter than the design wavelength. A bi-modal dot size-distribution, characteristic for InP QDs was also revealed in the edge PL peak (second peak/sholder in the blue solid line in Fig. 4-15, around 760 nm, showing emission from a larger group of dots) for samples A and B. The laser emission wavelength is dominated by the gain profile of the dot ensemble indicated by two features in Fig. 4-15:

- The centre wavelength of the free running laser emission spectrum (red lines) is always close to the edge PL peak maximum.
- The tuning range (green solid line) for samples C and D describe closely the measured position and shape of the edge PL peak.

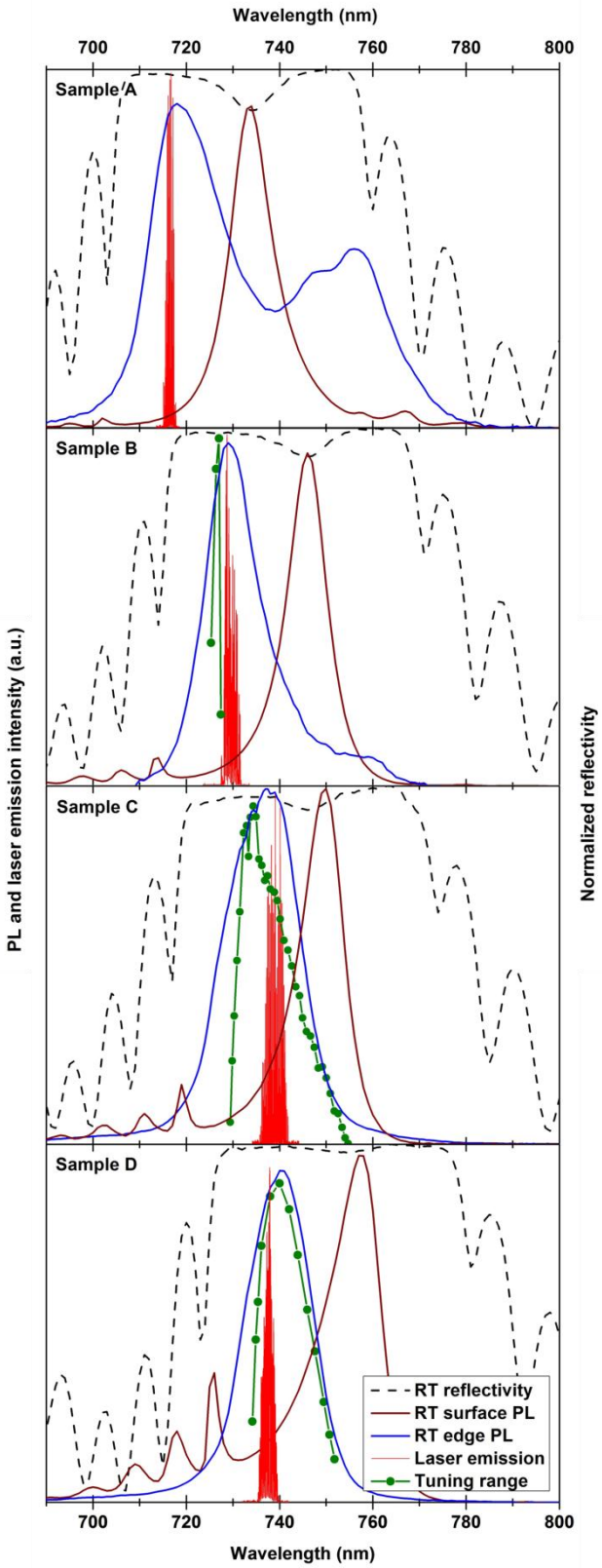

Fig. 4-15 Room temperature reflectivity (dashed black), surface PL (solid wine red) and edge PL (solid blue) spectra together with the detected free running laser emission spectrum (red) and measured tuning range (solid green line with full green circles), where applicable.

Samples C and D were cleaved at different wafer positions but their laser performance, including the emission wavelength was almost identical. Differences can be seen in comparison with samples A and B, which have lower laser emission wavelengths and higher threshold pump powers. With decreasing laser emission wavelength the peak gain of the dot ensemble moves further from the RPG wavelength, which reduces the overlap. Higher pump threshold powers are thus required to reach the transparency carrier density condition. As the differential efficiency and point of rollover were not affected by these variations, the maximum achieved output power increased with decreasing pump threshold power and was highest for sample C. The reduced overlap could also be responsible for the absent and very narrow tuning range of samples A and B respectively. The trends described in Fig. 4-15 and Table 4-5 are a strong indication that better laser performance with lower threshold and higher output power could be achieved for structures with a better overlap between QD gain and RPG wavelength.

4.4.3 Edge photoluminescence of a working laser

Edge PL measurements were done for low excitation densities on a cleaved sample. The measurement ideally probes the non-modulated spontaneous emission of the gain material. In this experiment, the edge photoluminescence emission was detected within a working cavity in order to examine the photoluminescence behaviour below and above the laser threshold. The point of interest here is to find out the mechanism which sets the laser emission wavelength and how the PL and laser emission wavelength change with pump intensity.

4.4.3.1 Experiment

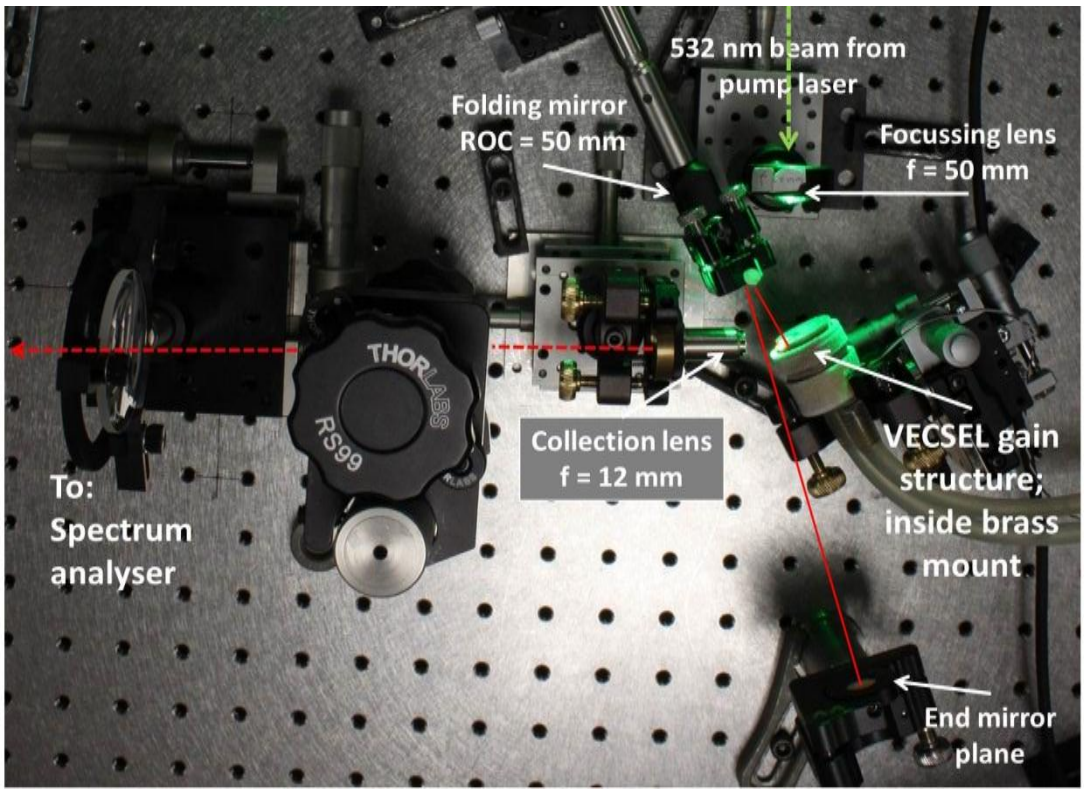

Fig. 4-16 Picture of the experimental setup, showing the active laser, mounted and bonded to a brass mount. The green colouring comes from scattered pump light. PL collection occurred via the short microscope objective near the left side of the mount on the upper right side of the picture.

The cavity for this measurement was slightly altered compared to the laser performance tests. As the incident pump power of the 532 nm laser unit in the spectroscopic set-up was restricted to below 1 W, the pump intensity had to be increased in order to allow the coverage of the entire working range from zero up to threshold and thermal rollover. A feature of this laser type is the power scalability, meaning the possibility to alter the pump spot/cavity mode size and thus the pump intensity in order to optimize the threshold power, but also the thermal rollover point as required. A three mirror V-shaped cavity with all high reflective mirrors was used. The folding mirror (FM) had a radius of curvature of 50 mm. The pump beam was focused to a measured diameter of $\emptyset = 35\ \mu m$; this corresponded to a total spot size of around $\emptyset = 45\ \mu m$ in the horizontal plane for an angle of incidence of 33 ^{0}C. The cavity dimensions were chosen to match this spot size, with the short cavity arm

(VECSEL – FM) and long cavity arm (FM – plane OC) being 26 and 145 mm respectively. A 500-µm-thick diamond heatspreader was optically bonded to the VECSEL intracavity surface and the sandwich mounted into a brass mount, modified to allow access to the cleaved edge. A $f = 12\,mm$ focal lens collected the emitted photoluminescence, which was focused into the spectrum analyser. The experimental set-up is shown in Fig. 4-16. The pump power was adjusted by the help of a $\lambda/2$-retarder in combination with a polarising beam splitter cube.

4.4.3.2 Results and discussion

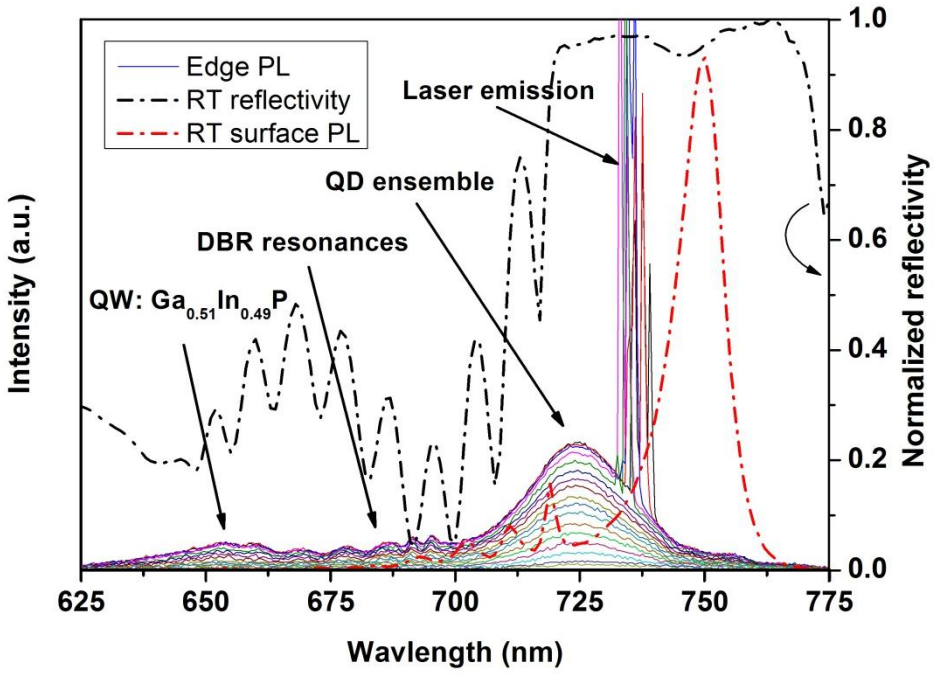

Fig. 4-17 Edge photoluminescence measurements within a working laser cavity in dependence on pump intensity, from zero to the point of rollover. The $Ga_{0.51}In_{0.49}P$ QW emission around 650 nm together with the InP QD ensemble emission at 725 nm and the laser emission around 738 nm is recognisable. Also shown in the graph is the measured room temperature reflectivity stopband (black dash-dotted line) and surface PL (red dash-dotted line).

Fig. 4-17 displays the measured edge PL spectra. The different features, starting from short wavelengths, could be attributed to the PL emission of the $Ga_{0.51}In_{0.49}P$ QWs

around 655 nm, the InP QD ensemble centred around 725 nm and laser emission spectrum at 738 nm (for pump power levels above threshold). The origin of the wavy line shape recognisable between the QW and QD ensemble PL peaks was caused by the DBR resonance features, adjacent to the reflectivity stopband. From this plot it is recognisable that the laser emission occurs at a point between the edge PL peak maximum of the QD ensemble and surface PL peak. This indicates a "pulling" effect of the free running laser mode towards the resonance position. The peak positions of the QD ensemble PL and the centre of the laser emission from these graphs is plotted against the incident pump power in Fig. 4-18. The blue-shift of the QD ensemble PL peak position with increasing pump intensity can be explained by the state filling effect. Large QDs have the deepest energy states and dominate the PL emission at low excitation. Smaller QDs with shallower energy states become more and more populated with increasing pump density, shifting the emission towards shorter wavelengths. This effect of the PL emission slows down gradually and flattens out above 300 mW pump power. The expected decrease of the bandgap energy with pump induced rise of temperature in the pumped area, described by Kemp et al. [34] is compensated by the state filling of higher lying QD states and the PL emission wavelength remains constant [35,36]. The centre of the laser emission wavelength decreases with pump intensity close to the laser threshold power, but reaches quickly a minimum at 430 mW after which the wavelength increases linearly with a rate of $\Delta\lambda/\Delta P = 2.8$ nm/W until thermal rollover ~750 mW. This behaviour is very similar to that described in the previous Section 3.3.2 on InAs/GaAs SML QD VECSELs. The sublinear behaviour at highest pump intensities might indicate the onset of thermal rollover. The inset in the figure illustrates the progression of the laser emission spectra for the different points (green triangles) in the graph supports this argument. A broadening of the total laser emission spectrum towards longer wavelength is recognisable with increasing pump intensity below 750 mW. The short wavelength side of the emission spectrum remains almost constant, independent on the pump level. Further broadening is prevented above a pump power of 750 mW. This 'saturation' level might be explained by the onset of thermal rollover and a lower emission efficiency of the dots in this region.

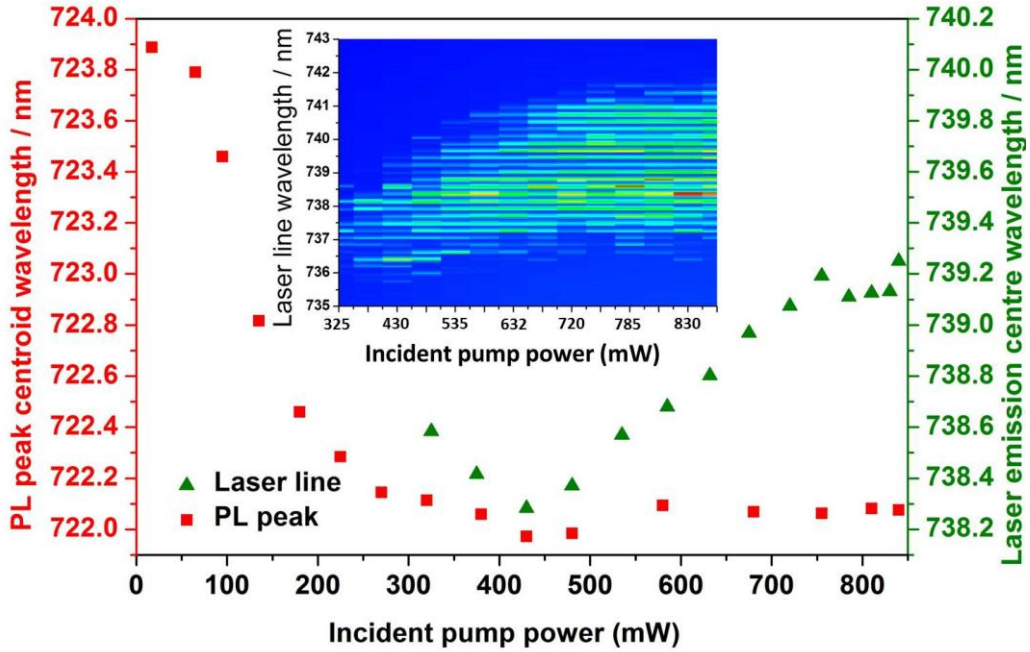

Fig. 4-18 Quantum dot structure: plot of the edge photoluminescence behaviour in dependence on the incident pump power (red squares). The laser emission wavelength is represented by the green triangles. The inset depicts the laser emission spectra in dependence on incident pump intensity, where the fringes are caused by the etalon effect of the diamond heatspreader.

A difference with respect to InAs/GaAs QD based VECSELs discussed in Section 3.3.1.1 (see Fig. 3-2 left) and also in [37] is the development of the full width of half maximum (FWHM) of the PL peak with increasing excitation, which is caused by the population of excited states in that case, creating a very broad and even PL spectrum. In case of the present InP QDs, where only ground state emission is present the $FWHM = 24\,nm$ remains almost constant over the complete laser working range with pump densities up to $90\,kW/cm^2$. The narrower gain spectrum makes a good match between gain and resonances more difficult compared to the InAs/GaAs QD case.

4.4.4 Time resolved PL decay measurements

This series of measurements was carried out at Cardiff University, School of Physics and Astronomy, in collaboration with the group of Prof. Peter M. Smowton. The experimental set-up and equipment was prepared and controlled by Dr. Julie Lutti, a postdoctoral researcher from this group.

Time resolved PL decay measurements can give information about the radiative lifetime of the charge carriers. An estimated radiative decay time in the 1 ns range for In(Ga)As QDs is stated in [16] and thought to be similar in the present InP/$Ga_{0.51}In_{0.49}P$ QDs. The intention for this experiment was to determine the actual recombination time for the current structures and any modulation effects due to the resonant cavity design.

4.4.4.1 Experimental setup

The experimental arrangement is shown in Fig. 4-19, where the tested samples were pumped by a frequency doubled Ti:sapphire laser from Coherent. The Mira 900 (Coherent), mode-locked Ti:sapphire laser unit, had a tuning range of 710-940 nm and provided pulse durations of 200 fs and a repletion time of 13 ns with a pulse energy of 2 nJ. The Ti:sapphire was pumped by a continuous wave 8 W Verdi V8 laser (Coherent) at 532 nm and set for an emission wavelength of 900 nm. The output beam passed through a glass beam splitter, where the reflected part was detected with a fast photodiode and the transmitted part passed through a nonlinear crystal arrangement for second harmonic generation to 450 nm. The nonlinear conversion efficiency was about 20 % and corresponded to a measured average power of $P_{av} = 34\,mW$ (pulse energy 400 pJ) after the conversion process. The beam passed through an attenuation wheel, allowing for continuous power adjustment and an achromatic lens with $f = 130\,mm$, focussing the beam to a pump

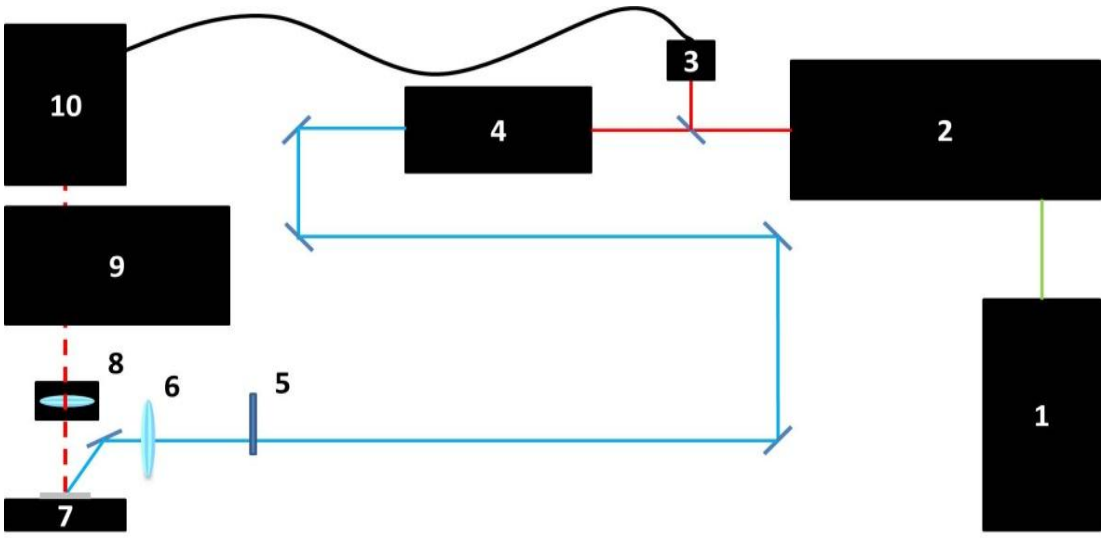

Number	Device description
1	Verdi V8; λ = 532nm; P = 8 W, (Coherent)
2	Mira 900; Mode Locked Ti:Sapphire laser; (Coherent) Pulse duration: 200 fs; Repetition time: 13 ns; wavelength tuning range: 710-940 nm
3	Fast photo diode (laser pulse used as trigger signal for streak camera)
4	Second harmonic generation unit (Coherent) Wavelength tuning range: 355-470 nm
5	ND-filter wheel (continuous attenuation)
6	Focal lens: achromatic (120 mm)
7	Sample holder and thermo-electric coupling device
8	Telescope optic for PL collection and focusing into a mono-chromator
9	Bentham M300 monochromator; Grating: 1800 l/mm
10	Streak camera sweep time triggered by fast photodiode (Hamamatsu)

Fig. 4-19 Experimental set-up of the time dependent PL measurements.

Spot size of $Ø = 50\,\mu m$. Emitted surface PL was collected by a telescope optic, having a $f = 130\,mm$ and focussed into a Bentham M300 monochromator where the PL signal was dispersed by a grating with 1800 lines/mm allowing a resolution of 1.5 nm. The output from the monochromator was finally directed into the streak camera (Hamamatsu) and the sweep time triggered by the pulse duration of the MIRA 900 unit, detected with the fast photodiode. Calibration of the monochromator was done with the help of an Hg-Ar spectral calibration lamp from Oriel (6025-M) and online available data of spectral lines of Ar and Hg atoms from the National Institute of Standards and Technology (NIST)[38]. All measurements were done for an entrance slit width of the spectrum analyser of 30 µm, which allowed an estimated resolution limit of 180 ps due to the time jitter of the detected signal on a time scale of 20 ns. The resolution limit for a shorter time scale of 5 ns was 70 ps. Temperature

and excitation dependent measurements were carried out. For the thermal behaviour tests, the samples were glued to a TEC with silver paste.

4.4.4.2 Results and discussion

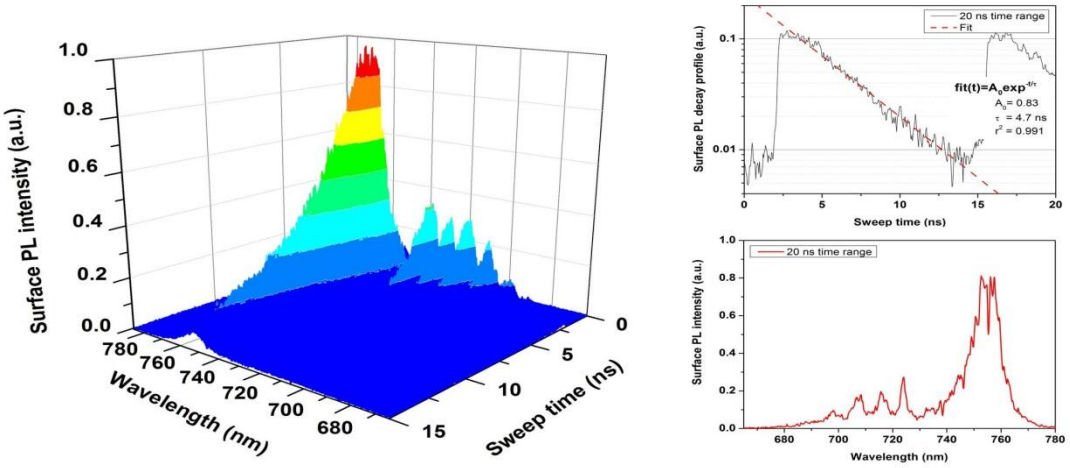

Fig. 4-20 Left: 3D data file, recorded by the streak camera. Right top: Extraction of the surface PL time decay profile, together with mono-exponential fit curve. Right bottom: extraction of the surface PL spectral profile.

Recorded data files are returned in a three dimensional matrix, giving the spectral resolution in the x direction, the time axis in the y direction and signal intensity as the z-axis. These data files were processed using a MathCad programme given in Appendix A.6 and extracted in several steps: Data import, calibration of the spectrum, definition of the time axis (5 or 20 ns sweep time), subtraction of background noise, and signal normalisation. An example for the extracted data files is given for a surface PL spectrum (Fig. 4-20, bottom right) and for the iso-chromatic line (surface PL time decay profile) at different wavelengths (Fig. 4-20, top right). The noise on the surface PL spectrum was caused by the roughness of the slit entrance to the streak camera. The time decay profile is well described by mono-exponential decay and the fitting parameters are determined by a linear fit on a semi-logarithmic plot as can be seen in Fig. 4-20. For the estimation of the relative error the standard deviation of the linear regression was added together with the estimated time jitter of about 120 ps. A further measure for the quality of the linear fit was the observation of the correlation coefficient [39], which was plotted, next to

the extracted PL decay time graphs. The spectral error was taken to be the resolution limit of the monochromator. Three different samples were probed in this way, a piece from the growth calibration wafer MR2598, sample A and sample C (see Fig. 4-15). The samples were chosen due to the absence or position of the subcavity resonance respectively. For the growth calibration sample, no resonance effect was expected, giving the actual decay time (radiative carrier lifetime) of the dots. Sample A had the largest separation between the edge PL peak/laser emission wavelength and the surface PL peak wavelength. For sample C, this difference was the smallest for the working samples.

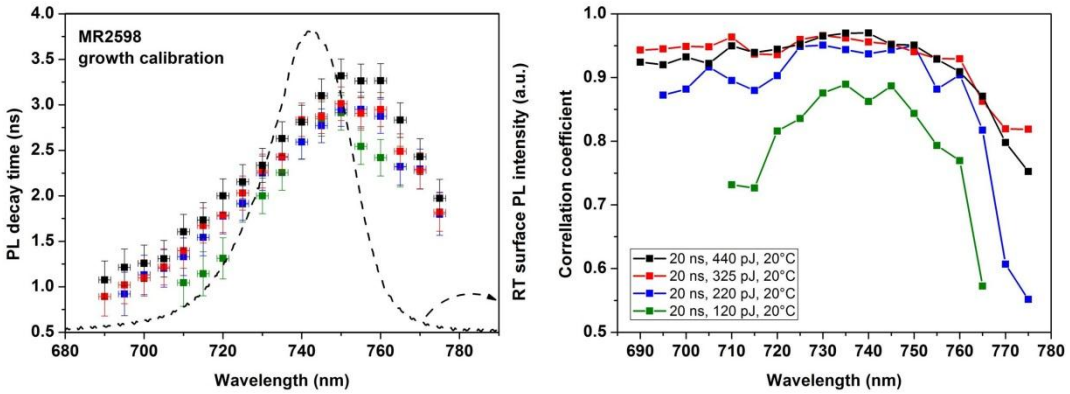

Fig. 4-21 Excitation density dependent PL decay measurements of the growth calibration structure. Black, red, blue and green squares for 440, 325, 220 and 120 pJ pulse energies. The surface PL signal (dashed line) is superimposed for clarification. Calculated correlation coefficients are represented on the right hand side.

In case of the growth calibration sample, the radiative carrier lifetime was probed in dependence on excitation density Fig. 4-21 and temperature Fig. 4-22. As the spectrum in this case is set solely by the contributing QDs of the ensemble, it can be concluded, that the radiative carrier lifetime increases with QD size (emission wavelength). Radiative carrier lifetimes in the range τ = 1-3.5 ns were measured in this case with no significant deviations for the different excitation densities, as the values lie all close or within the error bars. Small QDs have a poorer carrier confinement and thus thermal escape occurs more easily compared to larger QDs. The escaped carriers populate higher energy levels outside the dot states and recombine non-radiatively. The decreased PL decay time for values above 750 nm should be taken with caution, as the correlation coefficients indicate a poor fit due to weak signal strength and large noise levels in this region. Increasing temperature has

a stronger effect on the radiative carrier lifetime. For a constant excitation level of 440 pJ ($\emptyset_{pump} = 50\,\mu m$), the PL decay time at the highest point decreases with increasing temperature from around 3.5 ns down to 2 ns for the temperature range 20-80 ^{0}C. This could be understood by increasing thermal excitation of the charge carriers from dot levels into the wetting layer, capping QW or barrier states, mitigating the radiative recombination efficiency. It illustrates the impact of the thermal heat introduction on the radiative carrier lifetime.

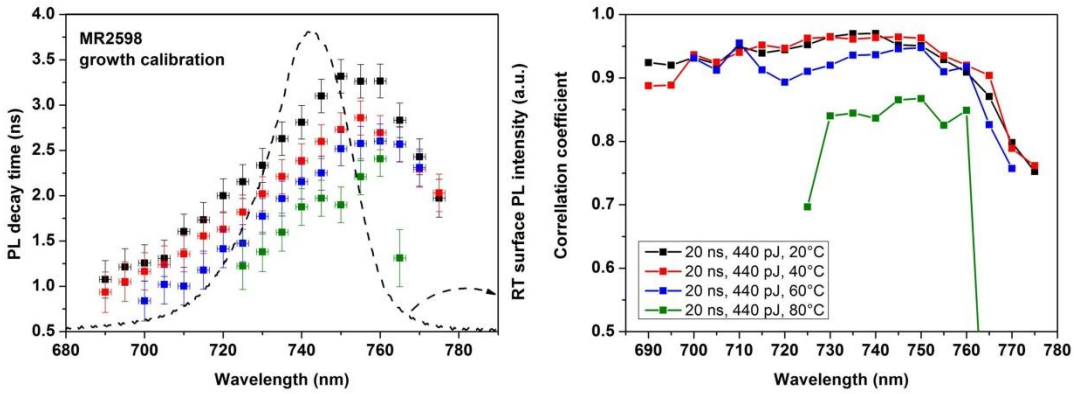

Fig. 4-22 Temperature dependent radiative carrier lifetime measurements of the growth test structure. Back, red, blue and green squares stand for 20, 40, 60 and 80 °C. The surface PL signal (dashed line) is superimposed for clarification. Calculated correlation coefficients for each point are represented on the right hand side.

For the next two samples (A & C) the resonance effects contribute an increased photon lifetime to the carrier lifetime for the overall PL decay time. The presence of the DBR creates a subcavity with the semiconductor/air interface; an etalon effect. This alters the photon lifetime in the cavity in dependence on the mirror reflectivity. A qualitative model of the cavity effect is described by following equations [40].

$$\tau_{ph} = \left[\frac{c}{n_{av}}\left(\alpha_i + \frac{1}{L_{cav}}\ln\left(\frac{1}{R}\right)\right)\right]^{-1}, \qquad \text{Equation [4-1]}$$

τ_{ph}, c, n_{av}, α_i , R , L_{cav} are the cavity photon lifetime, the speed of light in vacuum, the averaged refractive index of the layers inside the cavity, the total internal absorption coefficient, the reflectivity product of DBR and semiconductor/air interface and the cavity length. The transmission of this subcavity is calculated by [41]

$$T = \frac{T_{DBR} \cdot T_{SAI}}{(1 + R_{DBR}R_{SAI})^2 + 4\sqrt{R_{DBR}R_{SAI}}\sin^2\left(\frac{2\pi n_{av}L_{cav}}{\lambda}\right)}. \quad \text{Equation [4-2]}$$

Here T_{DBR}/R_{DBR} and T_{SAI}/R_{SAI} stand for transmission/reflection of the DBR and semiconductor/air interface in dependence on the wavelength respectively. Combining both formulas by the relation $R = 1 - T$ describes qualitatively the dependence of the cavity photon lifetime on the wavelength. This effect enhances the photon lifetime almost by a factor of 1.5 at the resonance position compared to the growth calibration structure and is recognisable in Fig. 4-23 (sample A). At the point where PL wavelength and resonance are matched a decay time of 5 ns is measured. In the range of applied pulse energies 40-440 pJ no significant deviation of the decay times is present. Larger deviations of single measurement points at either end of the detected spectrum are thought to be caused by the weak detected signal strength, indicated by the decreasing correlation coefficient. The cavity effect on the PL decay time is better illustrated for sample C in Fig. 4-24. Here, the PL decay time follows closely the shape of the photon lifetime with a maximum decay time of 5 ns at the peak position before it starts to decrease again. Fig. 4-24 on the right hand side depicts the temperature dependent decay time between 20-80 ^{0}C. A thermal red-shift of the maximum cavity photon lifetime position is recognisable. The highest decay time value also increases with temperature and reaches a maximum of τ = 5.5 ns around 60 ^{0}C. The red-shift is caused by the thermal dependence of the QD ensemble PL peak emission and the increase by an improving overlap between QD emission and resonance wavelength. Something else becomes visible as well. At lower wavelengths (smaller QDs) the thermal effect on the decay time is weaker and becomes only apparent towards the peak maximum position. This behaviour is different from that of the growth calibration sample, where the radiative carrier lifetime decreases with increasing temperature. In this case the decreased radiative carrier lifetime due to thermally induced carrier escape is compensated by the better overlap. Optimum conditions are expected where the QD ensemble emission and the subcavity resonance are matched.

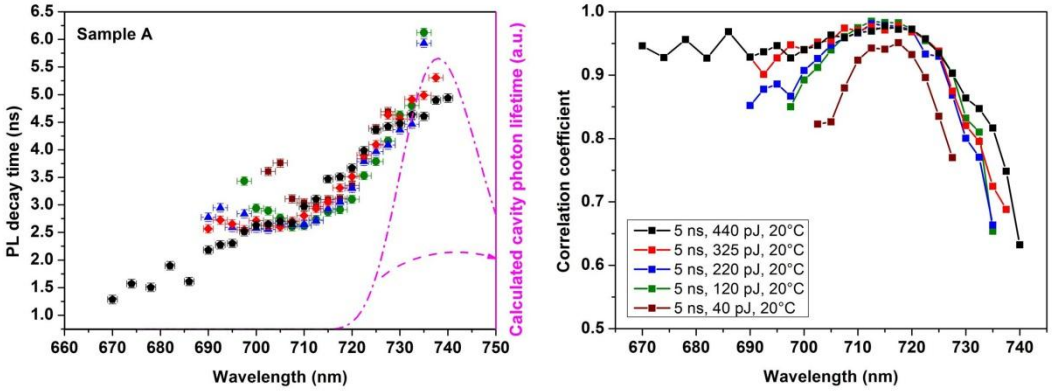

Fig. 4-23 Excitation density dependent PL decay time for sample A. Black, red, blue, green and wine red squares for 440, 325, 220, 120 and 40 pJ pulse energies. The calculated cavity photon lifetime (pink dash-dotted line) is superimposed for clarification. Calculated correlation coefficients for each point are represented on the right hand side.

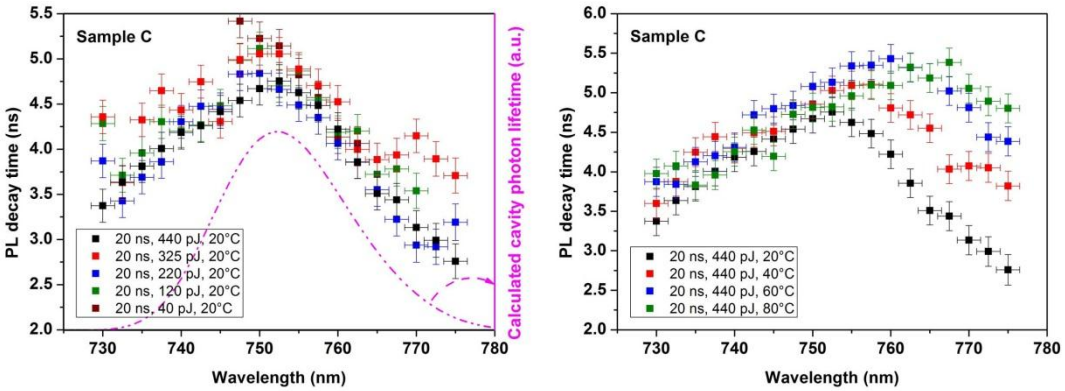

Fig. 4-24 Left: Surface PL decay time dependent on the excitation density for sample C. Back, red, blue, green and wine red squares stand for 440, 325, 220, 120 and 40 pJ pulse energies. The calculated cavity photon lifetime (pink dash-dotted line) is superimposed for clarification. Right: Temperature dependent radiative carrier lifetime. Back, red, blue and green squares stand for 20, 40, 60 and 80 °C.

4.4.5 Further growth quality characterisation

As explained in Section 2.2.4 the effective dissipation of any introduced heat from the gain region of the VECSEL structures is of high importance for the laser performance. Therefore the method of a transparent intra-cavity optically-contacted diamond heatspreader to the VECSEL surface is applied via liquid capillary bonding [31]. One problem making the laser performance tests of the presented QD samples difficult was the very rapid detaching of the diamond heatspreader from the structure

surface. This allowed a usual time window for the measurements of maximum few hours, including necessary cavity adjustments after mounting of the sample into the cavity. An attempt to circumvent this problem was by mechanical thinning of the substrate. The general ease to bond the heatspreader to the sample surface could be improved due to the increased flexibility of the thinned structure, but the time that the sample remained bonded didn't change significantly. In addition, the sample was much more vulnerable to destruction during the handling. It was assumed that the highly strained InP QD epilayers were the reason for the impaired bonding ability.

As part of the investigation into the reason for the poorer bonding behaviour with comparison to QW structures in the $(Al_xGa_{1-x})_{0.51}In_{0.49}P$ material system, simultaneous cathodoluminescence (CL) and secondary electron microscopy (SEM) imaging was carried out. Three QD samples (described in Table 4-2) and one similar QW sample were examined from wafers:

- MR2482: the first growth campaign, containing 24 QD with had two different barrier types making it the most complicated structure design. It was not possible to attach a heatspreader by liquid capillary bonding to the surface.
- MR2615: the successful VECSEL structure. Bonding of the heatspreader was possible but limited.
- MR2598: the growth calibration. Containing the complete active region (identical to MR2615) without the DBR. Bonding behaviour was best between the QD samples
- for comparison: a quantum well based $Ga_{0.413}In_{0.587}P/(Al_{0.6}Ga_{0.4})_{0.51}In_{0.49}P$ structure (further denoted as "QW sample") with an emission wavelength at 680 nm, containing an active region with 2 x 10 QWs, grown on top of a DBR with 45.5 pairs of $AlAs/Al_{0.4}Ga_{0.6}As$, similar to the structure reported in Hastie et al. [6].

The obtained results could additionally be verified by transmission electron microscopy (TEM) images for sample MR2598.

4.4.5.1 Experimental setup

The CL/SEM and TEM imaging was carried out at the School of Physics, Peking University with the help of Mr. Wang Lei, a PhD student at the School, who was trained in the use of the equipment. All samples were tested with a MonoCL3 system from Philipo-FEI, capable of simultaneous CL and SEM imaging of the observed sample area. All discussed CL images below for the QD samples were detected in a spectral range of 650-780 nm, covering both QD ensemble as well as QW emission. The detection wavelength of the QW sample was set around 680 nm. An applied voltage in the range from 2-30 kV accelerated the electron beam onto the samples' surface. The penetration depth of the electrons into the present structure was estimated by help of the open source programme CASINO version 2.42, supplied by Drouin et al. [42], where the designed multi-layer stack was recreated and used for the simulation. An estimation of the weighted electron beam penetration depth is displayed in Fig. 4-25.

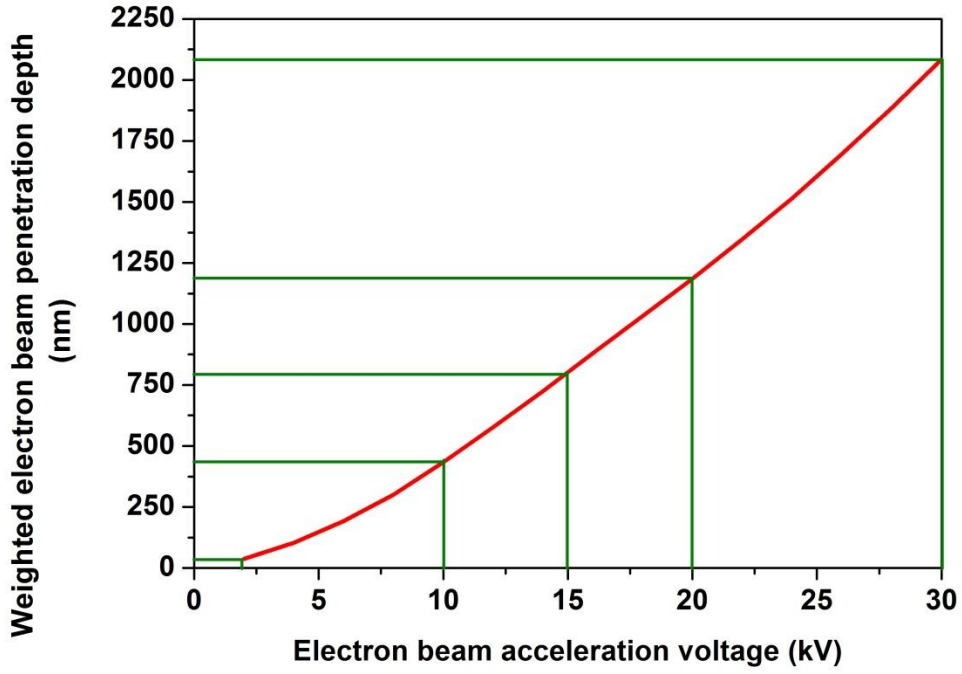

Fig. 4-25 This graph shows the weighted electron beam penetration depth into the AlGaInP structure.

4.4.5.2 Results

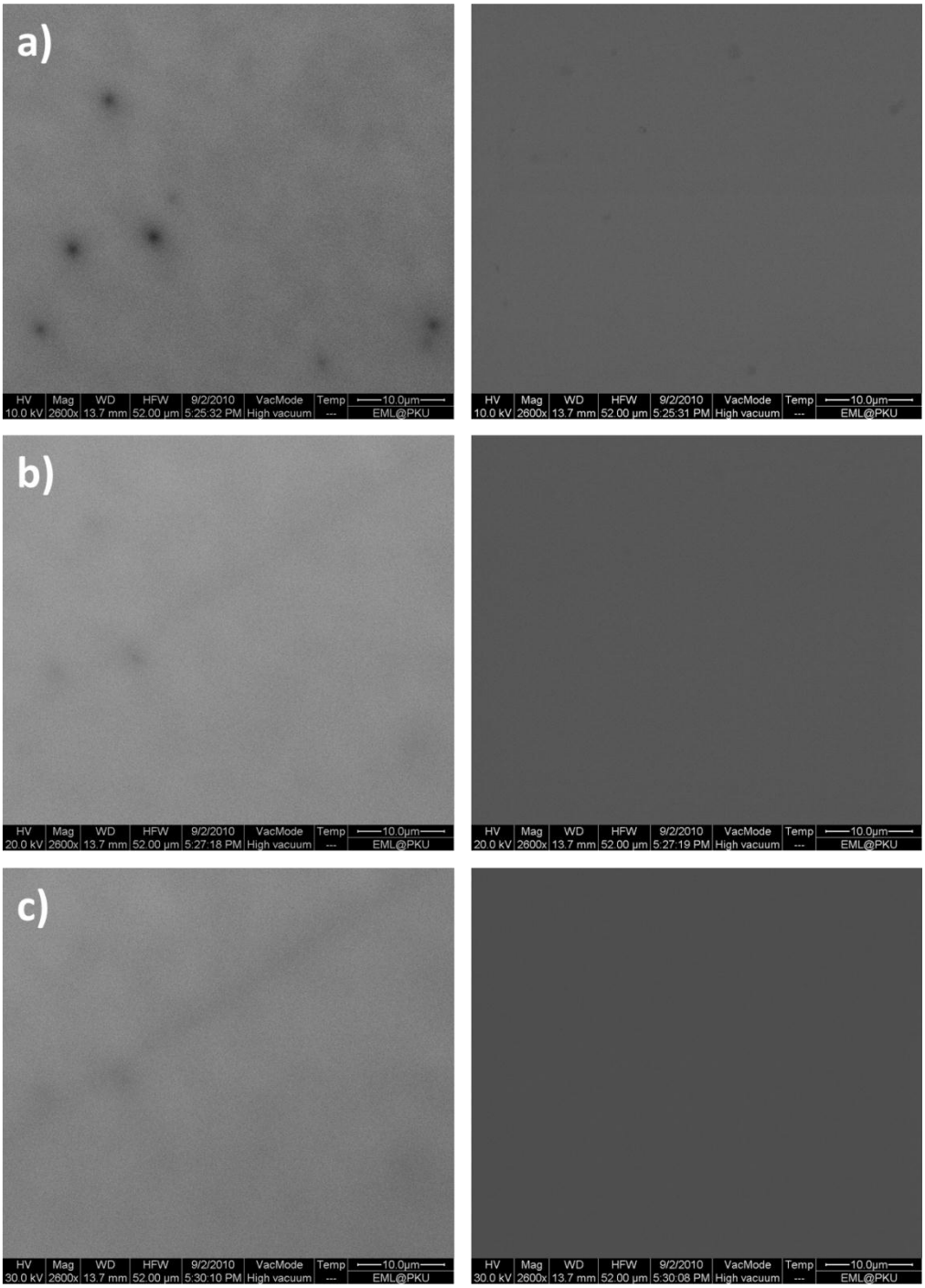

Fig. 4-26 CL (left) and SEM (right) images of the QW sample for different electron beam penetration length a) 10 kV, b) 20 kV, c) 30 kV. Dark spot defects are very shallow below the surface, whereas dark line defects are detected deeper inside the structures.

An optical pre-examination of the surfaces was carried out by eye and under the microscope. In case of the QW sample no surface defects (despite of scratches) were found and it was very easy to establish a long lasting bond between the diamond heatspreader and the sample surface. The observed defects in the CL images are mainly dark lines and some dark point like defects which couldn't be related to any features at the surface given by SEM imaging of the same area shown in Fig. 4-26 right side. Furthermore the point defects are only visible in the CL images for the lowest applied electron beam acceleration voltage of 10 kV (Fig. 4-26 a). This means that the defects are very close to the surface. Images with higher acceleration voltages (20 and 30 kV, Fig. 4-26 b and c) reveal very faint and deeper lying dark line defects. In general, the observed luminescence appeared to be homogeneous with only few defects. The dark points appear localised and might be an indication for relaxation of the high strain in the QWs (as stated by the grower; EPSRC National Centre for III-V Technologies at the University of Sheffield).

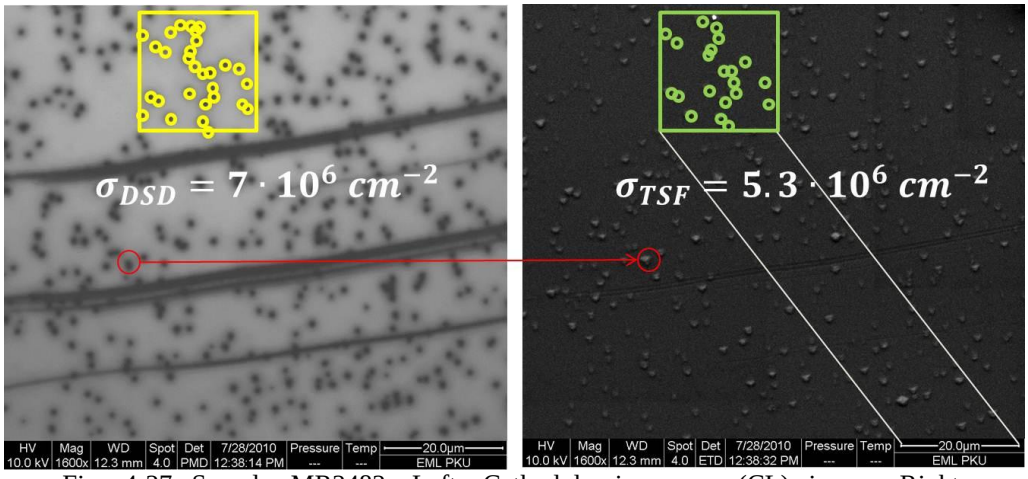

Fig. 4-27 Sample MR2482: Left: Cathodoluminescence (CL) image. Right: Secondary electron microscopy (SEM) image.

In contrast to this were all three quantum dot samples covered by dark spot defects (DSD) in the CL images, as depicted for example in Fig. 4-27. These DSDs are very likely to be threading dislocations [43,44]. SEM images depict these dislocations as triangular surface features (TSF) and are illustrated in the inset of Fig. 4-28 a). Application of CL imaging for different electron beam acceleration voltages show that the size and position of the dark spot defects do not change with penetration depth, indicating their parallel propagation to the growth direction. The DSD density

was estimated to be similar for all three samples in the range of $5 \cdot 10^6$ cm^{-2}. The number of TSF varied considerably between the three QD samples. A closer analysis of the CL and SEM images for all three samples is given below.

MR2482:

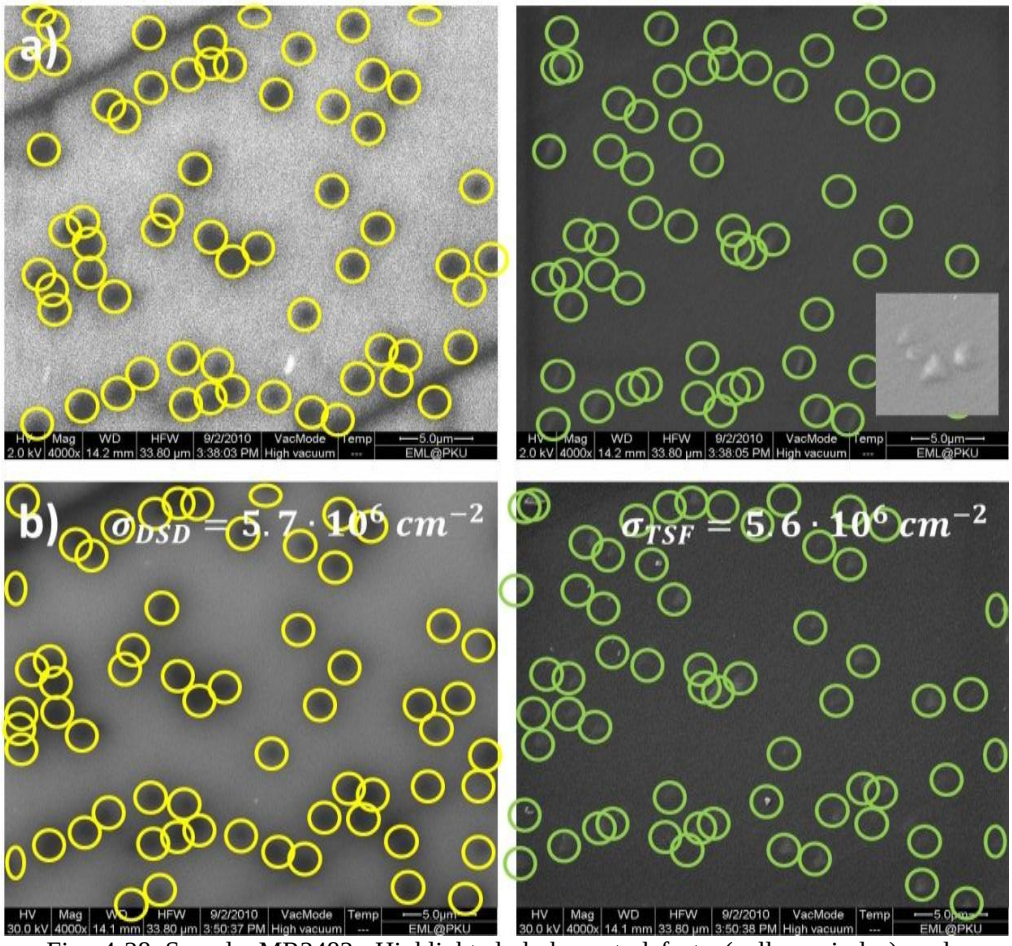

Fig. 4-28 Sample MR2482: Highlighted dark spot defects (yellow circles) and triangular surface features (green circles) in the CL (left) and SEM (right) images for lowest (a) 2 kV) and deepest (b) 30 kV) electron beam penetration. Position and shape of the dark spot defects remain unchanged. The inset of a) illustrates the shape of these defects.

Both, cathodoluminescence (CL) and secondary electron microscopy (SEM) images show a large number of defects. The CL-image is covered by many dark line defects, most of which can't be seen in the SEM image and appear below the surface. The dark spot defects can be directly correlated to the triangular shaped features seen in the SEM-images. The estimated density of the DSDs and TSFs for this sample are around $7 \cdot 10^6$ cm^{-2} and $5.3 \cdot 10^6$ cm^{-2} respectively, where the estimation was done manually by counting the number of defects within a box of 20 x 20 µm^2, as

illustrated in Fig. 4-27, having a magnification of x1600. In this case almost all threading dislocations propagate to the surface. The behaviour of the defects in dependence on electron beam acceleration voltage is illustrated in Fig. 4-28 (magnification x4000) for a) 2 kV and b) 30 kV. The shape, number and position of the DSDs don't change with electron acceleration voltage.

MR2615:

The SEM image (Fig. 4-29, magnification x4000) of the completed VECSEL has an estimated surface defect density of $5 \cdot 10^5$ cm^{-2} and a slightly reduced density of DSDs with respect to MR2482. This indicates that the progression of the threading dislocations into the surface could be decreased by a factor of 10, which improved the surface smoothness of this sample and might explain the better ability to bond the diamond heatspreader to the surface.

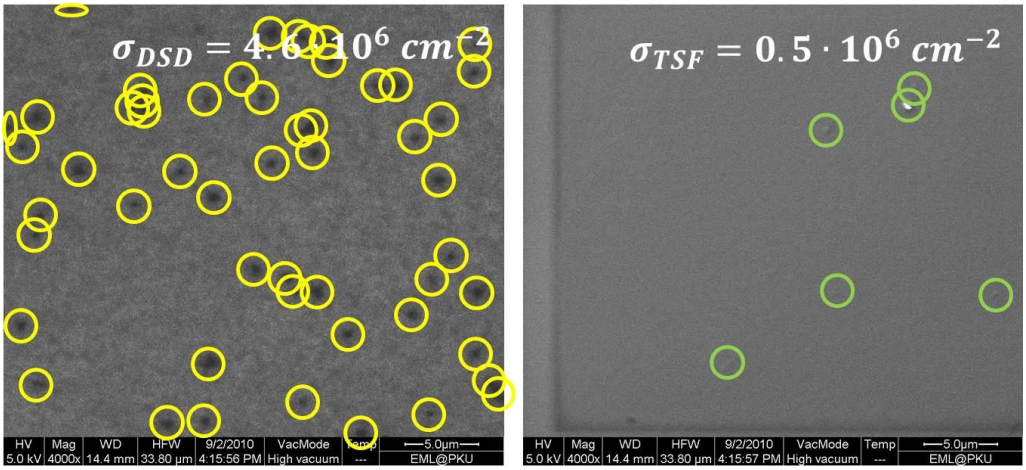

Fig. 4-29 Sample MR2615: Cathodoluminescence (CL) image; right: Secondary electron microscopy (SEM) image of the same area on the sample surface. The surface is much smoother compared to the first growth.

MR2598:

In case of this growth calibration sample it is expected that the overall built-in strain is smaller compared to the completed VECSEL (MR2615) due to the missing DBR. Although the DBR is near-lattice-matched, it is realistic that it is a source of strain,

due to its thickness of several micrometre and possible variations in layer composition. The estimated density of the DSDs is with $2.5 \cdot 10^6$ cm^{-2} by a factor of 2 lower and the number of TSFs is with $0.7\text{-}1.8 \cdot 10^6$ cm^{-2} by a factor of 4 lower compared to sample MR2482. The estimated size of the DSDs is less than $\emptyset \sim 1\ \mu m$ in diameter (resolution limited) as shown in Fig. 4-30 b). Fig. 4-30 a) and b) show areas on the same sample with same acceleration voltage but different magnifications of x4000 and x8000 respectively, which is also the reason for the difference in the estimated densities. As for the previous QD samples, it is possible to determine, that the density, size and position of the DSDs do not change with electron beam penetration depth.

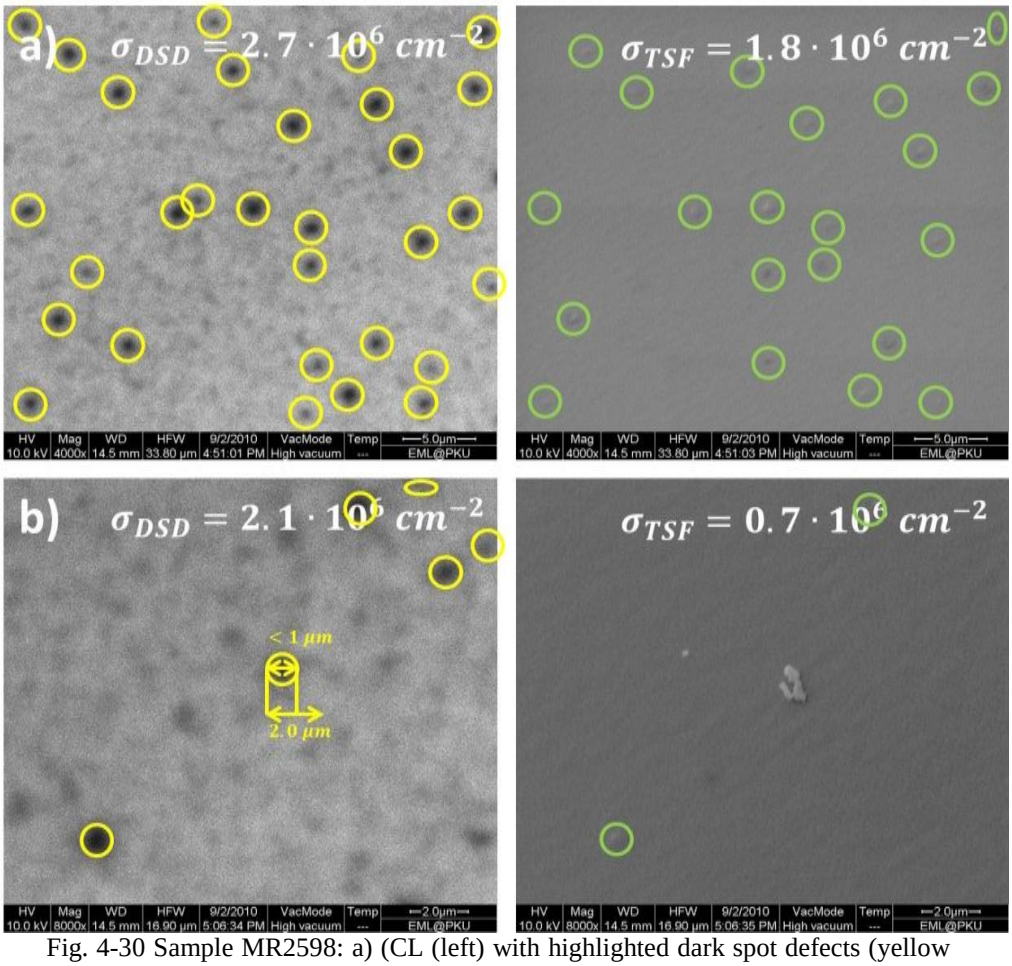

Fig. 4-30 Sample MR2598: a) (CL (left) with highlighted dark spot defects (yellow circles) and SEM (right). b) Estimation of dark spot size ($\emptyset < 1\ \mu m$).

A cross sectional TEM image of the active region of this sample is given in Fig. 4-31. It reveals the existence of threading dislocations originating within the first

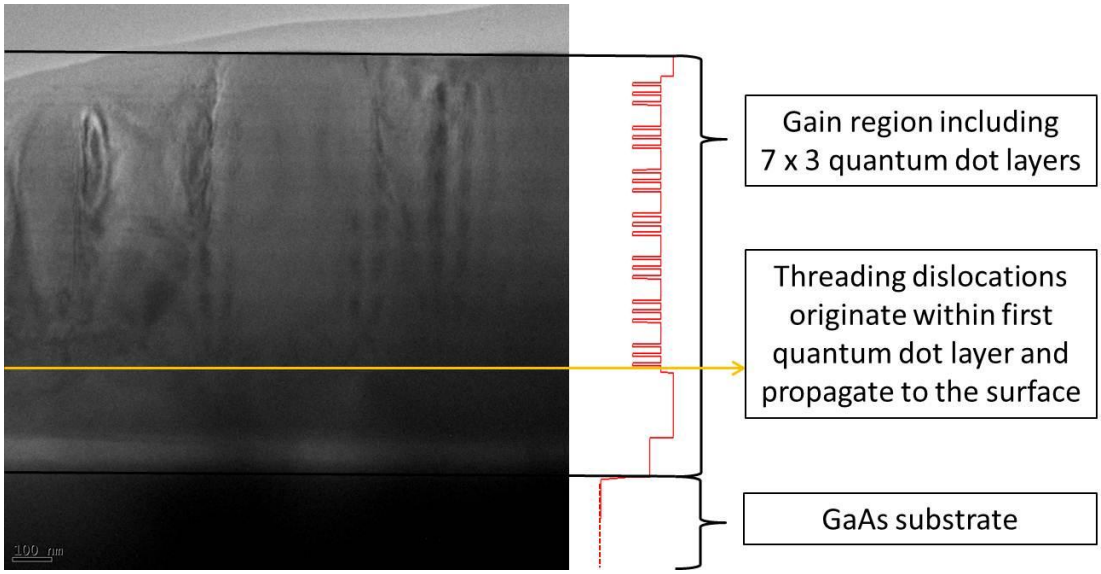

Fig. 4-31 TEM image of the gain region applying quantum dots as gain medium. This particular sample is was grown for calibration purposes and consists only of the gain region without the DBR. The seven groups of three dot-in-a-well layers are visible. The origin of the threading dislocations appears to be the first group of quantum dot layers.

QD-layer group. They propagate perpendicularly to the epitaxial layer planes towards the surface, where the majority of them terminate. Some of the threading dislocations terminate at interfaces within the structure, such as higher lying QD-layers. It is believed that these threading dislocations are the cause of the DSDs, visible in the CL measurements and also the reason for the TSFs in the SEM images. The image also resolves the QD-layers, spacer and barrier layers. The refractive index pattern of the designed active region is also depicted to the right hand side of the image illustrating the positioning of the different layers. Fig. 4-32 shows a further TEM image of the same structure with a larger magnification, allowing the estimation of the real layer thicknesses. The measured thickness of the dot-in-a-well was 8 nm (red line in graph), that of the separators between two dot-in-a-well layers within a group is 16 nm (blue line). Both correspond very well with the designed values. The designed barrier thickness was 54 nm, indicated by the dark green line. The TEM image shows an artefact, dividing the barrier into 16 nm (blue line) plus 38 nm (light green line) layers, resulting in a total length of 54 nm. The separator and barrier composition was the same and the whole active region was grown at a constant temperature of 710 ^{0}C. The origin of this ‘growth artefact’, indicated in the figure could not be explained so far by consultation of the growth procedure

(growers' remark). The total barrier thickness does not seem to be affected by this artefact and all layer thicknesses correspond well with the designed values. Nevertheless, this artefact could have an effect on the RPG wavelength and thus on the laser performance as this calibration growth structure is believed to be identical to the active region of VECSEL structure MR2615.

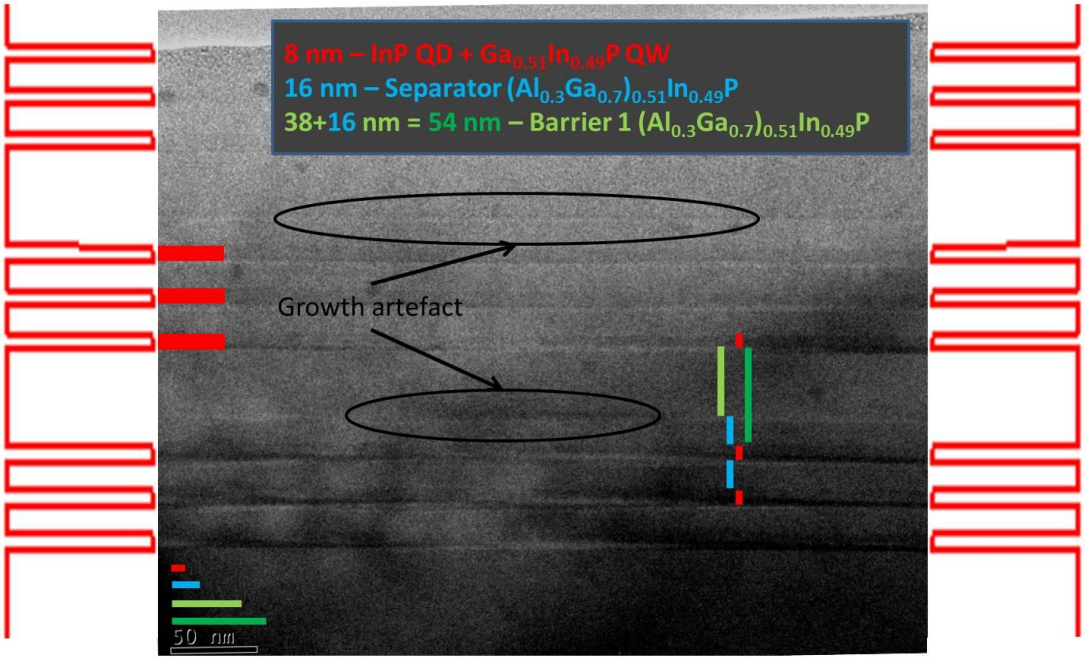

Fig. 4-32 Cross sectional TEM image showing, the dot-in-a-well layers (InP QD + $Ga_{0.51}In_{0.49}P$ QW), the separator and the barrier between two groups of QD-layers. Thicknesses are indicated by red (8 nm), blue (16 nm) and green (40 or 54 nm) lines for an estimation of the real thicknesses.

4.4.5.3 Discussion

Dark spot defects, covering the QD samples are caused by the presence of non-coherently strained islands (very large QDs, which undergo plastic relaxation via introduction of misfit dislocations) and are threading dislocations, which act as non-radiative recombination centres, appearing as dark spots in the CL images. Two factors can contribute to the occurrence of these dark spot defects. a) InP QDs have a bimodal growth distribution [25] and their optimum growth temperature is usually T = 600 ^{0}C [18,29]. The gain regions of the present structures were grown at

elevated temperatures of T = 700 (MR2482) to 710 ^{0}C (sample MR2615 and MR2598) in order to meet optimum growth conditions for the capping GaInP QWs [19]. The increased QD growth temperature on the other side leads to an increased diffusion length of the surface atoms, favouring a fast growth of larger dot sizes with smaller dot densities. b) A low growth rate favours in general larger QDs with a smaller dot density, whereas a high growth rate shifts this ratio towards higher dot densities but smaller sizes. The typical case for too high growth rates is the generation of small, coherent and large, fast growing, non-coherent QDs [45,46]. The InP QD-layers in the present work were grown at growth rates between 2.1-2.7ML/s. Given the effective layer thickness of 2.1 MLs per QD-layer, the total growth time was less than one second. This might have caused larger variations in the total layer thickness, by only small variations in growth time and might have enabled the conglomeration of large non-coherently strained islands.

Sample	T_{growth} (^{0}C)	th_{QD}/t_{growth} (ML/s)	DBR	Barrier2 x_{Al} = 0.6	σ_{DSD} (10^6cm^{-2})	σ_{TSF} (10^6cm^{-2})
MR2482	700	2.7	Yes	Yes	5.7	5.6
MR2615	710	2.4	Yes	No	2.7	1.8
MR2598	710	2.4	No	No	4.6	0.5

Table 4-7 Summary of some of the growth conditions is stated together with the density of the detected dark spot defects (DSD) and triangular surface features (TSF). T_{growth}, th_{QD}/t_{growth} is the growth temperature and the growth rate of the QD-layers respectively.

In summary, the high growth temperature, rate and other structural properties together with the short growth time are likely to have contributed to the appearance of the discussed defects as shown in Table 4-7. In case of sample MR2482, which had a lower growth temperature, but a faster growth rate and a second barrier type inside the active region, the defect density was highest of all tested samples. The laser structure MR2615 consisted only of one barrier type and was grown at 710 ^{0}C with a reduced growth rate had a reduced amount of dark spot defects and the lowest density of surface features. The growth calibration sample MR2598 is thought to have an identical active region compared to MR2615 but without the DBR. This fact might have caused a reduction of the total strain stored within the structure, which could have enabled the structure to accommodate the strain introduced by the dots more efficiently and resulted in the termination of more threading dislocations at

interfaces rather than the surface. The TSFs are likely the explanation of the difficulties to bond the diamond heatspreader to the sample surface. Furthermore dislocations reduce the laser efficiency, by acting as carrier traps and non-radiative recombination centres. It is believed that a reduction of the defect density can improve bonding as well as laser performance.

4.5 InP QDs for passive mode-locking of Ti:sapphire lasers

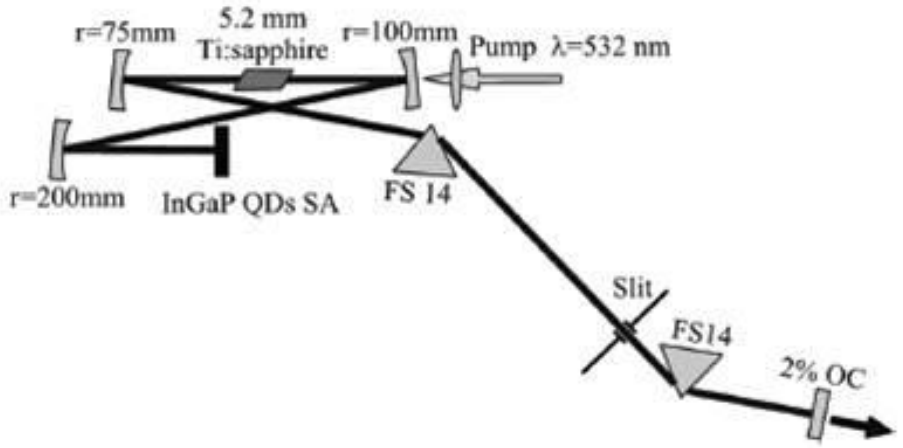

Fig. 4-33 Experimental arrangement of the Ti:sapphire laser cavity. The QD VECSEL device (InGaP QDs SA) used as a saturable absorber end mirror. FS14 – fused silica prisms for group dispersion compensation, Slit – intra-cavity aperture, 2 % OC – output coupler [1].

Properties of self-assembled QDs such as the relatively broad size distribution with its broad gain and absorption bandwidth together with the fast carrier dynamics and low saturation fluence are advantageous properties for the generation of short pulses. One possible application of these properties is stable, self-starting passive mode-locking. Mode-locked (ML) solid state, semiconductor and fibre lasers utilising InGaAs/InAs QDs based semiconductor saturable absorbers mirrors (SESAMs) were demonstrated in the infrared wavelength range [47] from 950-1600 nm. InP QDs allow the extension of the spectral range towards shorter wavelength around 750 nm. Therefore a sample from the first growth campaign (wafer MR2482) was used by Dr. Vasili G. Savitski to passively mode-lock a

Ti:sapphire laser by utilising it as a SESAM structure (see Fig. 4-33 - InGaP QDs SA). The experiments were conducted by Dr. Savitski and the results published in [1]. This work is mentioned at this place for completeness and in order to illustrate a further application range of these devices.

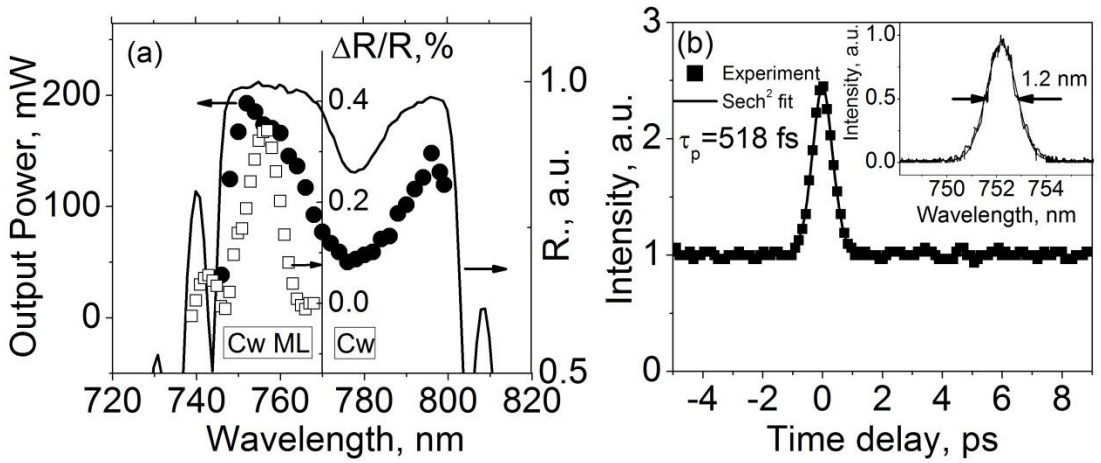

Fig. 4-34 a) Output power through the 2 % output coupling mirror with the InP saturable absorber (SA) mirror installed into the Ti:sapphire cavity (full black circles). Solid line – reflectivity stopband of the SA, saturable absorption spectrum ΔR/R (%) (centre scale, squares). b) autocorrelation trace of the ML pulse intensity with the corresponding optical spectrum (inset) [1].

The structure design of sample MR2482 can be found in Appendix A.1. The reflectivity of the DBR limited the tuning range of the Ti:sapphire laser to 745-790 nm. Despite the broad tuning range, stable cw ML operation was achieved in the range from 749-754 nm. The generated pulses, shown in Fig. 4-34 b) were as short as 518 fs with a time-bandwidth product of 0.33 (corresponding to a spectral width of 1.2 nm). The resonant subcavity setting of the structure (it was designed as a VECSEL device with a resonant subcavity, see Fig. 4-34 a) caused increased absorption losses in the range from 755-790 nm and prevented efficient cw mode-locking in this region. Although passive mode-locking was achieved between 754-767 nm, Q-switching instabilities were dominant in this region even for elevated pulse fluences at the saturable absorber. Above 767 nm, only cw laser operation was observed. Pump-probe measurements at 752 nm, using a commercial Ti:sapphire laser (tuning range 720-940 nm, pulse duration 150 fs) were used to examine the absorption recovery. A biexponential decay characteristic was found with a fast and slow response of 400±50 fs and 300±50 ps. The fast response was attributed to

intra-band carrier thermalisation or trapping and the slow component to band-to-band recombination or recombination through trapping states. Intensity dependent reflectivity measurements revealed a modulation depth of 0.35 %, non-saturable losses of 1.15 % and a saturation fluence of 28 μJ/cm^2. It is stated that particularly the non-saturable losses are considerably higher in this structures with respect to InGaAs samples.

Improvements in the structure design, such as the reduction of the number of QD-layers from 24 to below 10 and a possible use of a resonant or anti-resonant subcavity setting are suggested to reduce the non-saturable and parasitic losses, maintain a sufficient modulation depth, bandwidth, saturation fluence and dispersion.

4.6 Conclusion

The topic of this chapter was the design and characterisation of InP QD based VECSEL structures for emission in the visible red, above 700 nm. Laser structures emitting in the range between 716-752 nm were demonstrated, achieving a maximum output power of over 50 mW for maximum output coupling of 0.2 %, a differential efficiency around 5 % and a near diffraction limited beam profile of $M^2 < 1.1$. The very low output coupling indicates a low tolerance of these structures towards any loss. Wide tuning ranges up to 25 nm were demonstrated within high finesse cavities with a maximum output power of 0.5 mW.

The free running laser emission wavelength is believed to be set by the overlap between the gain of the QD ensemble and the subcavity resonance, as indicated in Fig. 4-17. The close match of the tuning curves with the edge PL peaks during the wavelength tuning experiment suggests that the laser emission is following the gain of the QD ensemble. For none of the examined samples was the PL peak of the QD ensemble matched to the cavity resonance, which lead only to a partial overlap between both. Samples with the best overlap showed better laser performance in terms of threshold power, output power and tuning range. The differential

efficiencies and thermal rollover were similar in all cases, thus it is believed that a better match would lower the threshold power further and allow even higher output powers.

Photoluminescence decay measurements of growth calibration structures without DBR and thus no cavity resonance revealed an increasing PL decay time between 1 and 3.5 ns with increasing QD size. This is related to the increasing confinement of the carriers with increasing dot size. Temperature increase from room temperature up to 80 ^{0}C causes a gradual decrease in lifetime and indicates enhanced thermal carrier escape. The presence of the cavity resonance effect in a complete VECSEL increases the photon lifetime and hence the PL decay time to about 5 ns and is attributed to the resonance position.

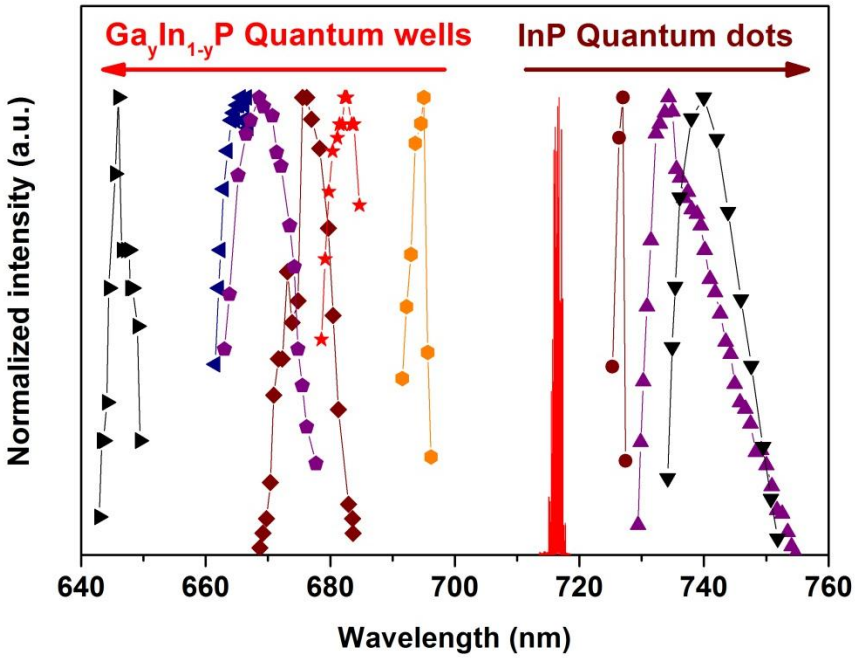

Fig. 4-35 Spectral coverage of VECSEL structures based on the $(Al_xGa_{1-x})_{0.51}In_{0.49}P$, including $Ga_{0.51}In_{0.49}P$ QWs for emission below 700 nm or InP QDs for emission in the range between 700-760 nm.

The thermal management of choice in the presented case was heat extraction from the intra-cavity surface via a liquid capillary bonded diamond heatspreader. This was inhibited by the very rough surface morphology in most of the cases (see Table 4-1). The reason for this roughness was investigated via SEM/CL and TEM imaging. Simultaneous SEM and CL images related every triangular surface feature (TSF) to a

specific dark spot defect (DSD). On the other hand, not every dark spot defect in the CL image was recognisable in the SEM image. This was explained by the use of TEM imaging where threading dislocations (dark spot defects) originated within the first QD-layer group from non-coherently strained QDs and progressed in growth direction towards the surface. Some terminated within the structure (possibly at the carrier confinement layer) before they could reach the surface. In general, the total number of dark spot defects was similar for all examined samples only the number of surface features varied on a larger scale. It was found that the bonding affinity of the surface tends to increase with decreasing surface defect density.

It was possible to extend the spectral coverage of VECSELs, based on the $(Al_xGa_{1-x})_{0.51}In_{0.49}P$ material system from previously 640-690 nm ($Ga_yIn_{1-y}P$ QWs - [6,48,49]) towards 760 nm (InP QDs – this work) and is illustrated in Fig. 4-35. The wavelength range between 700 and 780 nm can only be addressed by InP QDs in case of surface emitting semiconductor laser. A major drawback of the discussed structures is that the growth processes are not as well established as for their InAs counterparts. The discussion on surface roughness has shown that there are still considerable difficulties in the fabrication of defect free InP QD-layers with a high dot density. The optimum composition in terms of emission efficiency for these type of dots is $(Al_{0.2}Ga_{0.8})_{0.51}In_{0.49}P$. Use of tensile strained capping $Ga_yIn_{1-y}P$ QWs for the compensation of the compressive strain introduced by the three dimensional islands might improve also the emission efficiency. However, the increase of the Ga mole fraction (y_{Ga}) in the matrix and the QW cap shifts the emission wavelength towards the 700 nm range and thus closer to a range covered by QWs. It proved also difficult to match the dot ensemble position with the cavity resonances. This might be related to the circumstance that the QD ensemble PL peak emission is established by the help of the growth calibration structures. The actual peak position for the VECSEL structure differed somewhat from the design. The fabrication processes have to be further refined, which would allow the growth of defect free dot layers, necessary for reliable laser devices.

In future, new structures might be grown with the focus on an improved overlap between QD ensemble gain and the RPG/subcavity resonance wavelength. The

comparison in Table 4-7 suggests that a higher tolerance of the structure towards the accommodation of strain could lead to an improved surface smoothness and the termination of more threading dislocations at interfaces. This might be possible by use of slightly tensile strained QWs or strain balancing layers compensating the compressive strain introduced by the QD-layers and could lead to an improvement of both, the emission efficiency and the surface smoothness. The fabrication of completely defect free InP QDs would be very desirable for the further development of InP QD based VECSELs, but seem to be very difficult to achieve at the moment. All this different issues might be addressed in further research projects in order to overcome the current limitations and open up the full potential of InP based QD VECSELs.

References

1. V. G. Savitski, P. J. Schlosser, J. E. Hastie, A. B. Krysa, J. S. Roberts, M. D. Dawson, D. Burns, and S. Calvez, "Passive Mode-Locking of a Ti : Sapphire Laser by InGaP Quantum-Dot Saturable Absorber," Photonics Technology Letters, IEEE **22**, 209-211 (2010).

2. J. Lutti, P. M. Smowton, G. M. Lewis, A. B. Krysa, J. S. Roberts, P. A. Houston, Y. C. Xin, Y. Li, and L. F. Lester, "740 nm InP/GaInP quantum-dot laser with 190 A cm^{-2} room temperature threshold current density," Electronics Letters **41**, 247-248 (2005).

3. N. N. Ledentsov, M. Grundmann, F. Heinrichsdorff, D. Bimberg, V. M. Ustinov, A. E. Zhukov, M. V. Maximov, Z. Alferov, and J. A. Lott, "Quantum-dot heterostructure lasers," Selected Topics in Quantum Electronics, IEEE Journal of **6**, 439-451 (2000).

4. M. V. Maximov, I. V. Kochnev, Y. M. Shernyakov, S. V. Zaitsev, N. Yu. Gordeev, A. F. Tsatsul'nikov, A. V. Sakharov, I. L. Krestnikov, P. S. Kop'ev, N. N. Ledentsov, D. Bimberg, A. O. Kosogov, P. Werner, and U. Gösele, "InGaAs/GaAs Quantum Dot Lasers with Ultrahigh Characteristic Temperature (T_0=385 K) Grown by Metal Organic Chemical Vapour Deposition," Jpn. J. Appl. Phys. **36**, 4221-4223 (1997).

5. J. E. Hastie, L. G. Morton, A. J. Kemp, M. D. Dawson, A. B. Krysa, and J. S. Roberts, "Tunable ultraviolet output from an intracavity frequency-doubled red

vertical-external-cavity surface-emitting laser," Applied Physics Letters **89**, 061114-3 (2006).

6. J. Hastie, S. Calvez, M. Dawson, T. Leinonen, A. Laakso, J. Lyytikäinen, and M. Pessa, "High power CW red VECSEL with linearly polarized TEM00 output beam," Opt. Express **13**, 77-81 (2005).

7. J. Hastie, L. Morton, S. Calvez, M. Dawson, T. Leinonen, M. Pessa, G. Gibson, and M. Padgett, "Red microchip VECSEL array," Opt. Express **13**, 7209-7214 (2005).

8. B. Chance, M. Cope, E. Gratton, N. Ramanujam, and B. Tromberg, "Phase measurement of light absorption and scatter in human tissue," Review of Scientific Instruments **69**, 3457-3481 (1998).

9. I. Vurgaftman, J. R. Meyer, and L. R. Ram-Mohan, "Band parameters for III-V compound semiconductors and their alloys," Journal of Applied Physics **89**, 5815-5875 (2001).

10. S. P. Najda, A. H. Kean, M. D. Dawson, and G. Duggan, "Optical measurements of electronic bandstructure in AlGaInP alloys grown by gas source molecular beam epitaxy," Journal of Applied Physics **77**, 3412-3415 (1995).

11. J. H. Ryou, R. D. Dupuis, G. Walter, J. Holonyak, D. T. Mathes, R. Hull, C. V. Reddy, and V. Narayanamurti, "Properties of InP self-assembled quantum dots embedded in $In_{0.49}(Al_xGa_{1-x})_{0.51}P$ for visible light emitting laser applications grown by metalorganic chemical vapor deposition," Journal of Applied Physics **91**, 5313-5320 (2002).

12. W. M. Schulz, M. Eichfelder, R. bach, M. Jetter, and P. Michler, "Low Threshold InP/AlGaInP Quantum Dot In-Plane Laser Emitting at 638 nm," Appl. Phys. Express **2**, 112501 (2009).

13. P. J. Schlosser, J. E. Hastie, S. Calvez, A. B. Krysa, and M. D. Dawson, "InP/AlGaInP quantum dot semiconductor disk lasers for CW TEM_{00} emission at 716 - 755 nm," Opt. Express **17**, 21782-21787 (2009).

14. W. M. Schulz, R. bach, M. Reischle, G. J. Beirne, M. Bommer, M. Jetter, and P. Michler, "Optical and structural properties of InP quantum dots embedded in $(Al_xGa_{1-x})_{0.51}In_{0.49}P$," Phys. Rev. B **79**, 035329 (2009).

15. Krysa, A. B., Influence of the Ga content in the InGaP cap on InP QDs emission., Personal communication, Personal Communication, 2011.

16. D. Bimberg, M. Grundmann, and N. N. Ledentsov, *Quantum Dot Heterostructures*, D. Bimberg, ed., (John Wiley & Sons Ltd, Baffins Lane, Chichester, West Sussex PO 19 1UD, England, D-69469 Weinheim, Germany, 1999).

17. Qiu, Y, Krysa, A. B., and Walther, T. STEM imaging of InP/AlGaInP quantum dots. Journal of Physics: Conference Series 245[1], 012087. 2010.

18. J. Porsche, A. Ruf, M. Geiger, and F. Scholz, "Size control of self-assembled InP/GaInP quantum islands," Journal of Crystal Growth **195**, 591-595 (1998).

19. A. B. Krysa, S. L. Liew, J. C. Lin, J. S. Roberts, J. Lutti, G. M. Lewis, and P. M. Smowton, "Low threshold InP/AlGaInP on GaAs QD laser emitting at ~740nm," Journal of Crystal Growth **298**, 663-666 (2007).

20. T. D. Germann, A. Strittmatter, U. W. Pohl, D. Bimberg, J. Rautiainen, M. Guina, and O. G. Okhotnikov, "Quantum-dot semiconductor disk lasers," Journal of Crystal Growth **310**, 5182-5186 (2008).

21. M. Butkus, J. Rautiainen, O. G. Okhotnikov, C. J. Hamilton, G. P. A. Malcolm, S. S. Mikhrin, I. L. Krestnikov, D. A. Livshits, and E. U. Rafailov, "Quantum Dot Based Semiconductor Disk Lasers for 1-1.3 μm," Selected Topics in Quantum Electronics, IEEE Journal of **PP**, 1-9 (2011).

22. C. M. Reaves, V. Bressler-Hill, S. Varma, W. H. Weinberg, and S. P. DenBaars, "Characterization of MOCVD-grown InP on InGaP/GaAs(001)," Surface Science **326**, 209-217 (1995).

23. P. M. Smowton, J. Lutti, G. M. Lewis, A. B. Krysa, J. S. Roberts, and P. A. Houston, "InP-GaInP quantum-dot lasers emitting between 690-750 nm," Selected Topics in Quantum Electronics, IEEE Journal of **11**, 1035-1040 (2005).

24. P. M. Smowton, M. Al-Ghamdi, and A. B. Krysa, "CMD6 - InP / AlGaInP on GaAs Quantum Dot Lasers," in *CLEO 2007 Conference on Lasers and Electro-Optics*, (2007), pp. 1-2.

25. J. Lutti, P. M. Smowton, G. M. Lewis, P. Blood, A. B. Krysa, J. C. Lin, P. A. Houston, A. J. Ramsay, and D. J. Mowbray, "Gain saturation in InP/GaInP quantum-dot lasers," Applied Physics Letters **86**, 011111-011113 (2005).

26. G. M. Lewis, J. Lutti, P. M. Smowton, P. Blood, A. B. Krysa, and S. L. Liew, "Optical properties of InP/GaInP quantum-dot laser structures," Applied Physics Letters **85**, 1904-1906 (2004).

27. T. D. Germann, A. Strittmatter, J. Pohl, U. W. Pohl, D. Bimberg, J. Rautiainen, M. Guina, and O. G. Okhotnikov, "Temperature-stable operation of a quantum dot semiconductor disk laser," Applied Physics Letters **93**, 051104-3 (2008).

28. F. Scholz, A. Hangleiter, H. Schweizer, and M. Pilkuhn, "Ordering in GaInP: epitaxy, basic characteristics and device relevance," III-Vs Review **10**, 38-42 (1997).

29. J. Porsche, M. Ost, T. Riedl, A. Hangleiter, and F. Scholz, "Lasing from excited states in self-assembled InP/GaInP quantum islands," Materials Science and Engineering B **74**, 263-268 (2000).

30. I. Friel, S. L. Clewes, H. K. Dhillon, N. Perkins, D. J. Twitchen, and G. A. Scarsbrook, "Control of surface and bulk crystalline quality in single crystal diamond grown by chemical vapour deposition," Diamond and Related Materials **18**, 808-815 (2005).

31. Z. L. Liau, "Semiconductor wafer bonding via liquid capillarity," Applied Physics Letters **77**, 651-653 (2000).

32. C. Y. Liu, S. Yuan, J. R. Dong, S. J. Chua, M. C. Y. Chan, and S. Z. Wang, "Temperature-dependent photoluminescence of GaInP/AlGaInP multiple quantum well laser structure grown by metalorganic chemical vapor deposition with tertiarybutylarsine and tertiarybutylphosphine," Journal of Applied Physics **94**, 2962-2967 (2003).

33. J. E. Hastie, "High power surface emitting semiconductor lasers," (2004).

34. A. J. Kemp, A. J. Maclean, J. E. Hastie, S. A. Smith, J. M. Hopkins, S. Calvez, G. J. Valentine, M. D. Dawson, and D. Burns, "Thermal lensing, thermal management and transverse mode control in microchip VECSELs," Applied Physics B: Lasers and Optics **83**, 189-194 (2006).

35. S. C. Auzanneau, M. Calligaro, M. Krakowski, F. Klopf, S. Deubert, J. P. Reithmaier, and A. Forchel, "High brightness GaInAs/(Al)GaAs quantum-dot tapered lasers at 980 nm with high wavelength stability," Applied Physics Letters **84**, 2238-2240 (2004).

36. F. Klopf, S. Deubert, J. P. Reithmaier, and A. Forchel, "Correlation between the gain profile and the temperature-induced shift in wavelength of quantum-dot lasers," Applied Physics Letters **81**, 217-219 (2002).

37. T. D. Germann, A. Strittmatter, J. Pohl, U. W. Pohl, D. Bimberg, J. Rautiainen, M. Guina, and O. G. Okhotnikov, "High-power semiconductor disk laser based on InAs/GaAs submonolayer quantum dots," Applied Physics Letters **92**, 101123 (2008).

38. http://physics.nist.gov/PhysRefData/Handbook/download.htm, NIST, "Handbook of Basic Atomic Spectroscopic Data," 2011, National Institute of Standards and Technology (NIST)

39. Hingsammer, J. Messunsicherheiten. 2003.

40. S. L. Chuang, *Physics of Photonic Devices*, (John Wiley & Sons, Inc., Hoboken, New Jersey, 2009).

41. Carl Wilmsen, Henryk Temkin, and Larry A.Coldren, *Vertical-Cavity Surfrace-Emitting Lasers: Design, Fabrication, Characterization, and Applications*, (Cambridge University Press, Cambridge, UK, 1999).

42. D. Drouin, A. R. Couture, D. Joly, X. Tastet, V. Aimez, and R. Gauvin, "CASINO V2.42 - A Fast and Easy-to-use Modeling Tool for Scanning Electron Microscopy and Microanalysis Users," Scanning **29**, 92-101 (2007).

43. D. B. Darby and G. R. Booker, "Scanning electron microscope EBIC and CL micrographs of dislocations in GaP," Journal of Materials Science **12**, 1827-1833 (1977).

44. T. Akagi, K. Kosaka, S. Harui, D. Muto, H. Naoi, T. Araki, and Y. Nanishi, "Correlation Between Threading Dislocations and Nonradiative Recombination Centers in InN Observed by IR Cathodoluminescence," Journal of Electronic Materials **37**, 603-606 (2008).

45. F. Bugge, U. Zeimer, M. Sato, M. Weyers, and G. Tränkle, "MOVPE growth of highly strained InGaAs/GaAs quantum wells," Journal of Crystal Growth **183**, 511-518 (1998).

46. W. Seifert, N. Carlsson, J. Johansson, M. E. Pistol, and L. Samuelson, "In situ growth of nano-structures by metal-organic vapour phase epitaxy," Journal of Crystal Growth **170**, 39-46 (1997).

47. E. U. Rafailov, M. A. Cataluna, and W. Sibbett, "Mode-locked quantum-dot lasers," Nat Photon **1**, 395-401 (2007).

48. A. Smith, J. E. Hastie, H. D. Foreman, T. Leinonen, M. Guina, and M. D. Dawson, "GaN diode-pumping of red semiconductor disk laser," Electronics Letters **44**, 1195-1196 (2008).

49. S. Calvez, J. E. Hastie, M. Guina, O. G. Okhotnikov, and M. D. Dawson, "Semiconductor disk lasers for the generation of visible and ultraviolet radiation," Laser & Photonics Review **3**, 407-434 (2009).

Chapter 5:

Intra-cavity sum frequency generation of 593 nm light

A common way to expand the wavelength coverage of lasers, especially into the application rich near-UV and visible region, is via harmonic frequency generation using non-linear optical effects. Efficient non-linear conversion requires an intense optical field and therefore high brightness beams, often high pulse energy. For cw lasers high intensities are accessed intracavity.

High pump intensities are usually achieved by tight beam focussing inside a non-linear crystal. Efficient mode-matching of the fundamental and generated modes requires a high beam quality. This is usually difficult to achieve with standard edge emitting laser devices and makes beam reshaping arrangements necessary. More advanced edge-emitters, such as tapered laser diodes, are able to give good beam qualities together with high output powers, but their use within an extended cavity, in order to get access to wavelength tunable, high intra-cavity powers, is not straightforward.

VECSELs with high intra-cavity powers and near diffraction limited beam are ideal for this purpose. As it was shown in the introduction Chapter 1, the availability of different semiconductor materials, alloy compositions and substrates has enabled the extension of the fundamental wavelength coverage of VECSELs, e.g. with GaAs substrates from 1 μm [(Al)InGaAs] down to the visible red 640 nm [(Al)GaInP] and into the near- IR region up to 1.3 μm using dilute Nitride [GaInNAs]. Further material development and quality of II-VI materials and III-Nitrides are promising for the extension of the fundamental emission coverage of semiconductor lasers and possibly VECSELs towards shorter wavelength into the visible and near UV range. Despite these potentials and achievements with respect to wavelength coverage, there

are application rich regions which are not easily accessed by this laser type via fundamental emission. Especially the visible range, important for many bio-photonic and medical applications is affected by this shortcoming [1,2]. The current way to achieve these wavelengths is via harmonic generation from the near-IR. VECSELs are low gain devices with an optimum output coupling coefficient in the range of only few per cent. In order to match this, non-linear crystals do not need high non-linear coefficients. Semiconductors are not able to store gain due to the short upper state carrier lifetimes in the nanosecond range and thus avoid dynamic fluctuations, which are common in solid-state laser devices, with upper state lifetimes in the microsecond range, as explained in [3]. Furthermore semiconductor lasers on the other hand exhibit a strong gain coupling, where neighbouring modes have a similar spectral gain and gain distribution [4] and thus tend to operate single mode. The generated output beam intensity is thus more stable as VECSELs are not affected by the so called 'green problem'.

VECSELs were already used in 1999 to produce SHG laser light and to date there have been a variety of visible wavelengths accessible at high output powers from the near-UV to the red [5-9]. Even QD-based VECSEL structures have recently been reported to be used for SHG, which was already mentioned in previous chapters. Simultaneous SHG and SFG in a VECSEL for mode coupling experiments was reported before by Hartke et al. [4], where the VECSEL was forced to operate with two longitudinal modes, and where their spectral mode separation was adjusted via etalons. Commercial products utilising SHG inside VECSELs have also been available for several years now [6,10].

Despite the good performance of VECSELs towards high power and tunable SHG, wavelengths in the visible range can only be covered where adequate devices in the IR exist. In this term, SFG introduces some more versatility as the contributing fundamental waves (λ_1, λ_2) are non-degenerate and new wavelengths can be generated according to mixing equation [5-1]:

$$\frac{1}{\lambda_{SFG}} = \frac{1}{\lambda_1} + \frac{1}{\lambda_2} \qquad \text{Equation [5-1]}$$

The aim of this project was to demonstrate coherent light at 593 nm via sum frequency mixing of the high intra-cavity field of an InGaAs QW-based VECSEL emitting around 1064 nm with a single passing diode pumped Nd:YVO_4 laser beam at a wavelength of 1342 nm. The diode-pumped solid-state laser (DPSL) together with the nonlinear crystal were provided by our collaborators at the Technical University of Denmark (DTU). The experiment was conducted in our laboratory at the Institute of Photonics in collaboration with Martin T. Andersen, a visiting PhD student from DTU. The results were reported in [11].

5.1 Theory of nonlinear frequency mixing

This theoretical section is based mainly on the study of the first two chapters of Robert W. Boyd's "Nonlinear Optics" book [12] and is herewith explicitly mentioned as the source of most of the used formulas, derivations and theoretical explanations. Where information was received from other sources, citations are given.

In conventional optics, where the electrical field strength, $\tilde{E}(z,t)$, of a collimated and monochromatic beam propagating in the z direction is low, it is linearly proportional to the induced polarisation, $\tilde{P}(z,t)$, with the linear susceptibility $\chi^{(1)}$ as proportionality constant.

$$\tilde{P}^{(1)}(z,t) = \epsilon_0 \chi^{(1)} \cdot \tilde{E}(z,t) + c.c \qquad \text{Equation [5-2]}$$

and where

$$\tilde{E}(z,t) = Ae^{i(kz-\omega t)} + c.c \qquad \text{Equation [5-3]}$$

$$k = \frac{n\omega}{c}, \qquad n = \sqrt{\epsilon^{(1)}(\omega)}, \qquad \text{Equation [5-4]}$$

The tilde symbol describes a rapidly-varying unit with time and c.c. stands for complex conjugate terms. ϵ_0 is the vacuum permittivity, A, and ω are the amplitude and angular frequency respectively. k is the wave-vector, experiencing a refractive index n at the angular frequency ω. c the speed of light in free space. The amplitude

$A(\omega)$ is slowly changing with propagation in the direction z and can be approximated as a constant; it can thus be defined as $E = Ae^{-ikz}$ and equation [5-3] becomes:

$$\tilde{E}(t) = E \cdot e^{-i\omega t} + c.c \qquad \text{Equation [5-5]}$$

The invention of the laser allowed the generation of electric field strengths in the optical range that were strong enough to force a nonlinear response. For this purpose, equations [5-2] and [5-5] can be extended to a more general form including the nonlinear terms.

$$\tilde{P}(t) = \tilde{P}^{(1)}(t) + \tilde{P}^{(2)}(t) + \cdots. \qquad \text{Equation [5-6]}$$

Here, $\tilde{P}^{(2)}(t)$ is the second-order nonlinear polarization. Higher order nonlinear processes are not regarded here as they are not necessary for the discussion of sum frequency generation (SFG). The second-order nonlinear polarisation is defined as the sum over the contributing beam components with their amplitude E_n and frequency, ω_n:

$$\begin{aligned}\tilde{P}^{(2)}(t) = \epsilon_0\chi^{(2)}\big[&E_1^2e^{-2i\omega_1 t} + E_2^2e^{-2i\omega_2 t} \\ &+ 2E_1E_2e^{-i(\omega_1+\omega_2)t} + 2E_1E_2^*e^{-i(\omega_1-\omega_2)t} \\ &+ c.c.\big] + 2\chi^{(2)}[E_1E_1^* + E_2E_2^*]\end{aligned} \qquad \text{Equation [5-7]}$$

with $\chi^{(2)}$ being the second-order nonlinear optical susceptibility. This can be also expressed as:

$$\tilde{P}^{(2)}(t) = \sum_n P(\omega_n)e^{-i\omega_n t}, \qquad \text{Equation [5-8]}$$

The first and second term in equation [5-7] describe second harmonic generation (SHG - $\omega_3 = 2\omega_{1,2}$) of an incident field. The third and fourth term stand for sum frequency generation (SFG → $\omega_3 = \omega_1 + \omega_2$) and difference frequency generation (DFG →$\omega_3 = \omega_1 - \omega_2$) respectively. DFG is also referred to as optical parametric amplification as the incident field with lower frequency (ω_1) is amplified at the expense of the higher frequency incident field ($\omega_2 > \omega_1$). These are so-called parametric processes; that is the contributing photon energies need to be conserved because of the very short-lived virtual energy levels taking part in the conversion

process, where energy storage such as in absorption processes is not possible. A schematic illustration of these processes is shown in Fig. 5-1. The frequency independent fifth term is known as optical rectification (OR) and describes the building up of a DC polarisation dependent on the intensity of the incident beam [13]. Table 5-1 summarises the different components of the second-order nonlinear polarisation and sets them into context to the specific non-linear processes. Second order non-linear processes are only possible in non-linear crystals which have no centre of inversion (non-centrosymmetric). For a crystal with a centre of inversion the contribution of the $\chi^{(2)}$-susceptibility disappears.

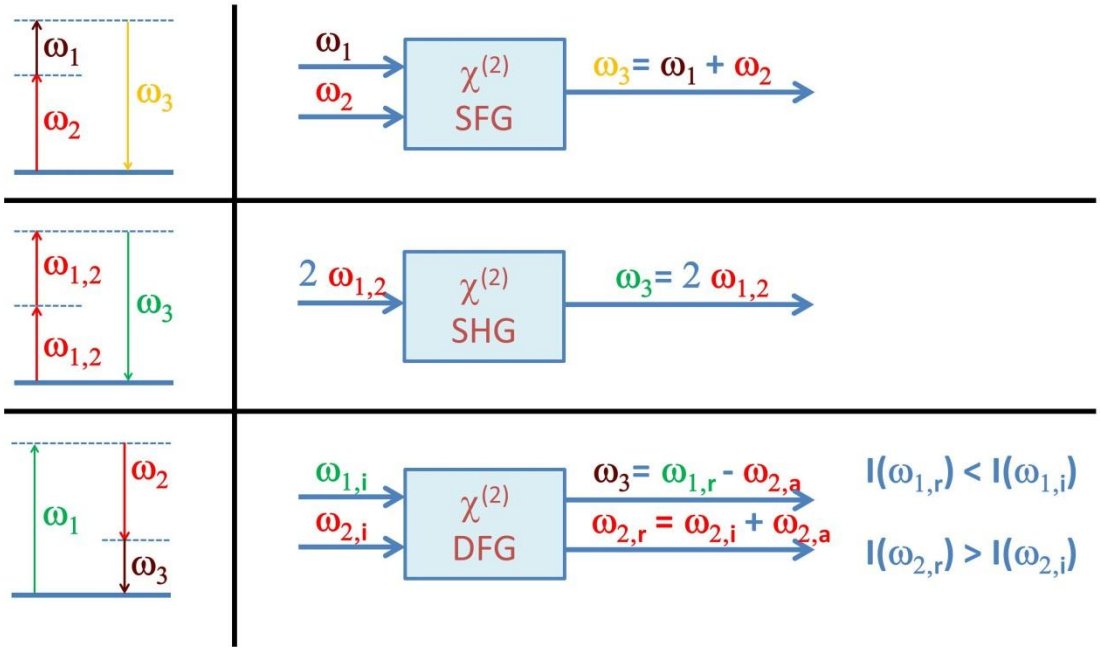

Fig. 5-1 Left: Virtual energy level diagram (dashed horizontal lines) describe the frequency generation processes SFG, SHG and DFG. Right: Schematic of the conversion processes in a second-order nonlinear medium. Indexes i, r and a denote incident, residual and amplified beams respectively

Name	Formula
SHG	$P(2\omega_1) = \epsilon_0\chi^{(2)}E_1^2$ or $P(2\omega_2) = \epsilon_0\chi^{(2)}E_2^2$
SFG	$\boldsymbol{P(\omega_1 + \omega_2) = 2\epsilon_0\chi^{(2)}E_1E_2}$
DFG	$P(\omega_1 - \omega_2) = 2\epsilon_0\chi^{(2)}E_1E_2^*$
OR	$P(0) = 2\epsilon_0\chi^{(2)}(E_1E_1^* + E_2E_2^*)$

Table 5-1 Second-order nonlinear optical processes, describing second harmonic generation (SHG), sum frequency generation (SFG), difference frequency generation (DFG) and optical rectification (OR).

Effects related to sum frequency generation such as angle, temperature and wavelength tuning as well as phase-matching and quasi-phase-matching in nonlinear crystals can be described by coupled wave-equations in a lossless but dispersive medium. This is introduced in the following on the example of SFG, where two incident collimated and monochromatic optical fields with amplitudes A_1, A_2 and angular frequencies ω_1, ω_2 propagate in z direction. Their interaction with the nonlinear medium causes the generation of the sum frequency $\omega_3 = \omega_1 + \omega_2$ with amplitude A_3.

Combining equations [5-3] and [5-8] under consideration that $\omega_3 = \omega_1 + \omega_2$, the nonlinear polarisation can be expressed by equation [5-9]:

$$\tilde{P}_3^{(2)}(\omega_3 = \omega_1 + \omega_2) = 4 d_{eff} A_1 A_2 e^{i[(k_1+k_2)z - i(\omega_2+\omega_1)t]} \qquad \text{Equation [5-9]}$$

where d_{eff} is the effective nonlinear coupling coefficient. d_{eff}, is a scalar defined for each direction of beam propagation and polarisation with respect to the optic axis (i.e. uniaxial crystals). It can be calculated for each crystal class and for each phase matching condition (type I, II or QPM) of the incident fundamental waves by using the crystal symmetry and its effects on the interacting fields. This was described for uniaxial crystal symmetry by Midwinter et al in [14] under consideration of the contracted notation of the Kleinman symmetry in [15].

With the help of equation [5-9] three coupled-amplitude equations can be derived, of which only one is important for SFG and stated here:

$$\frac{dA_3}{dz} = \frac{8\pi i d_{eff} \omega_3^2}{k_3 c^2} A_1 A_2 e^{-i\Delta k z} \qquad \text{Equation [5-10]}$$

where momentum mismatch Δk is defined by:

$$\Delta k = k_1 + k_2 - k_3 \qquad \text{Equation [5-11]}$$

Perfect phase-matching requires $\Delta k = 0$, i.e. there is no variation in the phase relationship between the SFG wave and the nonlinear polarisation $\tilde{P}_3^{(2)}(k_3)$ according to $k_3 = k_1 + k_2$ and the conversion efficiency is at its highest. Equation

[5-11] assumes low conversion, where the amplitudes of the two fundamental waves are not depleted by the generation process and can be regarded to remain constant. The amplitude of the generated coherent beam A_3 increases linearly with the penetration length z in the crystal and the beam intensity increases with z^2.

In the more typical case of mismatched phase condition ($\Delta k \neq 0$), the amplitude A_3 emerging from the crystal can be expressed by equation [5-12] with respect to the boundary conditions $z = 0..L$, where L is the crystal length.

$$A_3(L) = \frac{8\pi i d_{eff}\omega_3^2 A_1 A_2}{k_3 c^2}\int_{z=0}^{z=L} e^{-i\Delta k z}dz \qquad \text{Equation [5-12]}$$

resulting in the intensity dependent relation of the generated sum frequency field:

$$I_3 = I_1 I_2 \frac{2d_{eff}^2\omega_3^2}{\epsilon_0 c^3 n_1 n_2 n_3} L^2 sinc^2\left(\frac{\Delta k L}{2}\right) \qquad \text{Equation [5-13]}$$

where $I_i = \frac{n_i c|A_i|^2}{2\pi}$, and $\left|\frac{e^{-i\Delta k L}-1}{i\Delta k}\right|^2 \equiv L^2 sinc^2\left(\frac{\Delta k L}{2}\right)$, is the phase mismatch factor.

This equation can be also expressed with respect to the power of a circular beam by the relation, $P_i = I_i \pi r_i^2$ where r_i is the beam radius. Substitution yields,

$$P_3 = P_1 P_2 \frac{2d_{eff}^2\omega_3^2}{\pi\epsilon_0 c^3 n_1 n_2 n_3}\frac{r_3^2}{r_1^2 r_2^2} L^2 sinc^2\left(\frac{\Delta k L}{2}\right) \qquad \text{Equation [5-14]}$$

For focussed Gaussian beams, the sum frequency power is expressed as [16]:

$$P_3(k) = P_1 P_2 \frac{4d_{eff}^2\omega_3^2 L}{\pi\epsilon_0 c^3 n_1 n_2 n_3}\frac{k_1 k_2}{k_3} h_m \qquad \text{Equation [5-15]}$$

where h_m is the Boyd-Kleinman factor and dependent on the "optimisable parameters" phase mismatch, focal position and strength of focussing, furthermore on the birefringence and absorption coefficient.

Fig. 5-2 (left) illustrates the dependence of the conversion efficiency on the phase mismatch factor. As the phase mismatching increases, the phase of the generated wave differs increasingly from the nonlinear polarization $\tilde{P}_3^{(2)}(k_3)$ until it is

completely out of phase for $L \gtrsim {}^{1}/_{\Delta k}$ and energy can flow back from the SFG to the fundamental waves, as illustrated on the right hand side of Fig. 5-2 (red graph). This is defined as the coherent build-up length $L_{coh} \gtrsim {}^{2}/_{\Delta k}$, which is limited by the de-phasing due to the dispersion between generated and fundamental beams [17]. As mentioned before, it is sometimes not possible to achieve perfect phase-matching, e.g. for the present case of three-wave mixing processes, for collinear beam propagation and a normal dispersive medium; where the refractive index of the nonlinear crystal behave according to the relation $n_1(\omega_1) \leq n_2(\omega_2) \leq n_3(\omega_3)$, with the angular frequencies $\omega_1 \leq \omega_2 \leq \omega_3$. There are nonetheless technical procedures to achieve phase matching (PM), such as the application of:

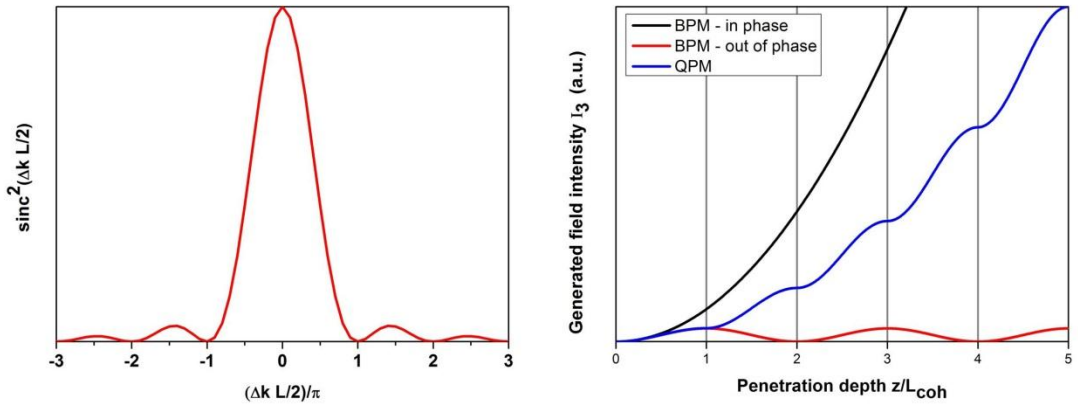

Fig. 5-2 Left: Calculated phase mismatch factor $sinc^2\left(\frac{\Delta kL}{2}\right)$ as a function of the phase mismatch and/or the interaction length. Right: The generated field intensity behavior with penetration length inside a nonlinear medium in the case of perfect BPM (black), out of phase BPM (red), and QPM (blue).

- Anomalous dispersion near the absorption levels of a material where the refractive index decreases with frequency.
- Birefringence where the difference of the ordinary (o) and extraordinary (e) index of refraction of a crystal is used to compensate for the dispersion. Due to birefringence of some crystal classes the refractive index of the two polarization components of a passing beam are different and can be used for so called birefringent phase-matching (BPM). In this case the sum of the phase velocities of the fundamental waves is adjusted via the refractive indexes in a way to equal the generated group velocity. Two types of BMP can be distinguished in uniaxial crystals[12,14]:

Table 5-2 illustrates the relationship between the polarization directions of the incident and generated waves. For type I birefringent phase-matching the wave polarization of the incident beams is in the same direction, whereas for type II perpendicular to each other. Besides that, BPM can be achieved in different ways by: a) Critical or angle phase-matching [18] [17]; b) Noncritical, temperature or 90^0 phase-matching; c) non-colinear phase-matching [19].

- Quasi phase-matching (QPM) is the method of choice in this project. QPM is a method of extending the nonlinear interaction length by compensation of the accumulated phase mismatch inside the non-linear medium via a periodic succession of antiparallel oriented crystal directions (effective nonlinear coupling coefficient, d_{eff}) with thicknesses equal to the L_{coh}. It was first suggested by Armstong et al. in 1962 [20].

Type of PM	Polarization relation	PM condition	Type of uniaxial crystal
Type I	ooe	$n_1^o\omega_1 + n_2^o\omega_2 = n_3^e\omega_3$	negative ($n_e < n_o$)
	eeo	$n_1^e\omega_1 + n_2^e\omega_2 = n_3^o\omega_3$	positive ($n_e > n_o$)
Type II	oeo	$n_1^o\omega_1 + n_2^e\omega_2 = n_3^o\omega_3$	negative ($n_e < n_o$)
	eoe	$n_1^e\omega_1 + n_2^o\omega_2 = n_3^e\omega_3$	positive ($n_e > n_o$)

Table 5-2 Types of phase matching condition for uniaxial crystals together with the relation of the contributing beam polarization directions required to meet these conditions.

In contrast to BPM, where the polarization of the interacting beams and the birefringence behaviour are critical conditions, this is not a requirement for QPM. Furthermore, wavelength interactions impossible for BPM become accessible. QPM is also not restricted to birefringent materials. Noncritical phase-matching for all interactions is possible, e.g. where all three waves are polarized in the same direction, hence allowing access to the d_{33} nonlinear coefficient. The d_{33} nonlinear coefficient is usually the largest accessible coefficient and can be much larger than the highest accessible BPM nonlinear coefficient [21] for a specific material.

The periodic inversion of the effective nonlinear coefficient d_{eff} used for QPM introduces a further wave vector into equation [5-11], the phase momentum mismatch.

$$\Delta k_{QPM} = k_1 + k_2 - k_3 - \frac{2\pi \cdot m}{\Lambda} \qquad \text{Equation [5-16]}$$

In this form m stands for an integer multiple of L_{coh} and thus of the required poling period for phase-matching, where $\Delta k_{QPM} = 0$.

$$\Lambda = 2 \cdot m \cdot L_{coh} = \frac{2\pi \cdot m}{k_1 + k_2 - k_3} \qquad \text{Equation [5-17]}$$

For optimum conversion efficiency, $m = 1$. Poling periods with a higher order of twice L_{coh} also meet the phase-matching criteria, but the efficiency decreases with any increase in poling-order. Further development of the poling processes made structures with aperiodic and chirped [22], fan-out [23] and multi-sectioned (channelled) poling possible as can be seen schematically in Fig. 5-3. Especially chirped, fan-out and aperiodically poled crystals are used not only for frequency generation and tuning purposes but also in ultra-fast laser applications for beam reshaping etc.

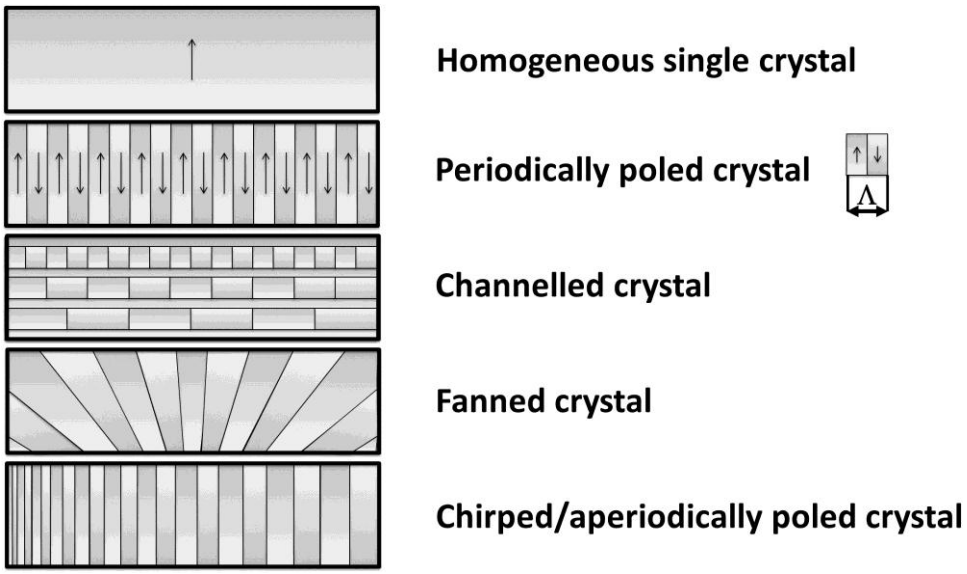

Fig. 5-3 Different types of quasi phase-matching. From top to bottom, homogeneous single crystal, periodically poled crystal with poling period Λ, multi-section crystal with differently poled channels, fan-out poling and chirped/aperiodic poled crystal.

As equation [5-7] implies, all interactions (SHG, SFG, DFG and OR) are permitted by the second-order susceptibility at the same time. Practically, only one of the frequency dependent effects is present as the phase-matching condition, required for an efficient conversion, is usually met only for a single case. Thus the crystal properties have to be carefully designed for a specific purpose.

5.2 Nonlinear crystals

Reviewing the literature on the use of nonlinear crystals for intra-cavity SHG inside VECSEL cavities revealed a variety of different materials, even for the generation of the same wavelength, as can be found in [24] and shown in Table 5-3 In most cases, Lithium Triborate (LBO) or β-Barium Borate (BBO) are used. The reason for this might be found in the large acceptance bandwidth around room temperature and the high damage threshold of these two crystals. The larger effective conversion efficiencies of periodically-poled Lithium Niobate (ppLN), periodically-poled Potassium Titanyl Phosphate (ppKTP) and Potassium Niobate (KNbO) were possibly the criteria of choice for the other groups. The choice of crystal is not always straightforward and one has to decide on the basis of the specific application. In general, BPM crystals can be produced with larger dimensions, and thus larger apertures compared to QPM crystals. With respect to power scaling, this enables BPM crystals with high damage threshold to be used in high power applications. QPM crystals in this respect are restricted to apertures of 1-2 mm due to limitations of their poling process. On the other hand QPM enables the exploitation of the highest nonlinear coefficient (NLC), the d_{33} direction. Other important considerations are the thermal, angular and spectral acceptance bandwidths, i.e. whether the nonlinear crystal has to be temperature controlled or whether phase-matching is very sensitive towards mechanical misalignments.

In this work, a Brewster-cut periodically-poled potassium titanyl phosphate ($ppKTiOPO_3$ or ppKTP) crystal was used for quasi-phase-matched sum frequency mixing of a single passing 1342 nm beam and a resonant 1064 nm beam within the

VECSEL cavity. The crystal length was 10 mm and fabricated for first order QPM with a poling period of 12.65 μm. This crystal allowed the utilization of the large d_{33} nonlinear coefficient for efficient noncritical phase matching, with all contributing waves being polarized in the same direction. This in turn allowed the use of a Brewster-cut crystal, cut for the resonant wavelength so that AR coatings were not required. While 1064 nm is an almost arbitrary wavelength within the tuning range of the VECSEL, the crystal was already available having been used for previous work done by our collaborators at DTU for the generation of 593 nm coherent light via mixing of a resonant 1342 nm field and a single passing 1064 nm beam, both from diode-pumped Nd:YVO4 lasers [25].

Crystal	**Transparency range (nm)**	**Damage threshold (MW/cm^2)**	**highest NLC (pm/V)**	**Operation mode**	**Phase matching**	**Remarks**
BBO [9,26,27]	190-3500	NA	d_{31}=±2.22 d_{32}=±0.16	M-H, USP	Type I, II	55^0C thermal ABW
BiBO [7,28]	286-2500	>300	d_{11}=2.53 d_{25}=2.8	M-H		Broad thermal ABW
KNbO [29]	400-4500	350	d_{31}=-15.8 d_{32}=-18.3	L-M	Type I, NCPM	Narrow thermal ABW Tuning: -40 to 180^0C
ppKTP	350-4500	>500	d_{32}=±3.9 d_{33}=±16.9	L-M, cw	QPM	Broad angular & thermal ABW
LBO [30-32]	160-2600	>1000	d_{31}=1.09 d_{32}=1.17	H, cw & P	Type I, II, NCPM	Broad angular ABW small walk-off angle
ppLN [33]	420-5200	100	d_{31}=-4.52 d_{33}=31.5	L-M	QPM	Broad, tunable PM

Table 5-3 Selection of some non-linear crystals used in VECSEL devices for up-conversion from the NIR to near-UV and VIS range. BBO – β-Barium Borate, BiBO – Bismuth Triborate, KNbO – Potassium Niobate, KTP – Potassium Titanyl Phosphate, LBO – Lithium Triborate, LN – Lithium Niobate, NLC – non-linear coefficient; L, M, H – low, middle, high power range respectively, cw – continuous wave, P – pulsed, USP – ultra short pulses, NCPM – non-critical phase matching, ABW – acceptance bandwidth.This information is taken from manufacturer crystal data sheets [34,35].

5.3 Experimental arrangement

Fig. 5-4 shows a schematic of the experimental arrangement, which is divided into the 1064 nm InGaAs QW-based VECSEL cavity and the Nd:YVO_4 solid-state laser cavity with the beam redirection and focussing arrangement.

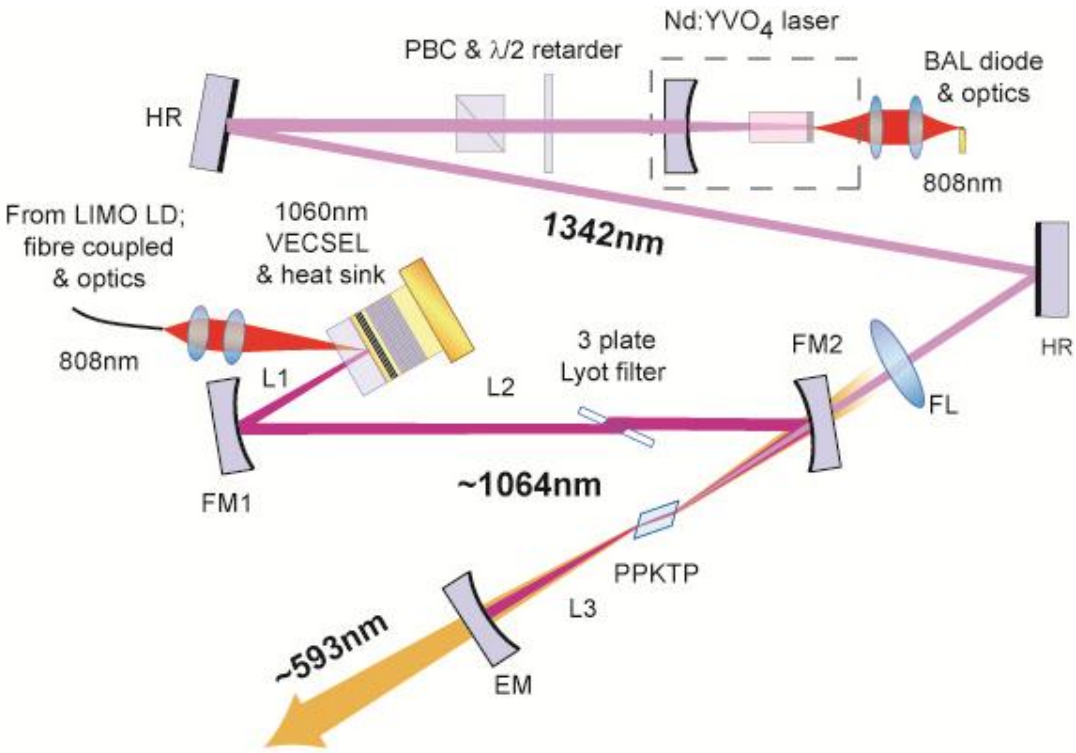

Fig. 5-4 Schematic layout of the experimental setup for the generation of 593 nm light by sum frequency mixing. The PPKTP crystal is positioned inside the VECSEL cavity with a resonating field at 1064 nm. A single passing beam from a Nd:YVO_4 laser with a wavelength of 1342 nm is focussed into the nonlinear crystal. LD – Laser diode, BAL – broad area laser diode, PBC – polarising beam splitter cube, HR – high reflector, EM – end mirror, FM_i – folding mirrors, Lyot – three plate birefringent filter, L_i – lengths of the different VECSEL cavity arms.

The QW-based VECSEL gain structure was designed and optimized for high output power at an emission wavelength around 1060 nm. It was grown in a low pressure (100 mbar) horizontal flow Metal-Organic Chemical Vapour Deposition (MOCVD) reactor on top of a (001) GaAs substrate. A DBR, consisting of 35 periods of λ/4 thick $Al_{0.2}Ga_{0.8}As$/AlAs pairs was grown on top of the substrate, followed by an 8-λ thick resonant subcavity with 15 single quantum wells (QWs) placed for resonant

periodic gain (RPG) at the electric field antinodes. The 7-nm-thick $In_{0.28}Ga_{0.72}As$ QWs were compressively strained; a layer pair of $GaAs_{0.9}P_{0.1}$ and GaAs was introduced between the QW layers, where the first acted as strain compensation and the latter as a pump absorbing layer. The active region was completed by an $Al_{0.3}Ga_{0.7}As$ window layer for carrier confinement and a 10 nm thick anti-oxidation GaAs capping layer. The growth temperature varied between 600-750°C, depending on the composition [36]. This structure was chosen for the sum frequency mixing experiment because the emission wavelength range allowed phase-matching for the available PPKTP crystal. This VECSEL gain structure, had previously been used to demonstrate second harmonic generation (SHG) to the green [8,37,38].

The VECSEL was pumped by an 808 nm fibre-coupled diode laser from LIMO with a maximum output power of up to 50 W. The pump beam was focused down to a spot size of $Ø = 80\ \mu m$ onto the VECSEL. A four mirror Z-shaped laser cavity was set up, which was able to accommodate a BRF and the non-linear crystal. Therefore two folding mirrors (FM1,2) and one end mirror (EM), all HR coated at 1060 nm and with 100 mm radius of curvature, were placed at distances L1 = 53 mm, L2 = 457 mm and L3 = 156 mm outgoing from the VECSEL-FM1, FM1-FM2 and FM2-EM respectively, with the VECSEL structure itself acting as a plain end mirror. This cavity setup matches the intracavity mode size to the pump spot at the VECSEL gain structure and creates a beam waist in the third cavity arm L3, where the nonlinear crystal is placed and where the calculated beam waist size inside the crystal is $Ø_h = 89\ \mu m$ and $Ø_v = 43\ \mu m$ in the horizontal and vertical direction respectively. The second cavity arm L2 accommodated the BRF for wavelength selective tuning and spectral narrowing as the free running emission spectrum was broader than 4 nm (see Fig. 5-5), very broad compared to the PPKTPs acceptance bandwidth of 0.25 nm for the 1064 nm beam. This is important, as the conversion efficiency depends strongly on the spectral width of the passing fundamental beams. Four different quartz BRFs with thicknesses 2, 4, 6 mm and a three plate Lyot filter were used for wavelength tuning in order to determine the optimum spectral filtering. The Lyot filter consisted of a succession of 1-, 2- and 4-mm-thick birefringent plates. In this configuration the thickest plate defines the peak/spectral width and the thinnest

defines the free spectral range [39]. The laser allowed a tuning range of more than 30 nm around a centre wavelength of 1055 nm. For thermal management, a 500-µm thick diamond heatspreader was liquid capillary [40] bonded to the intra-cavity surface of the otherwise unprocessed VECSEL structure, which was mounted in a water/glycol cooled brass mount kept at 0 °C.

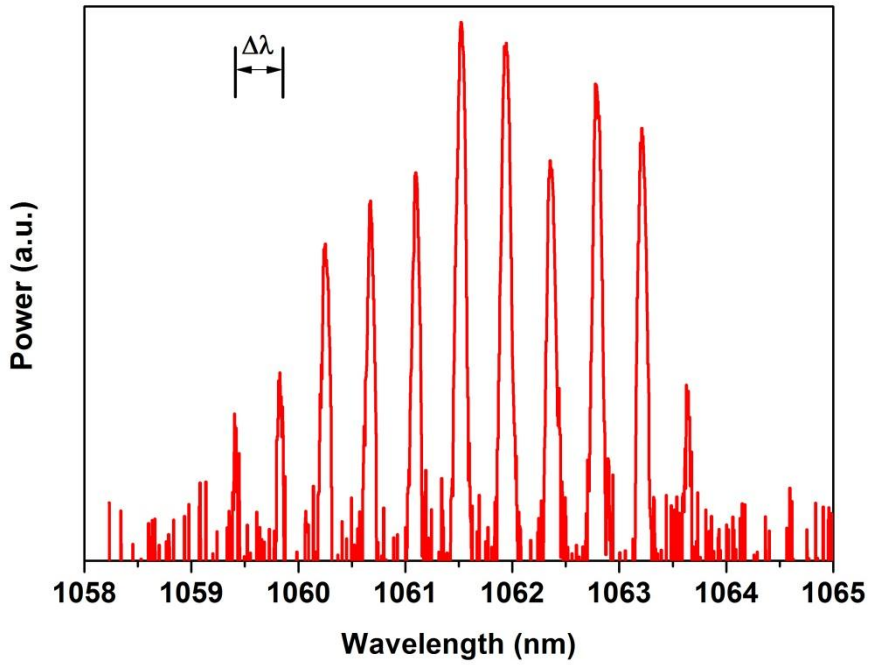

Fig. 5-5 Free running laser emission spectrum for the VECSEL, centred a 1061.5 nm and over 4 nm wide. The separation between the fringes $\Delta\lambda$ = 0.43 nm is caused by the etalon effect of the 500 mm thick diamond heatspreader.

The 8 mm long a-cut 1342 nm Nd:YVO_4 laser crystal (0.5 atm% Nd-doped) was pumped by an 808 nm 4 W broad area laser (BAL) diode. The laser resonator consisted of a 2 % output coupling (OC) mirror of 200 mm radius of curvature and the plane end facet of the laser crystal, which was coated for high reflection (HR) at 1342 nm and high transmission (HT) at 808 nm. The laser crystal was pumped through this facet. An anti-reflective coating at the generated laser wavelength was applied to the intra-cavity surface of the crystal. An etalon glass plate was used for spectral narrowing and emission wavelength adjustment, see Fig. 5-9. In order to couple the 1342 nm beam co-axially to the 1064 nm circulating VECSEL beam into the periodically poled Potassium Titanyl Phosphate (PPKTP) crystal, the light had to be redirected via two HR plane steering mirrors and enter the VECSEL cavity

through the second folding mirror (FM2) with a transmission coefficient of $T_{FM2}(1342\,nm) = 87\,\%$. A lens with a focal length (FL) of $f_{FL} = 120\,mm$ and a measured transmission coefficient of $T_{FL}(1342\,nm) = 93\,\%$ was used to focus the beam into the crystal. In order to keep the thermal load of the Nd:YVO_4 crystal constant for stability reasons, the pump power was unchanged and the output power varied extra-cavity via a $\lambda/2$-retarder plate and a polarising beamsplitter cube (PBC).

The PPKTP crystal was placed at the beam waist in the third VECSEL cavity arm L3, for efficient generation of 593 nm light. The poling-period was 12.65 μm for first order quasi-phase-matched sum frequency generation of a circulating 1064 and single passing 1342 nm beam. The Brewster cut crystal had a length of 10 mm and was temperature controlled to 42 °C in order to meet the phase-matching condition. The calculated temperature acceptance bandwidth of the nonlinear crystal was $T_{FWHM} = 7.4\,^0C$ for a spectral width $\lambda_{FWHM,1064nm} = 0.25\,nm$ of the 1064 nm beam and $\lambda_{FWHM,1342nm} = 0.4\,nm$ of the 1342 nm beam [41]. These conditions were met during the experiment, as will be discussed later. The generated light was coupled out though the curved end mirror (EM), which had a measured transmission coefficient of $T_{EM}(593\,nm) = 85\,\%$.

5.4 Optimisation and results

As a first means of characterizing the InGaAs VECSEL the output power leakage through the high reflecting curved mirrors was determined, which allowed an estimation of the intra-cavity power. A plane mirror with 2 % OC was paced between FM1 and FM2. This created a three mirror V-shaped cavity and allowed the output coupling of high power at the wavelength of interest in order to determine the transmission coefficient of the used mirrors. The output power was measured simultaneously at the HR FM1 and at the plane end mirror. Plane mirrors coated for 1 %, 2 % output coupling were placed consecutively between the 2 % output coupling plain end mirror and the power meter and the transmitted power was

detected accordingly. Average transmission coefficients of $T_{2\%} = 1.962\,\%$ and $T_{1\%} = 1.097\,\%$ where measured. Using these mirrors as output couplers and detecting the power through FM1 revealed a transmission of $T_{OC} = 0.017\,\%$ according to the small output coupling approximation [42] in equation [5-18]. It was assumed that all curved HR mirrors had the same transmission as they were coated in the same batch.

$$T_{leakage} \approx \frac{P_{leakage}}{P_{output}} \cdot T_{OC} \qquad \text{Equation [5-18]}$$

With $P_{leakage}$ and P_{output} being the measured power leaking through and $T_{leakage}$ and T_{OC} the transmission coefficients of the FM1 and the plane output coupling mirror. After these measurements the four mirror Z-shaped cavity was restored. The emission spectrum of the free running laser can be seen in Fig. 5-5. It is centred at 1061.5 nm with a total width of more than 4 nm having distinct peaks in the spectrum with an average separation of around $\Delta\lambda = 0.43\,nm$, caused by the etalon effect of the 500 µm thick intra-cavity diamond heatspreader. Power transfer and wavelength tuning curves were taken in the four mirror Z-cavity, described above for different output couplers (OC) with different birefringent filters (BRF) placed at Brewster's angle ($\theta_{Br} \approx 57^{0}$) into the second cavity arm, L2. The measurements for 3 % OC are given in Fig. 5-6. As can be seen from the figure, the laser behaves similarly for the different BRFs in terms of pump threshold and differential efficiency. The optimum output coupling coefficient of 3 % was determined for a three mirror V-cavity with a plane end mirror of either HR, 1%, 2% 3% and 5% transmission. The pump power of the 808 nm fibre coupled diode laser was set to 16 A, which corresponded to 13 W effective pump power absorbed in the VECSEL structure and was chosen according to the maximum output power achieved for the use of the Lyot filter, as can be seen in Fig. 5-6 a).

The tuning ranges for 3% OC for the different BRFs and pumped by a constant power of 13 W can be seen in Fig. 5-6 b). Broad wavelength tuning was demonstrated in a range between 1040-1070 nm. The 4 mm BRF shows superior output powers in this case. The restricted rotation range of the Lyot filter is evident

in this figure, where the filter mount didn't permit for further tuning below 1046 nm. This didn't prevent the use of this filter, as the wavelength of interest was 1064 nm.

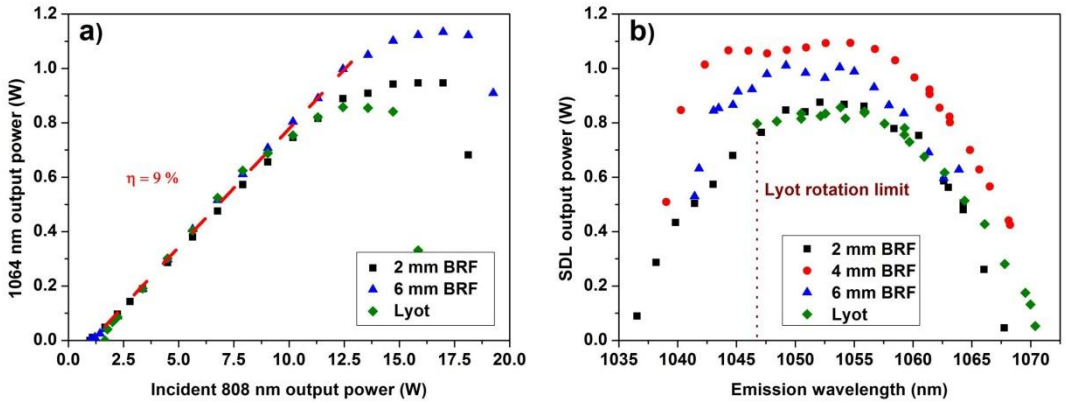

Fig. 5-6 a) Power transfer curves for different quartz BRF thicknesses placed inside a four mirror Z-shaped cavity with 3 % OC and without PPKTP crystal. b) Tuning ranges for different BRF thicknesses for a constant pump power of 13 W. The tuning range of the Lyot–filter is limited by the rotation mount. (BRF thickness = 2mm black squares, 4 mm red circles, 6 mm blue triangles, Lyot green diamonds).

A further study of the spectral narrowing and free spectral range of the different BRFs was also carried out. Fig. 5-7 shows the different emission spectra of the VECSEL for a) 2 mm, b) 4 mm, c) 6mm and d) Lyot BRF. From the detected number of diamond fringes it becomes clear that the spectral width decreases with increasing filter thickness. Narrow single peak spectra were obtained only for the 6 mm thick BRF and the Lyot filter, having a full width at half maximum (FWHM) of around 0.07 nm, which corresponds to the width of one single diamond fringe. The free spectral ranges of the different filters were calculated according to the following approximation for an angle of incidence close to Brewsters' angle [43]:

$$\Delta\lambda_{FSR} \approx \frac{\lambda^2}{\Delta n \cdot t_{BRF}} \qquad \text{Equation [5-19]}$$

where $\Delta n = n_e - n_o$ and t_{BRF} is the thickness of the BRF. For quartz, $n_e = 1.54296$ and $n_o = 1.53422$ [44]. The estimated FSR of the BRFs are listed in Table 5-4 and compared with the measured values, shown in Fig. 5-8.

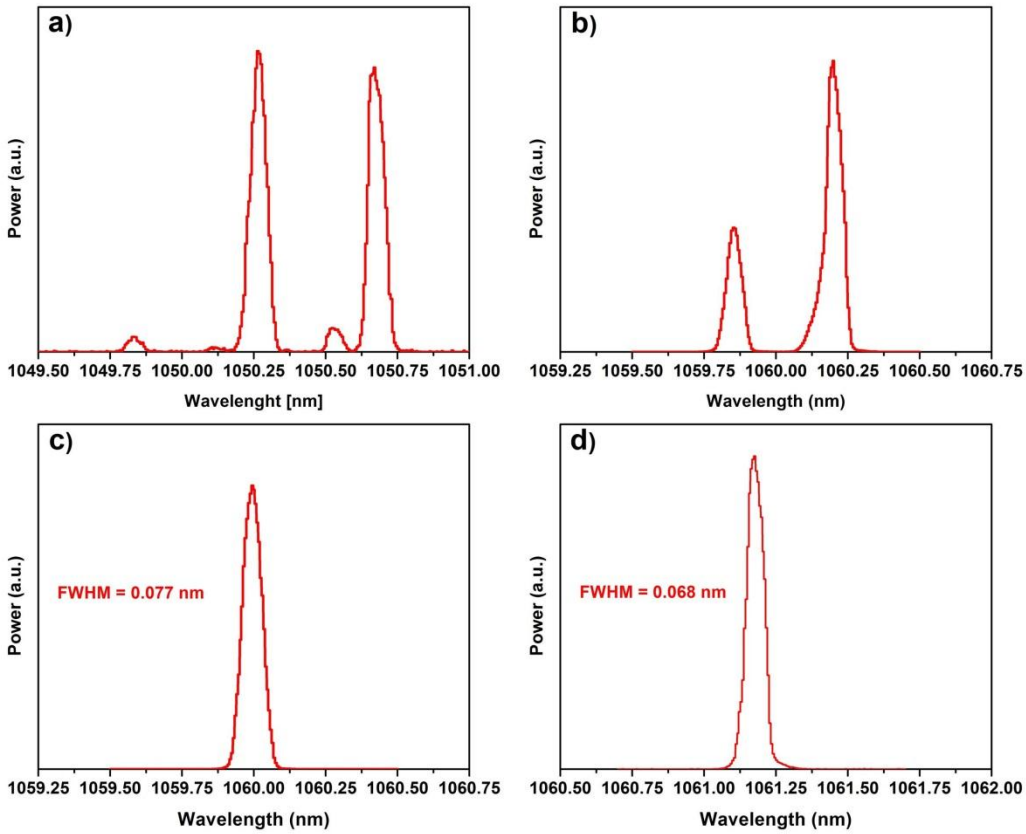

Fig. 5-7 Laser emission spectra with the use of a BRF filter, a) 2 mm, b) 4 mm, c) 6 mm and d) Lyot filter. The spectral width becomes smaller with increasing BRF thickness. The emission spectra are similar for the 6mm and the Lyot filter, only difference is in the FWHM being narrower for the Lyot filter.

BRF thickness t_{BRF} (mm)	**Calculated BRF free spectral range $\Delta\lambda_{FSR}(nm)$**	**Measured BRF free spectral range $\Delta\lambda_{FSR}(nm)$**
2	64	-
4	32	31.5 ± 0.4
6	21	17.3 ± 0.4
Lyot	130	-

Table 5-4 Free spectral range of the different quartz birefringent filters of thicknesses 2, 4, 6 mm and the Lyot filter (three-plate BRF).

The estimated FSR of the 2 mm thick BRF is 64 nm, much broader than the VECSEL gain bandwidth and thus could not be measured. Likewise the Lyot filter, as the FSR is defined by the thinnest plate (1 mm) and was calculated to be around 130 nm. The measured FSR of the 4-mm-thick BRF is similar to the VECSEL's gain bandwidth/tuning range but showed a broad emission spectrum, which would minimize the conversion efficiency of the VECSEL. Despite the good spectral

narrowing performance of the 6 mm thick BRF it had a measured free spectral range (FSR) of only 17.3 nm. This was considerably lower than the broad gain bandwidth (> 30 nm) of the VECSEL and enabled the laser to bypass the increased conversion losses after introduction of the nonlinear crystal by shifting its emission wavelength to a non-phase-matched condition. The three plate Lyot filter was therefore chosen for wavelength selection and spectral narrowing.

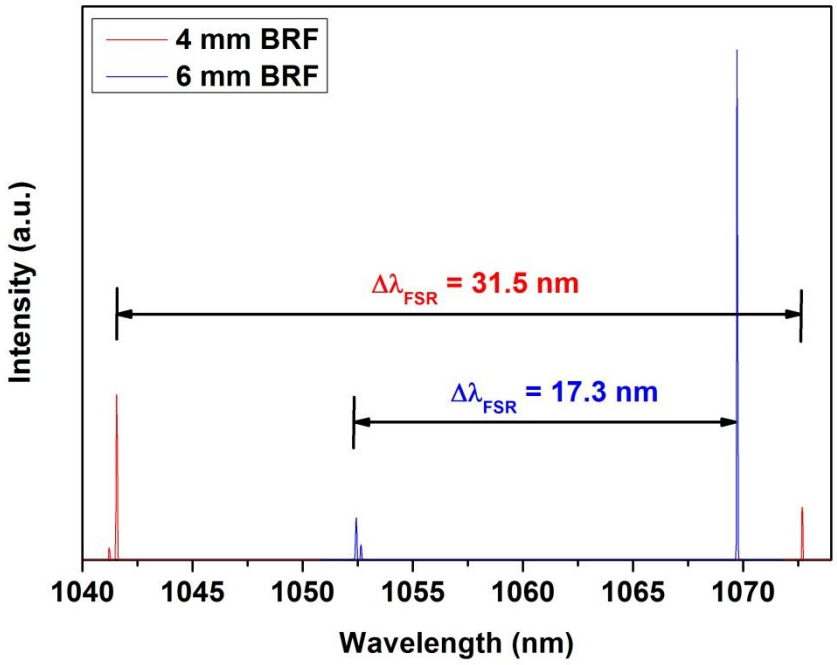

Fig. 5-8 Free spectral range of different BRFs with thicknesses 4 mm (red) and 6 mm (blue).

Measurement of the beam propagation factor (M^2) was not performed due to time constraints. Near diffraction limited beam qualities are easily achieved by these lasers via the matching of the intra-cavity mode to the pump spot size. Observation of the mode shape by help of IR detector cards confirmed circular beams throughout the experiment.

The diode pumped Nd:YVO_4 laser was characterized in terms of output power, differential efficiency, tuning range, polarization and beam propagation factor. A power transfer curve for pump powers up to 4 W, delivered by an 808 nm BAL diode is presented in Fig. 5-9 a). The differential efficiency was close to $\eta = 30\ \%$ with a maximum output power of $P_{max} = 890\ mW$. Rollover at elevated pump powers is

caused by thermal lensing in the laser crystal [45]. The red solid curve in Fig. 5-9 b) displays the free running emission spectrum, whereas the other peaks depict tuning spectra achieved with the introduction of a 0.3-mm-thick glass etalon into the DPSL laser cavity, narrowing the peak width to less than $0.2\,nm$. A total tuning range of $2.5\,nm$ was achieved by tilting the etalon. The 1342 nm output beam had beam propagation factors of $M_H^2 = 1.3$ and $M_V^2 = 1.4$ for the horizontal and vertical direction respectively as seen in Fig. 5-10 left. About 20 % of the output power was lost during redirection and focussing for focal and collinear mode matching of the two fundamental fields inside the PPKTP crystal, via two plane HR steering mirrors, the focusing lens and the VECSEL cavity folding mirror FM2. This set an upper limit to the input power of $P_{1342} < 700\,mW$.

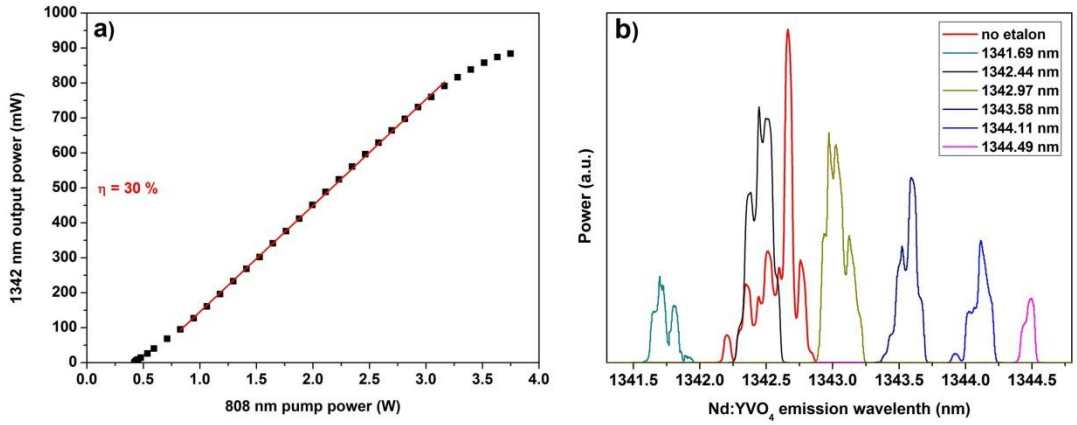

Fig. 5-9 a) Power transfer curve for the 1342 nm solid-state Nd:YVO_4 laser showing a slope efficiency of $\eta = 30$ % and a maximum output power of $P_{max} = 884$ mW. b) Free running laser emission spectrum (red) and tuning spectra (colour) of the Nd:YVO_4 laser. The total tuning range is 2.5 nm.

The estimated focus size in the nonlinear crystal of the VECSEL intra-cavity beam in the horizontal and vertical plane were $w_{Hreal}^{1062nm} \approx 89\,\mu m$ and $w_{Vreal}^{1062nm} \approx 43\,\mu m$ respectively. This was set by the chosen cavity arrangement and equipment i.e. the radius of curvature of the cavity mirrors and the minimum cavity arm length required to accommodate the intracavity optics and mounts. The ellipticity of the focus in the nonlinear crystal is due to the use of the Brewster cut crystal. Calculations of optimum beam waist sizes, based on the Boyd-Kleinman factor for sum frequency generation were done by Martin T. Andersen [21] and are presented in Table 5-5. These values would be required for high conversion efficiency, e.g. in case of single

passing fundamental beams, because the generated power is indirectly proportional to the fundamental mode sizes (equation [5-14]) inside the non-linear crystal. However, in this case, as the non-linear conversion process occurs inside the VECSEL cavity, which has an optimum output coupling of around 3%, such tight focusing is not necessarily optimal. Other possible cavity designs to reduce the focus sizes were not tested because of the time constraints of this project. The focal length of FL was chosen to match the focus of the single passing 1342 nm beam as close as possible to the intra-cavity beam waist dimensions.

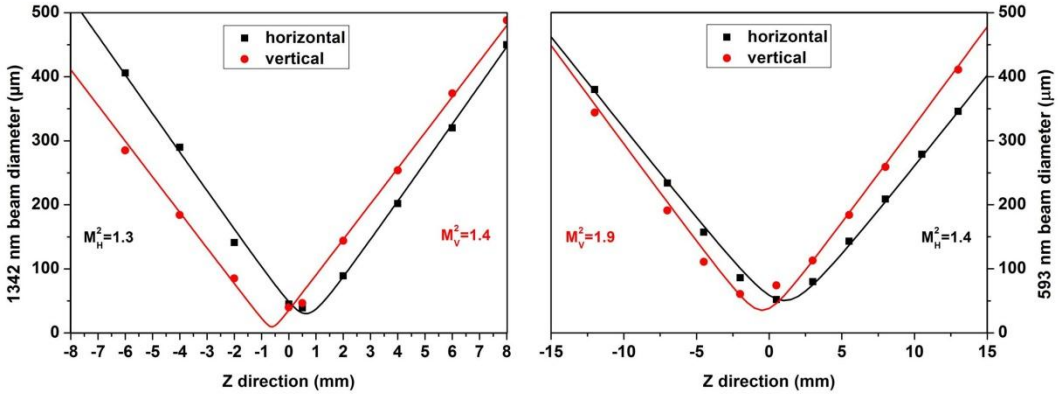

Fig. 5-10 Left: Beam profile of the 1342 nm diode pumped Nd:YVO_4 laser measured at the nonlinear crystal position inside the VECSEL cavity. Right: Beam profile of the generated 593 nm beam, measured after the curved end mirror of the VECSEL cavity.

1064 nm beam waist	1342 nm beam waist
$w_H^{1062nm} = 18.05\ \mu m$	$w_H^{1342nm} = 17.05\ \mu m$
$w_V^{1062nm} = 18.05\ \mu m$	$w_V^{1342nm} = 17.42\ \mu m$

Table 5-5 Theoretically calculated optimum beam waist sizes according to Boyd-Kleinman factor for SFG for both fundamental beams. Calculated by M. T. Andersen in [45]

The generated 593 nm light was examined in terms of output power, polarization, beam quality factor and wavelength tuning. A temperature scan of the nonlinear crystal was performed between 23-52 °C to determine the thermal acceptance bandwidth and the optimum operation temperature. Phase-matching condition was established at 42 °C for the two fundamental IR beams with wavelengths of $\lambda_{DPSL} = 1342.4\,nm$ and $\lambda_{VECSEL} = 1063.2\,nm$, where the Lyot filter was used to match the VECSEL emission wavelength to a pre-set DPSL wavelength. The

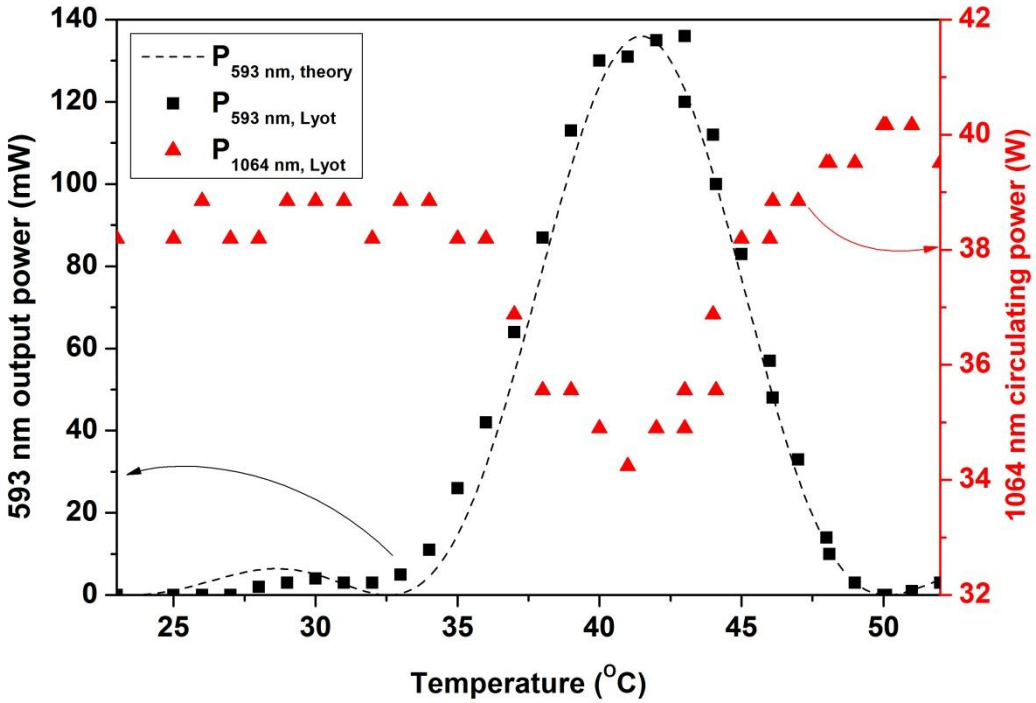

Fig. 5-11 Thermal acceptance bandwidth of the PPKTP crystal. Maximum conversion efficiency is reached at 42 °C (measured: black squares, theory: black dashed line). The circulating VECSEL intra-cavity field (red triangles) drops with the increasing conversion efficiency as output coupling losses increase.

theoretical plot (Fig. 5-11, dashed line) shows the acceptance bandwidth curve of the PPKTP crystal for a poling period of 12.65 µm [45,46] and reveals a FWHM of $T_{FWHM} = 7.4\,^{0}C$. It was calculated by the use of equation [5-15] for the power generation of the SFG beam under the consideration of the phase-momentum mismatch (equation [5-16], see also Fig. 5-2). The wave-vectors are dependent on the refractive index changes with temperature and are described by Sellmeier equations. The graph also shows the intra-cavity field power and its dependence on the conversion efficiency. A maximum output power of $P_{593nm} = 136\,mW$ was measured at the phase-matching point for an intra-cavity power of $P_{1064nm} = 35\,W$ and single pass power $P_{1342nm} = 680\,mW$. The beam propagation factors of the generated 593 nm light was measured after passing through the EM and had values of $M_H^2 = 1.4$ and $M_V^2 = 1.9$ for the horizontal and vertical plane respectively, Fig. 5-10 right. Fig. 5-12 shows the transmission of a cube polariser as it is rotated in the output beam. The extinction ratio of the polariser is 1/1000. The measurement revealed p-polarised ratios of 1/64, 1/1550 and 1/3300 for the 1064, 1342 and

593 nm beam respectively. The VECSEL gain is unpolarised due to the surface normal emission format; however, intra-cavity Brewster plates and the angled cavity arrangement enforce polarised emission in the horizontal plane (p-polarisation). Despite these polarising elements it is thought that a non-optimal alignment and the possible birefringence of the natural intra-cavity diamond heatspreader [47] caused the much smaller polarisation ratio of the VECSEL beam compared to the DPSL laser. Improvement of the VECSEL p-polarisation ratio would increase the efficiency of the conversion process, as every field component of the intra-cavity beam not polarised in this direction can not contribute to the mixing process. As can be seen in Fig. 5-12 the polarisation orientation of all three beams is identical, as can only be the case for quasi-phase-matching (QPM) as opposed to BPM.

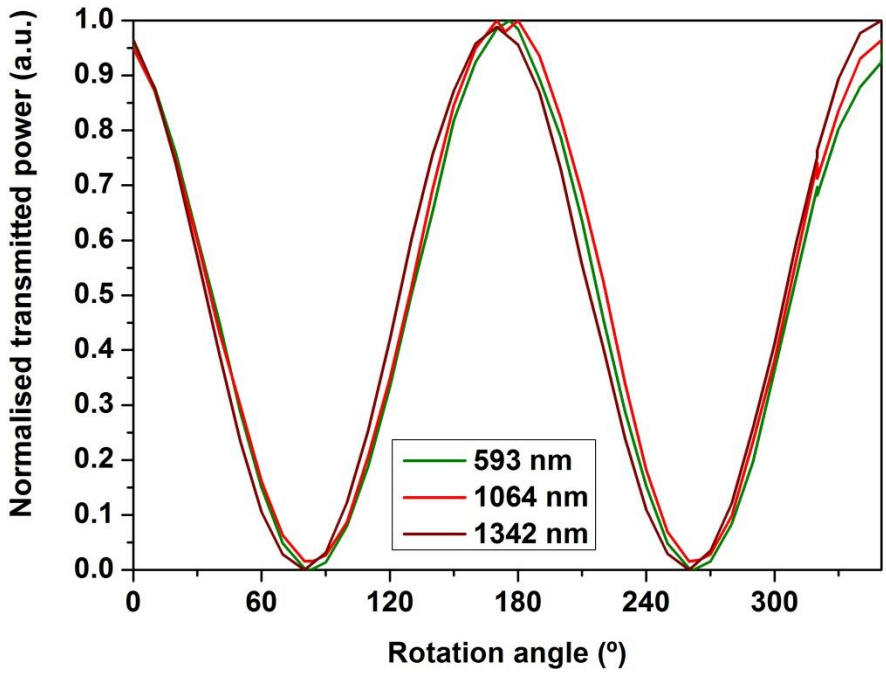

Fig. 5-12 Transmission of a cube polariser as it is rotated in the output beams. The incident 1342 nm beam from the DPSL showing a polarisation ratio of 1/1550 (wine), the circulating 1064 nm beam of the VECSEL has a relatively poor polarisation ratio of 1/64 (red) and the generated 593 nm beam a ratio of 1/3300 (green).

A conversion efficiency of 17 % with respect to the single passing 1342 nm beam was achieved, see Fig. 5-13. The linearity of the generated power with respect to the single passing beam is also maintained at very low input power, a behaviour explained by equation [5-15]. This is different to the parabolic behaviour in case of

SHG. The depletion of the VECSEL intra-cavity field was also measured versus the single passing beam during the sum frequency generation process. As discussed before, a VECSEL is a low gain structure and tolerates output coupling losses of only few per cent. The maximum output power increases with increasing output coupling for a constant pump power until it peaks at a maximum value. This point marks the optimum output coupling, for higher output coupling output power decreases [48]. The fact that the power transfer curve of the generated field is well described by a straight line, even at high pump power, is a good indication that the output coupling of the VECSEL due to the non-linear conversion is still much lower than the optimum value. A different VECSEL cavity arrangement, allowing for a tighter focus of the fundamental beams would increase the conversion efficiency in this case, leading to higher output powers.

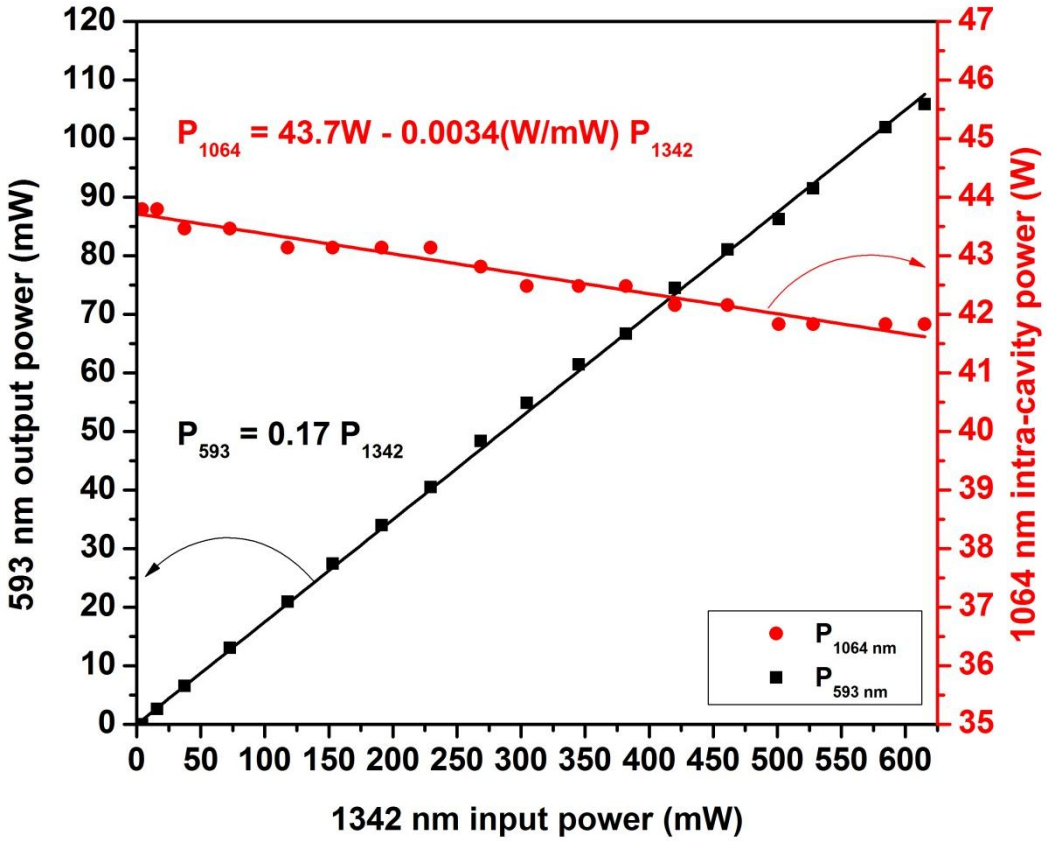

Fig. 5-13 Power transfer curve for 593 nm light generation in as a function of the single passing 1342 nm DPSL power (black squares). Circulating 1064 nm intra-cavity power recorded simultaneously (red dots).

In order to determine the wavelength tunability of the setup, the wavelength of the DPSL was fixed and the VECSEL wavelength tuned. This procedure was repeated

for crystal temperatures of 18, 43 and 52 °C. No significant tuning of the generated 593 nm beam was observed. A simulation of the phase matching conditions for the two fundamental beams with regard to the specific crystal parameters was created by Martin T. Andersen [45] in order to investigate the prospects for tuning. The programme calculated the specific phase-matching conditions, under consideration of parameters such as:

- the crystal's temperature dependent Sellmeier equations
- poling period
- wavelengths of the generated and single passing beams.

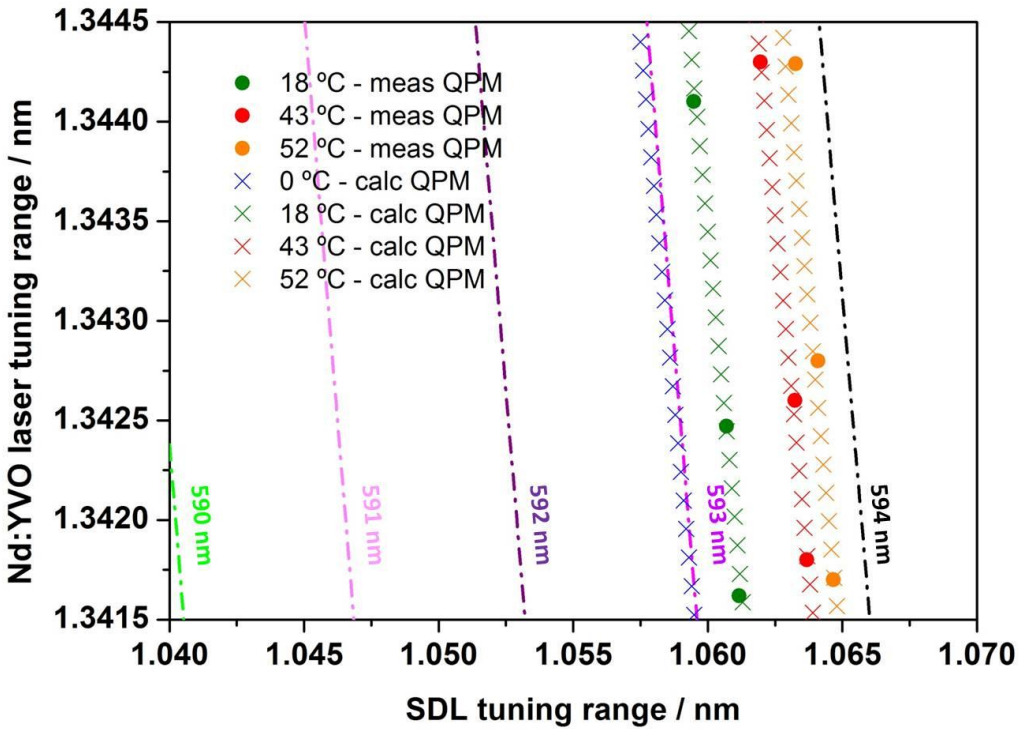

Fig. 5-14 Calculated phase-matching diagram for the PPKTP crystal. The range of the x- and y-axis was chosen to be the tuning range of the two lasers respectively. Coloured crosses and full circles depict calculated and measured phase-matching conditions respectively. The coloured dash-dotted lines are lines of constant generated wavelength (iso-wavelength).

The calculated and measured phase-matching conditions for the DPSL and VECSEL wavelength at the previously mentioned nonlinear crystal temperatures are shown by coloured crosses and full circles respectively in Fig. 5-14, where the measured values are very accurately described by the theory. The tuning ranges of the two laser beams

are illustrated by the x- and y-axis for the VECSEL and the DPSL respectively. The limited tunability becomes clear when the phase-matching conditions (coloured crosses) are compared to the progression of the iso-wavelength lines (lines describing the sum frequency generation of constant wavelength by the variation of the two incident fundamental wavelengths, as described in equation [5-1]). The gradients of these lines are very similar and hence explain why an adequate wavelength tuning of the generated light could not be achieved by the use of this crystal. A total thermal tuning rate of $\Delta\lambda/\Delta T = 0.035\, nm/℃$ was measured in the range of 18-52 ℃. In order to make use of the whole VECSEL tuning range, an inpractical temperature tuning over 250 ℃ would be necessary for the present PPKTP crystal. Nonlinear crystals with different dispersion coefficients might allow broader wavelength tuning. Nonlinear crystals with a multi-section and fan-out poling could also be used although at the expense of mechanical alignment. Chirped and aperiodical poling could lead to wavelength tuning without mechanical and thermal adjustments at the expense of conversion efficiency.

5.5 Conclusion

In conclusion 136 mW coherent yellow-orange light at 593 nm was generated via sum frequency mixing of a single passing 1342 nm beam from a Nd:YVO_4 laser and the high power multi-Watt resonating intra-cavity field of VECSEL with an emission wavelength around 1064 nm. The nonlinear crystal was a 10 mm long Brewster cut periodically poled KTP crystal, for first order sum frequency generation. A total conversion efficiency of 17% could be achieved with respect to the single passing DPSL beam. The setup could be further optimized in terms of VECSEL beam waist size inside the nonlinear crystal and the minimisation of reflection losses at the many intra-cavity surfaces and mirrors/lenses with the right coatings for all the contributing wavelengths. Despite the broad tuning range of the VECSEL of over 30 nm, direct phase-matched tuning by variation of the two fundamental wavelengths and crystal temperature was not possible, mainly due to the intrinsic properties of the PPKTP

crystal. Nevertheless, tunable light generation in the visible region still remains interesting for many applications in biophotonic sensing and for medical applications and the nonlinear wave mixing is a promising way in achieving this. Tuning could be possible by the use of nonlinear crystals with different dispersion relations and thermal acceptance bandwidths. The use of periodically poled crystals with a chirped, fan-out or multi-sectioned poling is also possible although under the expense of mechanical movement or decreased efficiencies.

References

1. B. C. Wilson, "Photodynamic therapy for cancer: Principles," The Canadian Journal of Gastroenterology **16**, 393-396 (2002).

2. T. J. Dougherty, C. J. Gomer, B. W. Henderson, G. Jori, D. Kessel, M. Korbelik, J. Moan, and Q. Peng, "Photodynamic therapy," J. Natl. Cancer Inst. **90**, 889-905 (1998).

3. T. Baer, "Large-amplitude fluctuations due to longitudinal mode coupling in diode-pumped intracavity-doubled Nd:YAG lasers," J. Opt. Soc. Am. B **3**, 1175-1180 (1986).

4. R. Hartke, E. Heumann, G. Huber, M. Kühnelt, and U. Steegmüller, "Efficient green generation by intracavity frequency doubling of an optically pumped semiconductor disk laser," Applied Physics B: Lasers and Optics **87**, 95-99 (2007).

5. L. Fan, C. Hessenius, M. Fallahi, J. Hader, H. Li, J. V. Moloney, W. Stolz, and S. W. Koch, "Highly strained InGaAs/GaAs vertical-external-cavity surface-emitting laser for the generation of coherent yellow-orange light," W. A. Clarkson, N. Hodgson, and R. K. Shori, eds., (SPIE, San Jose, CA, USA, 2008), pp. 687119-8.

6. J. L. A. Chilla, S. D. Butterworth, A. Zeitschel, J. P. Charles, A. L. Caprara, M. K. Reed, and L. Spinelli, "High-power optically pumped semiconductor lasers," R. Scheps and H. J. Hoffman, eds., (SPIE, San Jose, Ca, USA, 2004), pp. 143-150.

7. S. Lutgen, M. Kuehnelt, U. Steegmueller, P. Brick, T. Albrecht, W. Reill, J. Luft, B. Kunert, S. Reinhard, K. Volz, and W. Stolz, "Green semiconductor disk laser with 0.7W cw output power," C. Lei and K. D. Choquette, eds., (SPIE, San Jose, CA, USA, 2005), pp. 109-112.

8. J. Y. Kim, S. Cho, S. M. Lee, G. B. Kim, J. Lee, J. Yoo, K. S. Kim, T. Kim, and Y. Park, "Highly efficient green VECSEL with intra-cavity diamond heat spreader," Electronics Letters **43**, 105-107 (2007).

9. J. Rautiainen, A. Harkonen, P. Tuomisto, J. Konttinen, L. Orsila, M. Guina, and O. G. Okhotnikov, "1-W red light generation by intracavity doubling in a 1240 nm GaInNAs semiconductor disk laser," W. A. Clarkson, N. Hodgson, and R. K. Shori, eds., (SPIE, San Jose, CA, USA, 2008), pp. 68711A-8.

10. Coherent. TracER - Portable, Compact Forensic Laser Systems. 2008.

11. M. T. Andersen, P. J. Schlosser, J. E. Hastie, P. Tidemand-Lichtenberg, M. D. Dawson, and C. Pedersen, "Singly-resonant sum frequency generation of visible light in a semiconductor disk laser," Opt. Express **17**, 6010-6017 (2009).

12. R. W. Boyd, *Nonlinear Optics*, (Academic Press, 2003).

13. M. Bass, P. A. Franken, J. F. Ward, and G. Weinreich, "Optical Rectification," Phys. Rev. Lett. **9**, 446 (1962).

14. Midwinte, J. E. and Warner, J. The effects of phase matching method and of uniaxial crystal symmetry on the polar distribution of second-order non-linear optical polarization. British Journal of Applied Physics 16[8], 1135. 1965.

15. D. A. Kleinman, "Nonlinear Dielectric Polarization in Optical Media," Phys. Rev. **126**, 1977 (1962).

16. G. D. Boyd and D. A. Kleinman, "Parametric Interaction of Focused Gaussian Light Beams," Journal of Applied Physics **39**, 3597-3639 (1968).

17. P. D. Maker, R. W. Terhune, M. Nisenoff, and C. M. Savage, "Effects of Dispersion and Focusing on the Production of Optical Harmonics," Phys. Rev. Lett. **8**, 21 (1962).

18. J. A. Giordmaine, "Mixing of Light Beams in Crystals," Phys. Rev. Lett. **8**, 19 (1962).

19. http://www.rp-photonics.com/encyclopedia.html, Paschotta, R., "Encyclopedia of Laser Physics and Technology," 18-5-2010, RP Photonics Consulting GmbH

20. J. A. Armstrong, N. Bloembergen, J. Ducuing, and P. S. Pershan, "Interactions between Light Waves in a Nonlinear Dielectric," Phys. Rev. **127**, 1918 (1962).

21. M. T. Andersen, "General approach to high power, coherent visible and ultraviolet light sources," (DTU Physics, Department of Physics, Technical University of Denmark, (2009).

22. A. Galvanauskas, D. Harter, M. A. Arbore, M. H. Chou, and M. M. Fejer, "Chirped-pulse-amplification circuits for fiber amplifiers, based on chirped-period quasi-phase-matching gratings," Opt. Lett. **23**, 1695-1697 (1998).

23. P. E. Powers, T. J. Kulp, and S. E. Bisson, "Continuous tuning of a continuous-wave periodically poled lithium niobate optical parametric oscillator by use of a fan-out grating design," Opt. Lett. **23**, 159-161 (1998).

24. V. Wesemann, J. A. L'Huillier, L. K. Friess, .Loewis of Menar, G. Bitz, A. Borsutzky, R. Wallenstein, T. Salva, S. Vernay, and D. Rytz, "Optical properties of BiB_3O_6 with different phase matching orientations," Applied Physics B: Lasers and Optics **84**, 453-458 (2006).

25. J. Janousek, S. Johansson, P. Tidemand-Lichtenberg, S. Wang, J. Mortensen, P. Buchhave, and F. Laurell, "Efficient all solid-state continuous-wave yellow-orange light source," Opt. Express **13**, 1188-1192 (2005).

26. J. E. Hastie, L. G. Morton, A. J. Kemp, M. D. Dawson, A. B. Krysa, and J. S. Roberts, "Tunable ultraviolet output from an intracavity frequency-doubled red vertical-external-cavity surface-emitting laser," Applied Physics Letters **89**, 061114-3 (2006).

27. J. Rautiainen, I. Krestnikov, J. Nikkinen, and O. G. Okhotnikov, "2.5 W orange power by frequency conversion from a dual-gain quantum-dot disk laser," Opt. Lett. **35**, 1935-1937 (2010).

28. R. Hartke, V. Baev, K. Seger, O. Back, E. Heumann, G. Huber, M. Kuhnelt, and U. Steegmüller, "Experimental study of the output dynamics of intracavity frequency doubled optically pumped semiconductor disk lasers," Applied Physics Letters **92**, 101107-3 (2008).

29. T. D. Raymond, W. J. Alford, M. H. Crawford, and A. A. Allerman, "Intracavity frequency doubling of a diode-pumped external-cavity surface-emitting semiconductor laser," Opt. Lett. **24**, 1127-1129 (1999).

30. S. Du, Y. Kaneda, and M. Yarborough, "Retracted: 488 nm ultraviolet light generated by VECSEL and V-cavity second-harmonic generation using lithium triborate," Microw. Opt. Technol. Lett. **50**, 2892-2894 (2008).

31. E. Gerster, I. Ecker, S. Lorch, C. Hahn, S. Menzel, and P. Unger, "Orange-emitting frequency-doubled GaAsSb/GaAs semiconductor disk laser," Journal of Applied Physics **94**, 7397-7401 (2003).

32. E. Schiehlen, M. Golling, and P. Unger, "Diode-pumped semiconductor disk laser with intracavity frequency doubling using lithium triborate (LBO)," Photonics Technology Letters, IEEE **14**, 777-779 (2002).

33. U. Steegmüller, M. Kühnelt, H. Unold, T. Schwarz, R. Schulz, S. Illek, I. Pietzonka, H. Lindberg, M. Schmitt, and U. Strauss, "Green laser modules to fit laser projection out of your pocket," W. A. Clarkson, N. Hodgson, and R. K. Shori, eds., (SPIE, San Jose, CA, USA, 2008), pp. 687117-687118.

34. http://www.gwu-group.com/cmslaser/index.php?option=com_content&task=view&id=82&Itemid=161, GWU Lasertechnik, 2011,

35. http://www.ilphotonics.com/cdv2/Crystech-Crystals/Crystals-Crystech/Non_Linear_Crystals/KNbO3.pdf, Crystech, 2011,

36. K. S. Kim, J. R. Yoo, S. M. Lee, S. J. Lim, J. Y. Kim, J. H. Lee, S. H. Cho, T. Kim, and Y. J. Park, "Highly efficient InGaAs QW vertical external cavity surface emitting lasers emitting at 1060nm," Journal of Crystal Growth **287**, 629-632 (2006).

37. A. J. Maclean, A. J. Kemp, S. Calvez, K. Jun-Youn, K. Taek, M. D. Dawson, and D. Burns, "Continuous Tuning and Efficient Intracavity Second-Harmonic Generation in a Semiconductor Disk Laser With an Intracavity Diamond Heatspreader," Quantum Electronics, IEEE Journal of **44**, 216-225 (2008).

38. K. Jun-Youn, C. Soohaeng, L. Junho, B. K. Gi, L. Seong-Jin, Y. Jaeryung, K. Ki-Sung, L. Sang-Moon, S. Jongin, K. Taek, and P. Yongjo, "A Measurement of Modal Gain Profile and Its Effect on the Lasing Performance in Vertical-External-Cavity Surface-Emitting Lasers," Photonics Technology Letters, IEEE **18**, 2496-2498 (2006).

39. D. R. Preuss and J. L. Gole, "Three-stage birefringent filter tuning smoothly over the visible region: theoretical treatment and experimental design," Appl. Opt. **19**, 702-710 (1980).

40. Z. L. Liau, "Semiconductor wafer bonding via liquid capillarity," Applied Physics Letters **77**, 651-653 (2000).

41. M. T. Andersen, "Development of laser systems for bio-photonic applications," (Denmark Technical University (DTU), (2005).

42. A. E. Siegman, "Fundamentals of laser oscillations," in *Lasers*, A. Kelly, ed., (University Science Books, 1990), pp. 473-477.

43. S. Zhu, "Birefringent filter with tilted optic axis for tuning dye lasers: theory and design," Appl. Opt. **29**, 410-415 (1990).

44. CVI Melles Griot Catalog. 2009. CVI Melles Griot.

45. M. T. Andersen, "General approach to high power, coherent visible and ultraviolet light sources," (DTU Physics, Department of Physics, Technical University of Denmark, (2009).

46. M. T. Andersen, P. J. Schlosser, J. E. Hastie, P. Tidemand-Lichtenberg, M. D. Dawson, and C. Pedersen, "Singly-resonant sum frequency generation of visible light in a semiconductor disk laser," Opt. Express **17**, 6010-6017 (2009).

47. P. Millar, R. B. Birch, A. J. Kemp, and D. Burns, "Synthetic Diamond for Intracavity Thermal Management in Compact Solid-State Lasers," Quantum Electronics, IEEE Journal of **44**, 709-717 (2008).

48. S. J. McGinily, R. H. Abram, K. S. Gardner, R. Erling, A. I. Ferguson, and J. S. Roberts, "Novel Gain Medium Design for Short-Wavelength Vertical-External-Cavity Surface-Emitting Laser," Quantum Electronics, IEEE Journal of **43**, 445-450 (2007).

Chapter 6:

General summary and future perspective

This thesis describes the first VECSELs to have QD active regions. The generic VECSEL design concept was introduced in the second chapter. First designs and characterisation measurements of QD based VECSEL structures where demonstrated and discussed in the third and fourth chapter of this work for InAs/GaAs SML QDs and InP/GaInP dot-in-a-well respectively. Non-linear sum frequency conversion of a resonating intra-cavity field of a near infra-red QW VECSEL, in combination with a single passing infra-red beam from a solid state laser was presented and discussed in Chapter 5. Here, a very brief general summary of the previous chapters is given together with a perspective of what the future may hold in stock for this laser concept, both for QD and QW based structures.

6.1 InAs QD VECSELs

Chapter 3: Collaboration in the project for the demonstration of laser emission from an InAs/GaAs based QD VECSEL structure for emission around 1030 nm [1]. Output powers up to 0.5 W were achieved with a differential efficiency of 17 %. The structure was designed to have a resonant subcavity and with an offset between the peak QD ensemble PL emission and RPG wavelength. This was done to insure a low pump threshold power for the first demonstration of laser emission, but is believed to have introduced a stronger thermal sensitivity with respect to an anti-resonant structure design. Fast structure degradation could be associated to a growth related increased carbon dopant concentration, of the Al containing layers due to the used

alternative precursors for the fabrication of the DBR; causing higher absorption especially in these regions and leading to permanent damage due to heating. The first designs had a non-uniform QD layer distribution, following the exponentially declining pump field. They were designed to be resonant at the emission wavelength and the total number of gain layers was limited not only by the total absorption length of the pump absorbing barriers, but also by the available spacer layer thickness.

All published QD samples, including the work herein show a high sensitivity towards any cavity loss. This was revealed in Chapter 3 for InAs/GaAs based QD VECSELs, having an optimum output coupling coefficient of 0.8 % and in Chapter 4 in case of InP QD based VECSELs, tolerating a maximum output coupling of 0.2 %. This is an indication for the relatively low modal gain, defined by the dot density per gain layer and the size distribution of the dot ensemble. This circumstance explains the trend to integrate as many QD-layers as possible inside the VECSEL active region. In short, the higher modal gain value delivered by a larger number of QD-layers is more favourable under the expense of a decreased RPG enhancement and increased pump threshold powers. The very promising results of the first InAs/GaAs SML QD VECSELs discussed in the present thesis were grown in 2007 and from a very early stage in the QD VECSEL development. Huge improvements have been achieved up-to-date in terms of maximum modal gain with the implementation of a large number of gain layers inside the subcavity. This was made possible, especially due to a drastic reduction of the spacer layer thickness, separating the gain layers from each other, but also by a uniform dot layer distribution. Anti-resonant subcavity designs are thought to allow the fabrication of more temperature stable devices, enabled by the very broad and flat gain spectrum at high excitation levels [2]. The wavelength coverage increased in comparison to QW devices and covers now a range from 0.95 to over 1.3 µm. Multi Watt output power almost across the whole region was demonstrated by several different groups. They offer especially above 1.2 µm the real opportunity towards a convenient replacement for dilute nitride GaInNAs quantum well based structures. Recent work concerning the harmonic generation also show their potential for single semiconductor compound based high brightness red-

green-blue emitting devices [3], i.e. for displays. Best results in the InAs/GaAs material system have been achieved with the so called submonolayer QD growth concept, where alternating submonolayer InAs and GaAs layers are grown on top of each other, allowing the fabrication of defect free gain layers with a high dot density. InAs/GaAs QDs were already a well-established gain material for the use in edge emitting devices and VCSEL structures, which explains the very steep improvement rate in terms of QD VECSELs.

6.2 InP QD VECSELs

Chapter 4: Structure design, characterisation and successful demonstration of laser emission around 730 nm from the first InP/AlGaInP based QD VECSEL device [4]. Laser emission in the range between 716-752 nm was demonstrated with a maximum output power over 50 mW and a differential efficiency of > 5 % for 0.2 % output coupling. A high finesse cavity permitted wavelength tuning over a range of more than 25 nm with maximum output powers of 0.5 mW and near diffraction limited output beam, having a propagation factor $M^2 < 1.1$.

Although edge emitting devices were reported prior to the start of this project in a range from 650-740 nm no experience was made with the implementation of these QDs inside a surface emitting laser. The VECSEL results for InP QDs covered by $Ga_yIn_{1-y}P$ QWs demonstrated emission wavelengths above 700 nm with broad tuning range (> 25 nm). This range is considerably wider than the 16 nm demonstrated by compressively strained $Ga_yIn_{1-y}P$ QWs and is defined by the broader gain bandwidth of the InP QD ensemble. Microscopic characterisation discussed in Chapter 3 also revealed a high density of defects, originating in non-coherently strained QDs, degrading the growth quality and introducing a very rough interface and surface morphology. This is detrimental in three ways. Firstly, the high defect density decreases the overall efficiency by acting as non-radiative recombination centres and carrier traps. Secondly, threading dislocations also affect the growth quality and interface smoothness, having possibly an effect on the carefully placed resonances

and cause increased scattering losses. The third drawback is the rough surface itself. Thermal management requires optical contacting of a transparent crystalline heatspreader onto the surface, especially for small pump/cavity mode sizes [5]. This was in most of the cases impossible; only a few samples permitted bonding for a limited time. It was also difficult to match the QD ensemble peak emission to the cavity resonance, which set a limit to the maximum achievable output and increased also the pump threshold power. Further development on the growth processes might lead to defect free QDs, where the peak gain is well matched to the resonances. It is expected that laser performance will improve in that case [4,6].

6.3 Singly-resonant SFG inside a InGaAs QW VECSEL

Chapter 5: Collaboration in a pump prime project utilising the intra-cavity field of a QW based VECSEL together with a single passing solid-state laser beam for the sum frequency generation of orange-yellow light [7]. A maximum output power of 136 mW at 593 nm was achieved with a total conversion efficiency of 17 % with respect to the single passing beam. The results indicate that the setup would allow further improvement by application of a tighter focus within the non-linear crystal but also by improvement of the polarisation ratio of the intra-cavity field.

The sum frequency mixing project illustrated again the potential of this laser type towards intra-cavity non-linear frequency conversion [7], after second harmonic generation and optical parametric oscillation. The presented results of 136 mW coherent light emission with a conversion coefficient of 17 % with respect to the single passing solid state beam are very encouraging. The detected power transfer curve suggested that there was room for improvement of the experimental arrangement to achieve optimised conversion. Polarization measurements of the fundamental and generated beams also indicated a poorer polarization ratio of the intra-cavity VECSEL beam, which might be caused by the large number of possibly not optimally aligned intra-cavity elements. Further optimisation of the cavity and the use of more suitable mirrors in terms of transmission and reflection are only two

other points for improvement, which could not be addressed due to the short duration of this pump prime project.

Wavelength flexible, high intra-cavity fields in combination with good beam quality, short carrier lifetimes and single mode emission are desirable features for stable, low noise non-linear conversion. High conversion efficiencies are not required within the intra-cavity set-up, because the pump is recycled as it passes the non-linear crystal with each round trip. The output coupling losses due to the nonlinear conversion can be adjusted via the focus size(s) inside the non-linear crystal (external cavity arrangement) to match the optimum output coupling coefficient of the VECSEL, which lies usually in the few per cent range. It is very likely that these devices will expand their application range in this area considerably.

6.4 Future perspective

Recent developments in research on VECSEL devices are pointing to the use of the high brightness and high intra-cavity powers (properties of solid state lasers) combined with other advantageous properties such as the wavelength versatility, tunability etc. (of semiconductor based lasers), as brightness & colour converters and as pump lasers, replacing solid state and gas ion lasers especially in the visible range. Examples for this are the various publications on harmonic generation [8-19], to name a few, which were also stated in the introduction (Chapter 1). Further results on harmonic frequency mixing are the results on sum frequency generation to the visible Hartke et al. and Härkönnen et al. [20,21] respectively and by Andersen et al. [7], which is discussed in Chapter 5, but also the publication on intra-cavity optical parametric oscillation by Stothard et al. [22], from the near into the mid-infrared region. Recently tunalbe non-linear Raman conversion has also been reported, using a KGW crystal as nonlinear medium by Parrotta et al. [23]. These results are very promising for the generation of light waves for specific applications (VIS – medical, bio-photonic, near-IR - telecommunication, mid-IR – spectroscopy, trace gas detection etc.), but one restriction remains to be mentioned. Almost all results on

non-linear conversion are based on InGaAs QW devices with a fundamental emission around 1 μm. This is not further surprising, as this material system is the highest advanced, offering the best reliability, highest growth quality, gain and output powers available for VECSELs and is illustrated in Fig. 1.10 in Chapter 1. Nevertheless, further advances in fabrication, such as the use of wafer-fusion, combining the gain region with a dissimilar DBR will certainly lead to improvements [24]. Adapted from VCSEL fabrication and processing [25], this approach enables the production of the active region and the DBR structure independently for near lattice-matched growth, resulting in lower defect densities and better performance. Expansion of the fundamental emission to towards shorter wavelength, e.g. to the near-UV to blue region by GaInN/GaN devices [26,27] was realised. In this case the problem of suitable pump laser diodes is still unsolved. The red range is covered by AlGaInP compounds [4,28-31]; both with QW and QD based gain layers, leaving a coverage gap in the green/yellow. Group II-VI semiconductors based on ZnCdSe QWs grown on top of GaAs and InP substrates could be suitable compounds to cover the whole visible range, from the blue to the red [32,33]. The drawback of these compositions is the difficulty of p-doping for electrical pumping (but not necessary for optical pumping) and Cd out-diffusion from QWs, limiting the lifetime despite high quality growth [34]. MgZnSSe and MgZnCdSe DBR structures also suffer from a low refractive index difference and increasingly difficult growth with increasing Mg composition for near lattice matched conditions [35,36] limiting the maximum reflectivity and stopband width, mitigating the tunability and efficiency of possible devices. Group IV-VI (Lead-salt) devices for fundamental emission in the 3-10 μm range consist of a bulk gain region and have reached the stage of room temperature cw laser action [37]. The development of devices in the near- and mid-IR region covered by GaAs [38] and InAlGaAs [39] QWs for the 850 nm range, InGaAs QWs [40] from 920-1180 nm and InGaAs QDs [41] 950-1300 nm range, dilute nitride InGaNAs [42] QWs from 1180-1350 nm, all monolithically grown on GaAs substrates speaks for itself. InP substrate based compounds are InGaAsP [43] and InAlGaAs [24] both emitting around 1550 nm, GaInSb [44] and GaInAsSb [45] for 2000-3000 nm range. Still gaps or poor laser performance, due to lack of adequate materials remain which have to be closed in future, possibly by new lattice matched

compositions (II-VI, IV-VI, quaternaries and quinternaries), offering larger refractive index differences for DBRs and better optical and/or carrier confinement. All this has the potential to improve VECSEL performance as brightness enhancer and colour converters required for exotic laser crystal materials [46]. Development goes as well in direction of further integration, e.g. mode-locked devices with an integrated SESAM structure inside in the gain mirror [47]. Such structures are thinkable even with electrical pumping as discussed in [48]. Optically pumped devices, where the pump diode laser was integrated between the DBR and gain region have also been realised [49]. Many of these applications are scientifically and commercially driven, which shows their potential as one of the most versatile 'solid-state' laser on the market.

References

1. T. D. Germann, A. Strittmatter, J. Pohl, U. W. Pohl, D. Bimberg, J. Rautiainen, M. Guina, and O. G. Okhotnikov, "High-power semiconductor disk laser based on InAs/GaAs submonolayer quantum dots," Applied Physics Letters **92**, 101123 (2008).

2. F. Klopf, S. Deubert, J. P. Reithmaier, and A. Forchel, "Correlation between the gain profile and the temperature-induced shift in wavelength of quantum-dot lasers," Applied Physics Letters **81**, 217-219 (2002).

3. M. Butkus, J. Rautiainen, O. G. Okhotnikov, C. J. Hamilton, G. P. A. Malcolm, S. S. Mikhrin, I. L. Krestnikov, D. A. Livshits, and E. U. Rafailov, "Quantum Dot Based Semiconductor Disk Lasers for 1-1.3 μm," Selected Topics in Quantum Electronics, IEEE Journal of **PP**, 1-9 (2011).

4. P. J. Schlosser, J. E. Hastie, S. Calvez, A. B. Krysa, and M. D. Dawson, "InP/AlGaInP quantum dot semiconductor disk lasers for CW TEM_{00} emission at 716 - 755 nm," Opt. Express **17**, 21782-21787 (2009).

5. O. G. Okhotnikov, D. Bimberg, M. Guina, D. Burns, S. Calvez, M. D. Dawson, J. E. Hastie, J.-M. Hopkins, A. J. Kemp, U. Keller, M. Kuznetsov, N. Laurand, D. J. H. C. Maas, A. Mooradian, U. W. Pohl, M. Rattunde, B. Rösener, A. Shchergrov, T. Südmeyer, A. Tandon, J. Wagner, and G. Yoffe, *Semiconductor Disk Lasers. Physics and Technology*, O. G. Okhotnikov, ed., (WILEY-VCH Verlag GmbH & Co. KGaA, Weinheim, Weinheim, 2010).

6. J. S. Peter, Jennifer E.Hastie, C. Stephane, B. K. Andrey, and D. D. Martin, "Semiconductor Disk Lasers Incorporating InP/GaInP Quantum Dots for 716-755 nm Emission," (Optical Society of America, 2010), pp. AWB5.

7. M. T. Andersen, P. J. Schlosser, J. E. Hastie, P. Tidemand-Lichtenberg, M. D. Dawson, and C. Pedersen, "Singly-resonant sum frequency generation of visible light in a semiconductor disk laser," Opt. Express **17**, 6010-6017 (2009).

8. E. Schiehlen, M. Golling, and P. Unger, "Diode-pumped semiconductor disk laser with intracavity frequency doubling using lithium triborate (LBO)," Photonics Technology Letters, IEEE **14**, 777-779 (2002).

9. T. D. Raymond, W. J. Alford, M. H. Crawford, and A. A. Allerman, "Intracavity frequency doubling of a diode-pumped external-cavity surface-emitting semiconductor laser," Opt. Lett. **24**, 1127-1129 (1999).

10. A. Rantamäki, A. Sirbu, A. Mereuta, E. Kapon, and O. G. Okhotnikov, "3 W of 650 nm red emission by frequency doubling of wafer-fused semiconductor disk laser," Opt. Express **18**, 21645-21650 (2010).

11. A. J. Maclean, A. J. Kemp, S. Calvez, K. Jun-Youn, K. Taek, M. D. Dawson, and D. Burns, "Continuous Tuning and Efficient Intracavity Second-Harmonic Generation in a Semiconductor Disk Laser With an Intracavity Diamond Heatspreader," Quantum Electronics, IEEE Journal of **44**, 216-225 (2008).

12. J. Y. Kim, S. Cho, S. J. Lim, J. Yoo, G. B. Kim, K. S. Kim, J. Lee, S. M. Lee, T. Kim, and Y. Park, "Efficient blue lasers based on gain structure optimizing of vertical-external-cavity surface-emitting laser with second harmonic generation," Journal of Applied Physics **101**, 033103-033104 (2007).

13. G. B. Kim, J. Y. Kim, J. Lee, J. Yoo, K. S. Kim, S. M. Lee, S. Cho, S. J. Lim, T. Kim, and Y. Park, "End-pumped green and blue vertical external cavity surface emitting laser devices," Applied Physics Letters **89**, 181106-3 (2006).

14. J. E. Hastie, L. G. Morton, A. J. Kemp, M. D. Dawson, A. B. Krysa, and J. S. Roberts, "Tunable ultraviolet output from an intracavity frequency-doubled red vertical-external-cavity surface-emitting laser," Applied Physics Letters **89**, 061114-3 (2006).

15. R. Hartke, V. Baev, K. Seger, O. Back, E. Heumann, G. Huber, M. Kuhnelt, and U. Steegmüller, "Experimental study of the output dynamics of intracavity frequency doubled optically pumped semiconductor disk lasers," Applied Physics Letters **92**, 101107-3 (2008).

16. E. Gerster, I. Ecker, S. Lorch, C. Hahn, S. Menzel, and P. Unger, "Orange-emitting frequency-doubled GaAsSb/GaAs semiconductor disk laser," Journal of Applied Physics **94**, 7397-7401 (2003).

17. M. Fallahi, C. Hessenius, F. Li, J. Hader, L. Hongbo, J. V. Moloney, W. Stolz, and S. W. Koch, "High power tunable yellow laser using InGaAs/GaAs vertical external-cavity surface-emitting lasers," in *Semiconductor Laser Conference, 2008. ISLC 2008. IEEE 21st International*, (2008), pp. 169-170.

18. S. Du, Y. Kaneda, and M. Yarborough, "Retracted: 488 nm ultraviolet light generated by VECSEL and V-cavity second-harmonic generation using lithium triborate," Microw. Opt. Technol. Lett. **50**, 2892-2894 (2008).

19. M. Butkus, C. J. Hamilton, D. Jackson, G. P. A. Malcolm, I. Krestnikov, D. Livshits, and E. U. Rafailov, "Green second harmonic generation in quantum dot semiconductor disc lasers," in *Laser Optics, St. Petersburgh, Russia 2010*, (2010).

20. R. Hartke, E. Heumann, G. Huber, M. Kühnelt, and U. Steegmüller, "Efficient green generation by intracavity frequency doubling of an optically pumped semiconductor disk laser," Applied Physics B: Lasers and Optics **87**, 95-99 (2007).

21. A. Härkönen, J. Rautiainen, T. Leinonen, Y. A. Morozov, L. Orsila, M. Guina, M. Pessa, and O. G. Okhotnikov, "Intracavity Sum-Frequency Generation in Dual-Wavelength Semiconductor Disk Laser," Photonics Technology Letters, IEEE **19**, 1550-1552 (2007).

22. D. J. Stothard, J. M. Hopkins, D. Burns, and M. H. Dunn, "Stable, continuous-wave, intracavity, optical parametric oscillator pumped by a semiconductor disk laser (VECSEL)," Opt. Express **17**, 10648-10658 (2009).

23. D. C. Parrotta, W. Lubeigt, A. J. Kemp, D. Burns, M. D. Dawson, and J. E. Hastie, "Continuous-wave Raman laser pumped within a semiconductor disk laser cavity," Opt. Lett. **36**, 1083-1085 (2011).

24. J. Rautiainen, J. Lyytikäinen, A. Sirbu, A. Mereuta, A. Caliman, E. Kapon, and O. G. Okhotnikov, "2.6 W optically-pumped semiconductor disk laser operating at 1.57-μm using wafer fusion," Opt. Express **16**, 21881-21886 (2008).

25. Y. Qian, Z. Zhu, Y. Lo, D. Huffaker, D. Deppe, H. Hou, B. Hammons, W. Lin, and Y. Tu, "Long wavelength 1.3 μm vertical-cavity surface-emitting lasers with a wafer-bonded mirror and an oxygen-implanted confinement region," Appl. Phys. Lett. **71**, 25 (1997).

26. S. H. Park, J. Kim, H. Jeon, T. Sakong, S. N. Lee, S. Chae, Y. Park, C. H. Jeong, G. Y. Yeom, and Y. H. Cho, "Room-temperature GaN vertical-cavity surface-emitting laser operation in an extended cavity scheme," Applied Physics Letters **83**, 2121-2123 (2003).

27. S. H. Park and H. Jeon, "Microchip-Type InGaN Vertical External-Cavity Surface-Emitting Laser," Optical Review **13**, 20-23 (2006).

28. M. Müller, N. Linder, C. Karnutsch, W. Schmid, K. P. Streubel, J. Luft, S. S. Beyertt, A. Giesen, and G. H. Doehler, "Optically pumped semiconductor thin-disk laser with external cavity operating at 660 nm," C. Lei and S. P. Kilcoyne, eds., (SPIE, San Jose, CA, USA, 2002), pp. 265-271.

29. A. Smith, J. E. Hastie, H. D. Foreman, T. Leinonen, M. Guina, and M. D. Dawson, "GaN diode-pumping of red semiconductor disk laser," Electronics Letters **44**, 1195-1196 (2008).

30. T. Schwarzbäck, M. Eichfelder, W. M. Schulz, R. Roßbach, M. Jetter, and P. Michler, "Short wavelength red-emitting AlGaInP-VECSEL exceeds 1.2 W continuous-wave output power," Applied Physics B: Lasers and Optics 1-6 (2010).

31. J. Hastie, S. Calvez, M. Dawson, T. Leinonen, A. Laakso, J. Lyytikäinen, and M. Pessa, "High power CW red VECSEL with linearly polarized TEM00 output beam," Opt. Express **13**, 77-81 (2005).

32. M. C. Tamargo, S. Guo, O. Maksimov, Y. C. Chen, F. C. Peiris, and J. K. Furdyna, "Red-green-blue light emitting diodes and distributed Bragg reflectors based on ZnCdMgSe lattice-matched to InP," Journal of Crystal Growth **227-228**, 710-716 (2001).

33. A. Smith, "Diode pumped visible Vertical External Cavity Surface Emitting Lasers," (University of Strathclyde, (2010).

34. K. Kishino and I. Nomura, "Yellow-green emitters based on beryllium-chalcogenides on InP substrates," phys. stat. sol. (c) **1**, 1477-1486 (2004).

35. T. Morita, H. Shinbo, T. Nagano, I. Nomura, A. Kikuchi, and K. Kishino, "Refractive index measurements of MgZnCdSe II--VI compound semiconductors grown on InP substrates and fabrications of 500--600 nm range MgZnCdSe distributed Bragg reflectors," Journal of Applied Physics **81**, 7575-7579 (1997).

36. S. Guo, O. Maksimov, M. Tamargo, F. Peiris, and J. Furdyna, "Distributed Bragg reflectors for visible range applications based on (Zn,Cd,Mg)Se lattice matched to InP," Appl. Phys. Lett. **77**, 4107 (2000).

37. M. Rahim, A. Khiar, F. Felder, M. Fill, D. Chappuis, and H. Zogg, "Above Room Temperature Lead Salt VECSELs," Physics Procedia **3**, 1145-1148 (2010).

38. S. S. Beyertt, U. Brauch, F. Demaria, N. Dhidah, A. Giesen, T. Kubler, S. Lorch, F. Rinaldi, and P. Unger, "Efficient Gallium-Arsenide Disk Laser," Quantum Electronics, IEEE Journal of **43**, 869-875 (2007).

39. S. J. McGinily, R. H. Abram, K. S. Gardner, R. Erling, A. I. Ferguson, and J. S. Roberts, "Novel Gain Medium Design for Short-Wavelength Vertical-External-

Cavity Surface-Emitting Laser," Quantum Electronics, IEEE Journal of **43**, 445-450 (2007).

40. S. Lutgen, T. Albrecht, P. Brick, W. Reill, J. Luft, and W. Späth, "8-W high-efficiency continuous-wave semiconductor disk laser at 1000 nm," Appl. Phys. Lett. **82**, 3620 (2003).

41. T. D. Germann, A. Strittmatter, U. W. Pohl, D. Bimberg, J. Rautiainen, M. Guina, and O. G. Okhotnikov, "Quantum-dot semiconductor disk lasers," Journal of Crystal Growth **310**, 5182-5186 (2008).

42. V. M. Korpijärvi, M. Guina, J. Puustinen, P. Tuomisto, J. Rautiainen, A. Härkönen, A. Tukiainen, O. Okhotnikov, and M. Pessa, "MBE grown GaInNAs-based multi-Watt disk lasers," Journal of Crystal Growth **311**, 1868-1871 (2009).

43. H. Lindberg, M. Strassner, and A. Larsson, "Improved spectral properties of an optically pumped semiconductor disk laser using a thin diamond heat spreader as an intracavity filter," Photonics Technology Letters, IEEE **17**, 1363-1365 (2005).

44. J. M. Hopkins, N. Hempler, B. Rösener, N. Schulz, M. Rattunde, C. Manz, K. Köhler, J. Wagner, and D. Burns, "High-power, (AlGaIn)(AsSb) semiconductor disk laser at 2.0 μm," Opt. Lett. **33**, 201-203 (2008).

45. B. Rösener, M. Rattunde, R. Moser, S. Kaspar, T. Töpper, C. Manz, K. Köhler, and J. Wagner, "Continuous-wave room-temperature operation of a 2.8 μm GaSb-based semiconductor disk laser," Opt. Lett. **36**, 319-321 (2011).

46. N. Hempler, J. M. Hopkins, B. Rösener, M. Rattunde, J. Wagner, V. V. Fedorov, I. S. Moskalev, S. B. Mirov, and D. Burns, "Semiconductor disk laser pumped Cr^{2+}:ZnSe lasers," Opt. Express **17**, 18136-18141 (2009).

47. J. Rautiainen, J. inen, L. Toikkanen, J. Nikkinen, A. Sirbu, A. Mereuta, A. Caliman, E. Kapon, and O. G. Okhotnikov, "1.3 μm mode-locked disk laser with wafer fused gain chip and SESAM," in *Lasers and Electro-Optics (CLEO) and Quantum Electronics and Laser Science Conference (QELS), 2010 Conference on*, (2010), pp. 1-2.

48. Y. Barbarin, M. Hoffmann, P. Pallmann, I. Dahhan, P. Kreuter, M. Miller, J. Baier, H. Moench, M. Golling, T. Sudmeyer, B. Witzigmann, and U. Keller, "Electrically Pumped Vertical External Cavity Surface Emitting Lasers Suitable for Passive Modelocking," Selected Topics in Quantum Electronics, IEEE Journal of **PP**, 1-8 (2000).

49. S. Illek, T. Albrecht, P. Brick, S. Lutgen, I. Pietzonka, M. Furitsch, W. Diehl, J. Luft, and K. Streubel, "Vertical-External-Cavity Surface-Emitting Laser With Monolithically Integrated Pump Lasers," Photonics Technology Letters, IEEE **19**, 1952-1954 (2007).

Appendices:

A.1 Design for VECSEL structures listed in Table 4-2

MR2482/83 - 755 nm VECSEL - 24 QD-layers - barrier1 x=0.3 - barrier2 x=0.6					
Layer	**Material**	**Mole fraction x**	**Mole fraction y**	**Thickness (nm)**	**Purpose**
15	$Ga_yIn_{1-y}P$		0.51	10	Capping layer
14	$(Al_xGa_{1-x})_yIn_{1-y}P$	0.6	0.51	72	Barrier 2
13 x 8	$(Al_xGa_{1-x})_yIn_{1-y}P$	0.3	0.51	8	Active region 8 x 3 QD+QW-layers, including Barrier1 and Barrier2
12 x 8	$InP/Ga_yIn_{1-y}P$ - QD+QW		0.51	8	
11 x 8	$(Al_xGa_{1-x})_yIn_{1-y}P$	0.3	0.51	16	
10 x 8	$InP/Ga_yIn_{1-y}P$ - QD+QW		0.51	8	
9 x 8	$(Al_xGa_{1-x})_yIn_{1-y}P$	0.3	0.51	16	
8 x 8	$InP/Ga_yIn_{1-y}P$ - QD+QW		0.51	8	
7 x 8	$(Al_xGa_{1-x})_yIn_{1-y}P$	0.3	0.51	8	
6 x 8	$(Al_xGa_{1-x})_yIn_{1-y}P$	0.6	0.51	41	
5	$(Al_xGa_{1-x})_yIn_{1-y}P$	0.6	0.51	37	Barrier 2
4	AlAs			62	40.5 period DBR
3 x 40	$Al_xGa_{x-1}As$	0.35		54.2	
2 x 40	AlAs			62	
1	GaAs			500	Buffer

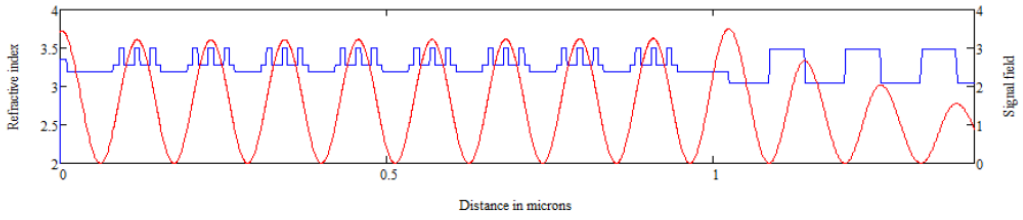

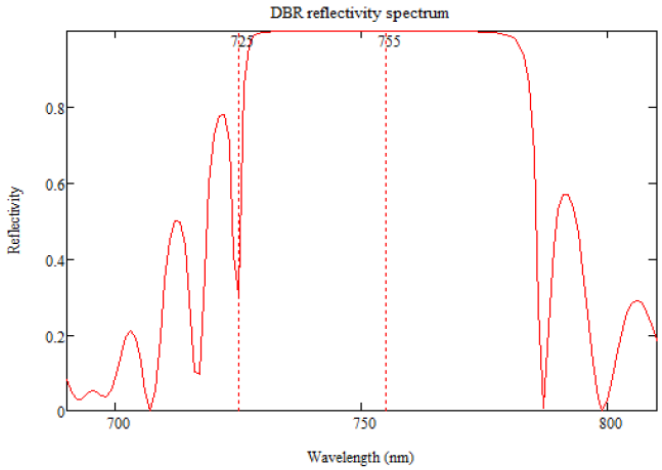

MR2484 - 755nm VECSEL - 21 QD-layers - barrier1 x=0.3

Layer	Material	Mole fraction x	Mole fraction y	Thickness (nm)	Purpose
13	$Ga_yIn_{1-y}P$		0.51	10	Capping layer
12	$(Al_xGa_{1-x})_yIn_{1-y}P$	0.3	0.51	83	Barrier 1
11 x 7	$InP/Ga_yIn_{1-y}P$ - QD+QW		0.51	8	Active region 7 x 3 QD+QW-layers, including Barrier1
10 x 7	$(Al_xGa_{1-x})_yIn_{1-y}P$	0.3	0.51	16	
9 x 7	$InP/Ga_yIn_{1-y}P$ - QD+QW		0.51	8	
8 x 7	$(Al_xGa_{1-x})_yIn_{1-y}P$	0.3	0.51	16	
7 x 7	$InP/Ga_yIn_{1-y}P$ - QD+QW		0.51	8	
6 x 7	$(Al_xGa_{1-x})_yIn_{1-y}P$	0.3	0.51	56	
5	$(Al_xGa_{1-x})_yIn_{1-y}P$	0.3	0.51	145	Barrier 1
4	AlAs			62	40.5 period DBR
3 x 40	$Al_xGa_{x-1}As$	0.35		54.2	
2 x 40	AlAs			62	
1	GaAs			500	Buffer

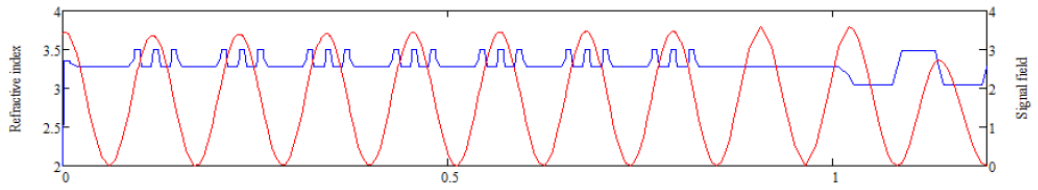

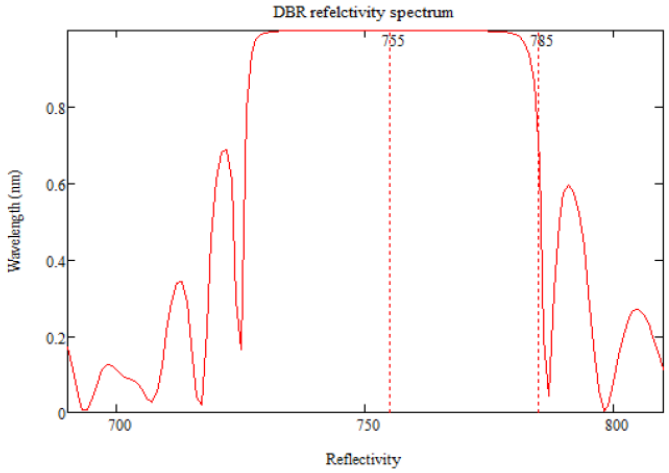

MR2603/09/17 - 740 nm VECSEL - 21 QD-layer - barrier1 x=0.3					
Layer	**Material**	**Mole fraction x**	**Mole fraction y**	**Thickness (nm)**	**Purpose**
13	$Ga_yIn_{1-y}P$		0.51	10	Capping layer
12	$(Al_xGa_{1-x})_yIn_{1-y}P$	0.3	0.51	74	Barrier1
11 x 7	$InP/Ga_yIn_{1-y}P$ - QD+QW		0.51	8	Active region 7 x 3 QD+QW-layers, including Barrier1
10 x 7	$(Al_xGa_{1-x})_yIn_{1-y}P$	0.3	0.51	16	
9 x 7	$InP/Ga_yIn_{1-y}P$ - QD+QW		0.51	8	
8 x 7	$(Al_xGa_{1-x})_yIn_{1-y}P$	0.3	0.51	16	
7 x 7	$InP/Ga_yIn_{1-y}P$ - QD+QW		0.51	8	
6 x 7	$(Al_xGa_{1-x})_yIn_{1-y}P$	0.3	0.51	55	
5	$(Al_xGa_{1-x})_yIn_{1-y}P$	0.3	0.51	135	Barrier1
4	AlAs			62	40.5 period DBR
3 x 40	$Al_xGa_{x-1}As$	0.35		54.2	
2 x 40	AlAs			62	
1	GaAs			500	Buffer

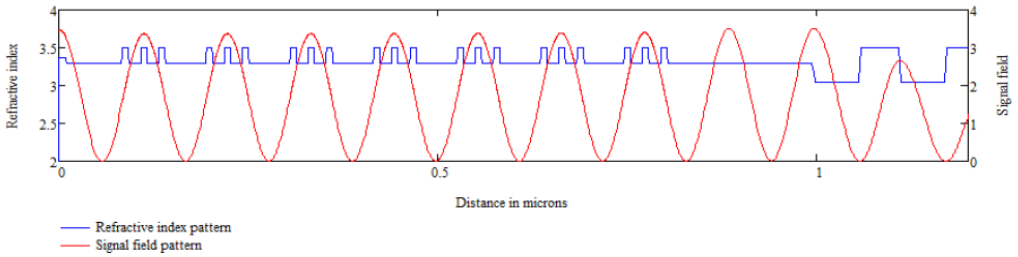

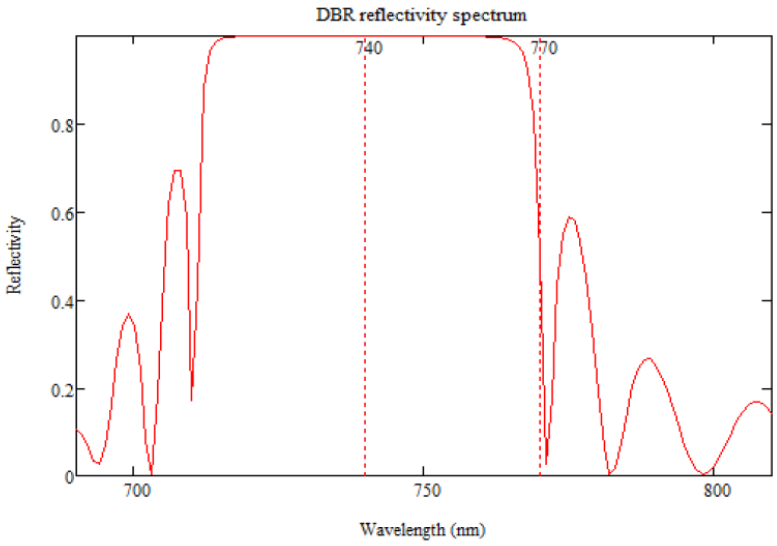

MR2609/15 - 740 nm VECSEL - 21-QD layer - barrier1 x=0.3 - confinement x=0.6

Layer	Material	Mole fraction x	Mole fraction y	Thickness (nm)	Purpose
20	$Ga_yIn_{1-y}P$		0.51	10	Capping layer
19	$(Al_xGa_{1-x})_yIn_{1-y}P$	0.6	0.51	62	Carrier confinement
18	$(Al_xGa_{1-x})_yIn_{1-y}P$	0.3	0.51	16	Barrier1
17 x 6	$InP/Ga_yIn_{1-y}P$ - QD+QW		0.51	8	Active region 7 x 3 QD+QW-layers, including Barrier1
16 x 6	$(Al_xGa_{1-x})_yIn_{1-y}P$	0.3	0.51	16	
15 x 6	$InP/Ga_yIn_{1-y}P$ - QD+QW		0.51	8	
14 x 6	$(Al_xGa_{1-x})_yIn_{1-y}P$	0.3	0.51	16	
13 x 6	$InP/Ga_yIn_{1-y}P$ - QD+QW		0.51	8	
12 x 6	$(Al_xGa_{1-x})_yIn_{1-y}P$	0.3	0.51	54	
11	$InP/Ga_yIn_{1-y}P$ - QD+QW		0.51	8	
10	$(Al_xGa_{1-x})_yIn_{1-y}P$	0.3	0.51	16	
9	$InP/Ga_yIn_{1-y}P$ - QD+QW		0.51	8	
8	$(Al_xGa_{1-x})_yIn_{1-y}P$	0.3	0.51	16	
7	$InP/Ga_yIn_{1-y}P$ - QD+QW		0.51	8	
6	$(Al_xGa_{1-x})_yIn_{1-y}P$	0.3	0.51	16	Barrier1
5	$(Al_xGa_{1-x})_yIn_{1-y}P$	0.6	0.51	66	Carrier confinement
4	AlAs			61	40.5 period DBR
3 x 40	$Al_xGa_{x-1}As$	0.35		52	
2 x 40	AlAs			61	
1	GaAs			500	Buffer

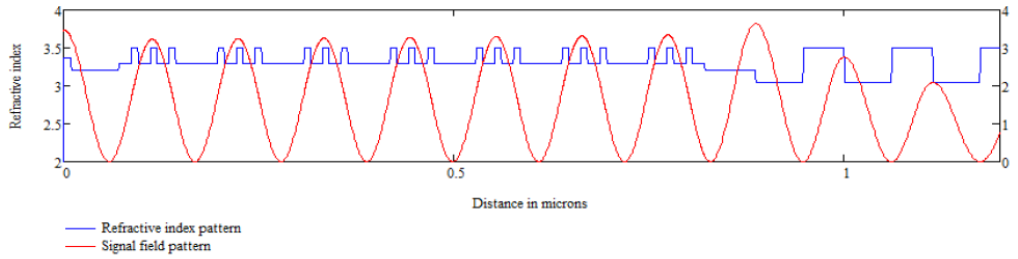

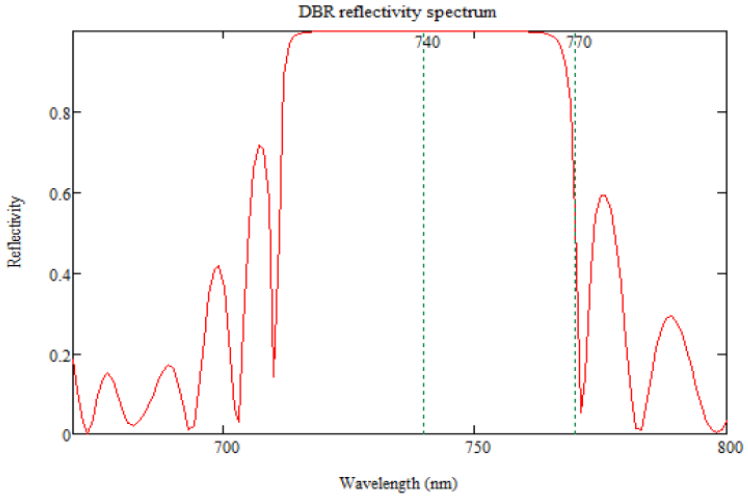

MR2961/62/63/64 - 730 nm VECSEL - 21 QD-layer - barrier1 x=0.3 - confinement x=0.6					
Layer	**Material**	**Mole Fraction x**	**Mole Fraction y**	**Thickness (nm)**	**Purpose**
20	$Ga_yIn_{1-y}P$		0.51	10	Capping layer
19	$(Al_xGa_{1-x})_yIn_{1-y}P$	0.6	0.51	44	Carrier confinement
18	$(Al_xGa_{1-x})_yIn_{1-y}P$	0.3	0.51	32	Barrier1
17 x 6	$InP/Ga_yIn_{1-y}P$ - QD+QW		0.54	8	Active Region 7 x 3 InP QD, including Barrier1
16 x 6	$(Al_xGa_{1-x})_yIn_{1-y}P$	0.3	0.51	16	
15 x 6	$InP/Ga_yIn_{1-y}P$ - QD+QW		0.54	8	
14 x 6	$(Al_xGa_{1-x})_yIn_{1-y}P$	0.3	0.51	16	
13 x 6	$InP/Ga_yIn_{1-y}P$ - QD+QW		0.54	8	
12 x 6	$(Al_xGa_{1-x})_yIn_{1-y}P$	0.3	0.51	51.5	
11	$InP/Ga_yIn_{1-y}P$ - QD+QW		0.54	8	
10	$(Al_xGa_{1-x})_yIn_{1-y}P$	0.3	0.51	16	
9	$InP/Ga_yIn_{1-y}P$ - QD+QW		0.54	8	
8	$(Al_xGa_{1-x})_yIn_{1-y}P$	0.3	0.51	16	
7	$InP/Ga_yIn_{1-y}P$ - QD+QW		0.54	8	
6	$(Al_xGa_{1-x})_yIn_{1-y}P$	0.3	0.51	32	Barrier1
5	$(Al_xGa_{1-x})_yIn_{1-y}P$	0.6	0.51	167	Carrier confinement
4	AlAs			60	40.5 period DBR
3 x 40	$Al_xGa_{x-1}As$	0.35		52	
2 x 40	AlAs			60	
1	GaAs			500	Buffer layer

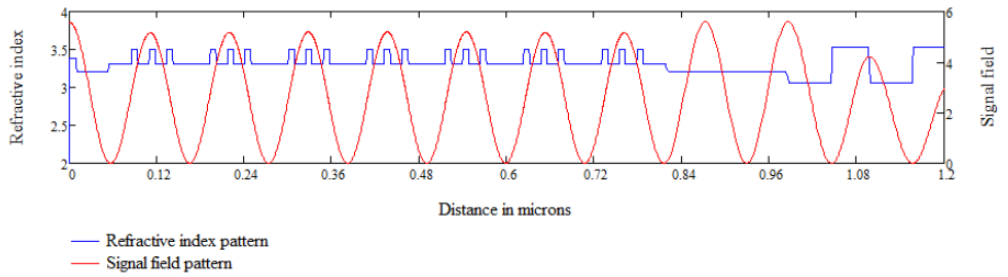

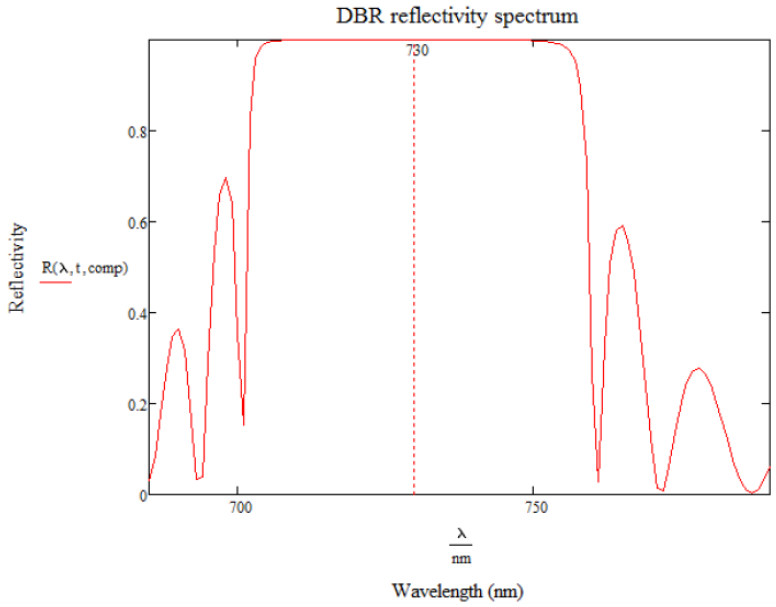

MR2965 - 730 nm VECSEL - 28 QD-layer - barrier1 x=0.3 - confinement x=0.6					
Layer	**Material**	**Mole Fraction x**	**Mole Fraction y**	**Thickness (nm)**	**Purpose**
24	$Ga_yIn_{1-y}P$		0.51	10	Capping layer
23	$(Al_xGa_{1-x})_yIn_{1-y}P$	0.6	0.51	32	Carrier confinement
22	$(Al_xGa_{1-x})_yIn_{1-y}P$	0.3	0.51	32	Active Region 7 x 4 InP QD
21 x 6	$InP/Ga_yIn_{1-y}P$ - QD+QW		0.56	8	
20 x 6	$(Al_xGa_{1-x})_yIn_{1-y}P$	0.3	0.51	16	
19 x 6	$InP/Ga_yIn_{1-y}P$ - QD+QW		0.56	8	
18 x 6	$(Al_xGa_{1-x})_yIn_{1-y}P$	0.3	0.51	16	
17 x 6	$InP/Ga_yIn_{1-y}P$ - QD+QW		0.56	8	
16 x 6	$(Al_xGa_{1-x})_yIn_{1-y}P$	0.3	0.51	16	
15 x 6	$InP/Ga_yIn_{1-y}P$ - QD+QW		0.56	8	
14 x 6	$(Al_xGa_{1-x})_yIn_{1-y}P$	0.3	0.51	28	
13	$InP/Ga_yIn_{1-y}P$ - QD+QW		0.56	8	
12	$(Al_xGa_{1-x})_yIn_{1-y}P$	0.3	0.51	16	
11	$InP/Ga_yIn_{1-y}P$ - QD+QW		0.56	8	
10	$(Al_xGa_{1-x})_yIn_{1-y}P$	0.3	0.51	16	
9	$InP/Ga_yIn_{1-y}P$ - QD+QW		0.56	8	
8	$(Al_xGa_{1-x})_yIn_{1-y}P$	0.3	0.51	16	
7	$InP/Ga_yIn_{1-y}P$ - QD+QW		0.56	8	
6	$(Al_xGa_{1-x})_yIn_{1-y}P$	0.3	0.51	32	
5	$(Al_xGa_{1-x})_yIn_{1-y}P$	0.6	0.51	150	Carrier confinement
4	AlAs			60	40.5 period DBR
3 x 40	$Al_xGa_{x-1}As$	0.35		52	
2 x 40	AlAs			60	
1	GaAs			500	Buffer layer

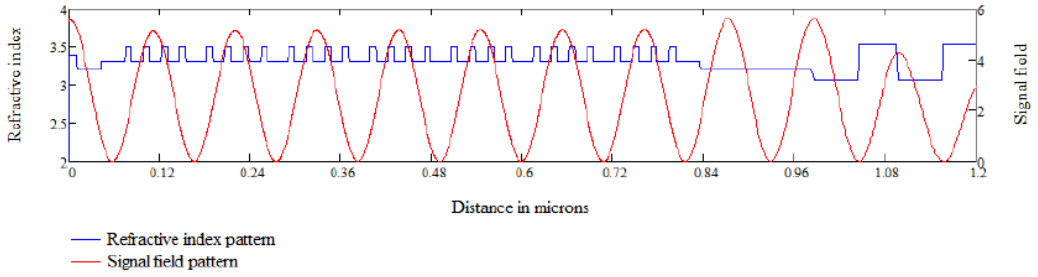

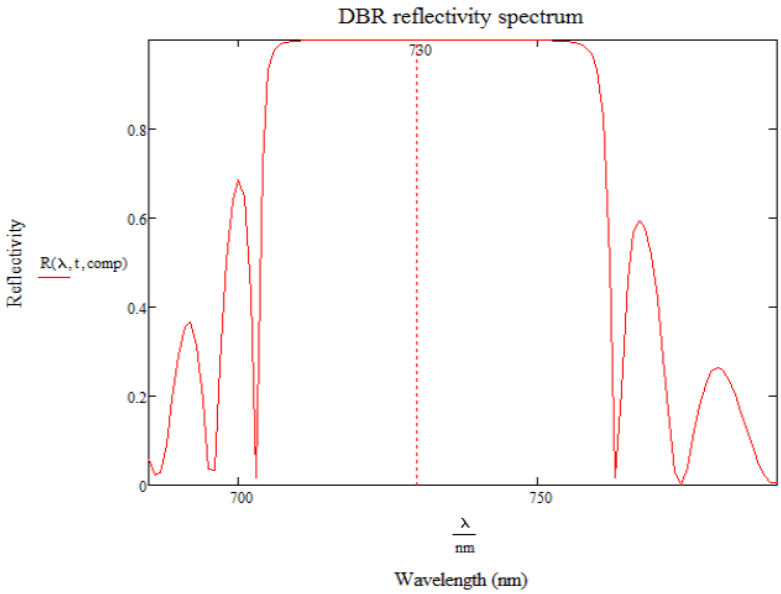

A.2 Surface PL (growth calibration MR2598)

ACCENT RPM2000

Date : February 16, 2009 18:39:24
Wafer ID :
Material : GaAs
Filename : e:
Description :
Recipe :
Calibration : N/A

Operator :
Batch ID :
Thickness : 500 µm

Scan parameters
Radius : N/A
Angle : N/A
Scan rate : 40 pts/s
Temperature : 19.9 C
Gain : x1 (corr.)
Filter : 570nm LP
Smoothed : No

Wavelength settings
Center : 730.0 nm
Range : 664.9 to 794.9 nm
Resolution : 0.25 nm/pixel
Pixels : 512
Slit width : 0.005 mm
Grating : 300 g/mm
Detector : CCD Array

Laser parameters
Name : 532 CW
Wavelength : 532.0 nm
Power : 2.6 mW

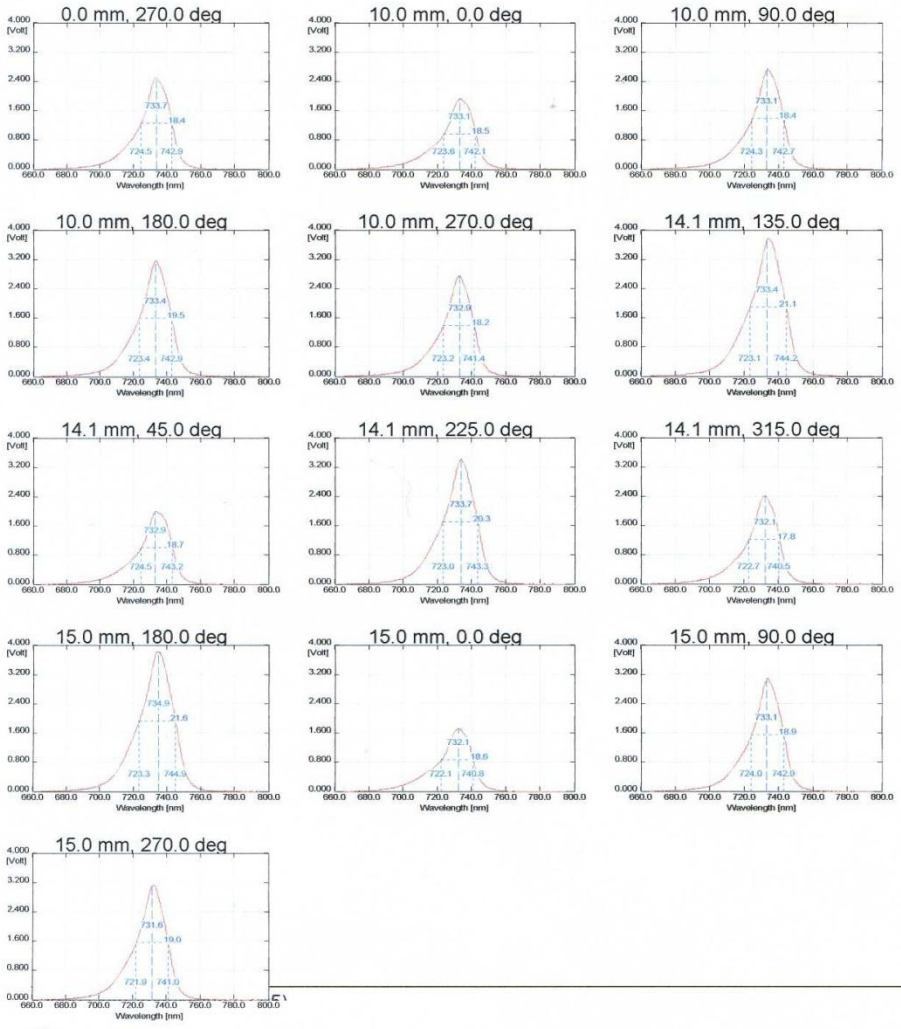

A.3 Wafer mapping (calibration growth MR2959)

ACCENT RPM2000

Date : April 20, 2011 15:50:20
Wafer ID : mr2959
Material : GaAs
Filename : c:\akspectra\mr2959\mr2959.spm
Description :
Recipe :
Calibration : (none)

Operator :
Batch ID :
Thickness : 500 µm

Scan parameters		Wavelength settings		Analysis Parameters		Laser parameters	
Wafer size	: 50.8 mm	Center	: 735.1 nm	Mode	: Standard	Name	: 532 nm
Scan diameter	: 50.0 mm	Range	: 669.7 to 799.6 nm	Min Limit	: 550.0 nm	Wavelength	: 532.0 nm
Resolution	: 1.0 mm	Resolution	: 1.01 nm/pixel	Max Limit	: 1856.0 nm	Power	: 2.42 mW
Scan rate	: 30 pts/s	Pixels	: 128	Threshold	: N/A		
Temperature	: 19.7 C	Slit width	: 0.100 mm	FWHM	: 50.0 %		
Gain	: x1 (corr.)	Grating	: 300g/mm				
Filter	: 650nm LP	Detector	: CCD				
Smoothed	: No						

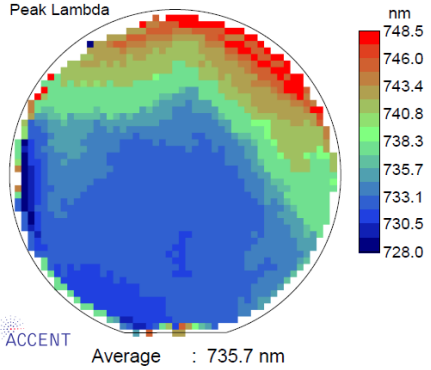

Average : 735.7 nm
Std dev : 4.273 nm (0.581 %)
Min : 728.0 nm
Max : 749.5 nm

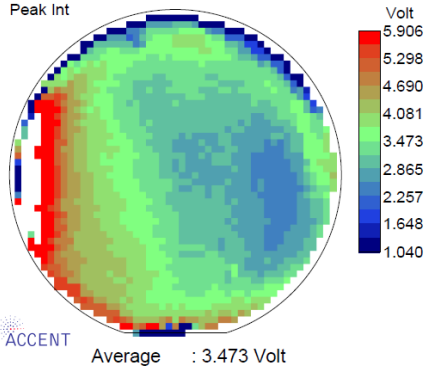

Average : 3.473 Volt
Std dev : 0.811 Volt (23.4 %)
Min : 0.299 Volt
Max : 6.598 Volt

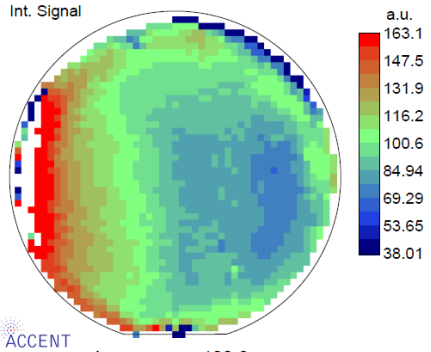

Average : 100.6 a.u.
Std dev : 20.86 a.u. (20.7 %)
Min : 25.88 a.u.
Max : 177.6 a.u.

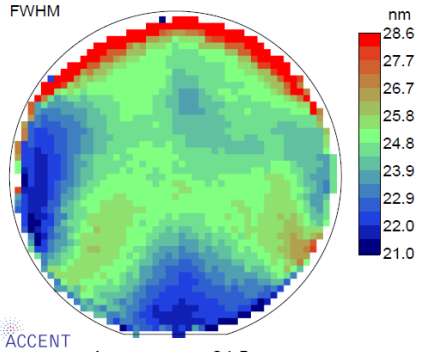

Average : 24.5 nm
Std dev : 1.385 nm (5.66 %)
Min : 21.0 nm
Max : 30.0 nm

ACCENT RPM2000 Data Acquisition, version 4.24 - Serial No: RPM-05-98 Sheffield

ACCENT RPM2000

Date	: April 20, 2011 15:50:20	Operator	:
Wafer ID	: mr2959	Batch ID	:
Material	: GaAs	Thickness	: 500 µm
Filename	: c:\akspectra\mr2959\mr2959.spm		
Description	:		
Recipe	:		
Calibration	: (none)		

Scan parameters		Wavelength settings		Analysis Parameters		Laser parameters	
Wafer size	: 50.8 mm	Center	: 735.1 nm	Mode	: Standard	Name	: 532 nm
Scan diameter	: 50.0 mm	Range	: 669.7 to 799.6 nm	Min Limit	: 550.0 nm	Wavelength	: 532.0 nm
Resolution	: 1.0 mm	Resolution	: 1.01 nm/pixel	Max Limit	: 1856.0 nm	Power	: 2.42 mW
Scan rate	: 30 pts/s	Pixels	: 128	Threshold	: N/A		
Temperature	: 19.7 C	Slit width	: 0.100 mm	FWHM	: 50.0 %		
Gain	: x1 (corr.)	Grating	: 300g/mm				
Filter	: 650nm LP	Detector	: CCD				
Smoothed	: No						

Peak Lambda		Peak Int		Int. Signal		FWHM	
Statistics		Statistics		Statistics		Statistics	
Average	: 735.7 nm	Average	: 3.473 Volt	Average	: 100.6 a.u.	Average	: 24.5 nm
Std dev	: 4.273 nm (0.581 %)	Std dev	: 0.811 Volt (23.4 %)	Std dev	: 20.86 a.u. (20.7 %)	Std dev	: 1.385 nm (5.66 %)
Median	: 734.1 nm	Median	: 3.349 Volt	Median	: 96.44 a.u.	Median	: 24.6 nm
Min	: 728.0 nm	Min	: 0.299 Volt	Min	: 25.88 a.u.	Min	: 21.0 nm
Max	: 749.5 nm	Max	: 6.598 Volt	Max	: 177.6 a.u.	Max	: 30.0 nm
10% cutoff	: 732.1 nm	10% cutoff	: 2.664 Volt	10% cutoff	: 79.27 a.u.	10% cutoff	: 22.5 nm
25% cutoff	: 732.1 nm	25% cutoff	: 2.938 Volt	25% cutoff	: 85.34 a.u.	25% cutoff	: 23.8 nm
75% cutoff	: 738.2 nm	75% cutoff	: 3.887 Volt	75% cutoff	: 111.8 a.u.	75% cutoff	: 25.1 nm
90% cutoff	: 742.3 nm	90% cutoff	: 4.465 Volt	90% cutoff	: 128.0 a.u.	90% cutoff	: 25.7 nm
Exc. zone	: 0.0 mm	Exc. zone	: 0.0 mm	Exc. zone	: 0.0 mm	Exc. zone	: 0.0 mm
Thresholds		Thresholds		Thresholds		Thresholds	
Upper Lmt	: 754.6 nm	Upper Lmt	: 7.600 Volt	Upper Lmt	: 202.7 a.u.	Upper Lmt	: 33.1 nm
Lower Lmt	: 716.6 nm	Lower Lmt	: -0.100 Volt	Lower Lmt	: 1.500 a.u.	Lower Lmt	: 16.2 nm
Specifications		Specifications		Specifications		Specifications	
Upper Lmt	: 754.6 nm	Upper Lmt	: 7.600 Volt	Upper Lmt	: 202.7 a.u.	Upper Lmt	: 33.1 nm
Lower Lmt	: 716.6 nm	Lower Lmt	: -0.100 Volt	Lower Lmt	: 1.500 a.u.	Lower Lmt	: 16.2 nm
In-Spec	: 98.87 %	In-Spec	: 97.37 %	In-Spec	: 96.46 %	In-Spec	: 98.66 %
Below	: 0.54 %	Below	: 0.00 %	Below	: 1.45 %	Below	: 1.34 %
Above	: 0.59 %	Above	: 2.63 %	Above	: 2.09 %	Above	: 0.00 %

ACCENT RPM2000 Data Acquisition, version 4.24 - Serial No: RPM-05-98 Sheffield

ACCENT RPM2000

Date	: April 20, 2011 15:50:20	Operator	:
Wafer ID	: mr2959	Batch ID	:
Material	: GaAs	Thickness	: 500 µm
Filename	: c:\akspectra\mr2959\mr2959.spm		
Description	:		
Recipe	:		
Calibration	: (none)		

Scan parameters		Wavelength settings		Analysis Parameters		Laser parameters	
Wafer size	: 50.8 mm	Center	: 735.1 nm	Mode	: Standard	Name	: 532 nm
Scan diameter	: 50.0 mm	Range	: 669.7 to 799.6 nm	Min Limit	: 550.0 nm	Wavelength	: 532.0 nm
Resolution	: 1.0 mm	Resolution	: 1.01 nm/pixel	Max Limit	: 1856.0 nm	Power	: 2.42 mW
Scan rate	: 30 pts/s	Pixels	: 128	Threshold	: N/A		
Temperature	: 19.7 C	Slit width	: 0.100 mm	FWHM	: 50.0 %		
Gain	: x1 (corr.)	Grating	: 300g/mm				
Filter	: 650nm LP	Detector	: CCD				
Smoothed	: No						

Peak Lambda Histogram

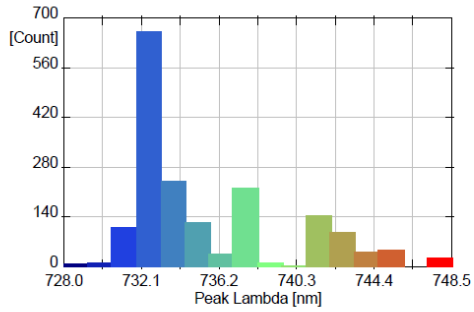

Max count : 664 at 732.5 nm
Bin size : 1.3 nm
Mean : 735.7 nm
Median : 734.1 nm

Peak Int Histogram

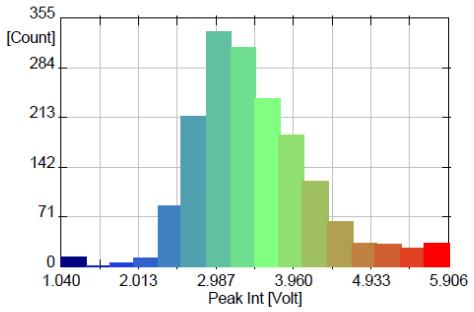

Max count : 336 at 3.017 Volt
Bin size : 0.304 Volt
Mean : 3.473 Volt
Median : 3.349 Volt

Int. Signal Histogram

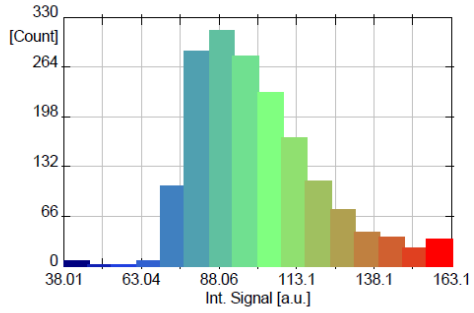

Max count : 313 at 88.85 a.u.
Bin size : 7.821 a.u.
Mean : 100.6 a.u.
Median : 96.44 a.u.

FWHM Histogram

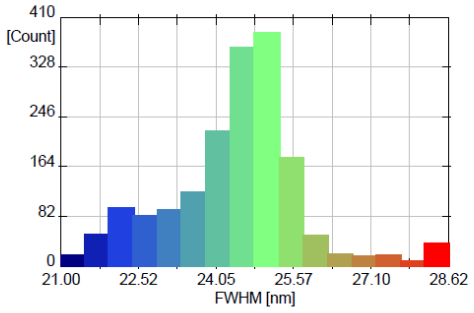

Max count : 387 at 25.0 nm
Bin size : 0.5 nm
Mean : 24.5 nm
Median : 24.6 nm

ACCENT RPM2000 Data Acquisition, version 4.24 - Serial No: RPM-05-98 Sheffield

ACCENT RPM2000

Date	: April 20, 2011 15:50:20	Operator	:
Wafer ID	: mr2959	Batch ID	:
Material	: GaAs	Thickness	: 500 µm
Filename	: c:\akspectra\mr2959\mr2959.spm		
Description	:		
Recipe	:		
Calibration	: (none)		

Scan parameters		Wavelength settings		Analysis Parameters		Laser parameters	
Wafer size	: 50.8 mm	Center	: 735.1 nm	Mode	: Standard	Name	: 532 nm
Scan diameter	: 50.0 mm	Range	: 669.7 to 799.6 nm	Min Limit	: 550.0 nm	Wavelength	: 532.0 nm
Resolution	: 1.0 mm	Resolution	: 1.01 nm/pixel	Max Limit	: 1856.0 nm	Power	: 2.42 mW
Scan rate	: 30 pts/s	Pixels	: 128	Threshold	: N/A		
Temperature	: 19.7 C	Slit width	: 0.100 mm	FWHM	: 50.0 %		
Gain	: x1 (corr.)	Grating	: 300g/mm				
Filter	: 650nm LP	Detector	: CCD				
Smoothed	: No						

Peak Lambda Profile

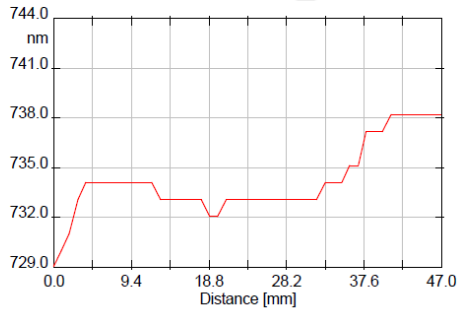

23.0, 270.0 to 24.0, 90.0 [mm, deg]
Average : 734.2 nm
Avge Dev : 1.6 nm (0.2 %)
Min : 729.0 nm
Max : 738.2 nm

Peak Int Profile

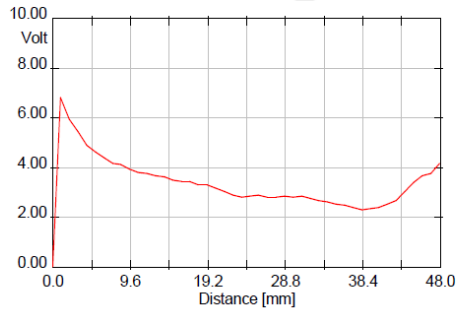

24.0, 270.0 to 24.0, 90.0 [mm, deg]
Average : 3.346 Volt
Avge Dev : 0.776 Volt (23.2 %)
Min : 0.005 Volt
Max : 6.843 Volt

Int. Signal Profile

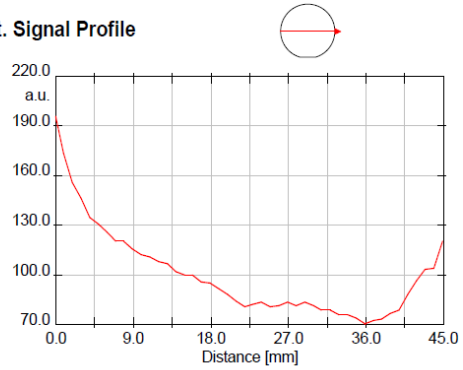

21.0, 270.0 to 24.0, 90.0 [mm, deg]
Average : 100.3 a.u.
Avge Dev : 20.85 a.u. (20.8 %)
Min : 70.29 a.u.
Max : 195.8 a.u.

FWHM Profile

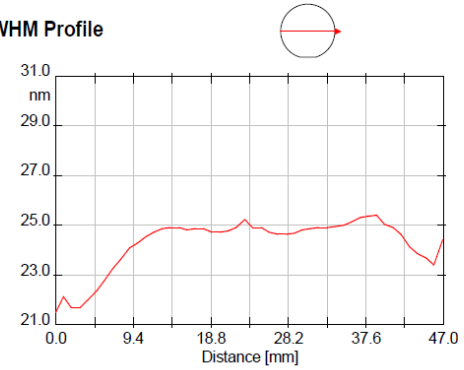

23.0, 270.0 to 24.0, 90.0 [mm, deg]
Average : 24.3 nm
Avge Dev : 0.8 nm (3.4 %)
Min : 21.5 nm
Max : 25.4 nm

ACCENT RPM2000 Data Acquisition, version 4.24 - Serial No: RPM-05-98 Sheffield

A.4 Reflectivity and Surface PL (VECSEL MR2615)

ACCENT RPM2000

Date
Wafer ID
Material
Filename
Description
Recipe :
Calibration : N/A

Operator :
Batch ID :
Thickness : 500 µm

Scan parameters
Radius : N/A
Angle : N/A
Scan rate : 100 pts/s
Temperature : 20.4 C
Gain : x1 (corr.)
Filter : ND1
Smoothed : No

Wavelength settings
Center : 740.2 nm
Range : 675.1 to 805.0 nm
Resolution : 0.25 nm/pixel
Pixels : 512
Slit width : 0.005 mm
Grating : 300 g/mm
Detector : CCD Array

Laser parameters
Name : 532 CW
Wavelength : 532.0 nm
Power : 2.6 mW

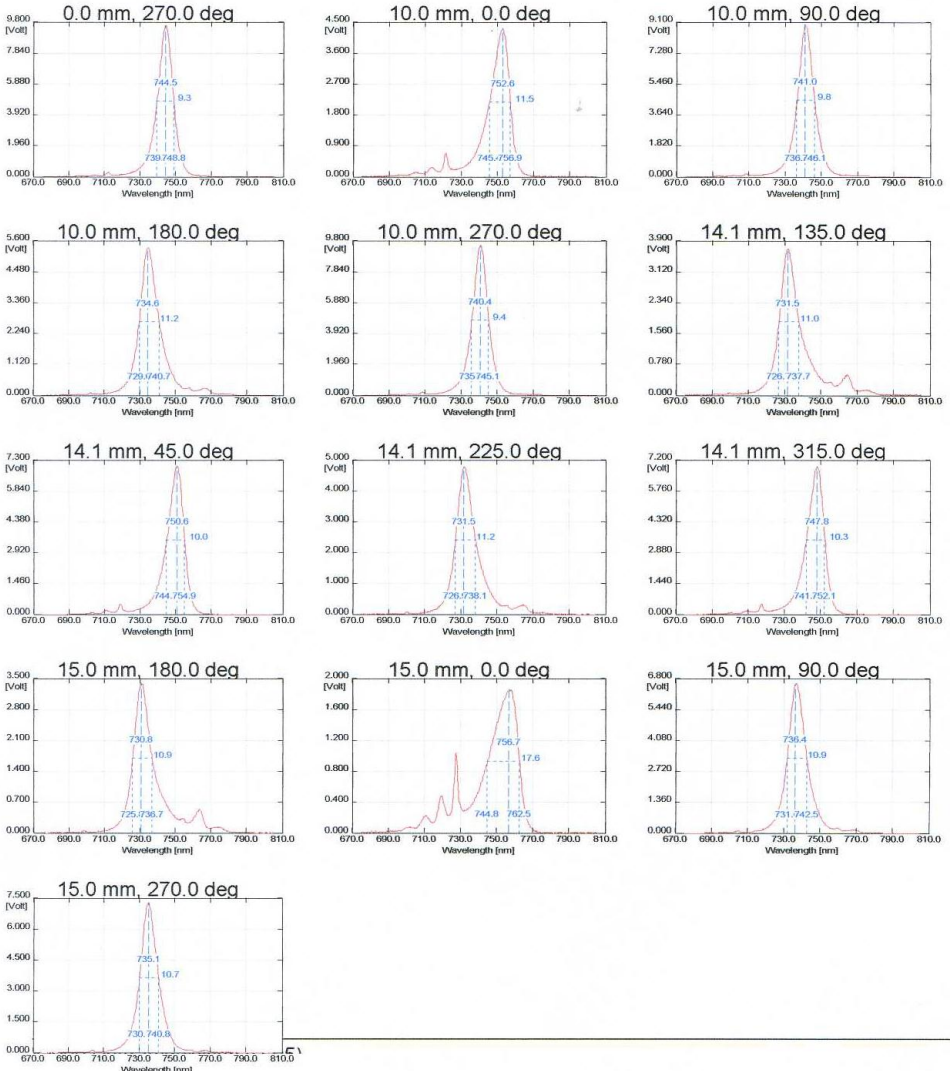

ACCENT RPM2000

Date
Wafer ID
Material
Filename
Description
Recipe
Calibration : g300ccd.cal

Operator :
Batch ID :
Thickness : 500 µm

Scan parameters
Radius : N/A
Angle : N/A
Scan rate : 30 pts/s
Temperature : 20.1 C
Gain : x1 (corr.)
Filter : 570nm LP
Smoothed : No

Wavelength settings
Center : 740.2 nm
Range : 675.1 to 805.0 nm
Resolution : 0.25 nm/pixel
Pixels : 512
Slit width : 0.005 mm
Grating : 300 g/mm
Detector : CCD Array

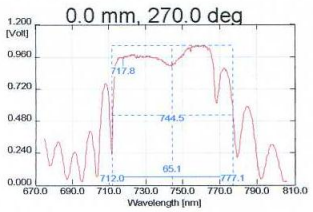

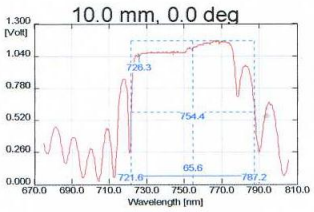

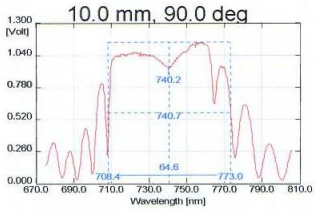

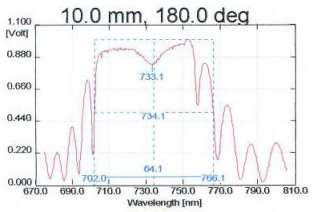

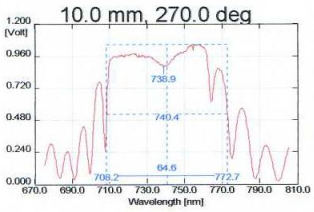

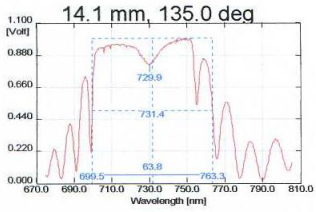

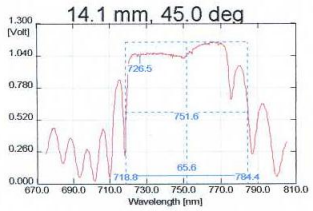

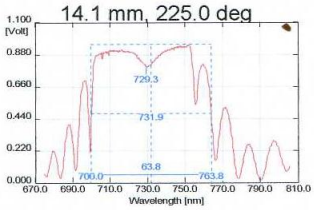

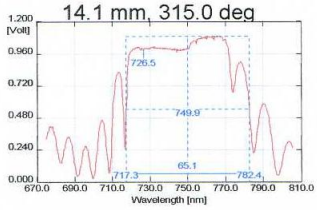

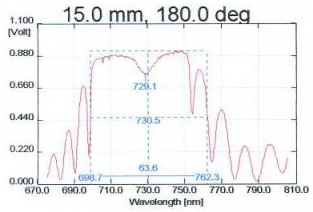

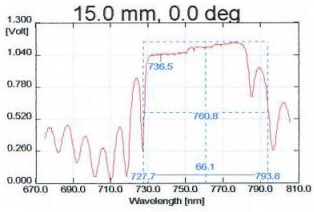

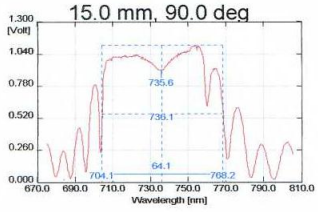

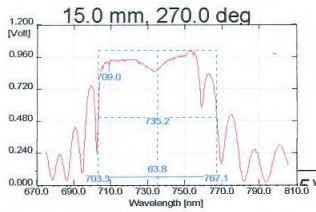

A.5 InP QD VECSEL design

InP QD project - 730nm Stranski-Krastanov QD in a Well VECSEL

- Resonant subcavity design
- no offset
- 21 S-K QD-layers / uniform distribution

Definition of physical constants and units:

Planck's constant (in Js):	$h \equiv 6.62 \cdot 10^{-34} \cdot joule \cdot sec$
Velocity of light in vacuum (in m/s):	$c \equiv 3 \cdot 10^{8} \cdot m \cdot sec^{-1}$
Elementary charge (in As):	$e \equiv 1.6021917 \cdot 10^{-19}$
Elementary charge unit (in eV):	$eV \equiv e \cdot joule$
Micrometer (in µm):	$\mu m \equiv 1 \cdot 10^{-6} \cdot m$
Nonometer (in nm):	$nm \equiv 10^{-9} m$
Angstrom (in A):	$A \equiv 1 \cdot 10^{-10} \cdot m$
Milli Watt (in mW):	$mW \equiv 10^{-3} \cdot watt$
Dielectric parameter of GaAs (external txt. file):	$D \equiv READPRN("GaAs.txt")$

Refractive index calculation:

AlGaAs for DBR and substrate:

Reference [1]: M.A.Afromowitz, "Refractive index of $Ga_{1-x}Al_xAs$", Solid State Comm. **15**, pp.59 (1974)
[2]: Sadao Adachi, "GaAs, AlAs, and $Al_xGa_{1-x}As$: Material parameters for use in research and device applications", J. Appl. Phys., Vol 58, N3, pp.R1-R29 (1985)

Choose model: $model \equiv 1$ **model = 0 from [1]** **model = 1 from [2]**

$$n_{AlGaAs}(\lambda, x) := \text{if } model = 0$$
$$E_0 \leftarrow \left(3.65 + 0.871 \cdot x + 0.179 \cdot x^2\right) \cdot eV$$
$$E_d \leftarrow (36.1 - 2.45 \cdot x) \cdot eV$$
$$E_\Gamma \leftarrow \left(1.424 + 1.266 \cdot x + 0.26 \cdot x^2\right) \cdot eV$$
$$E_f \leftarrow \sqrt{2 \cdot E_0^2 - E_\Gamma^2}$$
$$\eta \leftarrow \frac{\pi \cdot E_d}{2 \cdot E_0^3 \cdot \left(E_0^2 - E_\Gamma^2\right)}$$
$$M_a \leftarrow \frac{\eta \cdot \left(E_f^4 - E_\Gamma^4\right)}{2 \cdot \pi}$$
$$M_b \leftarrow \frac{\eta \cdot \left(E_f^2 - E_\Gamma^2\right)}{\pi}$$
$$K \leftarrow \frac{0.35}{eV}$$
$$E \leftarrow \frac{h \cdot c}{\lambda}$$
$$E_{\Gamma p} \leftarrow E_\Gamma - 25 \cdot 10^{-3} \cdot eV$$
$$m \leftarrow \text{floor}\left(\frac{2.34 - \frac{E}{eV}}{0.02}\right)$$
$$\sqrt{1 + M_a + M_b \cdot E_{\Gamma p}^2 + \frac{\eta \cdot E_{\Gamma p}^4 \cdot \ln\left(\frac{E_f^2 - E_{\Gamma p}^2}{E_\Gamma^2 - E_{\Gamma p}^2}\right)}{\pi} + K \cdot \left(E - E_{\Gamma p}\right) - i \cdot (x = 0) \cdot \left[D_{m,2} - \frac{\left(D_{m+1,2} - D_{m,2}\right) \cdot \left(\frac{E}{eV} - D_{m,0}\right)}{0.02}\right]} \quad \text{if } E > E_{\Gamma p}$$
$$\sqrt{1 + M_a + M_b \cdot E^2 + \frac{\eta \cdot E^4 \cdot \ln\left(\frac{E_f^2 - E^2}{E_\Gamma^2 - E^2}\right)}{\pi}} \quad \text{otherwise}$$

```
if model = 1
    E0 ← (1.425 + 1.155·x + 0.37·x^2)·eV
    Δ0 ← (0.34 − 0.04·x)·eV
    A0 ← 6.3 + 19.0·x
    B0 ← 9.4 − 10.2·x
    χso ← (h·c/λ) / (E0 + Δ0)
    χ ← (h·c/λ) / E0
    f ← χ^−2·[2 − (1 + χ)^(1/2) − (1 − χ)^(1/2)]
    ε ← A0·[f + (1/2)·(E0/(E0 + Δ0))^(3/2)·f] + B0
    n ← √ε
```

AlGaInP for active region:

Reference [3]: Schubert et al. "Isotropic dielectric functions of highly disordered $Al_xGa_{1-x}InP$ ($0 \le x \le 1$) lattice matched to GaAs", J. Appl . Phys., Vol. **86** (4), pp.2025-2027 (1999)

```
n_AlGaInp(λ, x) :=
    E ← 1239.84·nm·eV / λ
    εf ← 0.52 + x·−0.08 + x·(1 − x)·−0.17
    E0 ← [1.899 + x·0.683 + x·(1 − x)·−0.12]·eV
    A0 ← [10.44 + x·11.34 + x·(1 − x)·−0.47]·eV^1.5
    Γ0 ← [0.003 + x·0.005 + x·(1 − x)·0.05]·eV
    E1 ← [3.224 + x·0.421 + x·(1 − x)·−0.13]·eV
    A1 ← 5.27 + x·−0.64 + x·(1 − x)·−1
    Γ1 ← [0.334 + x·0 + x·(1 − x)·0.32]·eV
    A1x ← [1.79 + x·0.07 + x·(1 − x)·1.46]·eV
    Γ1x ← [0.295 + x·0.046 + x·(1 − x)·−0.09]·eV
    s1x ← [0.42 + x·0.6 + x·(1 − x)·0]·eV^−2
    p1x ← −0.76 + x·0 + x·(1 − x)·0
    E2 ← [4.832 + x·0.02 + x·(1 − x)·0]·eV
    A2 ← 2.19 + x·−0.68 + x·(1 − x)·0.66
    Γ2 ← [0.743 + x·−0.159 + x·(1 − x)·0.05]·eV
    s2 ← [0.88 + x·0.49 + x·(1 − x)·0]·eV^−2
    p2 ← 0.16 + x·0.1 + x·(1 − x)·−0.1
    χ0 ← (E + i·Γ0) / E0
    χ1 ← (E + i·Γ1) / E1
    ε0 ← A0·E0^−1.5·[χ0^−2·[2 − (1 + χ0)^0.5 − (1 − χ0)^0.5]]
    ε1 ← −A1·χ1^−2·ln(1 − χ1^2)
    ε1x ← A1x·exp(i·p1x) / (E1 − E − i·Γ1x·exp[−s1x·(E1 − E)^2])
    ε2 ← A2·exp(i·p2) / (1 − (E/E2)^2 − i·(E/E2)·(Γ2/E2)·exp[−s2·(E − E2)^2])
    ε ← εf + ε0 + ε1 + ε1x + ε2
    N ← √ε
    Re(N)
```

Refractive indices put together:

```
n(λ, x) := n_AlGaAs(λ, x)   if x ≥ 0 ∧ x ≤ 1
           3.5              if x = 2
           n_AlGaInp(λ, x − 3)   if x ≥ 3
```

Guessed Dwell refractive index

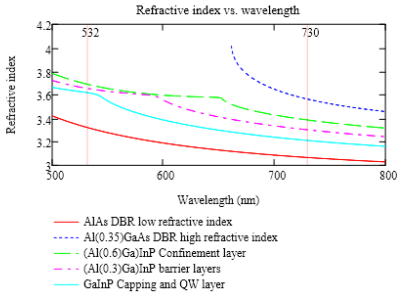

Global design variables/parameters:

Design wavelength: $\lambda_p \equiv 532nm$

Design wavelength: $\lambda_{opt} \equiv 730 \cdot nm$

QD emission wavelength at room temperature: $\lambda_{PL} \equiv 730 \cdot nm$

Offset between QD PL and design wavelength: $offset := 0nm$

Wavelength range:

start wavelength: $\lambda_{start} \equiv 650 \cdot nm$

stop wavelength: $\lambda_{stop} \equiv 800 \cdot nm$

step size: $\lambda_{step} \equiv 1 \cdot nm$

$$n_{step} \equiv \frac{\lambda_{stop} - \lambda_{start}}{\lambda_{step}} + 1$$

Refractive index of substrate: GaAs @ λ_{opt}: $n_{substrate}(\lambda) \equiv 3.5$ $n(\lambda_{opt}, 0) = 3.561 - 0.372i$

Last layer (= substrate): composition GaAs: $x_{substrate} \equiv 0$

chose condition: $cte\_n_{substrate} \equiv 0$ 1 = $n_{substrate}$ is constant; 0 = $n_{substrate}$ is depend on wavelength

refractive index:

$$n_1(\lambda) := \begin{cases} n_{substrate}(\lambda) & \text{if } cte\_n_{substrate} \\ Re(n(\lambda, x_{substrate})) & \text{otherwise} \end{cases} \qquad n_1(\lambda_{opt}) = 3.561$$

Refractive index of incident layer: $n_{top}(\lambda) \equiv 2.42$ diamond heatspreader

First layer: composition: $x_{top} \equiv 0$ necessary if layer is e.g. air or something else

chose condition: $cte\_n_{top} \equiv 1$ 1 = $n_{diamond}$ is constant; 0 = $n_{diamond}$ is depend on wavelength

refractive index:

$$n_1(\lambda) := \begin{cases} n_{top}(\lambda) & \text{if } cte\_n_{top} \\ n(\lambda, x_{top}) & \text{otherwise} \end{cases} \qquad n_1(\lambda_{opt}) = 2.42$$

Reflectivity and electric field calculation of a stratified dielectric medium

Reference
[2]: H.A. MacLeod, "Thin-film optical filters", 2nd edition, Higer Ltd (Bristol), 1986, pp40-48
[3]: M. Born and E. Wolf, "Principles of optics", Pergamon press, 1985, pp51-70

Characteristic matrix methode:

$$RT(\lambda, t, comp) := \left| \begin{array}{l} M \leftarrow identity(2) \\ \eta_i \leftarrow n_i(\lambda) \\ \text{for } j \in 1..N_{layer} \\ \quad \left| \begin{array}{l} M_r \leftarrow M \\ \eta \leftarrow n\left(\lambda, comp_{j-1}\right) \\ \beta \leftarrow \frac{2\cdot\pi}{\lambda}\cdot\eta\cdot t_{j-1} \\ M \leftarrow M_r \cdot \begin{pmatrix} \cos(\beta) & \frac{i}{\eta}\cdot\sin(\beta) \\ i\cdot\eta\cdot\sin(\beta) & \cos(\beta) \end{pmatrix} \end{array} \right. \\ \eta_l \leftarrow n_l(\lambda) \\ N \leftarrow M\cdot\begin{pmatrix} 1 \\ \eta_l \end{pmatrix} \\ r \leftarrow \frac{\eta_i\cdot N_0 - N_1}{\eta_i\cdot N_0 + N_1} \\ R \leftarrow (|r|)^2 \\ tr \leftarrow \frac{2\cdot\eta_i}{\eta_i\cdot N_0 + N_1} \\ T \leftarrow \frac{\eta_l}{\eta_i}\cdot(|tr|)^2 \\ Res \leftarrow \begin{pmatrix} R \\ T \\ r \\ tr \end{pmatrix} \\ Res \end{array} \right.$$

Reflectivity and transmission coefficients $R=|r^2|$, $T=|t^2|$ and amplidutes r, t:

Refractive index pattern calculations :

$$Pattern(z, \lambda, t, comp) := Re\left[n\left(\lambda, comp_0\right)\cdot\left(\Phi(z) - \Phi\left(z - \frac{t_0}{m}\right)\right) + \sum_{k=1}^{N_{layer}-1}\left[n\left(\lambda, comp_k\right)\cdot\left(\Phi\left(z - \frac{\sum_{l=0}^{k-1} t_l}{m}\right) - \Phi\left(z - \frac{\sum_{l=0}^{k} t_l}{m}\right)\right)\right]\right]$$

Electric field calculations :

$$field(\lambda, t, comp) := \left| \begin{array}{l} reflec \leftarrow RT(\lambda, t, comp)_2 \\ \eta_i \leftarrow n_i(\lambda) \\ Q_{init} \leftarrow \begin{bmatrix} 1 + reflec \\ \eta_i\cdot(1 - reflec) \end{bmatrix} \\ N_{stack} \leftarrow identity(2) \\ zcurrent \leftarrow 0 \\ index \leftarrow -1 \\ \text{for } j \in 1..N_{layer} \\ \quad \left| \begin{array}{l} nnmax \leftarrow \left(floor\left(\frac{4\cdot t_{j-1}}{\lambda}\right) + 1\right)\cdot 50 \\ N_r \leftarrow N_{stack} \\ \eta \leftarrow n\left(\lambda, comp_{j-1}\right) \\ \text{for } nn \in 1..nnmax \\ \quad \left| \begin{array}{l} thick \leftarrow \frac{nn\cdot t_{j-1}}{nnmax} \\ \beta \leftarrow \frac{2\cdot\pi}{\lambda}\cdot n\left(\lambda, comp_{j-1}\right)\cdot thick \\ N_{stack} \leftarrow \begin{pmatrix} \cos(\beta) & \frac{-i}{\eta}\cdot\sin(\beta) \\ -i\cdot\eta\cdot\sin(\beta) & \cos(\beta) \end{pmatrix}\cdot N_r \\ Q \leftarrow N_{stack}\cdot Q_{init} \\ Res_{0,\, index+nn} \leftarrow zcurrent + \frac{thick}{m} \\ Res_{1,\, index+nn} \leftarrow \left(\left|Q_0\right|\right)^2 \end{array} \right. \\ index \leftarrow index + nnmax \\ zcurrent \leftarrow zcurrent + \frac{t_{j-1}}{m} \end{array} \right. \\ Res_{0,0} \leftarrow 0 \\ Res_{1,0} \leftarrow \left(\left|Q_{init_{0,0}}\right|\right)^2 \\ Res \end{array} \right.$$

Layer thickenss and composition settings:

Capping layer thickness:	$Ga_{0.51}In_{0.49}P$	$n_{cap} := n(\lambda_{opt}, 3) = 3.387$	$t_{cap} \equiv 10nm$
Barrier layer thickness:	$(Al_{0.3}Ga_{0.7})_{0.51}In_{0.49}P$	$n_{barrier} := n(\lambda_{opt}, 3.3) = 3.303$	$t_{barrier} := \frac{\lambda_{opt}}{2 \cdot n_{barrier}} - 3t_{Dwell} - 2 \cdot t_{spacer} = 54.5\,nm$
Spacer layer thickness:	$(Al_{0.3}Ga_{0.7})_{0.51}In_{0.49}P$	$n_{spacer} := n(\lambda_{opt}, 3.3) = 3.303$	$t_{spacer} \equiv 16nm$
Confinement layer thickness:	$(Al_{0.6}Ga_{0.4})_{0.51}In_{0.49}P$	$n_{conf} := n(\lambda_{opt}, 3.6) = 3.212$	$t_{conf} := \frac{\lambda_{opt}}{2 \cdot n_{conf}} - t_{cap} - 2 \cdot t_{spacer} - \frac{3}{2} t_{Dwell} = 59.6\,nm$
Dwell thickness:	$InP/Ga_{0.51}In_{0.49}P$	$n_{Dwell} := n(\lambda_{opt}, 2) = 3.5$	$t_{Dwell} \equiv 8nm$
DBR layer thickness:	AlAs	$n_{low} := n(\lambda_{opt}, 1) = 3.067$	$t_{low} := \frac{\lambda_{opt}}{4 \cdot n_{low}} = 59.5\,nm$
	$Al_{0.35}Ga_{0.65}As$	$n_{high} := n(\lambda_{opt}, 0.35) = 3.564$	$t_{high} := \frac{\lambda_{opt}}{4 \cdot n_{high}} = 51.2\,nm$

Layer thicknesses:

```
t := | t_in_0 ← t_cap
     | t_in_1 ← t_conf − 0nm
     | t_in_2 ← t_spacer
     | for k ∈ 1..6
     |   t_in_6·(k−1)+3 ← t_Dwell
     |   t_in_6·(k−1)+4 ← t_spacer
     |   t_in_6·(k−1)+5 ← t_Dwell
     |   t_in_6·(k−1)+6 ← t_spacer
     |   t_in_6·(k−1)+7 ← t_Dwell
     |   t_in_6·(k−1)+8 ← t_barrier − 2nm
     | t_in_39 ← t_Dwell
     | t_in_40 ← t_spacer
     | t_in_41 ← t_Dwell
     | t_in_42 ← t_spacer
     | t_in_43 ← t_Dwell
     | t_in_44 ← t_spacer
     | t_in_45 ← t_conf + 8nm
     | for k ∈ 1..40
     |   t_in_2·(k−1)+46 ← t_low
     |   t_in_2·(k−1)+47 ← t_high
     | t_in_126 ← t_low
     | t ← t_in
```

t =

	0
0	10
1	59.6
2	16
3	8
4	16
5	8
6	16
7	8
8	52.5
9	8
10	16
11	8
12	16
13	8
14	52.5
15	8
16	16
17	8
18	...

·nm

Layer composition:

```
comp := | co_0 ← 3
        | co_1 ← 3.6
        | co_2 ← 3.3
        | for i ∈ 1..7
        |   co_6·(i−1)+3 ← 2
        |   co_6·(i−1)+4 ← 3.3
        |   co_6·(i−1)+5 ← 2
        |   co_6·(i−1)+6 ← 3.3
        |   co_6·(i−1)+7 ← 2
        |   co_6·(i−1)+8 ← 3.3
        | co_45 ← 3.6
        | for i ∈ 1..40
        |   co_2·(i−1)+46 ← 1
        |   co_2·(i−1)+47 ← 0.35
        | co_126 ← 1
        | comp ← co
```

comp =

	0
0	3
1	3.6
2	3.3
3	2
4	3.3
5	2
6	3.3
7	2
8	3.3
9	2
10	3.3
11	2
12	3.3
13	2
14	3.3
15	2
16	3.3
17	2
18	...

Number of layers:

$N_{layer} \equiv 127$

Total length of the structure :

$$length_{structure} := \sum_{k=0}^{N_{layer}-1} t_k = 5.364\,\mu m$$

$$length_{active} := \sum_{k=0}^{45} t_k = 0.876\,\mu m$$

Data output:

Reflectivity graph: $\lambda := \lambda_{start}, \lambda_{start} + \lambda_{step} .. \lambda_{start} + n_{step} \cdot \lambda_{step}$ x-axis

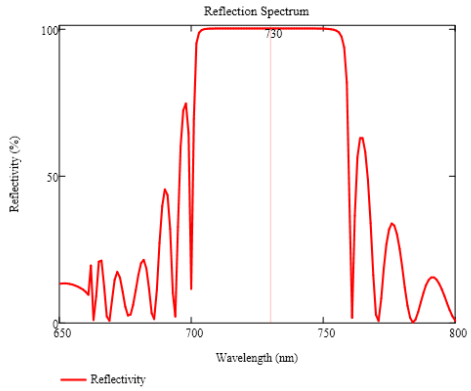

Design graphic:

x-axis $\lambda := \lambda_{start}, \lambda_{start} + \lambda_{step} .. \lambda_{start} + n_{step} \cdot \lambda_{step}$

Signal field intensity pattern: $F_s := field(\lambda_{opt}, t, comp)^T$

Refractive index pattern: $p(z) := Pattern(z, \lambda_{opt}, t, comp)$

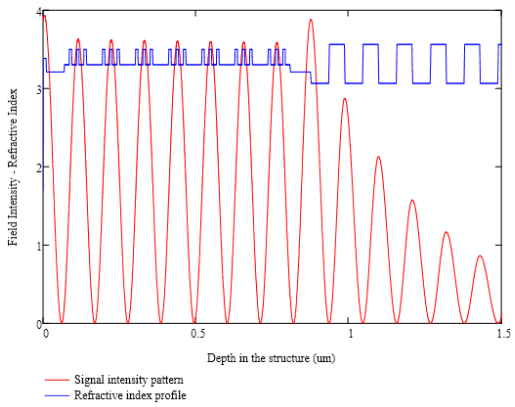

A.6 Time resolved PL measurement programme

Time resolved photoluminescence measurements

- Calibration of spectral axis
- Data processing
- Mono-exponential fit
- Data output

Data import:

5 ns time range (integrated signal file):

$int_{5ns} :=$

	0	1
0	$7.731 \cdot 10^3$	...

5 ns time range (background file):

$intb_{5ns} :=$

	0	1
0	$7.742 \cdot 10^3$	...

20 ns time range (integrated signal file):

$int_{20ns} :=$

	0	1
0	$7.701 \cdot 10^3$	...

20 ns time range (background file):

$intb_{20ns} :=$

	0	1
0	$7.762 \cdot 10^3$	...

Calibration of wavelength axis & definition of time axis:

Reference [1]: NIST - National Institute of Standard and Technology, "Handbook of Basic Atomic Spectroscopic Data", *(http://physics.nist.gov/PhysRefData/Handbook/download.htm)*

Wavelength axis calibration with Hg-Ar lamp lines:

Matching of the measured spectra to Hg-Ar lines:

Greating position at monochromator 61.0 = centre at 732 nm

pos610 :=

	0	1	2
0	0	682.319	-7.167
1	1	682.509	32.278
2	2	682.699	...

Greating position at monochromator 59.5 = centre at 714 nm

pos595 :=

	0	1	2
0	0	664.682	-25.222
1	1	664.872	36.278
2	2	665.061	...

Greating position at monochromator 55.8 = centre at 670 nm

pos558 :=

	0	1	2
0	0	617.269	-18.389
1	1	617.459	9.167
2	2	617.649	...

Definition of the wavelength axis according to specific greating settings:

```
yaxis := if pos = 1
           j ← 1
           i ← 0
           while i < 640
             out_{i,j-1} ← pos610_{i,j}
             i ← i + 1
             out
           Tout ← out^T
```

```
if pos = 2
    j ← 1
    i ← 0
    while i < 640
        out_{i,j-1} ← pos595_{i,j}
        i ← i + 1
        out
    Tout ← out^T
if pos = 3
    j ← 1
    i ← 0
    while i < 640
        out_{i,j-1} ← pos558_{i,j}
        i ← i + 1
        out
    Tout ← out^T
```

Definition of the wavelength axis according to specific greating settings:

20 ns time range:

```
xaxis_20ns := i ← 0
              TR ← (20·ns)/511
              for i ∈ 0..511
                  out_i ← i·TR/ns
                  i ← i + 1
                  out
              out
```

Attaches wavelength & time axis to the input files:

20 ns time range:

```
Inputfile_20ns := TBackgroundsubs ← int_20ns − intb_20ns
                  yax ← yaxis^T
                  for i ∈ 0..511
                    for j ∈ 0..639
                        TSignal_{i,j} ← TBackgroundsubs_{i,j}
                        TSignal
                  TSignal ← TSignal/max(TSignal)
                  for i ∈ 0..511
                      for j ∈ 0..639
                          Tsign_{i+1,j+1} ← TSignal_{i,j}
                          Tsign_{0,j+1} ← yax_j
                      Tsign_{i+1,0} ← xaxis20ns_i
                      Tsign
                  Tsign
```

Data processing:

PL time decay profile generation from input files: (Iso-chromatic lines)

Integmode = 0 **Profile for a chosen wavelength λ and integrated over a chosen wavelength range (number of adjacent columns)**
Integmode = 1 **Profile for a chosen wavelength λ for a specific wavelength**

20 ns time range:

```
Timeprof_20ns := if Integmode = 1
                     y ← yaxis
                     xaxis ← xaxis_20ns
                     for i ∈ 0..511
                         x_{i+1} ← xaxis_i
                         x
                     step ← (y_{0,639} − y_{0,0})/639
                     i ← yaxis_{0,0}
```

```
    while i < λ
      i ← i + step
    index ← (match(i, yaxis)_0)_1
    newindex ← index + 1 − range/2
    n ← newindex
    j ← j − 1
    for i ∈ 0..512
      j ← j + 1
      prof_i ← (Σ_{j=n}^{n+range−1} Inputfile20ns_{i,j}) / range
      prof
    prof
    for i ∈ 0..511
      profile_{i,0} ← x_{i+1}
      profile_{i,1} ← prof_{i+1}
      profile
    profile
  if Integmode = 0
    y ← yaxis
    xaxis ← xaxis20ns
    for i ∈ 0..511
      x_{i+1} ← xaxis_i
      x
    step ← (y_{0,639} − y_{0,0}) / 639
    i ← yaxis_{0,0}
    while i < λ
      i ← i + step
    index ← (match(i, yaxis)_0)_1
    newindex ← index
    n ← newindex
    for i ∈ 0..511
      profile_{i,0} ← x_{i+1}
      profile_{i,1} ← Inputfile20ns_{i+1,n}
      profile
    profile
  profile
```

Returns PL spectrum at the maximum signal position:

```
PLspec20ns := y ← yaxis^T
              index ← (match(1, Inputfile20ns)0)_0
              n ← index
              for i ∈ 0..639
                profile_{i,0} ← y_i
                profile_{i,1} ← Inputfile20ns_{n,i+1}
                profile
              profile
```

Mono-exponential fit:

PL time decay profile generation from input files: (Iso-chromatic lines)

20 ns time range:

$$
\begin{aligned}
&\text{Fitparam}_{20ns} := \left|
\begin{array}{l}
y \leftarrow yaxis \\
xaxis \leftarrow xaxis_{20ns} \\
step \leftarrow \frac{20}{511} \\
i \leftarrow xaxis_0 \\
\text{while } i < Tcursor1 \\
\quad i \leftarrow i + step \\
index1 \leftarrow match\left(i, Timeprof_{20ns}^{\langle 0 \rangle}\right) \\
c1 \leftarrow index1_0 \\
c10 \leftarrow Timeprof_{20ns_{c1,0}} \\
c11 \leftarrow Timeprof_{20ns_{c1,1}} \\
j \leftarrow xaxis_0 \\
\text{while } j < Tcursor2 \\
\quad j \leftarrow j + step \\
index2 \leftarrow match\left(j, Timeprof_{20ns}^{\langle 0 \rangle}\right) \\
c2 \leftarrow index2_0 \\
c20 \leftarrow Timeprof_{20ns_{c2,0}} \\
c21 \leftarrow Timeprof_{20ns_{c2,1}} \\
\text{for } i \in c1..c2 \\
\quad \left|
\begin{array}{l}
profile_{i-c1,0} \leftarrow Timeprof_{20ns_{i,0}} \\
profile_{i-c1,1} \leftarrow 10^{-10} \text{ if } Timeprof_{20ns_{i,1}} \le 0 \\
profile_{i-c1,1} \leftarrow Timeprof_{20ns_{i,1}} \text{ otherwise} \\
profile
\end{array}
\right. \\
profile \\
R \leftarrow regress\left(profile^{\langle 0 \rangle}, \ln\left(profile^{\langle 1 \rangle}\right), 1\right) \\
Amplitude \leftarrow \exp\left(R_3\right) \\
Lifetime \leftarrow \frac{-1}{R_4} \\
Absoluterror \leftarrow \left|
\begin{array}{l}
n \leftarrow c2 - c1 \\
x_{av} \leftarrow x_{av} \leftarrow \frac{\sum profile^{\langle 0 \rangle}}{n+1} \\
y_{av} \leftarrow \frac{\sum \ln\left(profile^{\langle 1 \rangle}\right)}{n+1} \\
s_x \leftarrow \sqrt{\frac{1}{(n+1)-1} \cdot \sum_{aa=0}^{n} \left(profile_{aa,0} - x_{av}\right)^2} \\
s_y \leftarrow \sqrt{\frac{1}{(n+1)-1} \cdot \sum_{aa=0}^{n} \left(\ln\left(profile_{aa,1}\right) - y_{av}\right)^2} \\
s_{xy} \leftarrow \frac{1}{(n+1)-1} \cdot \sum_{aa=0}^{n} \left[\left(profile_{aa,0} - x_{av}\right) \cdot \left(\ln\left(profile_{aa,1}\right) - y_{av}\right)\right] \\
r \leftarrow \frac{s_{xy}}{s_x s_y} \\
s_t \leftarrow \sqrt{\frac{1-r^2}{n-2}} \cdot \frac{s_y}{s_x} \\
measuredtimeuncertaintyinnanosec \leftarrow 0.180 \\
dt \leftarrow \left|\frac{measuredtimeuncertaintyinnanosec}{Lifetime}\right| + \left|\frac{s_t}{Lifetime}\right|
\end{array}
\right. \\
ret \leftarrow \begin{pmatrix} Amplitude \\ Lifetime \\ Absoluterror \\ s_t \\ r^2 \end{pmatrix}
\end{array}
\right.
\end{aligned}
$$

$$Fitparam_{20ns} = \begin{pmatrix} 1.545 \\ 4.539 \\ 0.04 \\ 1.062 \times 10^{-3} \\ 0.994 \end{pmatrix}$$

Amplitude 1 $TA1 := Fitparam_{20ns_0} = 1.545$

Lifetime 1 $T\tau1 := Fitparam_{20ns_1} = 4.539$

ERROR(%) $TError1 := 100 \cdot Fitparam_{20ns_2} = 3.989$

Standard deviation (1/ns) $s_{T1} := Fitparam_{20ns_3} = 1.062 \times 10^{-3}$

Correlation r^2 $r_{T1} := Fitparam_{20ns_4} = 0.994$

$$Timeprofilefit_{20ns}(t, TA1, T\tau1) := TA1 \cdot \exp\left(\frac{-t}{T\tau1}\right)$$

```
Timeprof20nsfit :=
  y ← yaxis
  xaxis ← xaxis20ns
  step ← 20/511
  i ← xaxis0
  while i < Tcursor1
    i ← i + step
  index1 ← match(i, Timeprof20ns^⟨0⟩)
  c1 ← index10
  c10 ← Timeprof20ns(c1, 0)
  c11 ← Timeprof20ns(c1, 1)
  j ← xaxis0
  while j < Tcursor2
    j ← j + step
  index2 ← match(j, Timeprof20ns^⟨0⟩)
  c2 ← index20
  c20 ← Timeprof20ns(c2, 0)
  c21 ← Timeprof20ns(c2, 1)
  for i ∈ c1.. c2
    profile(i−c1, 0) ← Timeprof20ns(i, 0)
    profile(i−c1, 1) ← Timeprof20ns(i, 1)
    profile
  profile
```

Data plot and analysis:

Choose greating position:

1 = pos610 - centre=730nm;
2 = pos595 - centre=715nm;
3 = pos558 - centre=670nm

pos ≡ 2

PL spectrum: (Use cursors to choose wavelength from the spectra)

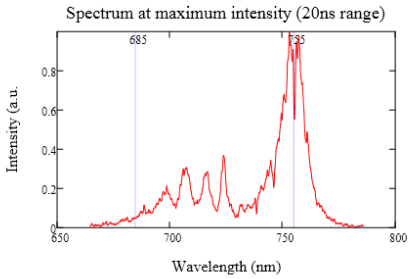

Start and stop wavelength for the chosen greating position:

λ_{start}: $yaxis_{0,0} = 664.682$

λ_{stop}: $yaxis_{0,639} = 785.868$

λ_{centre}: $\lambda_{centre} := yaxis_{0,0} + \frac{(yaxis_{0,639} - yaxis_{0,0})}{2} = 725.275$

Choose wavelength (in nm) of the PL decay profile:

$\lambda \equiv 755$

PL decay profile smoothening:

Integmode = 0 - Profile for a chosen wavelength (single column);
Integmode = 1 - Profile for a chosen wavelength l and integrated over the chosen column range

Integmode ≡ 1

Integration range - how many columns?

Integrate over 10 columns. (10 colums = 1.5nm = spectral resolution limit of the used monochromator greating)

range ≡ 10

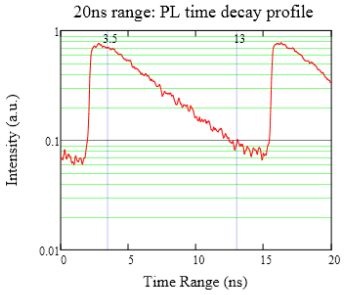

Cursor selection: columns?

Automatic generation of guess values for amplitude and lifetime /Cursor position are shown in the lower graph

Tcursor1 ≡ 3.5 Tcursor2 ≡ 13

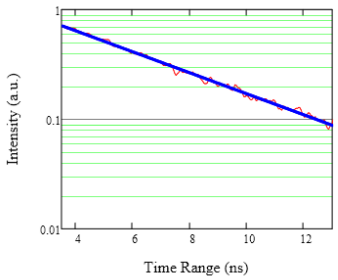

Lifetime (ns):	Tτ1 = 4.539
Amplitude:	TA1 = 1.545
Relative Error (%):	TError1 = 3.989
Standard deviation (1/ns):	$s_{T1} = 1.062 \times 10^{-3}$
Correlation r²	$r_{T1} = 0.994$

Data output files:

Input file with calibrated wavelenth and time axis:

20 ns time range:

$Inputfile_{20ns} =$

	0	1	2
0	0	664.682	664.872
1	0	$-4.631 \cdot 10^{-3}$	$-9.869 \cdot 10^{-4}$
2	0.039	$-6.832 \cdot 10^{-4}$	$-2.277 \cdot 10^{-4}$
3	0.078	$-2.657 \cdot 10^{-3}$	$-2.201 \cdot 10^{-3}$
4	0.117	$-3.188 \cdot 10^{-3}$	$-1.442 \cdot 10^{-3}$
5	0.157	$-3.34 \cdot 10^{-3}$	$-3.947 \cdot 10^{-3}$
6	0.196	$-6.073 \cdot 10^{-4}$	$-2.961 \cdot 10^{-3}$
7	0.235	$-1.67 \cdot 10^{-3}$	$-3.492 \cdot 10^{-3}$
8	0.274	$1.518 \cdot 10^{-4}$	...

PL time decay profile generation from input files + fitted curve:

$Decayprofilefile_{20ns} :=$ for $i \in 0..511$

$profi_{i,0} \leftarrow Timeprof_{20ns_{i,0}}$

$profi_{i,1} \leftarrow Timeprof_{20ns_{i,1}}$

$profi_{i,2} \leftarrow Fitparam_{20ns_0} \cdot \exp\left[\frac{\left(-Timeprof_{20ns}\right)_{i,0}}{Fitparam_{20ns_1}}\right]$

$profi$

$Decayprofilefile_{20ns} =$

	0	1	2
0	0	0.07	1.545
1	0.039	0.068	1.532
2	0.078	0.068	1.518
3	0.117	0.067	1.505
4	0.157	0.066	1.492
5	0.196	0.071	1.48
6	0.235	0.074	1.467
7	0.274	0.082	...

Fitting parameter output file:

Lifetime

$Fitparameterfile :=$

$fitparam_{0,0} \leftarrow \lambda$

Fitparameters 5ns time range

$fitparam_{0,1} \leftarrow Fitparam_{5ns_0}$

$fitparam_{0,2} \leftarrow Fitparam_{5ns_1}$

$fitparam_{0,3} \leftarrow Fitparam_{5ns_2}$

$fitparam_{0,4} \leftarrow Fitparam_{5ns_3}$

$fitparam_{0,5} \leftarrow Fitparam_{5ns_4}$

$fitparam_{0,6} \leftarrow \lambda$

Fitparameters 20ns time range 1

$fitparam_{0,7} \leftarrow Fitparam_{20ns_0}$

$fitparam_{0,8} \leftarrow Fitparam_{20ns_1}$

$fitparam_{0,9} \leftarrow Fitparam_{20ns_2}$

$fitparam_{0,10} \leftarrow Fitparam_{20ns_3}$

$fitparam_{0,11} \leftarrow Fitparam_{20ns_4}$

$fitparam$

$Fitparameterfile =$

	0	1	2	3	4	5
0	755	0.9	4.988	0.014	$2.065 \cdot 10^{-3}$	...

A.7 InAs/GaAs SML QD VECSEL design

NATAL project - 1040nm submonolayer QD VECSEL

- Resonant subcavity design
- 20nm offset
- 13 SML QD-layers / non-uniform distribution

Definition of physical constants and units:

Planck's constant (in Js):	$h \equiv 6.62 \cdot 10^{-34} \cdot joule \cdot sec$
Velocity of light in vacuum (in m/s):	$c \equiv 3 \cdot 10^{8} \cdot m \cdot sec^{-1}$
Elementary charge (in As):	$e \equiv 1.6021917 \cdot 10^{-19}$
Elementary charge (in eV):	$eV \equiv e \cdot joule$
Micrometer (in µm):	$\mu m \equiv 1 \cdot 10^{-6} \cdot m$
Nonometer (in nm):	$nm \equiv 10^{-9} m$
Angstrom (in A):	$A \equiv 1 \cdot 10^{-10} \cdot m$
Milli Watt (in mW):	$mW \equiv 10^{-3} \cdot watt$
Dielectric parameter of GaAs (external txt. file):	$D \equiv READPRN("GaAs.txt")$

Refractive index calculation:

AlGaAs for DBR and window capping layer:

Reference [1]: M.A.Afromowitz, "Refractive index of $Ga_{1-x}Al_xAs$", Solid State Comm. 15, 59 (1974)

$$n_{AlGaAs}(\lambda, x) := \begin{| l} E_0 \leftarrow \left(3.65 + 0.871 \cdot x + 0.179 \cdot x^2\right) \cdot eV \\ E_d \leftarrow (36.1 - 2.45 \cdot x) \cdot eV \\ E_{\Gamma} \leftarrow \left(1.424 + 1.266 \cdot x + 0.26 \cdot x^2\right) \cdot eV \\ E_f \leftarrow \sqrt{2 \cdot E_0^2 - E_{\Gamma}^2} \\ \eta \leftarrow \frac{\pi \cdot E_d}{2 \cdot E_0^3 \cdot \left(E_0^2 - E_{\Gamma}^2\right)} \\ M_a \leftarrow \frac{\eta \cdot \left(E_f^4 - E_{\Gamma}^4\right)}{2 \cdot \pi} \\ M_b \leftarrow \frac{\eta \cdot \left(E_f^2 - E_{\Gamma}^2\right)}{\pi} \\ K \leftarrow \frac{0.35}{eV} \\ E \leftarrow \frac{h \cdot c}{\lambda} \\ E_{\Gamma p} \leftarrow E_{\Gamma} - 25 \cdot 10^{-3} \cdot eV \\ m \leftarrow floor\left(\frac{2.34 - \frac{E}{eV}}{0.02}\right) \\ \sqrt{1 + M_a + M_b \cdot E_{\Gamma p}^2 + \frac{\eta \cdot E_{\Gamma p}^4 \cdot \ln\left(\frac{E_f^2 - E_{\Gamma p}^2}{E_{\Gamma}^2 - E_{\Gamma p}^2}\right)}{\pi}} + K \cdot \left(E - E_{\Gamma p}\right) - i \cdot (x = 0) \cdot \left[D_{m,2} - \frac{\left(D_{m+1,2} - D_{m,2}\right) \cdot \left(\frac{E}{eV} - D_{m,0}\right)}{0.02}\right] \text{ if } E > E_{\Gamma p} \\ \sqrt{1 + M_a + M_b \cdot E^2 + \frac{\eta \cdot E^4 \cdot \ln\left(\frac{E_f^2 - E^2}{E_{\Gamma}^2 - E^2}\right)}{\pi}} \text{ otherwise} \end{|}$$

Refractive indices put together:

$$n(\lambda, x) := \begin{cases} n_{AlGaAs}(\lambda, x) & \text{if } x \geq 0 \wedge x \leq 1 \\ 3.6 + i \cdot 0.00 \cdot \exp\left[-\left(\frac{\lambda - \lambda_{PL}}{20 \cdot nm}\right)^2\right] & \text{if } x = 1.5 \end{cases}$$

Guessed Quantum dot refractive index, including absorption term

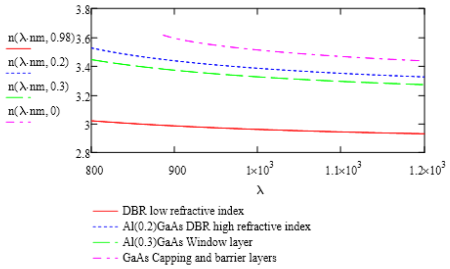

Global design variables/parameters:

Design wavelength: $\lambda_p \equiv 808nm$

Design wavelength: $\lambda_{opt} \equiv 1040 \cdot nm$

QD emission wavelength at room temperature: $\lambda_{PL} \equiv 1020 \cdot nm$

Offset between QD PL and design wavelength: $offset := 20nm$

Wavelength range:

start wavelength: $\lambda_{start} \equiv 800 \cdot nm$

stop wavelength: $\lambda_{stop} \equiv 1300 \cdot nm$

step size: $\lambda_{step} \equiv 2 \cdot nm$

$$n_{step} \equiv \frac{\lambda_{stop} - \lambda_{start}}{\lambda_{step}} + 1$$

Refractive index of substrate:

GaAs @ λ_{opt}: $n_{substrate}(\lambda) \equiv 3.49$ $\quad n(\lambda_{opt}, 0) = 3.491$

Last layer (= substrate):

composition GaAs: $x_{substrate} \equiv 0$

chose condition: $cte\_n_{substrate} \equiv 0$

1 = $n_{substrate}$ is constant

0 = $n_{substrate}$ is depend on wavelength

refractive index:

$$n_1(\lambda) := \begin{cases} n_{substrate}(\lambda) & \text{if } cte\_n_{substrate} \\ n(\lambda, x_{substrate}) & \text{otherwise} \end{cases} \qquad n_1(\lambda_{opt}) = 3.491$$

Refractive index of incident layer: $n_{top}(\lambda) \equiv 2.42$ diamond heatspreader

First layer:

composition: $x_{top} \equiv 0$ necessary if layer is e.g. air or something else

chose condition: $cte\_n_{top} \equiv 1$

1 = $n_{diamond}$ is constant

0 = $n_{diamond}$ is depend on wavelength

refractive index:

$$n_1(\lambda) := \begin{cases} n_{top}(\lambda) & \text{if } cte\_n_{top} \\ n(\lambda, x_{top}) & \text{otherwise} \end{cases} \qquad n_1(\lambda_{opt}) = 2.42$$

Spacer layer thickness: $t_{spacer} \equiv 20nm$

Reflectivity and electric field calculation of a stratified dielectric medium

Reference [2]: H.A. MacLeod, "Thin-film optical filters", 2nd edition, Higer Ltd (Bristol), 1986, pp40-48
[3]: M. Born and E. Wolf, "Principles of optics", Pergamon press, 1985, pp51-70

Characteristic matrix methode:

$RT(\lambda, t, comp) :=$

$M \leftarrow identity(2)$

$\eta_i \leftarrow n_i(\lambda)$

for $j \in 1..N_{layer}$

$M_r \leftarrow M$

$\eta \leftarrow n\left(\lambda, comp_{j-1}\right)$

$\beta \leftarrow \frac{2\cdot\pi}{\lambda}\cdot\eta\cdot t_{j-1}$

$M \leftarrow M_r \begin{pmatrix} \cos(\beta) & \frac{i}{\eta}\cdot\sin(\beta) \\ i\cdot\eta\cdot\sin(\beta) & \cos(\beta) \end{pmatrix}$

$\eta_l \leftarrow n_l(\lambda)$

$N \leftarrow M\cdot\begin{pmatrix} 1 \\ \eta_l \end{pmatrix}$

$r \leftarrow \frac{\eta_i\cdot N_0 - N_1}{\eta_i\cdot N_0 + N_1}$

$R \leftarrow (|r|)^2$

$tr \leftarrow \frac{2\cdot\eta_i}{\eta_i\cdot N_0 + N_1}$

$T \leftarrow \frac{\eta_l}{\eta_i}\cdot(|tr|)^2$

$Res \leftarrow \begin{pmatrix} R \\ T \\ r \\ tr \end{pmatrix}$

Res

Reflectivity and transmission coefficients $R=|r^2|$, $T=|t^2|$ and amplidutes r, t:

Refractive index pattern calculations :

$$Pattern(z, \lambda, t, comp) := Re\left[n\left(\lambda, comp_0\right)\cdot\left(\Phi(z) - \Phi\left(z - \frac{t_0}{m}\right)\right) + \sum_{k=1}^{N_{layer}-1}\left[n\left(\lambda, comp_k\right)\cdot\left(\Phi\left(z - \frac{\sum_{l=0}^{k-1} t_l}{m}\right) - \Phi\left(z - \frac{\sum_{l=0}^{k} t_l}{m}\right)\right)\right]\right]$$

Electric field calculations :

$field(\lambda, t, comp) :=$

$reflec \leftarrow RT(\lambda, t, comp)_2$

$\eta_i \leftarrow n_i(\lambda)$

$Q_{init} \leftarrow \begin{bmatrix} 1 + reflec \\ \eta_i\cdot(1 - reflec) \end{bmatrix}$

$N_{stack} \leftarrow identity(2)$

$zcurrent \leftarrow 0$

$index \leftarrow -1$

for $j \in 1..N_{layer}$

$nnmax \leftarrow \left(floor\left(\frac{4\cdot t_{j-1}}{\lambda}\right) + 1\right)\cdot 50$

$N_r \leftarrow N_{stack}$

$\eta \leftarrow n\left(\lambda, comp_{j-1}\right)$

for $nn \in 1..nnmax$

$thick \leftarrow \frac{nn\cdot t_{j-1}}{nnmax}$

$\beta \leftarrow \frac{2\cdot\pi}{\lambda}\cdot n\left(\lambda, comp_{j-1}\right)\cdot thick$

$N_{stack} \leftarrow \begin{pmatrix} \cos(\beta) & \frac{-i}{\eta}\cdot\sin(\beta) \\ -i\cdot\eta\cdot\sin(\beta) & \cos(\beta) \end{pmatrix}\cdot N_r$

$Q \leftarrow N_{stack}\cdot Q_{init}$

$Res_{0,\, index+nn} \leftarrow zcurrent + \frac{thick}{m}$

$Res_{1,\, index+nn} \leftarrow \left(|Q_0|\right)^2$

$index \leftarrow index + nnmax$

$zcurrent \leftarrow zcurrent + \frac{t_{j-1}}{m}$

$Res_{0,0} \leftarrow 0$

$Res_{1,0} \leftarrow \left(|Q_{init_{0,0}}|\right)^2$

Res

Layer thickenss and composition settings:

Layer thicknesses:

$t_{var} \equiv 4nm$

$t_{var1} \equiv -7nm$

$t_{var2} \equiv 2nm$

$t_{var3} \equiv -2nm$

$t_{var4} \equiv -12nm$

$t_{var5} \equiv -1nm$

$t_{var6} \equiv -3nm$

$t_{var7} \equiv -1nm$

$t :=$
- $t_{in_0} \leftarrow 10 \cdot nm$
- $t_{in_1} \leftarrow 230.6 \cdot nm - t_{var}$
- $t_{in_2} \leftarrow 55.3 \cdot nm$
- $t_{in_3} \leftarrow 0 \cdot nm$
- $t_{in_4} \leftarrow 0.5 \cdot nm$
- $t_{in_5} \leftarrow t_{spacer}$
- $t_{in_6} \leftarrow 0 \cdot nm$
- $t_{in_7} \leftarrow 0.5 \cdot nm$
- $t_{in_8} \leftarrow t_{spacer}$
- $t_{in_9} \leftarrow 0 \cdot nm$
- $t_{in_{10}} \leftarrow 0.1 \cdot nm$
- $t_{in_{11}} \leftarrow 110.52 \cdot nm + t_{var1}$
- $t_{in_{12}} \leftarrow 0 \cdot nm$
- $t_{in_{13}} \leftarrow 0.1 \cdot nm$
- $t_{in_{14}} \leftarrow t_{spacer}$
- $t_{in_{15}} \leftarrow 5 \cdot nm$
- $t_{in_{16}} \leftarrow 0.1 \cdot nm$
- $t_{in_{17}} \leftarrow t_{spacer}$
- $t_{in_{18}} \leftarrow 5 \cdot nm$
- $t_{in_{19}} \leftarrow 0.1 \cdot nm$
- $t_{in_{20}} \leftarrow (55.3 + 55.5) \cdot nm + t_{var2}$
- $t_{in_{21}} \leftarrow 0 \cdot nm$
- $t_{in_{22}} \leftarrow 0.1 \cdot nm$
- $t_{in_{23}} \leftarrow t_{spacer}$
- $t_{in_{24}} \leftarrow 0 \cdot nm$
- $t_{in_{25}} \leftarrow 0.1 \cdot nm$
- $t_{in_{26}} \leftarrow (75.5 + 55.5) \cdot nm + t_{var3}$
- $t_{in_{27}} \leftarrow 0 \cdot nm$
- $t_{in_{28}} \leftarrow 0.1 \cdot nm$
- $t_{in_{29}} \leftarrow t_{spacer}$
- $t_{in_{30}} \leftarrow 0 \cdot nm$
- $t_{in_{31}} \leftarrow 0.1 \cdot nm$
- $t_{in_{32}} \leftarrow (75.5 + 75.5) \cdot nm + t_{var4}$
- $t_{in_{33}} \leftarrow 0 \cdot nm$
- $t_{in_{34}} \leftarrow 0.1 \cdot nm$
- $t_{in_{35}} \leftarrow (75.5 + 75.5) \cdot nm + t_{var5}$
- $t_{in_{36}} \leftarrow 0 \cdot nm$
- $t_{in_{37}} \leftarrow 0.1 \cdot nm$
- $t_{in_{38}} \leftarrow (75.5 + 75.5) \cdot nm + t_{var6}$
- $t_{in_{39}} \leftarrow 0 \cdot nm$
- $t_{in_{40}} \leftarrow 0.1 \cdot nm$
- $t_{in_{41}} \leftarrow (75.5 + 75.5) \cdot nm + t_{var7}$
- for $k \in 1..35$
  - $t_{in_{2 \cdot (k-1)+42}} \leftarrow 88.07nm$
  - $t_{in_{2 \cdot k-1+42}} \leftarrow 74nm$
- $t_{in_{112}} \leftarrow 88.07 \cdot nm$
- $t \leftarrow t_{in}$

$t =$

	0
0	$1 \cdot 10^{-8}$
1	$2.266 \cdot 10^{-7}$
2	$5.53 \cdot 10^{-8}$
3	0
4	$5 \cdot 10^{-10}$
5	$2 \cdot 10^{-8}$
6	0
7	$5 \cdot 10^{-10}$
8	$2 \cdot 10^{-8}$
9	0
10	$1 \cdot 10^{-10}$
11	$1.035 \cdot 10^{-7}$
12	0
13	$1 \cdot 10^{-10}$
14	$2 \cdot 10^{-8}$
15	...

Layer composition:

$comp :=$
- $co_0 \leftarrow 0$
- $co_1 \leftarrow 0.3$
- for $k \in 0..12$
  - $co_{3 \cdot k+2} \leftarrow 0$
  - $co_{3 \cdot k+3} \leftarrow 0$
  - $co_{3 \cdot k+4} \leftarrow 1.5$
- $co_{41} \leftarrow 0$
- for $i \in 1..35$
  - $co_{2 \cdot (i-1)+42} \leftarrow 0.98$
  - $co_{2 \cdot i-1+43} \leftarrow 0.2$
- $co_{112} \leftarrow 0.98$
- $comp \leftarrow co$

$comp =$

	0
0	0
1	0.3
2	0
3	0
4	1.5
5	0
6	0
7	1.5
8	0
9	0
10	1.5
11	0
12	0
13	1.5
14	0
15	...

Number of layers:

$N_{layer} \equiv 113$

Total length of the structure :

$length_{structure} := \sum_{k=0}^{N_{layer}-1} t_k = 7.117 \times 10^3\ nm$

Number of layers: $N_{layer} \equiv 113$

Total length of the structure : $length_{structure} := \sum_{k=0}^{N_{layer}-1} t_k = 7.117 \times 10^3\ nm$

Data output:

Reflectivity graph: $\lambda := \lambda_{start}, \lambda_{start} + \lambda_{step} .. \lambda_{start} + n_{step} \cdot \lambda_{step}$ x-axis

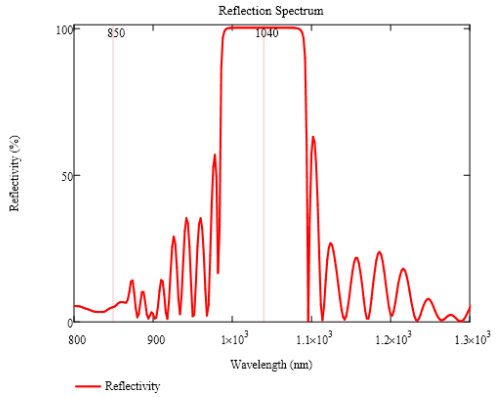

Design graphic: x-axis $\lambda := \lambda_{start}, \lambda_{start} + \lambda_{step} .. \lambda_{start} + n_{step} \cdot \lambda_{step}$

Signal field intensity pattern: $F_s := field(\lambda_{opt}, t, comp)^T$

Pump field intensity pattern: $F_p := field(\lambda_p, t, comp)^T$

Refractive index pattern: $p(z) := Pattern(z, \lambda_{opt}, t, comp)$

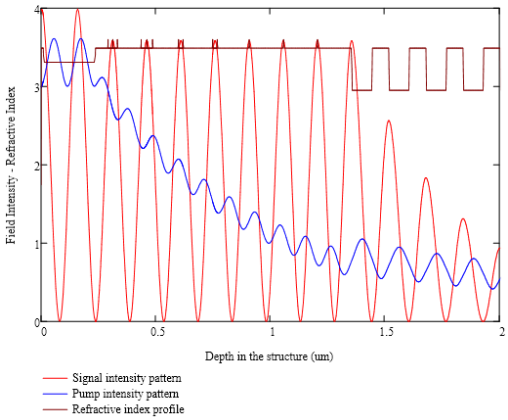

A.8 Experimental arrangement of the PL measurements

Edge-PL

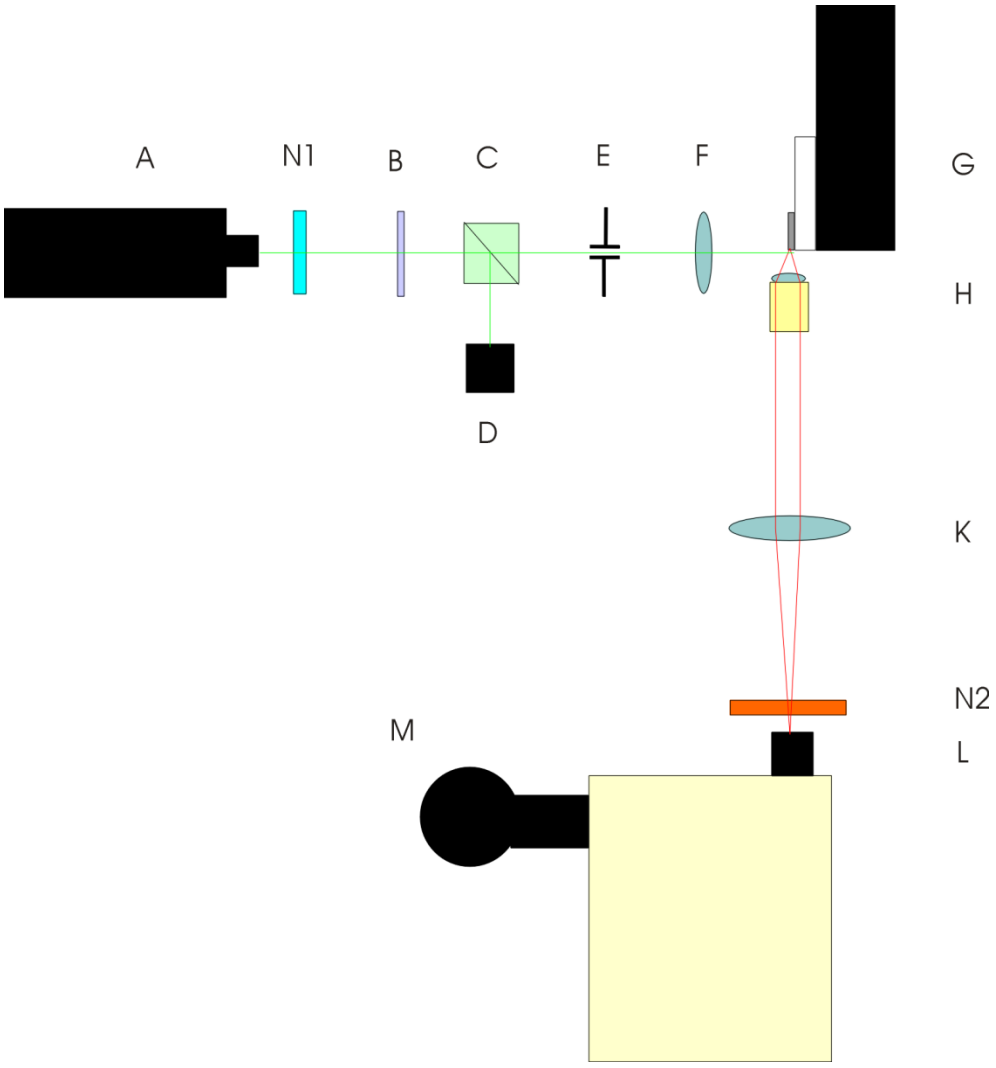

A – 532 nm Laser (P ~ 1.5 W)
B – λ/4 retarder for 532 nm
C – Polarising beam splitter cube for 532nm
D – Beam dump
E – Aperture
F – f=50mm focal length lens
G – Sample holder / TEC
H – Microscope lens f=6.2 mm
K – Focal lens, f=300mm
L – Spectrometer
M – Detector
N1/2 – Spectral filter

Polarisation Sensitive Edge-PL

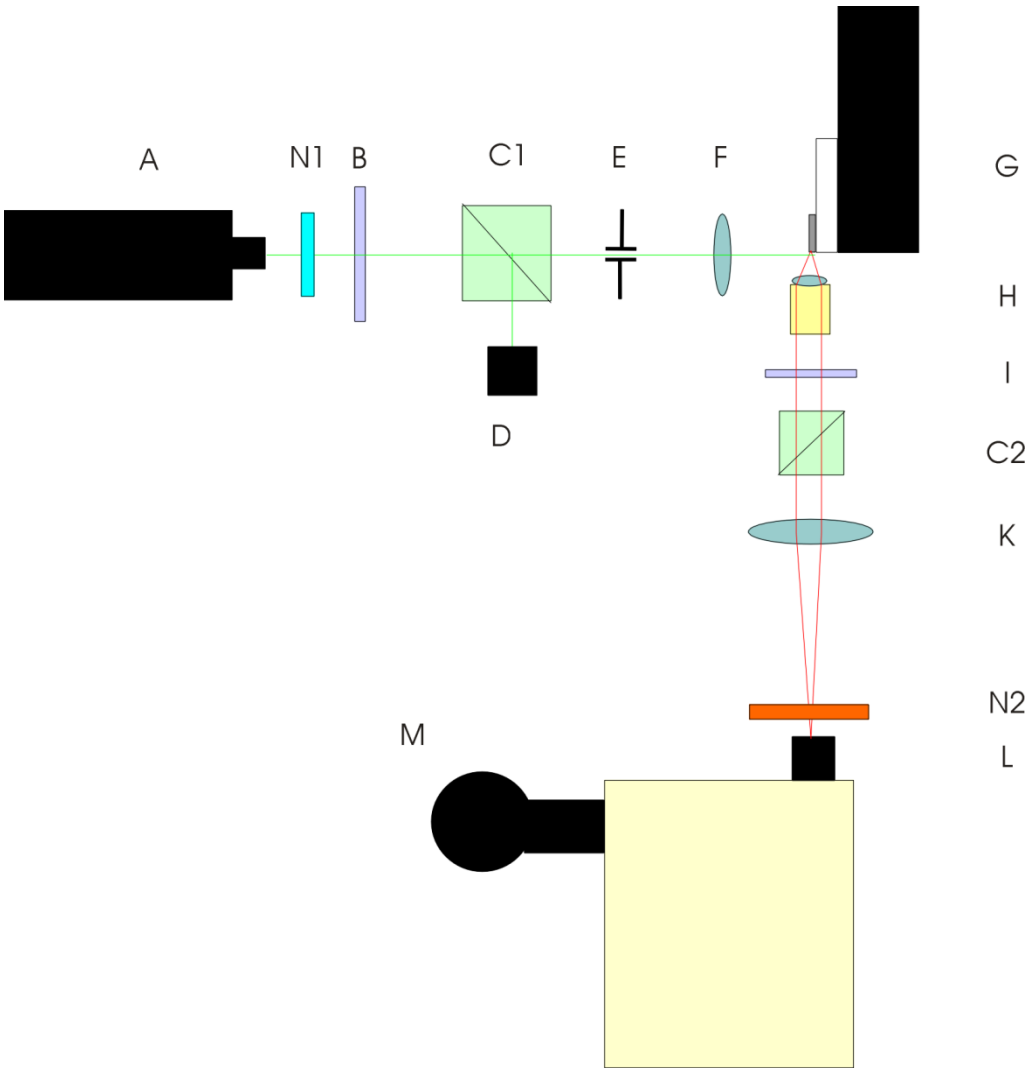

A – 532 nm Laser (P ~ 1.5 W)
B – λ/4 retarder for 532 nm
C1 – Polarising beam splitter cube
D – Beam dump
E – Aperture
F – f=50mm focal length lens
G – Sample holder / TEC
H – Microscope objective f=6.2 mm
I - λ/4 retarder (optional)
C2 – Polarising beam splitter cube (optiopnal)
K – Focal lens, f=300mm
L – Spectrometer
M – Detector
N1/2 – Spectral filter

Surface-PL

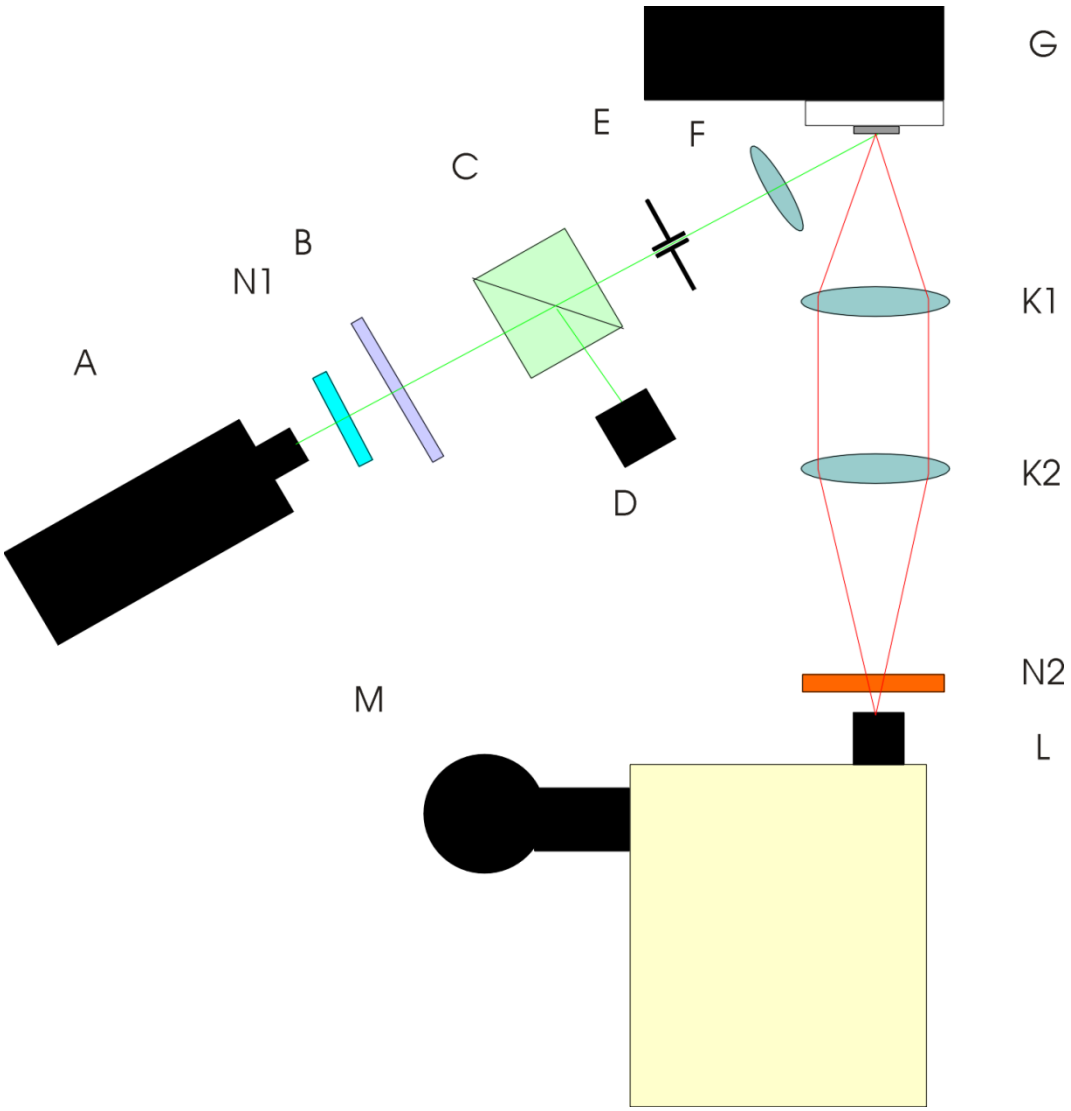

A – 532 nm Laser (P ~ 1.5 W)
B – λ/4 retarder for 532 nm
C1/2 – Polarising beam splitter cube
D – Beam dump
E – Aperture
F – f=50mm focal length lens
G – Sample holder / TEC
K1 – Focal lens, f=80mm
K1 – Focal lens, f=300mm
L – Spectrometer
M – Detector
N1/2 – Spectral filter

List of Publications:

Conference Publication List:

[1] Jennifer E. Hastie, Peter J. Schlosser, Stephane Calvez, Andrey B. Krysa, Martin D. Dawson, ”Semiconductor disk laser incorporating InP/GaInP quantum dots for 716 – 755 nm emission,” Advanced Solid-State Photonics Conference, Denver, USA, Paper AWB5 (2010).

[2] Peter J. Schlosser, Jennifer E. Hastie, Stephane Calvez, Andrey B. Krysa, and Martin D. Dawson, “InP/GaInP quantum dot semiconductor disk laser for TEM00 emission at 740 nm,” presented at the 22nd Annual Meeting of the IEEE Photonics Society, Paper ThP 5 (2009).

[3] Jennifer E. Hastie, Peter J. Schlosser, Martin Thalbitzer Andersen, Martin D. Dawson, and Peter Tidemand-Lichtenberg, “Intracavity frequency mixing in a semiconductor disk laser generating >100mW in the yellow-orange,” Advanced Solid-State Photonics Conference, Denver, USA, Paper MB22 (2009).

[4] Peter J. Schlosser, Stephane Calvez, Jennifer E. Hastie, Shirong Jin, Tim D. Germann, André Strittmatter, Udo W. Pohl, Dieter Bimberg, and Martin D. Dawson, “Characterisation of an InAs Quantum Dot Semiconductor Disk Laser,” Conference on Lasers and Electro-Optics 2008, California, Paper CWD5 (2008).

[5] Peter J. Schlosser, Shirong Jin, Tim D. Germann, Stephane Calvez, Jennifer E. Hastie, Andre Strittmatter, Udo W. Pohl, Dieter Bimberg and Martin D. Dawson, “ Characterisation of an InAs Quantum Dot VECSEL,” One Day Quantum Dot Meeting Imperial College Poster, UK, Poster (2008).

Journal Publication List

[1] V. G. Savitski, P. J. Schlosser, J. E. Hastie, A. B. Krysa, J. S. Roberts, M. D. Dawson, D. Burns, and S. Calvez, "Passive Mode-Locking of a Ti : Sapphire Laser by InGaP Quantum-Dot Saturable Absorber," Photonics Technology Letters, IEEE 22, 209-211 (2010).

[2] Peter J. Schlosser, Jennifer E. Hastie, Stephane Calvez, Andrey B. Krysa, Martin D. Dawson, ”InP/AlGaInP quantum dot semiconductor disk laser for TEM00 emission at 716 – 755 nm,” Optics Express 17 (24) 21782-87 (2009)

[3] Martin Thalbitzer Andersen, Peter J. Schlosser, Jennifer E. Hastie, Peter Tidemand-Lichtenberg, Martin D. Dawson, and Christian Pedersen, ”Singly-resonant sum frequency generation of visible light in a semiconductor disk laser,” Optics Express 17 (8) 6010-6017 (2009).

IEEE PHOTONICS TECHNOLOGY LETTERS, VOL. 22, NO. 4, FEBRUARY 15, 2010 209

Passive Mode-Locking of a Ti : Sapphire Laser by InGaP Quantum-Dot Saturable Absorber

Vasili G. Savitski, Peter J. Schlosser, Jennifer E. Hastie, *Member, IEEE*, Andrey B. Krysa, John S. Roberts, Martin D. Dawson, *Fellow, IEEE*, David Burns, and Stephane Calvez, *Member, IEEE*

***Abstract*—We demonstrate the use of a novel InGaP quantum-dot (QD) saturable absorber (SA) to induce passively mode-locked (ML) operation of a Ti : sapphire laser. Pulses as short as 518 fs are obtained at 752 nm with an average output power of up to 190 mW for 2.3 W of absorbed pump power at 532 nm. The absorption recovery of the SA is characterized by two decay coefficients: a fast and a slow component having time constants of 0.4 and 300 ps, respectively. The saturation fluence of the InGaP QDs was measured to be 28 μJ/cm^2, the initial low-signal absorption was 1.5%, where 1.15% was nonsaturable loss.**

***Index Terms*—Laser absorbers, mode-locked (ML) laser, spectroscopy, ultrafast optics.**

I. Introduction

THE use of SEmiconductor Saturable Absorber Mirrors (SESAMs) is a proven method to obtain robust self-starting mode-locked (ML) operation of solid-state lasers [1]–[3]. In this field, quantum-dot (QD)-based SESAMs have recently received considerable attention because they could, in principle, offer low saturation fluence and fast recovery time, parameters particularly attractive for high-performance ultrafast lasers [4], especially when operating at high repetition rate [5] (with possible application in metrology). Passive ML of several lasers in the 950- to 1600-nm wavelength band have been demonstrated using QD-based SESAMs [6]–[9] with output pulse durations varying from ~4 ps [7] to 114 fs [9]—dependent on the modulation depth and bleaching relaxation time of the SESAMs. In practice, these parameters are influenced by the growth technique as well as the materials used for growing QDs. To date, epitaxially grown QD-based SESAMs have mainly used In(Ga)As QDs.

In the present work, our intention was to extend the spectral coverage of this technique by using InGaP QD-based SESAMs and apply it in the passive ML of a Ti : sapphire laser operating around 750 nm.

Manuscript received July 08, 2009; revised November 02, 2009; accepted November 19, 2009. First published January 08, 2010; current version published January 20, 2010. This work was supported by the Engineering and Physical Sciences Research Council (EPSRC) programmes EP/E064450/1 and EP/E056989/1.

V. G. Savitski, P. J. Schlosser, J. E. Hastie, M. D. Dawson, D. Burns, and S. Calvez are with the Institute of Photonics, University of Strathclyde, Glasgow G4 0NW, U.K. (e-mail: vasili.savitski@strath.ac.uk; peter.schlosser@strath.ac.uk; jennifer.hastie@strath.ac.uk; m.dawson@strath.ac.uk; d.burns@strath.ac.uk; s.calvez@strath.ac.uk).

A. B. Krysa and J. S. Roberts are with EPSRC National Centre for III-V Semiconductors, University of Sheffield, Sheffield S1 3JD, U.K. (e-mail: a.krysa@sheffield.ac.uk; j.s.roberts@sheffield.ac.uk).

Digital Object Identifier 10.1109/LPT.2009.2037599

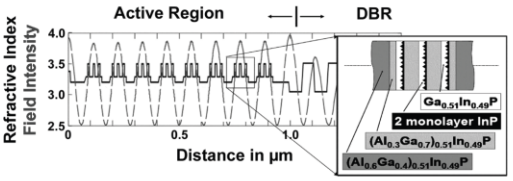

Fig. 1. Schematic of the InGaP QDs SESAM structure with the calculated field intensity (dashed line, minima correspond to zero field intensity).

II. SESAM and Laser Setup

The GaAs-based SESAM structure used here was originally designed as the active element of a semiconductor disk laser (laser results to be reported elsewhere). It consists of a QD-based saturable absorber (SA) section grown on top of a 40.5-pair AlAs–$Al_{0.35}Ga_{0.65}As$ distributed Bragg reflector (Fig. 1). A resonant, 4.5-λ-thick subcavity enabled the implementation of 24 InP QD layers, which were placed into groups of three QD-layers at the eight electric field antinodes for resonant periodic gain. The QD layers with a nominal thickness of two monolayers were grown on top of $(Al_{0.3}Ga_{0.7})_{0.51}In_{0.49}P$ and capped by an 8-nm-thick $Ga_{0.51}In_{0.49}P$ layer. The InP–$Ga_{0.51}In_{0.49}P$ layers within a group were separated by 16-nm-thick $(Al_{0.3}Ga_{0.7})_{0.51}In_{0.49}P$ for maximum gain. $(Al_{0.6}Ga_{0.4})_{0.51}In_{0.49}P$ barriers were used between the groups for maximized carrier confinement. A 10-nm $Ga_{0.51}In_{0.49}P$ capping layer was added to prevent oxidation of the underlying aluminium containing layers. The epitaxial growth was performed by metal–organic chemical vapor deposition (MOCVD) with a growth temperature of 700 °C for the QDs [10].

The QD-SESAM ML Ti : sapphire laser arrangement is shown in Fig. 2. The Brewster-cut Ti : sapphire crystal was 5.2 mm in length and was pumped at 532 nm by a frequency-doubled Nd : YVO_4 laser with a maximum output power of 5 W. The Ti : sapphire crystal was placed between two folding mirrors having radii of curvature of 75 and 100 mm for the long and short arms of the cavity, respectively. A focusing mirror with the radius of curvature of 200 mm was used to keep the appropriate mode spot size on the SA. The X-fold cavity geometry (see Fig. 2) gave mode radii within the Ti : sapphire crystal and on the SA of 35 and 31 μm, respectively. Two SF14 prisms, separated by 36 cm, were configured to compensate the positive intracavity group dispersion and hence promote optimized ML performance. Finally, the output coupler had a reflectivity of 98%. No damage or degradation

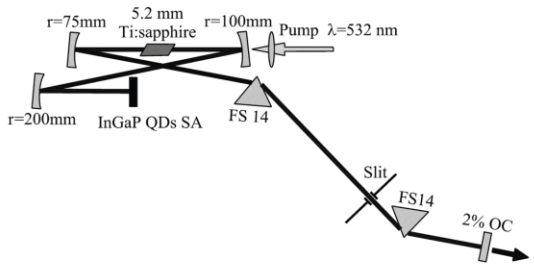

Fig. 2. Schematic of the passive ML Ti : sapphire laser arrangement. OC—output coupler. All curved mirrors are highly reflective within 700- to 825-nm spectral range.

of the QD-SESAM was observed during the laser experiments reported here.

III. Laser Results

In the continuous-wave (CW) regime with a high-reflecting (HR) mirror in place of the SESAM, the slope efficiency of the laser was 15.3% at 752 nm and the maximum output power was 330 mW at an absorbed pump power of 2.3 W. The measured tuning range of 700–825 nm was limited only by the reflectivity range of the cavity mirrors.

With the SA in place, self-starting ML (at 128 MHz) was obtained with a reduced slope efficiency of 10% [see Fig. 3(a)]. This observation is similar to the one made in [11] and can be attributed to the presence of unsaturable losses in the SESAM—specifically those having a large number of absorbing layers. The data on such losses will be presented below. The tuning range of 745–790 nm of the laser was limited by the reflectivity band of the SESAM as shown in Fig. 3(a); however, stable CW ML operation was only observed between ∼749 and 754 nm. Pulses as short as 518 fs in duration were generated with a corresponding spectral width of 1.2 nm implying a time-bandwidth product of 0.33 [Fig. 3(b)]. The corresponding intracavity pulse fluence on the SA was estimated to be ∼1.9 mJ/cm^2. Passive ML was also observed between $\lambda = 754$– 767 nm; however, Q-switching instabilities were dominant in this range even at elevated intracavity pulse fluences on the SA (a six-fold increase could be obtained by changing the focusing mirror to one with the radius of curvature of 75 mm). The resonant character of the SESAM in the wavelength range ∼755–792 nm [see Fig. 3(a)] effectively introduces higher passive losses, and so, inhibits efficient CW ML behavior. The output power of the laser within the spectral region of 754–776 nm was reduced by a factor of 4. At emission wavelengths beyond 767 nm, the laser operates only in the CW regime.

IV. SESAM Characterization and Laser Result Analysis

Some nonlinear spectroscopic investigations were undertaken in order to explain the observed features of the passive ML Ti : sapphire laser. The absorption recovery dynamics, the intensity-dependent reflectivity, and the absorption spectrum of

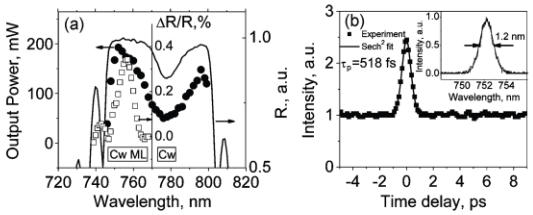

Fig. 3. (a) Reflectivity spectrum of the InGaP QDs SA (solid line); tunability range of Ti : sapphire laser with the InGaP QDs SA (circles); saturable absorption spectrum ($\Delta R/R$) of the InGaP QDs SA (open squares, and corresponding central scale). (b) Intensity autocorrelation trace of the ML pulse. Inset, corresponding optical spectrum (duration-bandwidth product $= 0.33$).

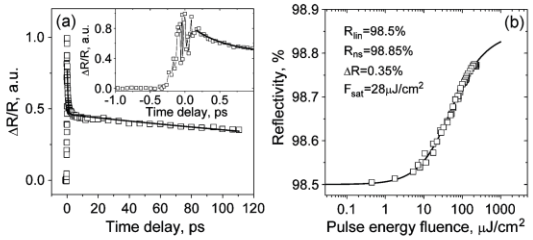

Fig. 4. (a) Dynamics of the saturable absorption in a InGaP QDs SESAM at 752 nm probed with 150-fs duration pulses. Pump pulse fluence—40 μJ/cm^2. Solid line—result of best fit using a biexponential decay model. Fast component time is 400 ± 50 fs and the slow component is 300 ± 50 ps. Inset: detail of measured dynamics over a truncated time window of ∼2 ps. Note the periodic beating of the measured signal observed during ∼0.2 ps before and after zero time delay. (b) Intensity-dependent reflectivity of the InGaP QDs SESAM under 150-fs excitation at 752 nm. Solid curve presents the results of the best fit after the analysis presented in [14].

the SA were examined using a standard pump–probe technique. A commercially available Ti : sapphire having a pulse duration of 150 fs and tunability throughout the 720- to 940-nm spectral range was used as an optical source. During these experiments, no indication of any permanent photodarkening effects in the sample could be seen.

The dynamics of the measured 752-nm reflectivity signal from the InGaP QD-doped sample pumped with a pulse fluence of 40 μJ/cm^2 is presented as Fig. 4(a)—the characteristic instrument-limited build-up time was ∼200 fs. Periodic beating of the bleaching signal within the build-up time [see inset to Fig. 4(a)] were only observed for this type of device—in more conventional single quantum-well saturable Bragg reflectors, this behavior was not present. We, therefore, conclude that this effect is an artefact (or a so-called coherent spike [12]) originating either within the resonant microcavity of the QD-SESAM or from stress-induced depolarization effects in the QD layers. Analysis of the absorption recovery for delays greater than ∼300 fs led to the conclusion that the absorption recovery exhibited a biexponential decay characteristic with the fast bleaching decay component of ∼ 400 ± 50 fs, and a slow response of ∼ 300 ± 50 ps. The fast decay component can be attributed to intraband carrier thermalization (with typical time constants of 100–200 fs) or carrier trapping [13]. The slower decay component could be related to band-to-band recombination or carrier recombination through trapping states

[13]. A detailed spectroscopic study of bleaching relaxation routes will be the subject of a separate paper.

Intensity-dependent reflectivity measurements were performed at 752 nm at zero delay time between the pump and the probe pulses. The experimental data were then analyzed using the equations provided in [14], taking into account the Gaussian spatial profile of the pump beam [see Fig. 4(b)]. The two-photon absorption parameter was not included as the characteristic roll-off was not observed [14]. The modulation depth, nonsaturable losses, and saturation fluence of the InGaP QD-based SESAM were estimated to be 0.35%, 1.15%, and 28 μJ/cm^2, respectively. We note that the range of the pulse energy fluence used for the measurement (up to 150 μJ/cm^2) was greater than three times the estimated saturation fluence and was considered sufficient for accurate evaluation of the SA nonlinear parameters [14]. The measured saturation fluence of this InGaP QD-SA is comparable with previous measurements of InGaAs QD SA devices (i.e., 25 μJ/cm^2 [9]). However, in [9], the reduced nonsaturable losses ($\sim$0.2%) and higher modulation depth of the SA resulted in 200-fs ML operation at 1 μm. The relatively high nonsaturable loss present in our QD-SA results in a reduced slope efficiency of the ML laser (10%) in comparison to CW operation (15.3%), when the SA was replaced with the HR mirror. Finally, the rather long pulse durations obtained from the QD-SA ML Ti : sapphire laser (0.5 ps) could be due to the low modulation depth of the material at 752 nm in conjunction with the slow absorption recovery component of 300 ps.

The saturable absorption spectrum of the InGaP QD-SA at zero delay between the pump and the probe pulses is plotted in Fig. 3(a) as open squares. With a pump pulse fluence of 62 μJ/cm^2, the highest modulation depth of the sample was observed at $\sim$756 nm. However, as previously mentioned, the Ti : sapphire laser operated in the Q-switch ML mode at this wavelength. It has been shown earlier [15] that the saturation fluence of the QD-based SA does not depend on wavelength. Therefore, this wavelength (756 nm) should be preferable for ML; however, we assume that the increased unsaturated losses of the SA preclude stable ML at this specific wavelength—and indeed in the extended range between 754 and 767 nm. The near-zero modulation depth measured for wavelengths greater than 767 nm explains that only CW operation can be obtained above $\lambda = 767$ nm.

Such evidence suggests that by decreasing the number of QD layers from the existing 24 down to, say, 5–7, and fully optimizing the growth procedure [15] would allow us to maintain a sufficient modulation depth, reduce parasitic losses, and potentially modify the width of the saturable absorption thereby improve performance of InGaP QD-based SAs. Furthermore, careful consideration of the use of resonant or antiresonant structures and associated changes in effective modulation depth, bandwidth, saturation fluence, and dispersion will be made to further optimize the overall device and laser performance taking into account that the current device resonance did not coincide with the QD peak absorption [see Fig. 3(a)]. These topics will be the subject of future work.

V. Conclusion

We have demonstrated the potential of InGaP QD-based SESAMs for passive ML of lasers emitting in the red spectral range. Pulses as short as 518 fs at 752 nm with output powers of 190 mW were obtained from a Ti : sapphire laser using QD-based material as a SA. The SESAM was characterized by way of pump–probe measurements to reveal a modulation depth of 0.35% (maximized at 756 nm), nonsaturable losses of 1.15%, 0.4-ps fast and 300-ps slow components of the absorption recovery.

References

[1] U. Keller, K. J. Weingarten, F. X. Kartner, D. Kopf, B. Braun, I. D. Jung, R. Fluck, C. Honninger, N. Matuschek, and J. Aus der Au, "Semiconductor saturable absorber mirrors (SESAM's) for femtosecond to nanosecond pulse generation in solid-state lasers," *IEEE J. Select. Top. Quantum Electron.*, vol. 2, pp. 435–453, 1996.

[2] R. Paschotta, L. Krainer, S. Lecomte, G. J. Spühler, S. C. Zeller, A. Aschwanden, D. Lorenser, H. J. Unold, K. J. Weingarten, and U. Keller, "Picosecond pulse sources with multi-GHz repetition rates and high output power," *New J. Phys.*, vol. 6, p. 174, 2004.

[3] O. Okhotnikov, A. Grudinin, and M. Pessa, "Ultra-fast fibre laser systems based on SESAM technology: New horizons and applications," *New J. Phys.*, vol. 6, p. 177, 2004.

[4] L. W. Shi, Y. H. Chen, B. Xu, Z. C. Wang, Y. H. Jiao, and Z. G. Wang, "Status and trends of short pulse generation using mode-locked lasers based on advanced quantum-dot active media," *J. Phys. D: Appl. Phys.*, vol. 40, pp. R307–R318, 2007.

[5] A. Bartels, D. Heinecke, and S. A. Diddams, "Passively mode-locked 10 GHz femtosecond Ti:sapphire laser," *Opt. Lett.*, vol. 33, pp. 1905–1907, 2008.

[6] D. Lorenser, H. J. Unold, D. J. H. C. Maas, A. Aschwanden, R. Grange, R. Paschotta, D. Ebling, E. Gini, and U. Keller, "Towards wafer-scale integration of high repetition rate passively mode-locked surface-emitting semiconductor lasers," *Appl. Phys. B*, vol. 79, pp. 927–932, 2004.

[7] E. U. Rafailov, S. J. White, A. A. Lagatsky, A. Miller, W. Sibbett, D. A. Livshits, A. E. Zhukov, and V. M. Ustinov, "Fast quantum-dot saturable absorber for passive mode-locking of solid-state lasers," *IEEE Photon. Technol. Lett.*, vol. 16, pp. 2439–2441, 2004.

[8] McWilliam, A. A. Lagatsky, C. T. A. Brown, W. Sibbett, A. E. Zhukov, V. M. Ustinov, A. P. Vasil'ev, and E. U. Rafailov, "Quantum-dot-based saturable absorber for femtosecond mode-locked operation of a solid-state laser," *Opt. Lett.*, vol. 31, pp. 1444–1446, 2006.

[9] A. Lagatsky, F. M. Bain, C. T. A. Brown, W. Sibbett, D. A. Livshits, G. Erbert, and E. U. Rafailov, "Low-loss quantum-dot-based saturable absorber for efficient femtosecond pulse generation," *Appl. Phys. Lett.*, vol. 91, pp. 231111-1–231111-3, 2007.

[10] A. B. Krysa, S. L. Liew, J. C. Lin, J. S. Roberts, J. Lutti, G. M. Lewis, and P. M. Smowton, "Low threshold InP/AlGaInP on GaAs QD laser emitting at $\sim$740 nm," *Journal of Crysal Growth*, vol. 298, pp. 663–666, 2007.

[11] V. G. Savitski, D. Burns, and S. Calvez, "Optically-pumped saturable absorber for fast switching between continuous-wave and passively mode-locked regimes of a Nd : YVO_4 laser," *Opt. Express*, vol. 17, pp. 5373–5378, 2009.

[12] C. W. Luo, Y. T. Wang, F. W. Chen, H. C. Shih, and T. Kobayashi, "Eliminate coherence spike in reflection-type pump-probe measurements," *Opt. Express*, vol. 17, pp. 11321–11327, 2009.

[13] I. D. Jung, F. X. Kärtner, N. Matuschek, D. H. Sutter, F. Morier-Genoud, Z. Shi, V. Scheuer, M. Tilsch, T. Tschudi, and U. Keller, "Semiconductor saturable absorber mirrors supporting sub-10-fs pulses," *Appl. Phys. B*, vol. 65, pp. 137–150, 1997.

[14] M. Haiml, R. Grange, and U. Keller, "Optical characterization of semiconductor saturable absorbers," *Appl. Phys. B*, vol. 79, pp. 331–339, 2004.

[15] D. J. H. C. Maas, A. R. Bellancourt, M. Hoffmann, B. Rudin, Y. Barbarin, M. Golling, T. Südmeyer, and U. Keller, "Growth parameter optimization for fast quantum dot SESAMs," *Opt. Express*, vol. 16, pp. 18646–18656, 2008.

InP/AlGaInP quantum dot semiconductor disk lasers for CW TEM_{00} emission at 716 – 755 nm

Peter J. Schlosser,[1,*] Jennifer E. Hastie,[1] Stephane Calvez,[1] Andrey B. Krysa,[2] and Martin D. Dawson[1]

[1]Institute of Photonics, University of Strathclyde, 106 Rottenrow, Glasgow G4 0NW, UK
[2]EPSRC National Centre for III-V Technologies, Department of Electronic and Electrical Engineering, University of Sheffield, Mappin Street, Sheffield S1 3JD, UK
**peter.schlosser@strath.ac.uk*

Abstract: Multiple layers of InP QDs, self-assembled during epitaxial growth, were incorporated into the active region of an $(Al_xGa_{1-x})_{0.51}In_{0.49}P$ based semiconductor disk laser with monolithic $Al_xGa_{1-x}As$ distributed Bragg reflector. Three gain structure samples were selected from the epitaxial wafer, bonded to single-crystal diamond heatspreaders and optically pumped at 532nm within a high finesse external laser cavity. Laser emission with peak wavelengths at 716, 729, and 739 nm, respectively, was achieved from the three samples; the latter demonstrating tuning from 729 to 755 nm. Maximum continuous wave output power of 52mW at 739nm was achieved with 0.2% output coupling; the threshold and slope efficiency were 220 mW and 5.7% respectively.

OCIS codes: (140.7270) Vertical emitting lasers; (140.5960) Semiconductor lasers.

References and links

1. M. Kuznetsov, F. Hakimi, R. Sprague, and A. Mooradian, "Design and characteristics of high-power (> 0.5-W CW) diode- pumped vertical-external-cavity surface-emitting semiconductor lasers with circular TEM_{00} beams," IEEE J. Sel. Top. Quantum Electron. **5**(3), 561–573 (1999).
2. S. Calvez, J. E. Hastie, M. Guina, O. Okhotnikov, and M. D. Dawson, "Semiconductor disk lasers for the generation of visible and ultraviolet radiation," Laser Photon. Rev. **3**(5), 407–434 (2009).
3. N. Schulz, J.-M. Hopkins, M. Rattunde, D. Burns, and J. Wagner, "High-brightness long-wavelength semiconductor disk lasers," Laser Photon. Rev. **2**(3), 160–181 (2008).
4. A. J. Kemp, G. J. Valentine, J. M. Hopkins, J. E. Hastie, S. A. Smith, S. Calvez, M. D. Dawson, and D. Burns, "Thermal management in vertical-external-cavity surface-emitting lasers: finite-element analysis of a heatspreader approach," IEEE J. Quantum Electron. **41**(2), 148–155 (2005).
5. B. Rudin, A. Rutz, M. Hoffmann, D. J. H. C. Maas, A.-R. Bellancourt, E. Gini, T. Südmeyer, and U. Keller, "Highly efficient optically pumped vertical-emitting semiconductor laser with more than 20 W average output power in a fundamental transverse mode," Opt. Lett. **33**(22), 2719–2721 (2008).
6. J. Lutti, P. M. Smowton, G. M. Lewis, A. B. Krysa, J. S. Roberts, P. A. Houston, Y. C. Xin, and L. F. Lester, "740nm InP/GaInP quantum -dot laser with 190 A cm-2 room temperature threshold current density," Electron. Lett. **298**, 41 (2005).
7. T. D. Germann, A. Strittmatter, J. Pohl, U. W. Pohl, D. Bimberg, J. Rautiainen, M. Guina, and O. Okhotnikov, "Quantum-dot semiconductor disk lasers," J. Cryst. Growth **310**(23), 5182–5186 (2008).
8. M. Butkus, K. G. Wilcox, J. Rautiainen, O. G. Okhotnikov, S. S. Mikhrin, I. L. Krestnikov, A. R. Kovsh, M. Hoffmann, T. Südmeyer, U. Keller, and E. U. Rafailov, "High-power quantum-dot-based semiconductor disk laser," Opt. Lett. **34**(11), 1672–1674 (2009).
9. J. E. Hastie, S. Calvez, M. D. Dawson, T. Leinonen, A. Laakso, J. Lyytikäinen, and M. Pessa, "High power CW red VECSEL with linearly polarized TEM_{00} output beam," Opt. Express **13**(1), 77–81 (2005).
10. A. B. Krysa, S. L. Liew, J. C. Lin, J. S. Roberts, J. Lutti, G. M. Lewis, and P. M. Smowton, "Low threshold InP/AlGaInP on GaAs QD laser emitting at ~740 nm," J. Cryst. Growth **298**, 663–666 (2007).
11. J. M. Hopkins, S. A. Smith, C. W. Jeon, D. Burns, S. Calvez, M. D. Dawson, T. Jouhti, and M. Pessa, "A 0.6W CW GaInNAs vertical external-cavity surface-emitting laser operating at 1.32μm," Electron. Lett. **40**(1), 30 (2004).

1. Introduction

Optically-pumped semiconductor disk lasers (SDLs), also known as vertical cavity surface emitting lasers (VECSELs) or optically-pumped semiconductor lasers (OPSLs), have shown a

#117994 - $15.00 USD Received 30 Sep 2009; revised 2 Nov 2009; accepted 8 Nov 2009; published 12 Nov 2009

dramatic increase in spectral coverage recently, due to the application of generic structural design and thermal management principles to a broad range of III-V semiconductor alloys. SDLs with Watt-level output power and characteristic high beam quality have been demonstrated at wavelengths from the red to the mid-infrared [1–5]. In addition, nonlinear frequency conversion techniques have provided selected coverage across the visible and into the ultraviolet [2]. Significant spectral gaps and regions of poor efficiency do remain, however, at the compositional and strain extremes between semiconductor alloy systems. Here, we address the important gap that exists between long-wavelength GaInP and short wavelength GaAs quantum well (QW) gain structure SDL's in the region 690 – 780 nm, for which we introduce gain structures based on InP quantum dots (QDs). Light in this spectral window is of interest for a range of applications including photodynamic therapy, sensing and biophotonics, for superior transmission through tissue and minimization of auto-fluorescence.

Quantum dots as laser gain media have generated a lot of interest, with desirable properties such as low threshold and low temperature sensitivity due to the discrete nature of the density of states. In addition, they allow the extension to longer wavelength emission over QWs since they enable the use of lower bandgap alloys with higher lattice mismatch. In recent work, Lutti et al. applied InP QDs within the gain region of electrically-injected edge emitting lasers to demonstrate room temperature emission at ~740 nm with record threshold current density of 190 A cm^{-2} [6]. Meanwhile, the feasibility of QD-based SDLs has been demonstrated with more widely-studied InAs QDs for emission wavelengths from 950 nm using submonolayer QDs to 1210 nm using QDs grown in the Stranski-Krastanow regime [7] and recently more than 4W output power has been demonstrated at 1032 nm [8]. Previously we have reported high power AlGaInP QW-based SDLs for emission up to 680nm [9]. The InP QD SDLs reported here are demonstrated to give circularly-symmetric TEM_{00} laser emission from 716 - 755nm and offer prospects for significant coverage in the red/deep red spectral region and into the near-ultraviolet by intracavity frequency doubling.

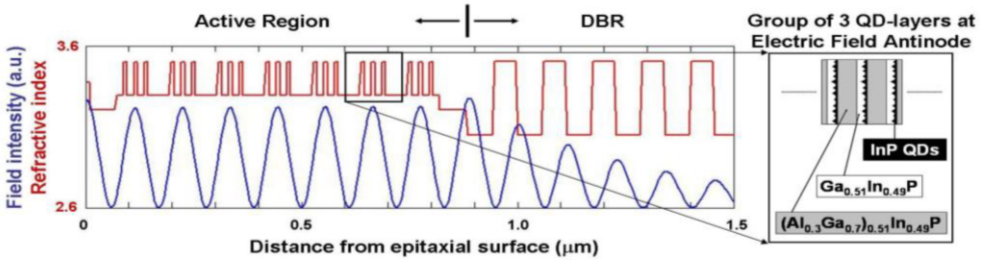

Fig. 1. Design of the SDL gain structure incorporating 7 x 3 layers of InP quantum dots within the resonant subcavity.

2. Design and growth

The SDL gain structure described in Fig. 1. consists of a multi-QD-layer active region directly on top of a distributed Bragg reflector (DBR), and was grown via metalorganic vapour phase epitaxy (MOVPE) in a low pressure (150 Torr) horizontal flow reactor with a non-rotating susceptor. The GaAs (100) substrate was misorientated 10° towards <111> to achieve disordered growth [10]. Details of the layer compositions and thicknesses are given in Table 1. The growth temperature, common for all layers, was 710 °C, with growth rates: ~7 $Å s^{-1}$ for AlGaInP, GaInP and InP; ~7.2 $Å s^{-1}$ for AlAs; ~10.2 $Å s^{-1}$ for AlGaAs. The peak photoluminescence (PL) emission of the QDs measured from previous calibration growths was 740 nm, thus the DBR centre reflectivity and subcavity resonances were designed to match. The 4λ-thick resonant subcavity, defined by the DBR and the semiconductor/air interface, absorbs ~98% of the 532nm incident pump light (after reflection losses). A total number of 21 QD-layers were incorporated within the subcavity in groups of 3 layers at each of the 7 available electric field antinodes for resonant periodic gain (RPG). Each layer of self-assembled InP QDs, having a nominal thickness of ~6.2Å, was deposited on top of the

#117994 - $15.00 USD Received 30 Sep 2009; revised 2 Nov 2009; accepted 8 Nov 2009; published 12 Nov 2009

$(Al_{0.3}Ga_{0.7})_{0.51}In_{0.49}P$ barrier material and capped by an 8-nm-thick $Ga_{0.51}In_{0.49}P$ QW to form a dot-in-well (DWELL) structure. At either end of the active region a layer of composition $(Al_{0.6}Ga_{0.4})_{0.51}In_{0.49}P$ provides additional carrier confinement and prevents carriers diffusing to the surface and recombining non-radiatively. A 10nm $Ga_{0.51}In_{0.49}P$ cap prevents oxidation of the underlying layers.

Table 1. SDL gain structure composition

Layer	Composition	x	Thickness (nm)	Description
20	$Ga_xIn_{1-x}P$	0.51	10	Cap
19	$(Al_xGa_{1x})_{0.51}In_{0.49}P$	0.6	58	Confinement
18	$(Al_xGa_{1x})_{0.51}In_{0.49}P$	0.3	16	Barrier
17 x 6	6.2Å InP +$Ga_xIn_{1-x}P$	0.51	8	QD + QW
16 x 6	$(Al_xGa_{1-x})_{0.51}In_{0.49}P$	0.3	16	Barrier
15 x 6	6.2Å InP + $Ga_xIn_{1-x}P$	0.51	8	QD + QW
14 x 6	$(Al_xGa_{1-x})_{0.51}In_{0.49}P$	0.3	16	Barrier
13 x 6	6.2Å InP + $Ga_xIn_{1-x}P$	0.51	8	QD + QW
12 x 6	$(Al_xGa_{1-x})_{0.51}In_{0.49}P$	0.3	53	Barrier
11	6.2Å InP + $Ga_xIn_{1-x}P$	0.51	8	QD + QW
10	$(Al_xGa_{1-x})_{0.51}In_{0.49}P$	0.3	16	Barrier
9	6.2Å InP + $Ga_xIn_{1-x}P$	0.51	8	QD + QW
8	$(Al_xGa_{1-x})_{0.51}In_{0.49}P$	0.3	16	Barrier
7	6.2Å InP + $Ga_xIn_{1-x}P$	0.51	8	QD + QW
6	$(Al_xGa_{1-x})_{0.51}In_{0.49}P$	0.3	16	Barrier
5	$(Al_xGa_{1-x})_{0.51}In_{0.49}P$	0.6	64	Confinement
4	AlAs		60	DBR
3 x 40	$Al_xGa_{x-1}As$	0.35	51.5	DBR
2 x 40	AlAs		60	DBR
1	GaAs		500	Buffer

3. Experimental details and results

3.1 Wafer characterization

Prior to growth of the SDL gain structure, a calibration growth run of the gain region without the DBR was carried out and the room temperature photoluminescence is shown in Fig. 2. The substrate was not rotated during epitaxial growth of the SDL gain structure resulting in non-uniformity of the layer thicknesses across the wafer. Reflectivity measurements undertaken at room temperature revealed that the centre of the DBR stopband under these conditions varied from 718 – 770nm, with the subcavity resonance wavelength, indicated by a dip in the reflectivity, typically positioned at the centre of the stopband. Photoluminescence, excited by pumping at 532nm and collected at normal incidence to the sample surface, had a characteristic peak at the subcavity resonance wavelength. The non-uniformity of the wafer allowed the selection of gain structure samples with varying resonance offsets. Three samples, A, B, and C, were cleaved from the wafer with subcavity resonance wavelengths of 733, 745 and 750 nm, respectively (see Fig. 2). Also shown is the free-running emission spectrum of the SDL for each sample, which will be discussed in the following section.

#117994 - $15.00 USD Received 30 Sep 2009; revised 2 Nov 2009; accepted 8 Nov 2009; published 12 Nov 2009

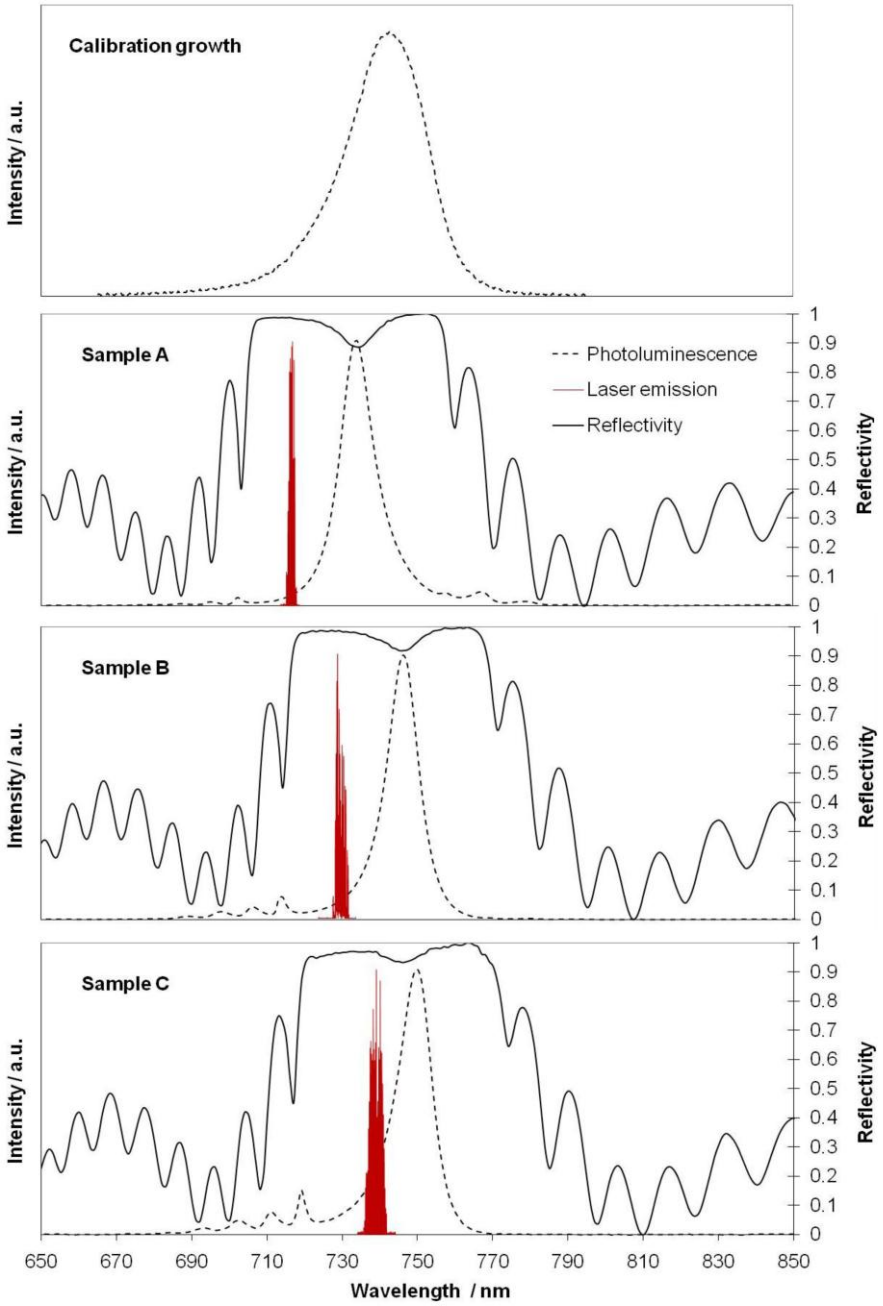

Fig. 2. Room temperature photoluminescence of the gain region calibration growth (top) and room temperature reflectance (bold) and photoluminescence (dashed) measurements for all three samples from the SDL gain structure. Also shown are the respective free-running SDL emission spectra.

3.2 Laser performance

In order to assess laser performance, a 'standard' 3-mirror resonator was set up, consisting of the SDL gain structure sample to be tested as one end mirror, a highly reflecting (HR) curved

#117994 - $15.00 USD Received 30 Sep 2009; revised 2 Nov 2009; accepted 8 Nov 2009; published 12 Nov 2009

folding mirror of 100 mm radius of curvature and a plane HR end mirror. A commercial frequency-doubled Nd:YVO_4 laser was used to optically-pump the SDL with up to 2.5W at 532 nm. The pump spot was ~74 μm in diameter with the SDL cavity aligned to match the intra-cavity mode; cavity arm lengths were, from the sample, 55mm and 270mm. For efficient thermal management, each sample was mechanically polished to remove ~150μm of the substrate (initial substrate thickness: 400μm) before a 500-μm-thick single crystal diamond heatspreader [11] was optically bonded to the intra-cavity surface. The sample and heatspreader were clamped in a brass mount kept at 7 °C via water cooling.

This arrangement yielded a near diffraction limited, circularly symmetric TEM_{00} output beam profile with M^2 measured to be less than 1.1. The SDL incorporating, in turn, gain structure samples A, B and C had centre emission wavelength of 716, 728 and 740 nm, respectively. The free running laser emission spectra in each case, shown in Fig. 3a, are modulated by the etalon effect of the diamond heatspreader with a fringe peak separation of ~0.2 nm.

A 1-mm-thick birefringent filter (BRF) was placed at Brewster's angle in the long arm of the cavity. By rotation of the BRF, a tuning range of 26 nm from 729 to 755 nm could be achieved using sample C (see Fig. 3b). Also shown is an example of the narrowed laser output spectrum with the BRF rotation angle set for transmission near the peak of the available tuning range (~732 nm). The FWHM of the spectrum is less than 0.05 nm, limited by the resolution of the optical spectrum analyser.

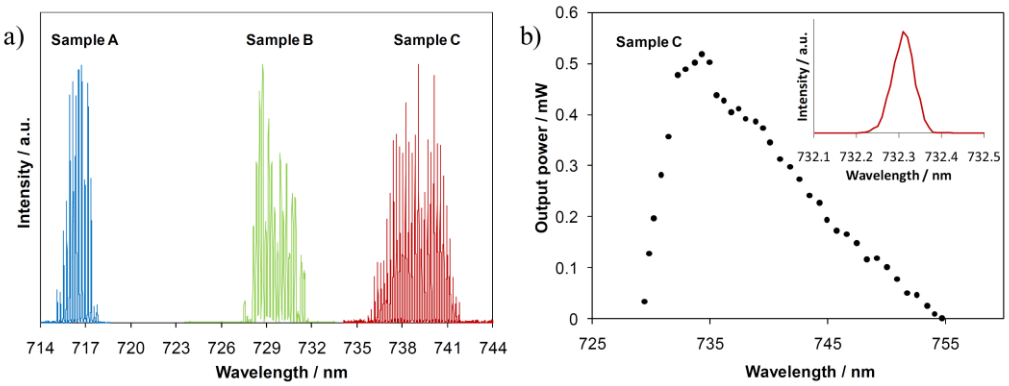

Fig. 3. SDL emission spectra. a) Emission spectra of the free-running SDL incorporating gain structure samples A, B, and C. b) Tuning curve obtained with sample C by insertion and rotation of an intracavity birefringent filter in an all-HR mirror cavity. Inset: an example of the narrowed laser emission spectrum during tuning.

The plane HR end mirror was replaced with an output coupler with measured transmission 0.22 ± 0.02% across the wavelength range of interest. Power transfer measurements were taken for the SDL incorporating each sample in turn (see Fig. 4). Laser characteristics are summarized in Table 2. The slope efficiency for all samples is ~5%, however the threshold, and by implication the transparency carrier density, varies with the emission wavelength, most likely due to variation of the overlap with the QD peak gain. Thermal rollover occurs for ~1.5W pump power for all samples, so that the highest output power, 52 mW, is achieved for the sample (C) with the lowest pump threshold (220mW).

#117994 - $15.00 USD Received 30 Sep 2009; revised 2 Nov 2009; accepted 8 Nov 2009; published 12 Nov 2009

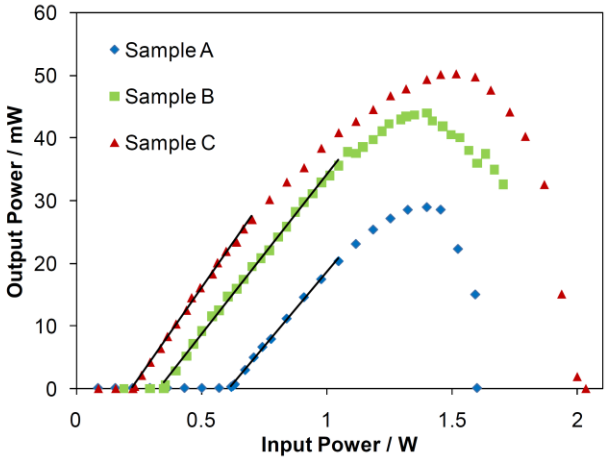

Fig. 4. Power transfer measurements for the SDL incorporating each gain structure sample. A linear fit to the data as shown was used to calculate the threshold and slope efficiency before rollover. Output coupling was 0.2%.

Table 2. Summary of SDL characteristics using different gain structure samples

Sample	Subcavity resonance λ (nm) [1]	Laser emission λ (nm) [2]	Threshold (mW) [3]	Slope Efficiency (%) [3]
A	733	716	610	4.8
B	745	729	330	5.1
C	750	739	220	5.7

[1]Measured via surface photoluminescence at room temperature.
[2]Free-running laser.
[3]Calculated via a linear fit to the data before rollover.

4. Conclusions

InP quantum dot gain structures have been investigated, for the first time to our knowledge, as a means to extend the wavelength coverage of semiconductor disk lasers into the applications-rich spectral gap between 690 and 780nm. Multiple layers of InP quantum dots embedded within InGaP quantum wells were incorporated into an AlGaInP gain region grown on top of an AlGaAs distributed Bragg reflector. Laser emission from 716 – 755 nm with wavelength tuning up to 26nm was demonstrated using different samples from a spatially graded gain structure. The threshold power was shown to increase with increasing offset between the laser operating wavelength and the peak emission wavelength of the QD distribution. The mechanism responsible for setting the laser wavelength is as yet unidentified, however it is believed to be due to non-optimised overlap of the sub-cavity resonance and the QD gain. For this particular gain structure, the emission wavelength was, on average, ~14 nm shorter than the measured surface photoluminescence peak. This first demonstration opens the way to a range of novel red/deep red and (via intracavity second harmonic generation) near-ultraviolet tunable laser sources. Improved output power and slope efficiency may be expected via the optimization of the number of quantum dot layers and the overlap of the resonances with the QD distribution.

Acknowledgements

The authors would like to thank Peter M. Smowton of the University of Cardiff for helpful discussions. This work was supported by the Engineering and Physical Sciences Research Council, UK under grant no. EP/E056989.

#117994 - $15.00 USD Received 30 Sep 2009; revised 2 Nov 2009; accepted 8 Nov 2009; published 12 Nov 2009

Singly-resonant sum frequency generation of visible light in a semiconductor disk laser

Martin Thalbitzer Andersen[1], Peter J. Schlosser[2], Jennifer E. Hastie[2], Peter Tidemand-Lichtenberg[1], Martin D. Dawson[2] and Christian Pedersen[1]

[1]DTU Physics, Department of Physics, Technical University of Denmark, 2800 Kgs. Lyngby, Denmark
[2]Institute of Photonics, SUPA, University of Strathclyde, Glasgow G4 0NW, Scotland
mand@fysik.dtu.dk

Abstract: In this paper a generic approach for visible light generation is presented. It is based on sum frequency generation between a semiconductor disk laser and a solid-state laser, where the frequency mixing is achieved within the cavity of the semiconductor disk laser using a single-pass of the solid-state laser light. This exploits the good beam quality and high intra-cavity power present in the semiconductor disk laser to achieve high conversion efficiency. Combining sum frequency mixing and semiconductor disk lasers in this manner allows in principle for generation of any wavelength within the visible spectrum, by appropriate choice of semiconductor material and single-pass laser wavelength.

OCIS codes: (140.3480) Lasers, diode-pumped; (140.5960) Semiconductor lasers; (140.7300) Visible lasers; (190.0190) Nonlinear optics.

References and links

1. K. Schneider, S. Schiller, and J. Mlynek, "1.1-W single-frequency 532-nm radiation by second-harmonic generation of a miniature Nd:YAG ring laser," Opt. Lett. **21**, 1999-2001 (1996).
2. T. A. Driscoll, H. J. Hoffman, R. E. Stone, and P. E. Perkins, "Efficient second-harmonic generation in KTP crystals," JOSA B, **3**, 683-686 (1986)
3. C. Schriever, S. Lochbrunner, P. Krok, and E. Riedle, "Tunable pulses from 300 to 970 nm with durations down to 14 fs based on a 2 MHz ytterbium-doped fiber system," Opt. Lett. **33**, 192-194 (2008).
4. J. H. Lundeman, O. B. Jensen, P. E. Andersen, S. Andersson-Engels, B. Sumpf, G. Erbert, and P. M. Petersen, "High power 404 nm source based on second harmonic generation in PPKTP of a tapered external feedback diode laser," Opt. Express **16**, 2486-2493 (2008).
5. J. Janousek, S. Johansson, P. Tidemand-Lichtenberg, S. Wang, J. L. Mortensen, P. Buchhave, and F. Laurell, "Efficient all solid-state continuous-wave yellow-orange light source," Opt. Express **13**, 1188-1192 (2005).
6. S. Johansson, S. Spiekermann, S. Wang, V. Pasiskevicius, F. Laurell, and K. Ekvall, "Generation of turquoise light by sum frequency mixing of a diode-pumped solid-state laser and a laser diode in periodically poled KTP," Opt. Express **12**, 4935-4940 (2004).
7. S. Johansson, S. Wang, V. Pasiskevicius, and F. Laurell, "Compact 492-nm light source based on sum-frequency mixing," Opt. Express **13**, 2590-2595 (2005).
8. E. Karamehmedović, C. Pedersen, M. T. Andersen, and P. Tidemand-Lichtenberg, "Efficient visible light generation by mixing of a solid-state laser and a tapered diode laser," Opt. Express **15**, 12240-12245 (2007).
9. S. Calvez, J. E. Hastie, M. Guina, O. Okhotnikov, and M. D. Dawson, "Semiconductor disk lasers for the generation of visible and ultraviolet radiation," Laser Photon. Rev. published on-line 13th January 2009.
10. A. Härkönen, J. Rautiainen, T. Leinonen, Y. A. Morozov, L. Orsila, M. Guina, M. Pessa, and O. G. Okhotnikov, "Intracavity sum-frequency generation in dual-wavelength semiconductor disk laser," IEEE Photon. Technol. Lett. **19**, 1550-1552 (2007).
11. J. Chilla, Paper PTuD3, in: Proceedings of the Conference on Photonic Applications Systems Technologies, San Jose, 2008.
12. J.-Y. Kim, S. Cho, J. Lee, G. B. Kim, S.-J. Lim, J. Yoo, K.-S. Kim, S.-M. Lee, J. Shim, T. Kim, and Y. Park, "A measurement of modal gain profile and its effect on the lasing performance in vertical-external-cavity surface-emitting lasers," IEEE Photon. Tech. Lett. **18**, 2496-2498 (2006).
13. D. R. Preuss and J. L. Gole, "Three-stage birefringent filter tuning smoothly over the visible region: theoretical treatment and experimental design," Appl. Opt. 19, 702-710 (1980).

#107978 - $15.00 USD Received 24 Feb 2009; revised 25 Mar 2009; accepted 25 Mar 2009; published 30 Mar 2009

1. Introduction

The development of efficient, compact and robust laser sources in the visible and UV spectral range is the subject of intensive research, for applications in areas as diverse as optical spectroscopy, projection displays, bio- and chemical sensing, and biomedical diagnostics. The generation of visible light from optically-pumped solid-state and semiconductor lasers is usually achieved via second harmonic generation (SHG), as the transition lines of most conventional doped dielectric laser crystals and the semiconductor bandgaps of the most common III-V semiconductor alloys are in the near infrared (NIR). SHG has been demonstrated for numerous diode-pumped solid-state (DPSS) lasers, both in continuous wave (CW) and pulsed [1, 2] operation, fiber lasers [3], and external cavity diode lasers (ECDL) [4]. One of the main limitations to the SHG-based visible light sources is that these devices are limited by the available NIR laser lines. One approach to reach spectral ranges difficult to access via SHG is through sum frequency generation (SFG), either combining two solid-state lasers [5], a solid-state and a semiconductor laser [6, 7] or an ECDL [8]. The latter allows for some tuning of the generated light, provided that the nonlinear process can accommodate phase-matching over the tuning range of the ECDL. The generated wavelength is calculated from the photon energy of the two mixed laser lines.

SHG has provided the main route to visible and UV light emission from semiconductor disk lasers (SDLs) also referred to as vertical-external-cavity surface-emitting-lasers (VECSELs) [9]. These devices have been developed into commercially available products, delivering Watt-level output power at specific wavelengths in the visible, as replacements for DPSS lasers and argon ion lasers. Despite broad tuneability in the NIR, gaps and regions of low efficiency remain in the spectral coverage of SDLs at the compositional and strain extremes of available semiconductor quantum well alloys, with corresponding gaps in the second harmonic spectrum [9].

SFG has also been demonstrated within SDLs where both fundamental wavelengths are generated within the laser cavity. Härkönen et al. mixed both fundamental wavelengths of a dual-wavelength infrared SDL in an intra-cavity LBO crystal for conversion to a single visible wavelength [10], and more recently Chilla demonstrated frequency tripling between the intra-cavity second harmonic and fundamental beams of an infrared SDL containing two nonlinear crystals (both LBO), providing access to the near UV [11].

In this work a generic 'hybrid' approach based on SFG between a single-pass NIR laser source and the intra-cavity field of a SDL is suggested. The approach is experimentally demonstrated through sum frequency mixing of a single-pass Nd:YVO_4 solid-state laser at 1342 nm and an InGaAs-based SDL with peak emission at 1064 nm to generate light at 593 nm. In the following the experimental setup is described, including the fundamental performance of each of the two laser sources, followed by analysis of the nonlinear frequency conversion and the measured parameters of the generated light. We conclude with a brief discussion on the prospects for broad wavelength tuning of this type of device.

2. Experimental configuration

Figure 1 depicts the experimental configuration. The SDL was designed as a 4-mirror, z-fold cavity with an InGaAs SDL gain structure, similar in design and structure to that reported earlier [12], acting as a planar end mirror. The cavity mirrors M1, M2 and M3 were high reflectivity (HR) coated at 1064 nm and high transmittance (HT) at 808 nm, all mirrors had a radius of curvature of -100 mm. In order to match the cavity mode to a pump spot size of ~80 μm at the SDL, the cavity arm lengths were set to be: 53 mm, 457 mm, and 156 mm, respectively. An additional beam waist (~53 μm) was located in one cavity arm, where the nonlinear crystal was positioned. For this experiment a 10 mm Brewster-cut periodically-poled $KTiOPO_4$ (PPKTP) crystal with an effective nonlinear coefficient of d_{eff} = 10 pm/V was used. The middle arm contained a three-plate birefringent filter (BRF) for wavelength tuning of around 30 nm, centered at an emission wavelength of 1055 nm.

#107978 - $15.00 USD Received 24 Feb 2009; revised 25 Mar 2009; accepted 25 Mar 2009; published 30 Mar 2009

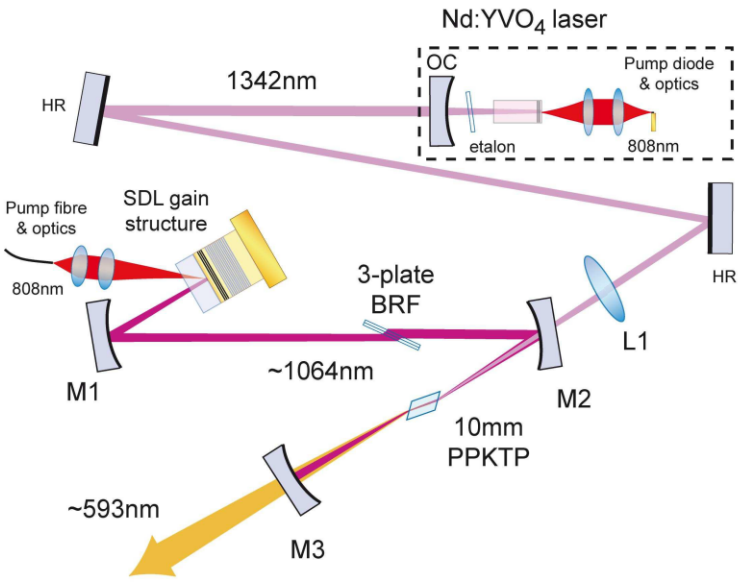

Fig. 1. Experimental setup for generation of 593 nm yellow-orange light within a high finesse SDL cavity, including PPKTP at an intra-cavity focus and a single-pass of the output beam of a diode-pumped Nd:YVO_4 solid-state laser. HR: high reflector; OC: output coupler; BRF: birefringent filter.

13 W of optical pump power were incident at the SDL structure applied by an 808 nm fiber-coupled diode laser. At this power level a high heat load is introduced into the semiconductor structure and therefore a 500-µm-thick diamond heatspreader was liquid capillary bonded to the intra-cavity surface of the semiconductor for thermal management and the structure kept at a temperature of 0 ºC via a water/glycol cooled brass mount.

The single-pass 1342 nm beam was generated by an 8 mm long *a*-cut Nd:YVO_4 crystal (0.5 atm% Nd-doped), pumped by an 808 nm 4 W broad area laser diode. The pump-side facet of the crystal was coated for HR and HT at 1342 nm and 808 nm respectively, whereas the intra-cavity facet was anti-reflection (AR) coated at 1342 nm. The cavity was established between the HR coated facet and a 2% output coupler (OC) of -200 mm radius of curvature. A 0.3-mm-thick intra-cavity etalon enabled wavelength tuning and line shape narrowing. The beam was aligned and focused into the PPKTP-crystal by two plane steering mirrors and a lens L1 (f = 120 mm, measured power transmittance at 1342 nm ~93 %). The 1342 nm beam was coupled into the PPKTP crystal through mirror M2, having a measured power transmittance of ~87 % at this wavelength.

The sum frequency generated beam at ~593 nm was coupled out through the end mirror M3 with a measured power transmittance of ~85 %.

3. Laser characterization

In order to achieve efficient sum frequency conversion, three conditions must be met: the fundamental power levels reaching the nonlinear crystal must be maximized; the spectrum of the fundamental fields must be within the spectral acceptance bandwidth of the nonlinear material; and the state of polarization of the fields must align with the highest possible second order susceptibility of the nonlinear material.

SDLs have a significant gain bandwidth, allowing for broad tuning around their design wavelength, which typically leads to broadband emission. It is therefore necessary to

#107978 - $15.00 USD Received 24 Feb 2009; revised 25 Mar 2009; accepted 25 Mar 2009; published 30 Mar 2009

introduce intra-cavity spectral filters to narrow and tune the emission spectrum. This was done by placing the three-plate quartz BRF (also known as a Lyot filter) within the SDL cavity, plate thicknesses 4-, 2-, and 1-mm where the thickest BRF determines the filter resolution and the thinnest the free spectral range [13]. Figure 3(a) illustrates the measured SDL spectrum using the three-plate BRF. The linewidth was measured to be less than 0.1 nm (corresponding to 125 longitudinal cavity mode spacings), which is comparable to the linewidth achievable by a single 4 mm BRF. The benefit of the three-plate filter in this case is to suppress the additional peaks allowed by the single BRF, Fig. 3(b), which broaden the emission spectrum, thus lowering the conversion efficiency. The separation of the additional peaks corresponds to the free spectral range (~0.4 nm) of the 500-μm-thick diamond heatspreader. By monitoring the fundamental power leakage through mirror M1 (measured transmission 0.017 %), the circulating power within the SDL was estimated to be approx. 40 W.

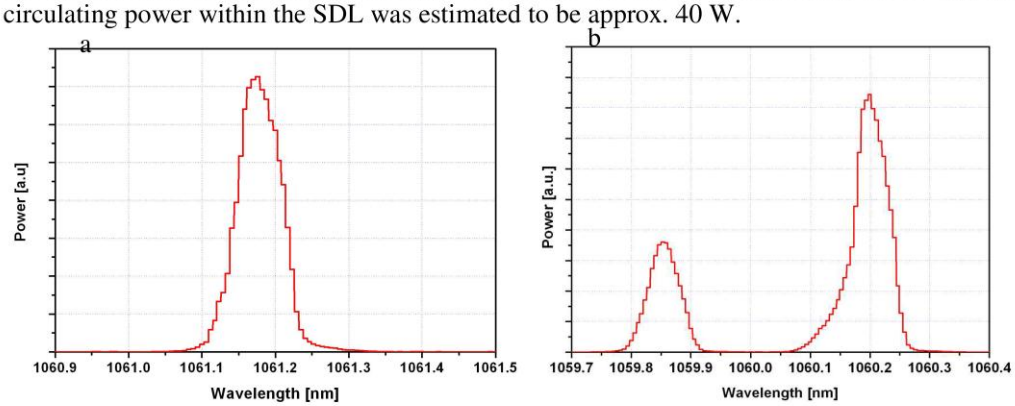

Fig. 3. Spectrum of the SDL: (a) using a three-plate BRF. The spectral line width is <0.1 nm, no additional peaks were seen using the three-plate filter. (b) using a simple 4mm BRF.

The 1342 nm transition line of Nd:YVO_4 has a narrow gain bandwidth compared to the SDL and therefore a thin intra-cavity etalon, in this case 0.3 mm thick, is sufficient to ensure a spectral emission of less then 0.2 nm (corresponding to 30 longitudinal mode spacings). The corresponding spectra and tuning range obtained by tilting the etalon are shown in Fig. 4(a). The measured power performance is shown in Fig. 4(b), for an emission wavelength of 1342.4 nm, corresponding to the red line spectrum of Fig. 4(a). The maximum output power of the Nd:YVO_4 laser was 900 mW at 1342.4 nm. Approximately 20 % is lost via the two steering mirrors, the mode matching lens L1 and mirror M2, lowering the maximum input power at the nonlinear material to less than 700 mW.

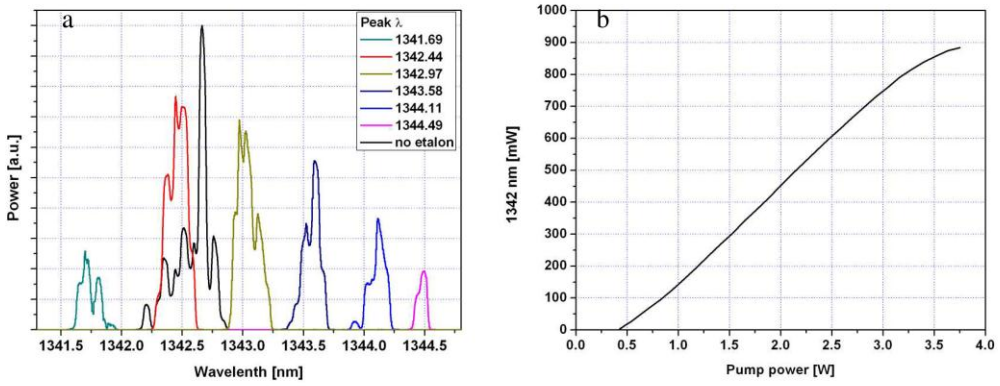

Fig. 4. Characteristics of the 1342 nm laser with intra-cavity 0.3 mm-thick etalon. (a) Output spectra obtained over the tuning range of the laser by means of tilting the etalon, and (b) slope efficiency at 1342.4 nm.

#107978 - $15.00 USD Received 24 Feb 2009; revised 25 Mar 2009; accepted 25 Mar 2009; published 30 Mar 2009

4. Sum frequency generation

For efficient phase-matching, the temperature of the PPKTP crystal could be regulated within the range 22 to 52 ºC. In order to generate the data plotted in Fig. 5, the wavelengths of the SDL and single-pass laser were kept fixed at 1063 nm and 1342.4 nm respectively, while the temperature of the PPKTP crystal was scanned through this temperature range. Optimum phase-matching was found for a PPKTP temperature of 42 °C, which is in close agreement with that predicted theoretically using the Sellmeier equations for KTP (PPKTP poling period 12.65 μm).

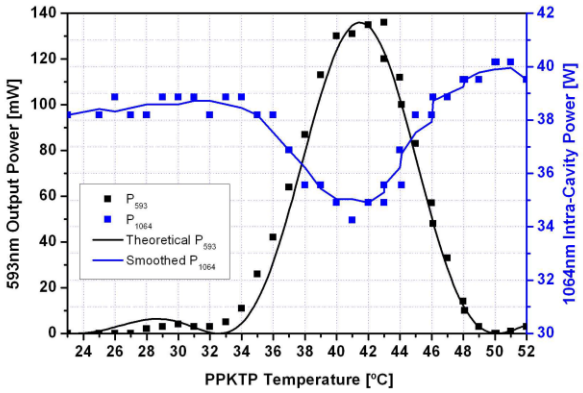

Fig. 5. Measured phase-matching temperature acceptance bandwidth of the PPKTP crystal shown as the generated output power at 593 nm as a function of crystal temperature. Close agreement with the theoretical curve is seen. Also shown is the simultaneous measurement of circulating intra-cavity power at 1064 nm. The data is averaged over 5 points using adjacent-averaging. The underlying decrease in intra-cavity power going from 50 to 24 degrees relates to alignment drift of the system during the course of the measurement.

A maximum generated power of 136 mW at 593 nm was obtained, corresponding to a conversion efficiency of ~20 % of the single-pass 1342 nm power. It is expected that the conversion efficiency of the system can be improved to more than 30 % by optimization of the polarization extinction ratio of the intra-cavity 1064 nm power. The extinction ratio was measured to be approx 1/65, see Fig. 6. The limited extinction ratio is due to the intrinsic unpolarized nature of the vertically-emitting semiconductor gain region, and imperfections in the alignment of the many intra-cavity Brewster's surfaces, which also adds to the intra-cavity losses limiting the circulating power in the 1064 nm cavity.

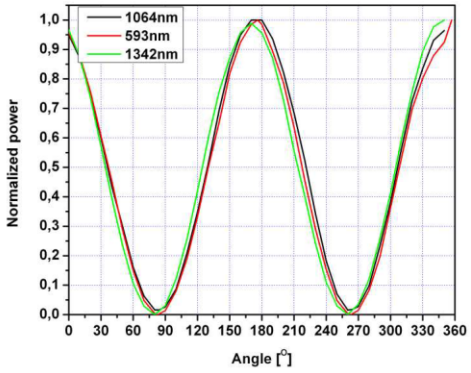

Fig. 6. Polarization characteristics of the fundamental and generated beams: measured power transmitted through a polarizing beamsplitter cube as it is rotated 360°.

#107978 - $15.00 USD Received 24 Feb 2009; revised 25 Mar 2009; accepted 25 Mar 2009; published 30 Mar 2009

The generated power is shown as a function of single-pass power in Fig. 7. It is worth noting the linear slope, even at low power levels, which is in strong contrast to second harmonic generation, as the up-conversion efficiency is independent of the power of the single-pass laser. This means that even very weak single-pass signals can be up-converted to a new wavelength with high efficiency.

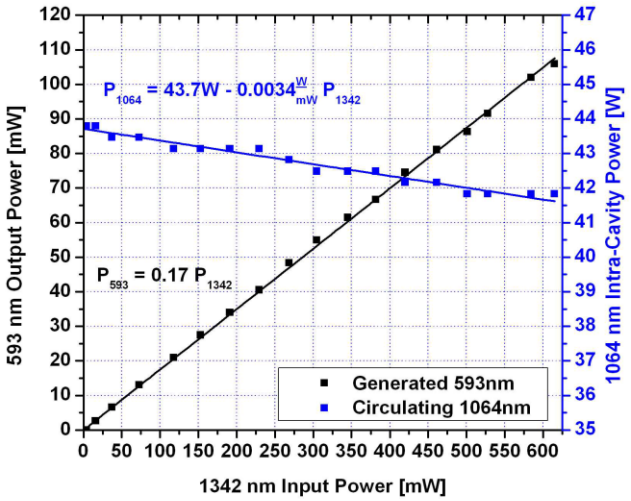

Fig. 7. Generated output power at 593 nm and intra-cavity circulating power at 1064 nm as a function of single-pass 1342 nm power.

5. Wavelength tuning

As mentioned in the introduction, and demonstrated in [9], one of the interesting features of using semiconductor materials as gain media is the significant gain bandwidth of these devices. To investigate the potential tuning range of the frequency-mixed system, a numerical model based on the Sellmeier equations for KTP and the available tuning range of the SDL was written and the results are shown in Fig. 8.

In Fig. 8(a) and (b) the dotted lines are iso-wavelength lines for the generated field; the line in the upper right corner corresponds to 600 nm and the lower left line corresponds to 582 nm. The blue crosses in Fig. 8(a) and (c) indicate phase-matching curves for PPKTP maintained at a fixed temperature of 18, 43 and 52 ^{o}C, respectively, and the solid blue lines indicate the possible tuning range of the 1342 nm laser. In order for the nonlinear PPKTP crystal to accommodate phase-matching over the entire tuning range available from the SDL, a temperature scan of more than 250 ^{o}C is needed. As shown, a wavelength tuning of less than 2 nm / 34 ^{o}C was achieved using PPKTP. Using type I phase-matched LBO a numerical calculation shows that a wavelength tuning of almost 10 nm in the generated field can be achieved by changing the LBO temperature 10 ^{o}C, see Fig. 8(b), however, using LBO compared to PPKTP reduces the nonlinear coefficient by almost one order of magnitude, thus reducing the overall conversion efficiency of the system. A magnified view of the indicated range in Fig. 8(a) is shown in Fig. 8(c) with experimentally measured points that are seen to agree closely with theoretically predicted values.

It is clearly seen that dual wavelength tuning to allow fixed temperature operation of the nonlinear material is not possible at the wavelengths investigated in the present setup. However, other wavelength ranges or alternative nonlinear materials with different dispersion relations would perhaps make dual wavelength tuning possible. Alternatively, chirped or fanned poling structures could enable significant tuning of such devices.

Another important consideration when making broadly tunable devices is to keep losses low over the entire tuning range. Using Brewster-cut nonlinear materials, as opposed to plane-cut AR coated crystals, ensures very low losses over a broad tuning range of the mixing

#107978 - $15.00 USD Received 24 Feb 2009; revised 25 Mar 2009; accepted 25 Mar 2009; published 30 Mar 2009

wavelengths. The use of the Brewster-cut also allows true single-pass configurations as the refraction angle is different for the different wavelengths, therefore there is no residual feedback for the single-pass laser. Finally the cost of Brewster-cut crystals in low quantities are significantly lower than for coated crystals.

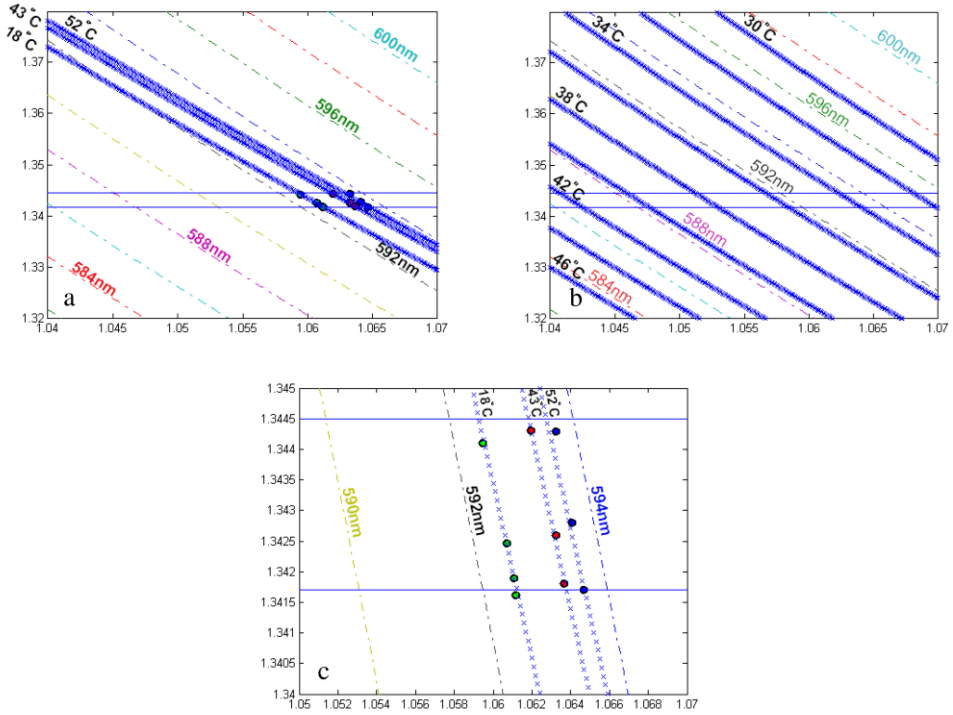

Fig. 8. Phase-matching diagrams for sum-frequency mixing between wavelengths centered around 1055 nm and 1342 nm for the full tuning ranges available from the lasers used. Dotted lines indicate iso-wavelength curves for the generated light, and blue crosses indicate phase-matching curves for the nonlinear crystal at different temperatures. (a) for PPKTP at three different temperatures, from left to right 18, 43 and 52 °C, (b) for type-I phase-matched LBO, (c) green, red and blue points show measured data for PPKTP at 18, 43 and 52 °C.

6. Conclusion

A generic approach to visible light generation has been presented, using a semiconductor disk laser as one of two mixing lasers, allowing for generation of high power single-frequency intra-cavity fields tunable over a broad range of wavelengths in the NIR (depending on the composition of the gain structure). Combining these devices with efficient quasi phase-matched nonlinear crystals and single-pass lasers delivering Watt levels of power, it is in principle possible to generate hundreds of mW of power anywhere in the visible spectrum with the possibility for tuning of the generated wavelength. However, if the full tuning potential of the SDL is to be transferred to the visible spectral region, tuning of the phase-match condition is needed, either using a fanned structure combined with mechanical movement or using a chirped structure at the expense of reduced efficiency.

As demonstrated in this experimental realization, 136 mW of output power in the orange spectral range has been reached. Although this first demonstration has a lower efficiency compared to more mature systems based on two solid-state lasers, the potential of using semiconductor disk lasers in combination with intra-cavity sum-frequency mixing has been demonstrated.

#107978 - $15.00 USD Received 24 Feb 2009; revised 25 Mar 2009; accepted 25 Mar 2009; published 30 Mar 2009

Acknowledgment

This work was supported by the Danish Technical Research Council, grant 274-05-0377.
JEH gratefully acknowledges the support of a research fellowship funded by the Royal Academy of Engineering and the Engineering and Physical Sciences Research Council.

#107978 - $15.00 USD Received 24 Feb 2009; revised 25 Mar 2009; accepted 25 Mar 2009; published 30 Mar 2009